Ocean data assimilation using the Temperature-Salinity relation and water mass diagnostics

Alberto Troccoli

Doctor of Philosophy
The University of Edinburgh
2000



Declaration

This thesis has been composed by myself, and all work reported herein is my own except where otherwise stated.

"The truth is rarely pure and never simple"
from "The Importance of Being Earnest" by Oscar Wilde

"It's easy to lose sight of the sea for the waves"
adapted from "It's easy to lose sight of the wood for the trees"

Acknowledgements

Many people have contributed to the successful completion of this thesis.

I'd like to thank my supervisor, Keith Haines, for the excellent opportunity he offered to me, for the inspiring discussions, for his help and support throughout this project. Thanks also to the members of the Department of Meteorology for the help I have received and for creating a good, friendly atmosphere in which to work. A particular thank you goes to Keith Weston for his precious advices.

Many thanks to David Anderson, Jochen Segschneider, Magdalena Alonso Balmaseda, Jerome Vialard and Tim Stockdale for the exciting and fruitful experience in the Seasonal Forecasting Group at the ECMWF.

Thanks also to Piero Lionello for allowing me to continue the writing up whilst working at the University of Padova.

Last but not least, special thanks must go to all my friends in Edinburgh and in Padova: in their hearts they know who they are! A special mention goes to Elena for her cheerful and indomitable support during the last year and to my family, who have supported me in everything I have done.

This work was almost entirely supported financially by the EC grant ENV-CT95-0113 AGORA project and a grant from SOC - thanks again to Keith Haines. Part of this work has been supported by the European Union Environment and Climate project DUACS (ENV4-CT96-0357) during a 3-month collaboration at the ECMWF - thanks again to David Anderson.

Abstract

In this thesis a novel method for assimilating upper ocean temperature profiles with salinity adjustments into numerical ocean models is presented. The approach uses a T–S relation more local in space and time than the climatological T–S used in previous studies. The assimilation method also avoids convective instability as the temperature data are introduced. In order to test the method, three sets of experiments are carried out.

First, Conductivity-Temperature-Depth measurements in the western tropical Pacific, and also instantaneous fields from an ocean model, are used to test the assimilation method by combining one profile with another. These tests recover the salinity profiles and the 0–500-m dynamic height very well (differences smaller than 1 dyn cm). By contrast, analyses using a climatological T–S relation did not provide a good salinity profile or dynamic height (greater than 3 dyn cm errors).

Second, a synthetic assimilation experiment using a 3-D primitive equation model is carried out. Four runs are considered: the truth (Tr), the parallel (Pa) and two assimilation runs, one in which the salinity method is applied (A_{ST}) and the other in which salinity is left unmodified during the temperature assimilation (A_{SZ}). The only difference between Pa and Tr is that Pa is forced by a wind stress 15% larger than Tr, so as to simulate a systematic observational error. A_{ST} and A_{SZ} use the same forcings as Pa. Vertical temperature profiles down to a depth of 525 m are taken as synthetic data from Tr and assimilated every 30 days for two years into A_{ST} and A_{SZ}. Results show that A_{ST} yields better salinity analyses than both Pa and A_{SZ}, which, in terms of rms errors, translate into at least 15% improvement at the end of the 2-year experiment. In addition to assessing the success of the assimilation method (e.g. using T and S rms), a more physical analysis of the model modifications, due to the assimilation, is presented.

Third, the salinity scheme was tested using real temperature observations on a global circulation model at the Seasonal Forecasting group used by the European Centre for Medium-Range Weather Forecasts (ECMWF). Two data assimilation experiments are performed for the 9-year period 1990-1998. These show that the salinity scheme is effective at maintaining the halocline and thermocline structures especially in tropical regions. In addition to the improvement of the mean state, the scheme allows more temporal variability than relaxation to climatological data. Some limitations of the scheme are on occasion apparent, however. These limitations might be reduced in the future by use of altimeter sea level or sea surface salinity observations from satellite.

Contents

Abstract iv

1 Introduction 1
- 1.1 State-of-the-art . . . 7
- 1.2 Aim of this work . . . 7
- 1.3 A T–S preservation application: water mass tracking . . . 8
- 1.4 Thesis outline . . . 9

2 Background 10
- 2.1 Properties of sea water . . . 10
  - 2.1.1 The T–S diagram . . . 17
- 2.2 Water masses and water types . . . 17
- 2.3 T–S preservation hypothesis . . . 19
- 2.4 T–S preservation and potential vorticity conservation . . . 21
- 2.5 Sea surface fluxes . . . 26
  - 2.5.1 The total heat flux . . . 27
  - 2.5.2 The mass flux and the salinity balance . . . 28
  - 2.5.3 The momentum flux . . . 29
- 2.6 Available observations . . . 29
- 2.7 Data assimilation methods . . . 32

3 A Salinity Analysis Algorithm 36
- 3.1 Introduction . . . 36
- 3.2 Vertical displacement . . . 37
- 3.3 T–S preservation . . . 40
  - 3.3.1 The monotonic case . . . 40
  - 3.3.2 Temperature inversions . . . 45
  - 3.3.3 The salinity method at work . . . 46
- 3.4 Enlarging the scope of the method: the inventory . . . 50

4 Data Analysis and Test of the Method 58
- 4.1 Data set . . . 58
- 4.2 Evaluation of the T–S for deriving salinity profiles . . . 60
  - 4.2.1 High-frequency analysis of 10-day period: $S(z)$ versus $S(T)$ . . . 61
  - 4.2.2 Weekly analysis: $S(z)$ versus $S(T)$ . . . 63
  - 4.2.3 Seasonal analysis: $S(T)$ versus $S_{cl}(T)$ . . . 65

4.3 Assimilation results . . . 66
4.3.1 Daily assimilation . . . 69
4.3.2 Weekly assimilation . . . 69
4.3.3 Seasonal assimilation . . . 71
4.3.4 Model field assimilation . . . 71
4.4 Summary and discussion . . . 76

5 Synthetic Data Experiment: Set-up and Preliminary Results 77
5.1 Introduction . . . 77
5.2 Model set-up: Truth run . . . 79
5.2.1 Time scales . . . 88
5.3 Parallel run . . . 91
5.4 Truth and parallel runs comparison . . . 93
5.5 Data assimilation experiment . . . 96
5.5.1 Sections selection . . . 97
5.5.2 Temperature analysis . . . 98
5.5.3 Salinity analysis . . . 100
5.5.4 Velocity analysis . . . 102

6 Synthetic Data Experiment: Assimilation Results 103
6.1 Aims of our experiment . . . 103
6.2 A global evaluation . . . 104
6.3 A closer look at the method performance . . . 110
6.3.1 First assimilation step . . . 110
6.3.2 Temperature rms errors . . . 112
6.3.3 Salinity rms errors . . . 115
6.3.4 Dynamic height rms errors . . . 118
6.3.5 Dynamic height . . . 120
6.3.6 Last assimilation step . . . 121
6.4 How is the velocity field modified? . . . 123
6.4.1 Zonal velocity . . . 125
6.4.2 Abyssal circulation . . . 126
6.5 Water mass structure . . . 130
6.5.1 Potential vorticity . . . 130
6.5.2 T–S relationships . . . 136
6.6 The Inventory . . . 144
6.6.1 Inventory evolution . . . 152
6.7 Surface flux modifications . . . 154
6.8 Summary and discussion . . . 158

7 Assimilation in a Global Ocean Model 163
7.1 Introduction . . . 163
7.2 Experimental set-up . . . 164
7.2.1 Ocean model . . . 165
7.2.2 Data assimilation system . . . 165
7.2.3 Description of the experiments . . . 166

7.3 Assimilation results 168
7.3.1 Analysis of the 9-year means 168
7.3.2 Salinity variability 175
7.3.3 Sea level variability 182
7.4 Summary and discussion 186

8 Conclusions **187**
8.1 Summary 187
8.2 Discussion 188
8.3 Suggested further work 190

Bibliography **193**

A.1 Assimilation Algorithm **201**

A.2 Include Files **220**

Chapter 1

Introduction

Measurements of sea surface temperature (SST) have been made routinely for many years, mainly by merchant or Navy ships, but also by satellite, and these have been the basis for detecting climate change over the ocean. Although SST is an important variable for the interaction between the atmosphere and the ocean, it does not give any information about the subsurface structure of the ocean. Therefore, along with SST measurements, other useful data were progressively collected (either by satellite or in situ measurements): currents, subsurface temperature and surface elevation. The need for ocean predictions and for improving the understanding of the oceans' influence on climate has encouraged several ocean observational campaigns. A considerable amount of oceanographic data has been collected by the TOGA (Tropical Ocean Global Atmosphere experiment) campaign, which has covered most of the tropical Pacific Ocean with the view of monitoring and predicting El-Niño – Southern Oscillation events. A large quantity of data has also been obtained by WOCE (World Ocean Circulation Experiment) observation campaigns, by COADS (Comprehensive Ocean-Atmosphere Data Set), by the satellite altimeter missions ERS1, ERS2, TOPEX/POSEIDON and by the volunteer observing ship (VOS) eXpendable BathyThermographs (XBT).

Two of the main purposes for which oceanographic data are collected are: a) their comparison with numerical model results - *model validation* - and b) their combination with ocean model data - *data assimilation*. Here we are mostly concerned with the latter, although we will also analyse the effect of the data assimilation on the model, which can be considered as a model validation. In particular, data assimilation is defined as the process of combining a physical model with observational data so to gain a better estimate of the system considered (Anderson *et al.*, 1996).

Ocean data assimilation has been investigated continuously over the last decade

(reviews are provided by Ghil and Malanotte-Rizzoli, 1991, Anderson *et al.*, 1996, and Malanotte-Rizzoli and Tziperman, 1996). Most research has focused on either satellite altimeter data or near-surface temperatures, as measured by either XBTs or moored buoys. As a result, many data assimilation schemes, such as Optimal (or Optimum) Interpolation (OI), Kalman filter, 3DVAR, 4DVAR, have been developed for ocean models. These data assimilation methods are usually borrowed from the sister discipline in meteorology, although two major differences prevent mere parroting. The first resides in the number of available oceanographic observations, which are far smaller than the number of meteorological observations. Relatively recent estimations showed that their ratio is several orders of magnitude (Ghil and Malanotte-Rizzoli, 1991). The second difference is that in the oceanographic case data assimilation has a broader meaning. Unlike Numerical Weather Prediction (NWP) in meteorology, it does not concentrate primarily on forecasting. In fact, three main objectives can be identified, even though the differences are sometimes subtle: a) to obtain a four dimensional picture of the oceanic flow (*state estimation*), consistent with both measurements and dynamics; b) to provide initial conditions for predictions of the oceanic circulation as in NWP; c) to improve the ocean model in order to get a better physical description of the real ocean (Malanotte-Rizzoli and Tziperman, 1996).

Owing to these discrepancies, the techniques borrowed from meteorology must be revisited and sometimes profoundly modified to make them applicable to oceanography. To this end, particular attention should be given to the different properties of the two fluids (water and air). Water is approximately 800 times denser than the air. As a consequence, the mass of the ocean is nearly 270 times that of the atmosphere (Gill, 1982). Also, water has a greater viscosity and heat capacity (mainly because of the large difference in mass), which implies lower velocities (of the order of 0.01 m s^{-1}) and hence longer time scales (Daley, 1991). Further, diabatic processes in the ocean interior are far less relevant than in the atmosphere.

As mentioned above, one of the purposes of data assimilation is to create good initial conditions for a numerical model in order to get reliable ocean predictions. A currently-used strategy to produce ocean analyses from which to begin seasonal forecasts is to force an ocean model with the recent history of wind stress, heat fluxes and precipitation minus evaporation fields, and then use the analysed ocean state as initial conditions in a coupled ocean-atmosphere model. In the tropics, for instance, it

is mainly the subsurface structure of the temperature fields which provides predictive skill on the time scale of a few months. The analysed ocean states are not perfect, however, as both forcing fields and ocean models contain errors. Ocean temperature data assimilation has proven to be capable of improving the simulated upper ocean temperature structure in such a way as to be beneficial for seasonal climate forecasting (e.g. Alves *et al.*, 1999, Ji *et al.*, 1998, Fischer *et al.*, 1997, Rosati *et al.*, 1997). For example, the seasonal forecasting system at the European Centre for Medium-Range Weather Forecasts (ECMWF) uses an ocean analysis in which in situ temperature data have been assimilated.

When initialising an ocean model a realistic vertical density structure is more vital than is a good initial velocity field (Gill, 1982, Philander *et al.*, 1987, Moore *et al.*, 1987) because the potential energy is generally greater than the kinetic energy. Since the density is dominated, especially in low latitudes, by temperature (T) as opposed to salinity (S), the latter was not included as a prognostic variable in tropical ocean models until the late 1980s (Cooper, 1988). However, Cooper (1988) showed that, even for a tropical ocean model, it is essential to include S along with T if the goal is to reduce rms errors in the velocity field, and that assimilating only T can be deleterious for the dynamics described by ocean models (Cooper, 1988; Woodgate, 1997). Also, more recently, salinity observations in the western equatorial Pacific revealed large interannual variations of salinity at subsurface levels (Kessler, 1999, Ji *et al.*, 2000) which might substantially contribute to the density field.

However, from a practical viewpoint, near real-time subsurface salinity observations simply are not available in most data assimilation situations. This is because the instrumentation for salinity measurements is more expensive than that for temperature measurements but also because, as explained above, salinity is second order in the equation for the sea water density and has received therefore less attention. As another result, not much attention has been given to salinity in the context of temperature data assimilation either. In fact, hitherto the most common approach has been to leave the salinity field unmodified when updating the temperature field. Apart from the issues raised by Cooper (1988), it has also been noticed that not modifying salinity when updating temperature may lead to the generation of artificial and possibly unrealistic water masses which subsequently can corrupt the simulated ocean state. This can cause serious errors not only in salinity, but also in the temperature field as highlighted by

Figure 1.1, which will be discussed thoroughly in chapter 7. For now, it is sufficient to note the unrealistic thermal field in the vicinity of the equator which is a consequence of assimilating thermal data, without correcting the salinity field, for three months (the T observations were assimilated every ten days).

Now, given the scarcity of the subsurface salinity observations and the importance of updating salinity in a temperature data assimilation system, a means of deriving salinity changes in terms of temperature is required. In particular, the density, ρ, at any given depth is a function of the independent variables S and T. However, if, for instance, S could be expressed as a single-valued function of T, then the variables for ρ would be reduced to only one, $\rho = \rho[T, S(T)]$, and S would not need to be known directly. This formulation would be an enormous simplification of the problem, for it would imply that, at a fixed depth, ρ can be derived from knowing T only. The underlying idea is quite common when one tries to derive one variable from related information, that is in an indirect way. In practice, one seeks variables that have a good correlation between each other. In the oceanographic case, it turns out that T and S are highly correlated. The degree of correlation will depend however on the geographical location and on the time interval between observations. An example is given in Figure 1.2. This figure shows a scatter plot in a T–S diagram for 104 Conductivity-Temperature-Depth (CTD) profiles collected in the western tropical Pacific ocean in a 10-day time interval. The 104 profiles, represented by dots, are quite close to each other thus indicating a high correlation between T and S, especially for $T < 14°\mathrm{C}$, which, in this case, corresponds to depths deeper than 230 m. An exception is the water mass intrusion represented by the spike at about 17°C and 35 psu. A more rigorous analysis of the $S = S(T)$ variability will be carried out in chapter 4 and, in anticipation, this will show a very good correlation between T and S.

To sum up, the solution to derive S from T is possible in circumstances for which the T–S relation does not vary much, or varies only slowly, in time. Of course, this is not always true, but there is observational evidence that it applies to many parts of the ocean (Emery and Dewar, 1982). This fact is usually referred to as T–S preservation (or conservation) and stems from the fact that the T–S water mass properties are often conserved for a long time. The T–S preservation hypothesis is the core assumption adopted in the present work.

It is clear that, for the method to work, a good T–S relation is required, from which

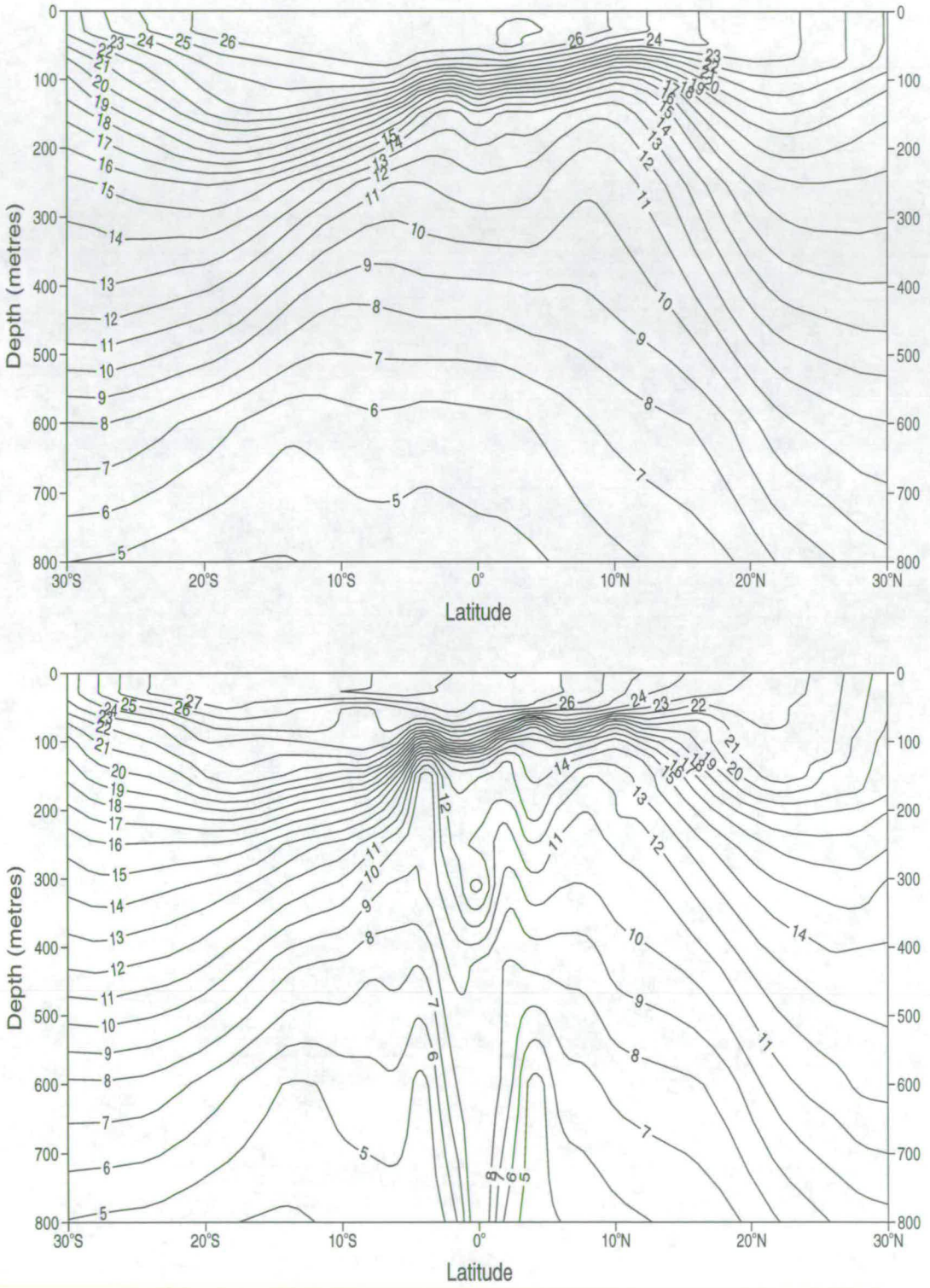


Figure 1.1: Temperature meridional section at 30°W. Above: initial conditions (i.e. climatology). Below: instantaneous field after 3 month ocean general circulation model integration with an OI temperature assimilation in the upper 425 m.

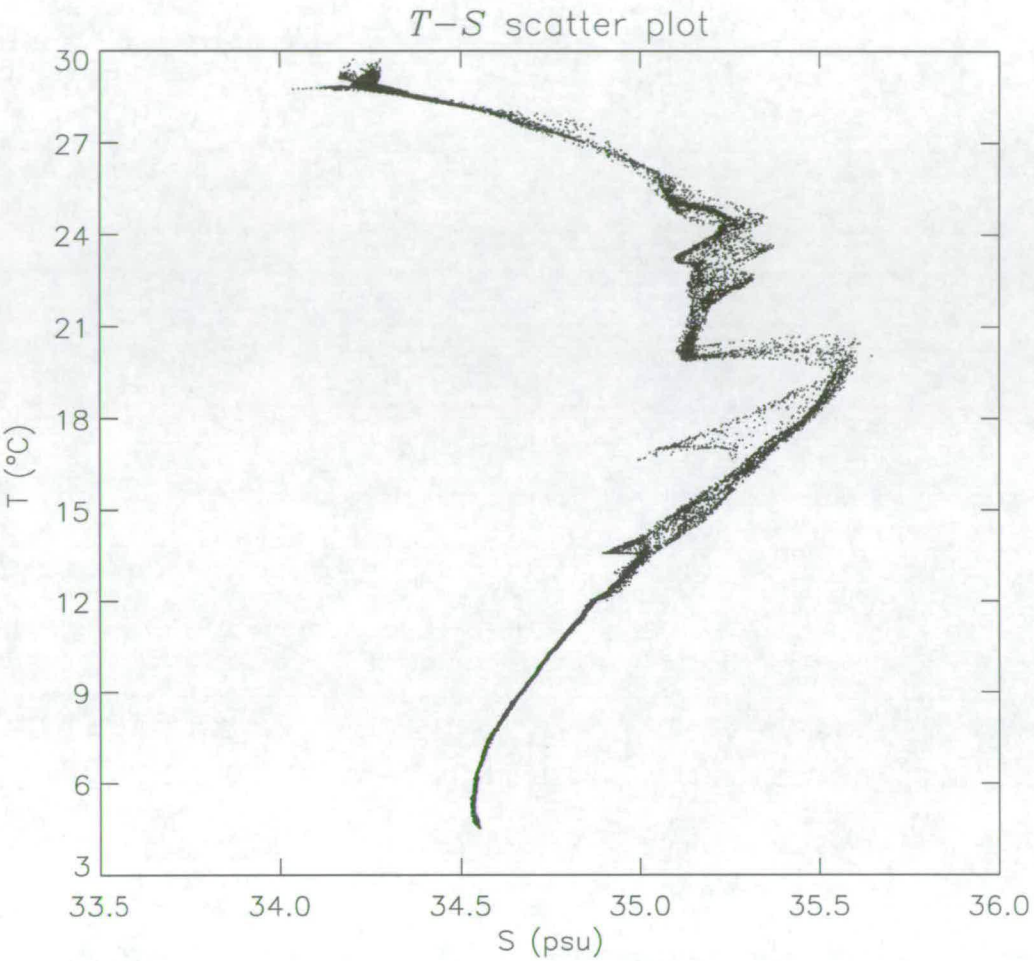


Figure 1.2: Scatter plot in a T–S diagram for 104 CTD profiles collected in the western tropical Pacific ocean (156.25°E, 1.5°S) in a 10-day time interval.

S can be derived, given T. Since the Lagrangian T–S properties undoubtedly are well preserved because of the weak mixing in most parts of the ocean, it would at first sight be plausible to use a long-term mean T–S relation based on some climatological data set, and this solution is in fact the most widely adopted. Although using a climatological T–S relation may be the most obvious choice it restricts considerably the variability in $S(T)$. Consider, for example, the tropical Pacific, which exhibits large interannual variations in water mass properties because of El Niño (e.g. Maes and Behringer, 2000). It is likely that these variations would not be captured by a climatological T–S relation.

1.1 State-of-the-art

Recently, several different attempts have been made to diagnose salinity even when temperature is the only subsurface data available, normally with reference to climatological T–S relations, such as Levitus *et al.* (1994) and Levitus and Boyer (1994) (together referred to hereafter as "Levitus"). Some of the proposed methods make use of Empirical Orthogonal Functions (EOFs) to decompose the vertical structure of temperature (T) and salinity (S) profiles observed over limited regions and periods. The EOFs thus obtained are used to derive salinity when direct observations of S are not available. For example, Vossepoel *et al.* (1999) used 9000 T and S observations in the equatorial Pacific for the period 1975–96 (i.e. an average of about 3 observations in a 1° by 1° region per year), and Maes *et al.* (2000) used 778 profiles within the 10°S–10°N band along 165°E for the period 1984–1992 (these were all the profiles for which S was also measured). In the case of Vossepoel *et al.* (1999), the EOFs of the data provide a correction to their first guess which is obtained from a climatological T–S relation (they used "Levitus"), so as to improve the S variability. Maes *et al.* (2000), on the other hand, utilise the EOFs as a first guess for reconstructing the salinity profiles (which might also be corrected towards a climatological value in case deviations become too large). In both cases, however, the representativeness of the EOFs depends on the availability of T and S observations. Because of the sparsity of S data, it is difficult to extend these results to regions outside the tropical Pacific. Further, the fact that EOFs can only represent structures that are present in the training data may prevent reconstructing S profiles that have not been observed in the past.

1.2 Aim of this work

An approach that overcomes some of the limitations of the methods described above is proposed with this work. The basic idea is to use the T–S relationships of the closest, in time and space, T and S profiles to reconstruct the salinity profile from temperature information only. In a data assimilation context this means considering the T–S relationship of the model background, which is derived locally from the model T and S profiles. The main advantage of this approach compared to employing EOFs is that no learning period is needed. On the other hand, the scheme relies on realistic model T and S profiles. By avoiding use of long-term averages (e.g. climatological

data), larger density variations for any given T profile are permitted. However, unlike the case in which a climatological T–S relation is used, this approach could permit large and possibly detrimental salinity drifts. A solution could be to prevent the T–S relation from drifting too far from the climatological one by using some weighted $S(T)$ between the model prediction and the climatological data. An advantage of using the model $S(T)$ alone, however, is that, given its local implementation, there is a considerable reduction of the computational costs. In this sense, this method is comparable to the technique suggested by Cooper and Haines (1996) for reconstructing hydrography from altimeter data.

To summarise, the aim of this work is to present and test a novel method which corrects the vertical profiles of salinity when vertical profiles of temperature (such as XBTs) are assimilated. The presentation and the test of the method can be split into four main periods:

1. Presentation and discussion of the method: during this stage vertical temperature and salinity profiles are used to test the method under several realistic events, in a model independent fashion;
2. Test of the method using observational data: CTD data from a limited, but geographically significant, region of the western equatorial Pacific are used to assess the method (results have been published, Troccoli and Haines, 1999);
3. A synthetic data assimilation experiment is run in order to test the impact of the method on a simplified configuration of a 3-D primitive equation ocean model;
4. A data assimilation experiment is run to test the impact of the method on a global ocean circulation model, the Hamburg Ocean Primitive Equation (HOPE) model, at the ECMWF (results have been submitted, Troccoli *et al.*, 2000a).

1.3 A T–S preservation application: water mass tracking

The fact that the relationship between T and S can be considered as fixed over a certain time interval (which will mainly depend on the geographical location), allows one to analyse, at least qualitatively, the time evolution of the water mass properties in a particular region from the sole knowledge of observations of vertical temperature profiles.

Based on this idea, the decadal water mass changes in the North Atlantic between 1950 and 1994 have been analysed by looking at the water mass structure, that is at the

inter-isotherm thicknesses. All the temperature observations available for the period considered (1950–1994) were included. We will not discuss the results of this work here. We mention only that, from this study, two very strong events in the sub-tropical gyre are identified, a cold anomaly in 1966–72 and an intense warm anomaly in 1988–94. Possible explanations for these decadal changes in the North Atlantic circulation are also proposed. Further particulars can be found in Grey *et al.* (2000), for which I contributed the part concerning the inter-isotherm thickness analysis during my PhD work.

1.4 Thesis outline

When a new method is proposed it is good practice to test it at increasing levels of complexity. This is the approach taken here for the salinity scheme introduced with this work.

After a discussion of the relevant fundamentals and data assimilation notions in chapter 2, the salinity method is presented and tested on single vertical profiles of temperature and salinity in chapter 3. Then, in chapter 4, using CTDs observations, the T and S variances and covariations in the tropical Pacific are analysed to obtain an estimate of the time scale over which the T–S relation is preserved. Results obtained by the assimilation of T profiles, taken both from CTDs and from model realisations of the HOPE model, are also shown in the same chapter. The next stage of the method test is represented by a synthetic data assimilation experiment. This type of experiment is very useful because, unlike with real data assimilation experiments, all the model variables can be accessed even for the "real" case. The model set-up and some preliminary results are introduced in chapter 5 and in the following chapter the results of this synthetic data assimilation experiment are discussed. Still in chapter 6, new tools for assessing the effects of a data assimilation system are also proposed. Lastly, experiments have been devised using a global ocean circulation model, in which real temperature observations are assimilated. These experiments have been performed by myself whilst working at ECMWF in collaboration with the scientists of the Seasonal Forecasting group and Keith Haines. These data assimilation experiments are discussed in chapter 7. Finally, in chapter 8 a discussion is provided and further work is suggested.

Chapter 2

Background

The components of the sea water density are explored. In particular, the role of salinity is analysed and compared with the competing one of temperature. Successively, the key pivot of this work, the T–S preservation hypothesis, is discussed from experimental and theoretical viewpoints. The latter will naturally lead us to the introduction of a fundamental dynamical quantity: the potential vorticity. Finally, a brief discussion of the data assimilation motivations and the description of simple techniques will be given, as well as the presentation of the relevant observational data available.

2.1 Properties of sea water

The density of sea water plays a fundamental role in the dynamics of the ocean. Consider, for instance, one of the simplest balances of the Navier-Stokes, momentum, equation for a geophysical fluid, that is the geostrophic approximation (for the horizontal, x and y, components):

$$f \cdot (\boldsymbol{k} \times \boldsymbol{V}) = -\frac{1}{\rho_0} \cdot \nabla_h p \tag{2.1}$$

where $f \equiv 2\Omega \sin\phi$, is the Coriolis parameter, with Ω the earth's angular velocity and ϕ the latitude, $\boldsymbol{k}$ is the vertical vector, $\boldsymbol{V} = (u, v, w)$ is the velocity vector, ρ_0, following the Boussinesq approximation, is an average density and ∇_h is the horizontal gradient defined as $\nabla_h = (\frac{\partial}{\partial x}, \frac{\partial}{\partial y})$.

Although density, apart from the constant ρ_0, does not appear in the equation (2.1) directly, it is essential in determining the pressure p. In fact, the approximated version of the vertical component of the momentum equation, i.e. the hydrostatic approximation, gives us the relation between pressure and density:

$$\frac{\partial p}{\partial z} = -g\,\rho \tag{2.2}$$

which integrated yields a relation for p as a function of ρ (and z).

Equation (2.1), therefore, highlights the vital role of density in the determination of the velocity field[1]. One exception is represented by the circulation in the mixed layer which is driven mainly by the winds (see e.g. Niiler, 1992).

In principle, one could measure ρ directly, for instance taking a sample to a laboratory, or by means of in situ measurements. However, the methods available are slow and not accurate enough (Pond and Pickard, 1983). Hence, one has to rely upon indirect estimation methods to determine ρ.

The density of sea water can be expressed as a function of three variables: temperature (T), salinity (S) and pressure (p). In particular, whilst the physical significance of T (i.e. indicator of the molecular kinetic energy) and p (i.e. the force exerted by neighbouring water parcels, per unit surface) is apparent, that of S needs to be clarified a little. As one can intuitively expect, S represents the salt content in a unit mass of pure water. But what is meant by salt content? The sea water is composed of several constituents, the main ones of which are shown in Table 2.1 (note that the salinity is specified in psu, practical salinity unit, which basically corresponds to the former parts per thousand, ppt).

Positive ions (g kg^{-1})		Negative ions (g kg^{-1})	
Na^{+}	10.752	Cl^{-}	19.345
Mg^{++}	1.295	SO_4^{--}	2.701
Ca^{++}	0.416	HCO_3^{-}	0.145
K^{+}	0.390	Br^{-}	0.066
Sr^{++}	0.013	$B(OH)_3$	0.027
		F^{-}	0.0013

Table 2.1: Major constituents of sea water for $S = 35$ psu, which corresponds to 965 ppt of H_2O and 35 ppt of dissolved materials. Adapted from Apel (1987).

It happens that the ratio between the concentrations of the salts in sea water (Table 2.1) is nearly constant (e.g. Gill, 1982). For this reason, for a long time salinity was determined on the basis of a linear relationship which only considered the chlorine[2]

[1] More precisely, Eq. (2.1) tells us that the density gradients determine the velocity field.

[2] Chlorinity is a concept originally defined (circa 1900) to circumvent the difficulties inherent in attempting to directly measure the salinity of sea water. It was determined by volumetric titration using silver nitrate and originally defined as "the weight in grammes (in vacuo) of the chlorides contained in

content of the sea water, which could be determined via a volumetric titration using silver nitrate. This measurement could be combined with the assumption of constant ionic ratios in sea water to obtain a measure of the salinity, with the relationship between the two quantities being defined as:

$$S(^o/_{oo}) = 0.030 + 1.8050 \text{ Cl } (^o/_{oo}) \tag{2.3}$$

(see Baum, 1997). It was later demonstrated that salinity can be well related to the conductivity of sea water. Thus, this more accurate and straightforward way to obtain salinity has been hitherto adopted (e.g. Pond and Pickard, 1983).

Now, the relationship $\rho = \rho(T, S, p)$, the equation of state, is not a simple one but it can be approximated by a polynomial expansion. The expression currently used is defined by the Joint Panel on Oceanographic Tables and Standards (UNESCO, 1981):

$$\begin{aligned}
\rho(T,S,0) \;=\; & 999.842594 + 6.793952 \cdot 10^{-2} \cdot T - 9.095290 \cdot 10^{-3} \cdot T^2 \\
& +1.001685 \cdot 10^{-4} \cdot T^3 - 1.120083 \cdot 10^{-6} \cdot T^4 + 6.536332 \cdot 10^{-9} \cdot T^5 \\
& +(0.824493 - 4.0899 \cdot 10^{-3} \cdot T + 7.6438 \cdot 10^{-5} \cdot T^2 \\
& -8.2467 \cdot 10^{-7} \cdot T^3 + 5.3875 \cdot 10^{-9} \cdot T^4) \cdot S \\
& +(-5.72466 \cdot 10^{-3} + 1.0227 \cdot 10^{-4} \cdot T - 1.6546 \cdot 10^{-6} \cdot T^2) \cdot S^{3/2} \\
& +4.8314 \cdot 10^{-4} \cdot S^2
\end{aligned} \tag{2.4}$$

where T is specified in °C and S in psu. The density at pressure p, i.e. $\rho(T, S, p)$, can then be obtained by another empirical polynomial expansion (see Gill, 1982, Appendix 3). The density thus obtained fits the available measurements with a standard error of 3.5 ppm for temperatures between freezing and 40°C, for salinities between 0 psu and 42 psu and for pressures up to 1000 bars (i.e. about 10000 m depth) (Gill, 1982).

In particular, ρ increases with S and p and decreases with T. As a rule of thumb, a variation of T, S and p of $\Delta T = -5$°C, $\Delta S = 1$ psu, $\Delta p = 200$ dbar (about 200 m) respectively, all give a density increase of 1 kg m^{-3}, or a $\Delta\rho/\rho \approx 0.1\%$.

It is not always necessary to employ the complete polynomial expression (2.4) for the calculation of ρ. In practice, the truncation of the polynomial expansion is determined

one gramme of sea water (likewise measured in vacuo) when all the bromides and iodides have been replaced by chlorides". This was defined in terms of the atomic weights known in 1902 and as such was dependent on any changes in their determinations. The weights did change so the definition was kept in terms of the 1902 atomic weights until a new definition was determined in 1937. The new definition of chlorinity as "the mass of silver required to precipitate completely the halogens in 0.3285234 kg of sample sea water" was free of this limitation (from Baum, 1997).

by the precision required by the problem to be tackled. Numerical models in which T and S are prognostic variables (i.e. not pre-assigned at each time step) which needs to be calculated with a large precision normally adopt the whole expression (2.4). However, for some applications a first order expansion in T and S is sufficient[3]. We discuss this first order expansion here for its pedagogical role. Let us start from the differential of density:

$$\begin{aligned} d\rho(T,S,p)\mid_p &= \left(\frac{\partial\rho}{\partial T}\right)_{S,p} dT + \left(\frac{\partial\rho}{\partial S}\right)_{T,p} dS \\ &= -\rho\,\alpha(T)\,dT + \rho\,\beta(S)\,dS \end{aligned} \tag{2.5}$$

where α and β are the coefficients of thermal expansion and haline contraction respectively, defined by:

$$\alpha(T) = -\frac{1}{\rho}\left(\frac{\partial\rho}{\partial T}\right)_{S,p} \qquad \text{and} \qquad \beta(S) = \frac{1}{\rho}\left(\frac{\partial\rho}{\partial S}\right)_{T,p} \tag{2.6}$$

Typical values of these two coefficients are shown in Figure 2.1. This figure shows also that both α and β are not very sensitive to salinity, whereas α varies markedly with temperature.

The equation (2.5), in finite terms, becomes:

$$\frac{\Delta\rho\mid_p}{\rho} = -\alpha\,\Delta T + \beta\,\Delta S \tag{2.7}$$

This approximation is quite useful it allows to get an estimate of the relative weight of the temperature and salinity on the value of density or, in other words, it shows what the density sensitivity is to changes in temperature and salinity, at a given pressure. In particular, the relative weight of T and S assumes different importance depending on their absolute values (through α and β) and on their variability (through ΔT and ΔS), that is they depend e.g. on the geographical location. To have an idea of the range of variability of T and S we show in Figure 2.2 the zonal averages of the temperature (top panel) and salinity (bottom panel) at two latitudes: at 1.5°S, i.e. in the tropics, and at 40.5°N, i.e. at mid latitudes.

If we now consider the temperature and salinity variability within the vertical profiles for the two cases, i.e. tropics and mid latitudes shown in Figure 2.2, we get the following approximate values:

[3]We shall ignore the pressure dependency here, i.e. we will consider p as a constant.

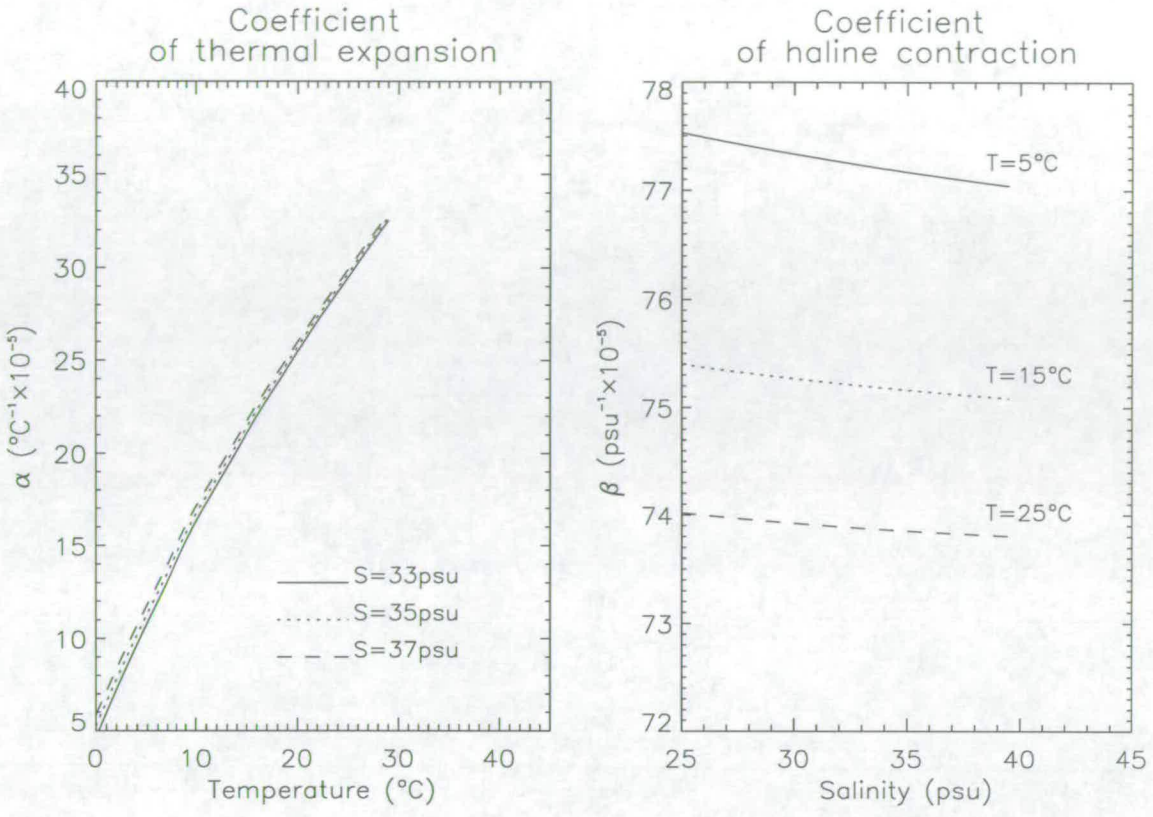


Figure 2.1: Coefficients of thermal expansion, α, and of haline contraction, β, for typical values of T and S.

$$
\begin{array}{llll}
\Delta T_{tr} \approx 22°\mathrm{C} & \text{and at } \bar{T}_{tr} \approx 16°\mathrm{C} & \Rightarrow \alpha(\bar{T}_{tr}) \approx 23 \cdot 10^{-5} °\mathrm{C}^{-1} \\
\Delta S_{tr} \approx 0.7 \text{ psu} & \text{and at } \bar{S}_{tr} \approx 35 \text{ psu} & \Rightarrow \beta(\bar{S}_{tr}) \approx 75 \cdot 10^{-5} \text{ psu}^{-1} \\
\Delta T_{ml} \approx 8°\mathrm{C} & \text{and at } \bar{T}_{ml} \approx 10°\mathrm{C} & \Rightarrow \alpha(\bar{T}_{ml}) \approx 16 \cdot 10^{-5} °\mathrm{C}^{-1} \\
\Delta S_{ml} \approx 1.2 \text{ psu} & \text{and at } \bar{S}_{ml} \approx 34 \text{ psu} & \Rightarrow \beta(\bar{S}_{ml}) \approx 76 \cdot 10^{-5} \text{ psu}^{-1}
\end{array}
$$

where the subscript tr stands for "tropics" and ml for mid latitude. Substituting these figures in the (2.7) and ignoring the relative signs, which are not relevant here, we obtain the following estimations:

$$\frac{\Delta\rho_{tr}\,|_p}{\rho_{tr}} = (23 \cdot 22 + 75 \cdot 0.7) \cdot 10^{-5} \approx (500 + 50) \cdot 10^{-5} \tag{2.8}$$

$$\frac{\Delta\rho_{ml}\,|_p}{\rho_{ml}} = (16 \cdot 8 + 76 \cdot 1.2) \cdot 10^{-5} \approx (130 + 90) \cdot 10^{-5} \tag{2.9}$$

These two estimations therefore tell us that in the tropical region temperature variations play a dominant role in the density variability, that is T is first order and, consequently, S is second order. As discussed in chapter 1, it is for this reason that not much attention has been given to salinity in the context of temperature data assimilation. However, as we will see in the course of this work, there are several

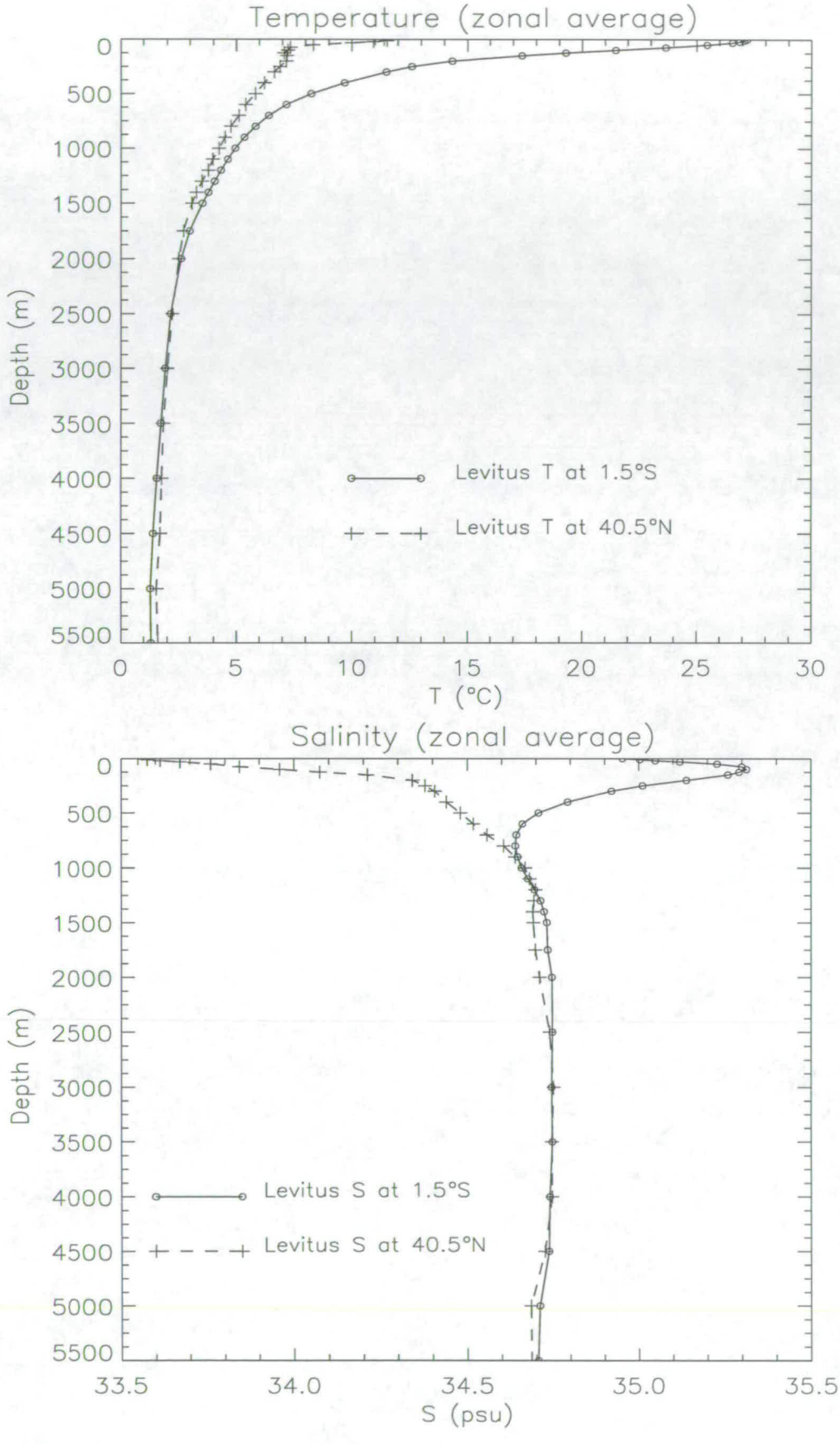


Figure 2.2: Zonally averaged temperature (top) and salinity (bottom) vertical profiles for two selected latitudes, 1.5°S and 40.5°N, as calculated by Levitus.

circumstances in which salinity is more relevant than is suggested by the approximate evaluation (2.8) (see also Maes, 1998). In particular, in section 7.3.1 we will show, by means of a stability analysis, that other features of the temperature and salinity profiles, and not just the estimates given above, have to be taken into account when considering the assimilation of thermal data. At mid latitude, instead, the T and S weights on the density are comparable to each other, even if temperature still dominates in the specific evaluation (2.9).

It is worth noting that the evaluations (2.8) and (2.9) also give us an estimate of the density error which would be introduced should one of the two variables, T or S, be neglected.

Before moving to the next section it is useful to introduce some definitions.

- Potential temperature (Θ): is the temperature that a parcel of fixed composition would acquire if moved adiabatically to a given pressure level. For depth variations of the order of hundreds of meters the potential and in situ temperatures basically coincide.
- Density anomaly (σ): is defined as ($\rho(T, S, p)$ - 1000). It is introduced to simplify the density notation as ρ is normally just larger than 1000 kg m^{-3}.
- Density anomaly at zero pressure (σ_t): it is used for the value of σ calculated at the pressure of the sea surface, taken to be equal to 1 bar.
- Potential density (ρ_θ): its definition is analogous to the potential temperature, that is $\rho_\theta = \rho(\Theta, S, p)$. For depth variations of the order of hundreds of meters the potential and in situ densities basically coincide.
- Dynamic height (D): this refers to the pressure associated with a column of water and is defined by:

$$D(p_1, p_2) = \int_{p_1}^{p_2} \delta(T, S, p)\, dp = \int_{p_1}^{p_2} [v_s(T, S, p) - v_s(0, 35, p)]\, dp \qquad (2.10)$$

  where p_1 and p_2 are two reference pressure levels, δ the specific volume anomaly and v_s the specific volume, $v_s = \rho^{-1}$. The dynamic height is measured in dynamic meters or centimeters (dyn m or dyn cm).

  Horizontal variations of dynamic height (due to horizontal variations in temperature and salinity) are mapped to determine what is called the dynamic topography and its corresponding geostrophic flow field in the ocean. This is analogous to a meteorologist's use of a pressure chart, with the direction of flow aligned

with the contours and the intensity of flow inversely proportional to the contour spacing.

2.1.1 The T–S diagram

Another useful way to evaluate the density dependency on temperature and salinity is by means of T–S diagrams. A T–S diagram is a graph showing the relationship between temperature and salinity as observed at, for example, various depths in a water column. We have already met an example of a T–S diagram representing CTD profiles in Figure 1.2. In this section, however, we only illustrate the role of a T–S diagram, i.e. with no reference to specific situations.

Figure 2.3 shows a T–S diagram to highlight the values of the density anomaly, σ_t, for typical values of temperature and salinity. This representation of the density anomaly is also useful to estimate graphically the density gradients. In fact, where the isolines are closer to each other the gradient will be evidently larger than where there is more distance between isolines. In particular, it can be observed that for a fixed S the isolines are tighter for higher T (i.e. $|\alpha|$ increases with T), whereas at fixed T the distance between isopycnals does not change much (i.e. β varies slowly with S).

For reference, in Table 2.2 we give also some values of the inverse of the density gradients. These are useful as they allow an estimation of how much either the temperature or the salinity needs to be changed in order to get a density variation of 1 kg m^{-3} (cf. the rule of thumb given earlier in section 2.1). It can be seen, therefore, that at constant S, equal to 35 psu in this case (first two columns in Table 2.2), smaller variations of temperature are needed at higher temperatures in order to get the same density variation, e.g. 3.3°C at 25° and 8.6°C at 5°C. On the other hand, at fixed temperature, $T = 15$°C in this case (third and fourth columns), and at different values of S, salinity variations of the same magnitude yield the same density variation, e.g. a salinity variation of 1.3 psu for any S in the range 27.5÷37.5 psu causes the density to vary by 1 kg m^{-3}.

2.2 Water masses and water types

Given the importance of the values of T and S in the calculation of ρ, it is usual practice in oceanography to employ T–S diagrams. These were first introduced by Helland-Hansen (1916) who observed that a typical T–S curve could be drawn for

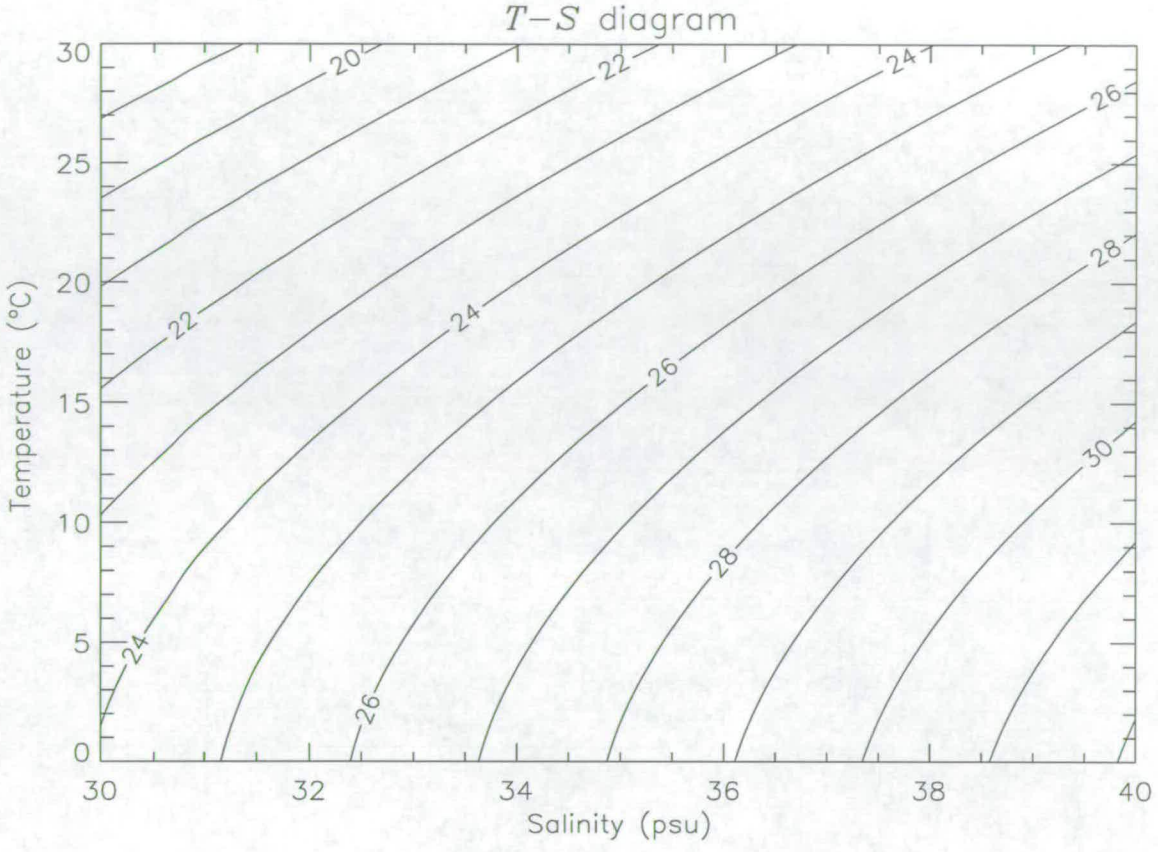


Figure 2.3: Density anomaly (σ_t) superimposed in T–S diagram for typical values of temperature and salinity with superimposed density anomaly (σ_t) isopycnal.

a large area of the eastern North Atlantic. He then introduced a useful operational definition of *water mass*, that is a *curve* in the T–S space. By contrast, a *point* in T–S space is usually denoted by *water type*. A single T–S point, i.e. a water type, along with its standard deviation, may be sufficient for the identification of a water mass (especially with deep water masses), although generally a set of T–S combinations, i.e. a function or curve in T–S space, is needed along with a standard deviation envelope.

Examples of water masses are (from Emery and Meincke, 1986):

Water mass		T (in °C)	S (in psu)
Atlantic Subarctic Upper Water	ASUW	0.0÷4.0	34.0÷35.0
Antarctic Intermediate Water	AAIW	2÷10	33.8÷34.8
Antarctic Bottom Water	AABW	-0.9÷1.7	34.64÷34.72
North Atlantic Deep Water	NADW	1.5÷4	34.8÷35.0

Since the time when the definitions of water mass and water type were introduced, it has been normal practice to adopt the T–S space to refer to a water mass char-

Inverse of density gradients			
at $S = 35$ psu		at $T = 15°C$	
T (°C)	$(\partial\rho/\partial T)^{-1}$	S (psu)	$(\partial\rho/\partial S)^{-1}$
5	8.6 °C (kg m^{-3})$^{-1}$	27.5	1.3 psu (kg m^{-3})$^{-1}$
10	5.8 "	30.0	1.3 "
15	4.6 "	32.5	1.3 "
20	3.8 "	35.0	1.3 "
25	3.3 "	37.5	1.3 "

Table 2.2: Inverse of density gradients for typical values of T and S.

acteristics[4] (or properties). This is because, as was progressively realised, the T–S relationship is often well defined locally and those curves, apart from being a powerful descriptive tool, have also been used for preliminary checks on the accuracy of observational measurements (Worthington, 1981).

Based on these considerations, classifications of the sea water masses in the ocean were performed. The results have been amazingly good, because it was noted that, for a certain region, fairly constant T–S curves were observed. Amongst other things, this has the implication that operationally the same curve can be used over a certain time interval because simple advection from a nearby location usually leaves water masses unchanged. This is certainly more true for deeper parts of the ocean where changes are much slower than, for instance, in the mixed layer where the time interval will be shorter. A specific evaluation of such time intervals will be carried out in this work (chapter 4).

2.3 T–S preservation hypothesis

As observed in the previous section, the empirical knowledge of the existence of a fixed relationship between the temperature and salinity for a water mass at a certain location has been appreciated for a long time. In particular, it is the sparsity of S observations that has rendered this relationship so salient! More generally, in several disciplines, it is normal practice to look for a correlation between two or more quantities for one may utilise such a relationship to derive one quantity from the other(s) when its direct observation is impractical. Obviously, for the relationship to be beneficial it needs to

[4]It is defined as the property value or, more often, range of property values by which a water mass can be identified and tracked through the ocean. The most commonly used are temperature, potential temperature, salinity, potential density or the density referenced to a particular depth or pressure. Less often used but still quite valuable for certain applications are oxygen, nitrate, phosphate, silicate, chlorofluorocarbon, carbon 14 and tritium. In this work, only T and S will be considered.

be stable, that is it needs to be one which keeps a nearly constant relationship between the considered quantities in time, at least for specified ranges of these quantities.

In our case, the fact that there is a good correlation between temperature and salinity can be expressed mathematically by saying that S, at a certain location, is a function of both T and the slow time variable τ, i.e. $S = f(T, \tau)$ such that:

$$S = f(T, \tau) = f(T, \tau + \Delta\tau) \tag{2.11}$$

where the time interval $\Delta\tau$ will be mainly dependent on the geographical location but also on the time (e.g. a particular season or a decade), i.e. $\Delta\tau = \Delta\tau(x, y, t)$. Therefore, the relation (2.11) tells us that the value of the function f for a certain value of T is time invariant[5], i.e. it yields the same salinity value at two times separated by the interval $\Delta\tau$. This is normally referred to as T–S *preservation* (or *conservation*). It can be also useful to think of the T–S preservation as a 'labelling' of a water type of a certain (T, S) value, which can be followed around the oceans. In other words, the T–S preservation is a Lagrangian property of the sea water.

To be more precise, because of possible temperature inversions, salinity is better defined by adding one more variable to the function f, namely the depth z. The relation (2.11) can then be re-written as:

$$S = g(T, \tau, z_1) = g(T, \tau + \Delta\tau, z_2) \tag{2.12}$$

where z_1 is the depth at which the water type of temperature T is at time τ and z_2 is the depth at which the water type of the same temperature T is at time $\tau + \Delta\tau$. Further, as seen from eq. (2.12), in general, the function that describes the relationship between T and S is different when the depth dependency is taken into account, i.e. the function g has substituted the function f. We will deal in more detail with the technicalities of the functions f and g which characterise the T–S relationship in chapter 3.

Several studies have dealt with the T–S preservation property of the sea water, showing that under specified circumstances this is a very good assumption. Just to mention some, they are: Stommel (1947), Emery (1975), Emery and O'Brien (1978), Emery and Dewar (1982), Maes (1999), Vossepoel *et al.* (1999), Maes and Behringer (2000). The most complete of them, however, is certainly the work by Emery and

[5]More rigorously, the second equality sign (=) in eq. (2.11) should be substituted by an approximation sign ($\approx$). The same holds true for the next eq. (2.12).

Dewar (1982) who analysed a very large quantity of observations, that is all the observations available at the time which covered the Pacific and Atlantic oceans for latitudes between 10°S and 60°N. These data were averaged over relatively large areas equal to $5° \times 5°$ so as to accommodate enough data, to be statistically significant, in each area. The mean and the rms of the functions $S = S(z)$ and $S = S(T)$ were computed[6] for each area. The mean functions thus obtained together with individual observed vertical temperature profiles were used to infer the corresponding vertical salinity profiles. These salinity profiles, again along with their relative observed temperature profiles, were then used to calculate the 0-500–m dynamic height for each pair of profiles. The results of such an evaluation showed that south of 40°N the mean $S = S(T)$ function generally yields a lower standard deviation for the dynamic height than does the mean $S = S(z)$ function. This can be re-stated by saying that the T–S preservation assumption generally holds well at low and mid latitudes, where the water column stratification is more pronounced (see Fig. 2.2) and the range of variability in T-space is larger.

2.4 T–S preservation and potential vorticity conservation

The T–S preservation has been thus far presented as an empirical rule. However, this rule can be derived more rigorously from the equations of motion of a fluid. In this section we will delineate the main theoretical arguments which underlies the experimental result of the T–S preservation assumption.

Let us write the momentum equation in terms of the absolute vorticity, $\boldsymbol{\omega_a}$, which is the sum of the relative vorticity, $\boldsymbol{\omega}$, and of twice the Earth's angular velocity vector, $2\,\boldsymbol{\Omega}$, i.e. $\boldsymbol{\omega_a} = \boldsymbol{\omega} + 2\,\boldsymbol{\Omega} = \nabla \times \boldsymbol{V} + 2\,\boldsymbol{\Omega}$, having defined the relative vorticity as the curl of the velocity field, $\boldsymbol{V}$. Following Pedlosky (1987):

$$\frac{D\boldsymbol{\omega_a}}{Dt} = \boldsymbol{\omega_a} \cdot \nabla \boldsymbol{V} - \boldsymbol{\omega_a} \nabla \cdot \boldsymbol{V} + \frac{\nabla\rho \times \nabla p}{\rho^2} + \nabla \times \frac{\mathcal{F}}{\rho} \tag{2.13}$$

where $\mathcal{F}$ is, in principle, any non-conservative force but, in our case, is the frictional force in the fluid.

Each term on the right-hand side of (2.13) alters the rate of change of $\boldsymbol{\omega_a}$ according to different physical processes. In particular, the first two terms are responsible for the

[6]The time dependency was removed, having considered the observations as collected at one single time.

vortex-tube stretching, that is the alteration of the vorticity parallel to the filament of fluid by convergence of the filament; and for the *vortex tilting* due to the variation along the direction of the filament of the velocity component perpendicular to the filaments of $\boldsymbol{\omega_a}$. The third term, then, describes the production of vorticity by baroclinicity and the fourth term represents the diffusive effect of friction.

If we now consider a scalar fluid property λ which satisfies an equation of the form:

$$\frac{D\lambda}{Dt} = \Psi \tag{2.14}$$

where Ψ is an unspecified source of the property λ. Multiplying the vector equation (2.13) by the vector $\frac{1}{\rho}\nabla\lambda$, (2.13) is transformed in a scalar form:

$$\frac{D}{Dt}\left(\frac{\boldsymbol{\omega_a}}{\rho}\cdot\nabla\lambda\right) = \frac{\boldsymbol{\omega_a}}{\rho}\cdot\nabla\Psi + \nabla\lambda\cdot\left[\frac{\nabla\rho\times\nabla p}{\rho^3}\right] + \frac{\nabla\lambda}{\rho}\cdot\left(\nabla\times\frac{\mathcal{F}}{\rho}\right) \tag{2.15}$$

Now if:

(1) λ is a conserved quantity for each fluid element, i.e. $\Psi = 0$,

(2) the frictional force is negligible, i.e. $\mathcal{F} = 0$,

and *either*

(3a) the fluid is barotropic, i.e. $\nabla\rho\times\nabla p = 0$,

or

(3b) λ can be considered a function only of p and ρ,

then the three terms on the right-hand side of (2.15) are identically zero and the *potential vorticity*:

$$\Pi = \frac{(\boldsymbol{\omega} + 2\,\boldsymbol{\Omega})}{\rho}\cdot\nabla\lambda \tag{2.16}$$

is conserved by each fluid element, that is:

$$\boxed{\frac{d\Pi}{dt} = 0} \tag{2.17}$$

This is the fundamental relation which expresses the *conservation of potential vorticity*. In oceanography, λ can be taken as the density ρ[7]. Further, for large enough horizontal scales, since the relative vorticity $\boldsymbol{\omega}$ is normally much smaller than the planetary vorticity $2\,\boldsymbol{\Omega}$, and so the contribution of the horizontal components in the scalar product of (2.16) compared to the vertical component is small, (2.16) can be simplified to:

$$\Pi \approx \frac{f}{\rho}\frac{\partial\rho}{\partial z} \tag{2.18}$$

[7]Rigorously, the potential density ρ_θ should be considered instead.

Equation (2.18) basically states that if the vertical distance between two adjacent density layers increases, i.e. $\partial\rho/\partial z$ decreases, the planetary vorticity must increase too, in order to keep the ratio constant (and vice-versa when $\partial\rho/\partial z$ increases). This means that, in the boreal hemisphere, the water parcel between the two density layers must move northward.

In the remainder of this work, following Cox (1985), we will use a slightly different definition of potential vorticity, namely the negative of Π multiplied by a reference density and we will indicate it by either q (e.g. Cox's notation) or the more intuitive PV. Namely:

$$q \equiv \mathrm{PV} = -f\,\frac{\partial\rho}{\partial z} \tag{2.19}$$

Now, how are the T–S preservation and the potential vorticity conservation linked to each other? To explain it we will follow an heuristic argument.

Consider the idealised situation in which a layer of water of density ρ can only move along zonal sections. According to the conservation of potential vorticity, the thickness (and the density) of this layer will remain constant for the planetary vorticity does not change and the relative vorticity is negligible. A constant density does not, in general, imply a fixed composition of the layer in terms of temperature and salinity as there exist several combinations of these two variables that yield the same value of density (cf. an isopycnal curve in Fig. 2.3). However, as the T–S characteristics are often determined by the sea surface forcings at the outcrop of the layer, their combination is normally fixed in that layer. In conclusion, thickness, density and, for the matter, T–S properties remain all constant for the layer considered. However, the opposite does not always hold, for in a high viscosity fluid the T–S water properties of a water parcel might still be preserved whereas the potential vorticity would certainly not be conserved.

In reality, deviations from the T–S preservation do happen. To understand the motives we can refer to the two main approximations in the derivation of the potential vorticity conservation which also affect the T–S preservation assumption.

The first one is the conservation of the density ρ. In particular, the density equation can be written as:

$$\frac{D\rho}{Dt} = \kappa_\rho \nabla^2 \rho - Q_\rho \tag{2.20}$$

which states that thermodynamic changes of density are due to molecular diffusion

(first term on the right-hand side) and to external sources (second term). Therefore, the assumption that Ψ must be zero [see (2.15)] implies that both terms on the right-hand side, are negligible. As concerns the molecular diffusion this is generally a very good assumption[8], whereas the external sources term is relevant close to the sea surface and in circumstances for which the dynamical advection acts as a source of water mass with different T–S properties from the local ones. This advection is sometimes referred to as *water mass intrusion* and causes some of the T–S relationships to vary locally in a way which might be difficult to detect from local analyses only. This water mass intrusion may represent a potential difficulty for the T–S preservation assumption and, in fact, we will find a few instances of this happening in the course of this work.

The second main approximation is that in (2.15) the frictional force $\mathcal{F}$ is negligible. This is certainly true for most of the oceans. Namely, away from the sea surface, where the wind stress is not important, and away from a thin layer at the closed boundaries.

However, so far we have not considered a fundamental mechanism which can generate instabilities in the ocean interior and hence mix the water mass properties: the *turbulence*[9]. The turbulence will cause the flow to deviate from the simplified behaviour dictated by the potential vorticity conservation.

Turbulence arises from the non-linear terms in the momentum equation. The importance of these terms is given by a non-dimensional number, the Reynolds' number Re, which is the ratio of the non-linear terms to the viscous terms:

$$Re = \frac{\text{Non}-\text{linear terms}}{\text{Viscous terms}} \approx U\frac{U}{L}\left(\nu\frac{U}{L^2}\right)^{-1} = \frac{U\,L}{\nu} \tag{2.21}$$

where U and L are typical velocity and length scales of the flow, respectively, and ν is the molecular viscosity of water which is equal to about 10^{-6} m^{2}s^{-1}. Because the flow becomes turbulent for very large Reynolds' numbers, typically for $Re > 10^4$, even for relatively small velocities such as $U \approx 10^{-3}$ m s^{-1}, turbulence is present on length scales of the order of 10 m.

Now, although the ocean often has a stable stratification, given by a negative density vertical gradient, instabilities in the ocean still sometimes occur. These instabilities lead to turbulent mixing. Also, unlike molecular viscosity, the eddy viscosity generated by turbulence is not isotropic. This is because vertical mixing requires more

[8] An exception will be discussed later in this section.

[9] It is tacitly included in the frictional force $\mathcal{F}$ too, though.

energy than horizontal mixing, for the former has to work against the buoyancy force (Cushman-Roisin, 1994). As a result, horizontal mixing along surfaces of constant density, the *isopycnal* mixing, is much larger than vertical mixing across surfaces of constant density, the *diapycnal* mixing (Stewart, 2000). In mathematical terms, this is expressed by the magnitude of the eddy viscosity coefficients. Denoting A_{x-y} and A_z the horizontal and the vertical eddy viscosity coefficient, respectively, the values estimated for A_{x-y} vary from 10 to 10^5 $\mathrm{m^2 s^{-1}}$, whereas for A_z they vary from 10^{-5} to 10^{-1} $\mathrm{m^2 s^{-1}}$, so that their ratio ranges between 10^2 and 10^{10}. The wide range for the estimate of the eddy viscosity coefficients is due to the diverse flow conditions present in the ocean. In fact, unlike the molecular viscosity coefficients which are constant for a particular fluid and T, S and p, the eddy viscosity coefficients are not properties of the *fluid* but of the *flow* (Pond and Pickard, 1983).

The density field is also affected by the turbulence, through its dependency on T and S. Thus, in analogy to A_{x-y} and A_z, the eddy diffusivity coefficients, K_{x-y} and K_z are defined for both T and S. Further, the ranges of values of eddy diffusivities, that is for salt and temperature, are similar to those of eddy viscosities, horizontal and vertical respectively, because they are properties of the turbulent flow field (Pond and Pickard, 1983), as highlighted above. In conclusion, the smaller the turbulent vertical eddy diffusivity, which decreases with the stratification, the better the T–S preservation hypothesis is followed.

To conclude the section, we mention another potential cause of instability for a statically stable water column, which would lead to the mixing of water mass properties. We are referring to the *double-diffusivity instability* which is triggered by *double diffusion* and leads to the phenomena of *salt fingering* and of *layering*. Double diffusion involves the molecular diffusivities, instead of the eddy diffusivities, of T and S and therefore it is important only when turbulence is negligible for otherwise the molecular diffusivities are at least 100 times smaller than K_z. In particular, double diffusion arises because the molecular diffusivity of temperature is about 200 times larger than that of salinity. More precisely:

$$\kappa_T = 0.13 \cdot 10^{-6} \mathrm{m^2 s^{-1}} \qquad \text{and} \qquad \kappa_S = 0.74 \cdot 10^{-9} \mathrm{m^2 s^{-1}} \tag{2.22}$$

where κ_T is the molecular heat diffusivity and κ_S is the molecular salinity diffusivity (Mellor, 1996).

For instance, if a layer of warmer, saltier water overlies a layer of cooler, fresher water such that the density of the upper layer is equal to or less than the density of the lower layer, the saltier water at the interface will diffuse heat to the cooler water below faster than it will diffuse salt because of the differences in molecular diffusivities. This may cause the water immediately above/below the interface to become denser/lighter which will cause it to sink/rise to the lower/upper layer. These fallings and risings occur in thin columns of the order of a few centimeters and the process is referred to as *salt fingering* (Stewart, 2000).

For what concerns the *layering* phenomenon, consider the case in which a layer of colder, fresher water overlies a layer of warmer, saltier water. In such a circumstance, the differences in molecular diffusivities between salt and heat will cause the water just above/below the interface to become lighter/heavier than that above/below it and thus it will tend to rise/sink. This phenomenon can lead to fairly homogeneous layers separated by thinner regions with large gradients (Pond and Pickard, 1983).

2.5 Sea surface fluxes

A water mass can often be traced to an origin at the sea surface and therefore its T–S properties are determined by the values of the forcings (or fluxes) at its formation site. The Antarctic Bottom Water, for instance, which is formed at high latitudes in the austral hemisphere, can be found in many parts of the oceans, at depth (see Emery and Meincke, 1986). It is important therefore to know what determines these forcings.

The main forcing for climatic, meteorological and oceanic processes is the electromagnetic energy radiated from the Sun. The incoming solar radiation flux in the vicinity of the Earth is on average equal to 1370 W m^{-2}, which is also called the solar constant (S_c)[10]. Since the Earth's surface is equal to $4\pi R^2$, with R the mean Earth's radius, the average flux incident on the Earth's surface is obtained by dividing the Earth's disc, whose area is πR^2, by the Earth's surface, that is $1/4\ S_c = 342$ W m^{-2}.

The solar energy activates several important processes. In particular, we will focus on those processes relevant to the air-sea interface. These can be described by three fluxes: the *total heat flux*, the *mass flux* and the *momentum flux*.

[10]Other forcings are also present but they are negligible with respect to the solar energy. The geothermal heat flux at the sea bottom, for instance, is about four orders of magnitude smaller, i.e. about 0.05 W m^{-2} (Mellor, 1996).

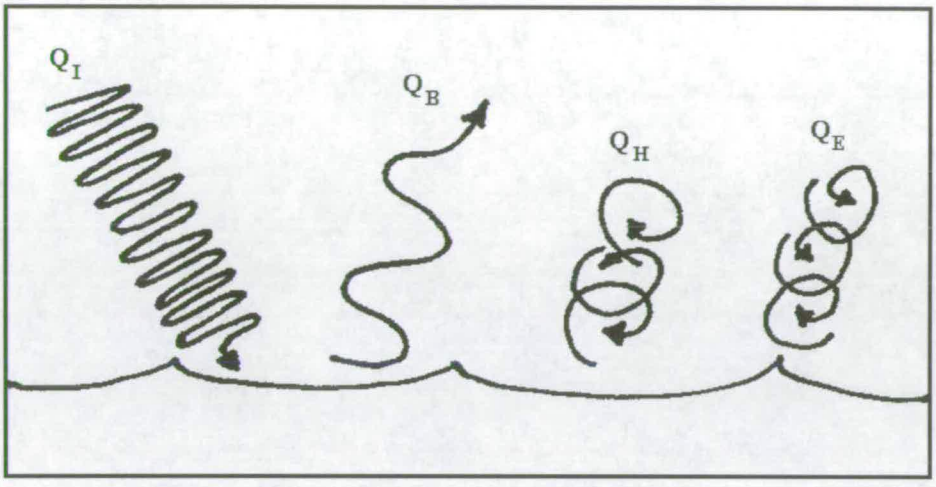


Figure 2.4: Schematic of the components of the total heat flux. Highlighted is the different nature of the individual components.

2.5.1 The total heat flux

The total (or net) heat flux across the air-sea interface is calculated as follows:

$$Q = Q_I - Q_B - Q_H - Q_E \tag{2.23}$$

where Q, Q_I, Q_B, Q_H and Q_E are the fluxes[11] of total heat, incident solar radiation, long-wave radiation, sensible heat and latent heat, respectively, with $[Q] = \text{W m}^{-2}$.

The fluxes on the right-hind side of equation (2.23) will be discussed individually in this section. It should be pointed out that there is not as yet an agreement on the empirical coefficients to be used for calculating fluxes from known quantities such as wind and temperature (e.g. Josey *et al.*, 1999). A criterion to double check and constrain the empirical coefficients is however given by the fact that, unless climatic variations are present, the equation (2.23) should average to zero over a sufficiently long time and on the global scale.

Incoming solar radiation The solar energy flux that reaches the sea surface is on average equal to 175 W m^{-2}, that is about half the flux that reaches the outer atmosphere. This reduction is due to the absorption and reflection of solar radiation by the atmosphere. The solar radiation, also called short-wave radiation for its wavelength is in the range $0.2 < \lambda < 4$ μm, once it has reached the sea surface is partly reflected, about 20 W m^{-2}, but mostly absorbed, about 155 W m^{-2}, by the ocean.

[11] Q_B, Q_H and Q_E are positive upward, whereas Q and Q_I are positive downward.

Long-wave radiation To a fair degree of accuracy, radiation from complicated surfaces such as the surfaces of the Sun or the Earth may be approximated as radiation from an ideal *black body* such that the radiation, I, is equal to $I = \sigma T^4$, where $\sigma = 5.67 \times 10^{-8}$ W m^{-2} K^{-4} is the Stefan-Boltzmann constant. However, corrective factors that take into account three main deviations to the ideal black body relation have to be introduced. These are due to: a) the fact that the sea surface is not an ideal black body; b) the radiation reflected back to the ocean from the atmosphere in a cloudless sky; c) the effect of the clouds. Also, the average sea surface temperature is $T_s \approx 288$ K and corresponds to a wavelength which ranges between 4 and 100 μm. This is why this radiation is referred to as long-wave.

Sensible heat The sensible heat flux is determined by turbulent activity of air masses which convects heat from higher to lower temperature zones. Given the convective-turbulent nature of this air-sea energy exchange, the sensible heat will depend, amongst other factors, on the wind speed, but it also depends on the the air-sea temperature difference.

Latent heat For latent heat it is meant latent heat of evaporation. The evaporation plays an important role both for the total heat flux and, as we will see shortly, for the mass flux. The latent heat flux is similar in character to the sensible heat flux in that it is due to turbulent motions which exchange water vapour between the sea surface and the air above (cf. Fig. 2.4).

2.5.2 The mass flux and the salinity balance

By *mass flux*, or more properly *fresh water budget*, it is meant the sum of all the processes that affect the salinity of the ocean[12]: the *precipitation* (P), the *evaporation* (E) and the *river inflow* (R). The latter contribution, although important, is generally localised. Therefore, modifications of water mass properties due to river inflows have to be evaluated regionally. Evaporation and precipitation instead act on a thin air-sea interfacial layer and on a global scale. Their balance affects the sea surface salinity in a way that can be described by the relation (Mellor, 1996):

$$j_S = (P - E)\, S_0 = -\left(K_z \frac{\partial S}{\partial z}\right)_{z=-\epsilon} \tag{2.24}$$

[12]In fact, the actual mass variation is negligible compared to the ocean mass.

where j_S is the diffusional salt flux at the ocean surface (with $[j_S]$ = psu m^{-1} s^{-1}), S_0 is the ocean surface salinity and $z = -\epsilon$ is a small distance below the sea surface. Therefore, if $(P - E)$ is positive the superficial water becomes fresher, and vice-versa. Evaporation dominates in the sub-tropics whereas precipitation dominates in the middle latitudes and along the equator (Da Silva *et al.*, 1994). Such salinity changes have important repercussions for the ocean dynamics.

2.5.3 The momentum flux

Across the air-sea interface the shear stress is continuous. This shear stress is generated by the winds that transfer momentum from the atmosphere to the ocean, through turbulent processes. The average momentum exchange is described by the *wind stress* τ which depends on the wind speed and on the sea surface roughness.

2.6 Available observations

The ocean is vast: it covers about 70% of the entire globe. Therefore it is very difficult to make measurements of the ocean, especially subsurface measurements. In fact, the available observations generally have an insufficient spatial, but also temporal, resolution to be of good use for assimilation into an ocean model, or even for mere comparison with model simulations, except for a few regions such as the tropical Pacific.

The variables normally measured are: sea surface temperature (SST), subsurface temperature, sea surface salinity (SSS), subsurface salinity, sea surface height (SSH) and velocity (or currents). For the purpose of this work, however, we will be almost exclusively interested in measurements of temperature and salinity, especially subsurface measurements, and therefore, in this section, we restrict ourselves mainly to these two variables.

In recent years, several large scale observational campaigns, such as the world ocean circulation experiment (WOCE) and the tropical ocean global atmosphere experiment (TOGA), along with the use of satellites, have markedly increased the number of available in situ and remote observations, respectively. Unfortunately, however, electromagnetic radiation does not penetrate the ocean more than a few millimeters, so, unlike the atmosphere, satellites can not be used for remotely sensing the interior of the ocean. Satellites are however very useful for they measure the SSH and the SST globally. In the near future even remotely retrieved SSS could become available

(Lagerloef *et al.*, 1995). In particular, the SSH is a very useful independent data set which can be used, through the related dynamic height quantity, to assess for example temperature data assimilation performances.

For the subsurface in situ measurement, the eXpendable BathyThermograph (XBT) is certainly the most common instrument on the global scale, about 60 000 XBT profiles collected per year (WOCE, 1997). The XBT is a probe which is dropped from a ship and measures the temperature as it falls through the water. Two very small wires transmit the temperature data to the ship where it is recorded for later analysis. The probe is designed to fall at a constant rate, so that the depth of the probe can be inferred from the time since it was launched. The probes are generally launched by research ships, naval vessels, and by the crew aboard volunteer merchant ships that transit regular shipping routes. The existing Ship of Opportunity Programme is in a transition from a successful research-managed network of XBT track lines (created by the TOGA and WOCE programs) to an operational network.

Although XBTs have been deployed for some time, it is only in the last few years that errors have been detected and corrected in the fall-rate equation coefficients and with the thermistors. Problems have also been detected in shipboard XBT recorders. Quality control of XBT data is now achieved through improved error-checking acquisition systems followed by several similar types of software that analyse (along with the operator's visual inspection) temperature profiles and flag known types of errors or problems. The Global Temperature Salinity Profile Programme (GTSPP) is a successful international effort to quality control XBT profiles exchanged over the Global Telecommunications System (GTS). It has successfully increased the quality and the number of profiles available by analysing real-time profiles and informing ship operators when problem data are suspected (see http://ioc.unesco.org/IGOSSweb/xbt.htm).

Most types of XBT are designed to measure the vertical temperature structure in the top 450 m to 750 m of the water column, although they can occasionally extend deeper. The temperature changes in the water surrounding the XBT probe, measured as change in electrical resistance, have a resolution of $\pm$ 0.01°C. The water depth is not sensed directly by the probe but calculated from the time elapsed since the probe contact with the water and the probe's expected fall rate. Therefore, the overall XBT probe accuracy is rated to $\pm$ 0.15°C (Bailey *et al.*, 1994).

Other types of in situ subsurface measurements, though less frequent than XBTs,

are also available but we only mention them here. The Mechanical BathyThermographs (MBT) measure temperature only, whereas instruments that measure both temperature and salinity are Profiling Autonomous Lagrangian Circulation Explorer (PALACE), Temperature/Salinity/Currents (TESAC), Bottles and Conductivity-Temperature-Depth (CTD). Overall the number of available subsurface measurements of salinity is much smaller than that of temperature and they are roughly in a ratio 1:10, which therefore makes temperature observations much more abundant than salinity observations [13] (e.g. WOCE, 1997). In addition, in the near future a new network of autonomous profiling floats (Argo), part of the Global Ocean Data Assimilation Experiment (GODAE) project, will become available. This network will enhance the present level of upper ocean temperature and salinity measurements (for more information see the web page http://WWW.BoM.GOV.AU/bmrc/mrlr/nrs/oopc/godae/homepage.-html).

Instruments like the CTD are more accurate than XBTs, for temperature. In fact, the temperature accuracy can be as high as $\pm$ 0.002°C (Hogg, 1996). In addition, the salinity accuracy is also high and equal to about $\pm$ 0.02 psu (Vossepoel, 1999). Unfortunately, as already noted, there are not enough CTD observations available for them to be usefully inserted in a data assimilation system. Yet, they represent a valuable piece of information for a model validation or for episodically and locally correcting the model T–S relationships.

Finally, a few words should be said on the SSS observations. In fact, as will become clear in this work, they would represent a very important constraint to the reconstruction of vertical salinity profiles, especially if they were widely available. This is not mere speculation for a recent investigation by Lagerloef *et al.* (1995) suggests that SSS remote sensing is technically feasible and can deliver a precision of 0.1–0.3 psu which is not particularly good but which would realistically improve with advancing technology. Moreover, the Soil Moisture and Ocean Salinity (SMOS) satellite mission, which should be launched between 2002 and 2004, has also, amongst its objectives, the retrieval of SSS observations (for more information refer to the web page: http://www-sv.cict.fr/cesbio/smos).

[13] Despite the presence of these rather sparse salinity measurements, we shall not consider them in the development of our data assimilation scheme.

2.7 Data assimilation methods

"Data assimilation is the name given to the process of combining a physical model with observational data to provide a state analysis of the system which is better than could be obtained using just the data or physical model alone" (Anderson *et al.*, 1996).

Essentially, two approaches to data assimilation have emerged in the oceanographic community (Ghil and Malanotte-Rizzoli, 1991). One is the development and use of sophisticated assimilation techniques, which have been mainly applied to simple dynamical models. These techniques can be divided into two groups: *sequential* (e.g. the Kalman filter or the Optimal Interpolation, OI) and *model-trajectory* (or *variational*, e.g. the 3DVAR or 4DVAR) methods. In recent years, a few groups have started to implement some of these techniques, especially OI but also Kalman filter, into primitive equation global ocean models (e.g. at ECMWF and at NASA).

The second approach adopts data assimilation schemes which are methodologically simpler than either sequential or model-trajectory technique and hence they are computationally more efficient. Therefore, this second approach allows more flexibility in designing data assimilation experiments. For instance, sensitivity experiments can be carried out more easily. Two important schemes in this category are the *blending* and the *nudging* methods (Ghil and Malanotte-Rizzoli, 1991), which are highly simplified versions of the sequential technique (Anderson *et al.*, 1996).

Let us start from the first approach. As discussed by Lorenc (1986), all the techniques, i.e. the sequential and the variational methods, stem from a common root which is estimation theory combined with a Bayesian analysis. Here, following the notation in Ghil and Malanotte-Rizzoli (1991), we just outline the main concepts behind estimation theory and say a few words on Bayes' theorem.

Estimation theory and Bayes' theorem Suppose we have two measurements y and z of the same observable x. The simplest estimate of x, $\hat{x}$, is given by the linear combination of y and z:

$$\hat{x} = \alpha_1 y + \alpha_2 z \tag{2.25}$$

For simplicity, we assume the two measurements to be unbiased, $Ey = Ez = Ex$, with E the expectation operator, that is the mean or average of a theoretically infinite number of measurements. The hypothesis that the estimate $\hat{x}$ itself is unbiased implies

also that $\alpha_1 + \alpha_2 = 1$. Therefore equation (2.25) can be rewritten as:

$$\hat{x} = y + \alpha_2(z - y) \tag{2.26}$$

We also assume that the measurement errors are uncorrelated, $E[(y-Ex)(z-Ex)] = 0$, and that their variances σ_1 and σ_2 are known:

$$\sigma_1 \equiv E[(y - Ex)^2] \qquad \text{and} \qquad \sigma_2 \equiv E[(z - Ex)^2] \tag{2.27}$$

The optimal linear unbiased estimate of x is given by choosing α_2, or α_1, so as to minimise the variance:

$$\sigma^2 = E[(\hat{x} - x)^2] \tag{2.28}$$

of the estimation error. This is attained by setting $\partial\sigma^2/\partial\alpha_2$ to zero, which yields:

$$\alpha_1 = \hat{\sigma}^2/\sigma_1^2 \qquad \text{and} \qquad \alpha_2 = \hat{\sigma}^2/\sigma_2^2 \tag{2.29}$$

where $\hat{\sigma}^2$ is the variance of the optimal estimate, $\hat{\sigma}^{-2} = \sigma_1^{-2} + \sigma_2^{-2}$. Therefore, $\hat{\sigma}^2$ is smaller than both σ_1^2 and σ_2^2. Note also that the weights α_1 and α_2 thus reflect the relative uncertainties in y and z, respectively. If we define the accuracy $A \equiv \sigma^{-2}$, that is the inverse of the variance of a random error, then the accuracy of a linear unbiased optimal estimate is equal to the sum of the accuracies of unbiased mutually uncorrelated measurements.

It can be shown that the estimate above can also be obtained by minimising the functional:

$$J \equiv \frac{1}{\sigma_1^2}(\hat{x} - y)^2 + \frac{1}{\sigma_2^2}(\hat{x} - z)^2 \tag{2.30}$$

with respect to $\hat{x}$. In order to solve (2.30), that is to find $\partial J/\partial\hat{x}$, information on σ_1 and σ_2 is required.

More specifically, the two measurements y and z can represent the model and observational data, respectively. The estimation theory therefore yields the best estimate of the state analysis with sole knowledge of the present information. However, if we found a way to relate the state of the system at the time of the assimilation with previous information we would improve the state analysis[14]. This is supplied by Bayes' theorem which states that the posteriori probability P of an event A occurring, given

[14] A big problem in data assimilation remains though and this is how to estimate the model error, i.e. the σ_1 keeping the previous example.

that event B is known to have occurred, is proportional to the prior probability of A, multiplied by the probability of B occurring given that A is known to have occurred:

$$P(A|B) \propto P(B|A)P(A) \tag{2.31}$$

This can be applied to the estimation problem. If A is the event $\boldsymbol{x} = \boldsymbol{x_t}$ and B is the event $\boldsymbol{y} = \boldsymbol{y_o}$, then:

$$P(\boldsymbol{x} = \boldsymbol{x_t}|\boldsymbol{y} = \boldsymbol{y_o}) \propto P(\boldsymbol{y} = \boldsymbol{y_o}|\boldsymbol{x} = \boldsymbol{x_t})P(\boldsymbol{x} = \boldsymbol{x_t}) \tag{2.32}$$

where the subscript $\boldsymbol{t}$ indicates the true value and $\boldsymbol{o}$ the observed value (Lorenc, 1986).

Based on the above discussion of estimation theory and Bayes' theorem, it can be shown that it is possible to obtain the equation which provides the analysis step in sequential assimilation methods (we are not interested here in variational methods). We only report the final result here (for the actual derivation see Lorenc, 1986):

$$\boldsymbol{x_a} = \boldsymbol{x_f} + \boldsymbol{K}(\boldsymbol{y_o} - \boldsymbol{F}\boldsymbol{x_f}) \tag{2.33}$$

where $\boldsymbol{x}$ represents the model state variables (e.g. temperature, velocities), the subscript $\boldsymbol{a}$ indicates analysis and subscript $\boldsymbol{f}$ the previous forecast, also known as background, and $\mathbf{y_o}$ is the observation vector. $\boldsymbol{K}$ is a matrix of weights, determined by the model and observation errors, used to convert the observed–model differences into the space of the model variables. $\boldsymbol{F}$ is the forward model which converts model variables into observation variables in the space of which it is easier to perform the error analysis. Equation (2.33) assumes that observed and model data are linearly related. More general expressions for the analysis are possible, but this equation serves our purpose (see Anderson *et al.*, 1996, and Lorenc, 1986, for further detail).

What distinguishes one sequential method from another is the way in which the weighting matrix $\boldsymbol{K}$ is determined. Here, we shall only present the two simplest methods, mentioned above, namely the blending and the nudging methods, which adopt highly simplified versions of the matrix $\boldsymbol{K}$. Let us consider the blending method first. This is best discussed using the, slightly modified, 1-D version of equation (2.33):

$$x_a = x_f + K(x_o - x_f) = (1 - K)x_f + Kx_o \tag{2.34}$$

which is analogous to (2.25). K is an empirical weight assigned to the observed value. For $K = 1$, the blending method reduces to direct insertion of the observed value in place of the model-predicted value (Ghil and Malanotte-Rizzoli, 1991).

The equation for a nudging, or relaxation, scheme, is:

$$\frac{\partial x}{\partial t} = \text{RHS} - G(\sigma, \delta t, \delta x)(x - x_o) \tag{2.35}$$

Equation (2.35) hence describes the time evolution of the variable x, i.e. it is the prognostic equation for x, in which a relaxation term is introduced. In fact, RHS (Right-Hand Side) contains the linear and non-linear terms of the prognostic equation for x and the relaxation function G is in principle a function of σ, the standard deviation of the observation, of δt, the time separation between observation time and model evaluation time, and of δx, the distance between the model grid point and the observational point. In practice, however, G is assumed to be a constant (Ghil and Malanotte-Rizzoli, 1991).

The nudging method can therefore be viewed as a variant of the blending technique. In fact, the state analysis x_a can be calculated through equation (2.34) and the increment, $x_a - x_f$ thus obtained can be divided by the number of model time steps between two adjacent assimilation steps and used instead of the relaxation term in eq. (2.35).

In particular, in this work we will use the blending method for the synthetic assimilation experiment in chapters 5 and 6, and an OI scheme in the assimilation experiment with real observations in chapter 7.

Chapter 3

A Salinity Analysis Algorithm

In this chapter we present our solution to the problem of how to combine a priori (or forecast) temperature and salinity fields with the measured in situ temperature (e.g. XBT) profile in order to get a new salinity profile. This salinity method is first presented formally and then a specific example is discussed. Also, a new diagnostic tool aimed at evaluating the effect of a data assimilation system, the inventory, *is introduced.*

3.1 Introduction

The deleterious effect on the temperature field of assimilating only temperature without changing the salinity has been shown in Fig. 1.1. In turn, and more importantly, this is detrimental for the density field too. Therefore we need to update the salinity field accordingly when new temperature data are assimilated. In this chapter we will introduce and discuss an alternative method, to those discussed in chapter 1 (e.g. the use of climatological T–S relationships), for updating the salinity field. The basic idea is to use the model temperature and salinity fields as a background from which to derive the new salinity profile.

Overall, the guidelines for this method are: 1) that model water masses should only be changed when experimental evidence is available (i.e. new temperature and/or salinity observations become available), as suggested in Haines (1994) and 2) that the method formulation and realisation should be as straightforward as possible. For what concerns point 1), this does not mean that we completely trust the composition of the model water masses but only that, rather than adding inconsistent information which could worsen the T–S properties of the model water masses (we will see examples of

such worsenings in chapters 6 and 7), we choose to utilise information supplied by the model. This approach should have the advantage of focusing more on the model errors and therefore it could help us to highlight them. Further, following point 2), we can attain a scheme which is, at the same time, easily portable and which also allows us to concentrate more on its physical impact on the model, rather than, for instance, on an optimal way to spread the salinity increments, which in any case relies on uncertain knowledge of statistics, as with more sophisticated data assimilation techniques (see section 2.7), or on the choice of alternative T–S relationships such as the use of limited data sets as in Maes *et al.* (2000).

The method consists essentially of two stages. The first stage is the completion of the temperature vertical profile through extension to greater depths and the second is the use of T–S relationships to obtain the new salinity profile. Both stages refer to a single horizontal grid point, that is we process each grid point individually.

In particular, the first stage is aimed at avoiding temperature jumps at the bottom of the observed temperature profile, when this is assimilated. In the second stage the scheme computes a salinity analysis, using the T–S relationships from the model temperature and salinity background profiles. For example, at a T observation of 20°C, the analysed S will be the same as the S present at the depth of the 20°C water type in the model profile. The two stages are discussed in more detail next[1].

3.2 Vertical displacement

When a vertical profile of temperature is observed, it is normally shallower than the local topography. Therefore, undesirable jumps in temperature could intervene when this profile is combined with that of the model to give the analysed temperature profile. One of the consequences could be the generation of water column instabilities, especially when the deepest observed temperature (hereafter T_{ref}) is cooler than the next deeper model level. Some data assimilation methods leave the water column unmodified below T_{ref}, trusting that the internal dynamics of the model will provide a realistic response. Another used approach is to make increments below T_{ref} according to some prior knowledge of vertical correlation scales. Here a different approach, similar to that used by Cooper and Haines (1996) for altimeter assimilation, is introduced.

[1]To keep the discussion of the salinity scheme as simple as possible, we do not include any error analysis at this stage, that is we shall consider the available model and 'observed' data as error-free.

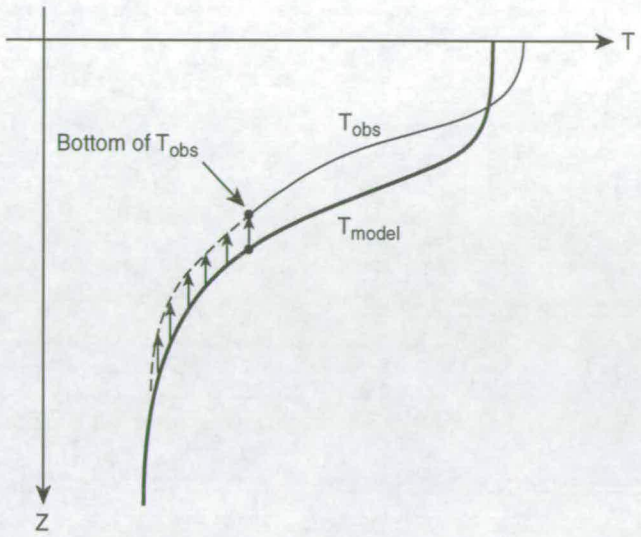


Figure 3.1: Schematic of the vertical displacement (first stage of the assimilation method). The displacement is the difference between the depth of the deepest observed temperature (thin solid line) and the depth of the same temperature in the model profile (bold solid line). This displacement is then used to lift (as in the figure) or lower the model profile in order to complete the observed profile below the deepest observed temperature (dashed line).

It requires that T_{ref} will match the model water type of the same temperature by vertically shifting the model water column until this match is the case. In other words, the vertical displacement corresponds to the difference between the depth of T_{ref} and the depth of the same temperature in the model profile. A schematic example is shown in Fig. 3.1, where "bottom of T_{obs}" is T_{ref}. The reason for vertically displacing the water column is that we want to maintain the density structure of the model. In fact, not only the temperature but also the salinity profile is shifted by the same vertical amount. Therefore, this action preserves that part of the T and S hydrography below the deepest temperature level, although T and S can change as a function of depth. This reflects that isopycnal surfaces are often displaced even below the depth to which observations usually extend, e.g. by internal waves. A big advantage of this vertical displacement is that it should help to prevent convective adjustments at the bottom of the observed profile when this is assimilated. In turn, this prevents the generation of new water masses below the depth of T_{ref}.

However, in the event that T_{ref} falls outside the temperature range of the model background, no displacement is performed. Typically, this may happen in coastal regions and at high latitudes.

Technically, the amount by which the vertical T and S structure is displaced is found by seeking T_{ref} starting from the bottom of the model profile. Subsequently, the part of the T and S profiles below the depth of T_{ref} are displaced contemporaneously. However, this sole assumption is not always sufficient. In fact, when the displacement is such that we need to add water mass at the bottom (i.e. we have to lift the water column), there is a further degree of freedom. In this eventuality, we impose that the properties of the added water mass are the same as the deepest existing water. This is certainly a good assumption for abyssal waters, for which the modification time is of the order of many years.

An effect of displacing the water column is a change in the amount of bottom water masses. In particular, if T_{ref} is cooler than the corresponding model temperature (as in Fig. 3.1), the model profile is lifted and hence water mass is added at the bottom. This typically happens when the thermocline of the model is too diffuse so that the isopycnal levels tend to deepen. Observed profiles must then make the thermocline shallower by lifting up the water masses below. Deep water mass is instead removed in the opposite case, that is when T_{ref} is higher than that of the model.

Both of these instances imply a change in the bottom pressure of the water column. However, at this stage no constraint is imposed on this induced change. We should also note that the modification of the density structure in the upper water column introduced by the second stage of the salinity scheme is also responsible for variations of the bottom pressure. At any rate, we should be aware that this bottom pressure modification might have undesirable side effects on the deep currents. To this end, a qualitative check will be performed in this work (section 6.4) to judge this effect.

It should also be pointed out that the vertical displacement, as formulated here, gives a large weight to T_{ref}. In fact, T_{ref} is the only datum we use to calculate the vertical displacement. In a data assimilation context which uses real observations, this very choice requires that the observed T_{ref} must be given with a good accuracy. Otherwise, the error associated to T_{ref} should also be taken into account.

Although the vertical displacement has been presented as the first stage of the assimilation procedure there is no conceptual difference in the order the vertical displacement and the T–S preservation (second stage) are applied. It is in order to give a more structured presentation that we decided to discuss the vertical displacement first.

Finally, we would like to comment on alternative approaches for the completion of the water column below T_{ref}. In fact, whilst the adopted solution has some advantages, such as its similarity with the well tested Cooper and Haines (1996)'s scheme and also the simplicity of its implementation, alternative solutions to it have been pondered (although they have not been tested). When the constraint of changing the bottom isopycnal layer only is released, the number of degrees of freedom becomes very large. In such a case, in fact, many ways of stretching the water column are possible. For example, one could add (or remove) an equal amount of water mass for each isopycnal layer below the T_{ref} level or, in the extreme case, add (or remove) the whole water mass mismatch either just below T_{ref} or at the very bottom of the water column (i.e. our approach). Possibly, a better alternative would be to add (or remove) the water mass mismatch according to a weighted procedure which takes into account the thickness of the individual isopycnal layers, that is to add (or remove) a small increment if the isopycnal layer is thin and vice-versa. The latter solution is probably more satisfactory from a physical point of view.

3.3 *T*–*S* preservation

In this section we present the second stage of the salinity method. We start by discussing the simpler case of monotonic vertical temperature profiles (section 3.3.1) and then we discuss the more general cases in which temperature inversions are present i.e. the non-monotonic case (section 3.3.2).

3.3.1 The monotonic case

Although instantaneous vertical profiles of temperature may often be non-monotonic, it is useful to start from the monotonic case to discuss the way in which the T–S relationships are used in our assimilation method.

Formalism

When we think about the temperature of a water column we usually associate it to a certain depth, that is we would say, for instance, that at 50 m the temperature is 15°C. In other terms, we usually know the temperature, or the potential temperature[2], as

[2] Although potential temperature should be used, for simplicity, temperature will be used hereafter, unless otherwise stated.

a function of depth: $T = f(z)$. This function is known for both the model and observation vertical profiles. For the latter, the vertical displacement of the previous section is used to complete it in case the observed temperature profile does not reach the sea bed. Note that, in models, as well as in observations, this is indeed a discrete function. Nonetheless we will assume for the time being that we have a continuous function.

Now, if we are to compare water mass properties, we need to know how much water of a certain type is present in a given water column, so we need to calculate the inverse of f. Let us call $z = g(T)$ the inverse of f, which represents the model profile, and $\zeta = \psi(T)$ the corresponding measured one.

To compare the two water columns, we start off from this simple relationship:

$$\int_{z_{bot}}^{\eta_1} d\zeta - \int_{z_{bot}}^{\eta_2} dz \approx 0 \tag{3.1}$$

where η_1 and η_2 are the sea surface elevations of the observed and model water column, respectively, and z_{bot} is the sea bottom. The relation (3.1) states that, if we neglect the difference in sea surface elevation between the two water columns, they have the same length. In most numerical ocean models this condition is automatically assured by the hypothesis that the velocity field is non divergent, i.e. $\nabla \cdot V = 0$. If we now go from z space to T space, where the comparison between the T water mass properties of the two profiles is more straightforward, (3.1) becomes:

$$\begin{aligned} \int_{-\infty}^{+\infty} \left(\frac{d\zeta}{dT} - \frac{dz}{dT}\right) dT = \int_{T_1}^{T_2} \left(\frac{d\zeta}{dT} - \frac{dz}{dT}\right) dT &= \\ \int_{T_1}^{T_2} (\psi'(T) - g'(T))\, dT &= 0 \end{aligned} \tag{3.2}$$

where T_1 and T_2 define the temperature range $[T_1, T_2]$, within which the temperatures of both water columns lay.

If we are to use equation (3.2) in a numerical code, we need to have a discrete formulation. For any finite temperature interval, ΔT, we can write:

$$\begin{aligned} \sum_{n=0}^{\overline{n}+1} \left(\frac{\Delta\psi}{\Delta T}(T_1 + n\Delta T) - \frac{\Delta g}{\Delta T}(T_1 + n\Delta T)\right) \Delta T &= \\ \sum_{n=0}^{\overline{n}+1} (\psi(T_1 + (n+1/2)\Delta T) - \psi(T_1 + (n-1/2)\Delta T)) &- \\ (g(T_1 + (n+1/2)\Delta T) - g(T_1 + (n-1/2)\Delta T))) &= 0 \end{aligned} \tag{3.3}$$

where $\overline{n}$ is equal to the integer of the ratio $(T_2 - T_1)/\Delta T$. In practice, in the numerical code, for each interval in the range $[T_1, T_2]$, we calculate the difference between the amount of water mass in the two water columns, i.e.:

$$\left(\psi(T_n^{''}) - \psi(T_n^{'})\right) - \left(g(T_n^{''}) - g(T_n^{'})\right) \qquad \forall n = 0, 1, ..., \overline{n} + 1. \tag{3.4}$$

where $T_n^{''} = T_1 + (n + 1/2)\Delta T$ and $T_n^{'} = T_1 + (n - 1/2)\Delta T$.

These water mass differences are then used to modify the model salinity profile according to the following procedure. First we increase the resolution of the vertical profile of the model salinity by a spline method. Second we project the high resolution profile thus obtained into the modified, through equation (3.4), water column. In this water column, water mass is added or removed according to the differences between observed and model temperature profiles. To help understand this procedure, a pictorial representation of it is discussed next. The numerical code for the assimilation algorithm is given in appendix A.1 (and its include files in appendix A.2).

Method schematic

Figure 3.2 shows in a schematic and pictorial way how the salinity method works for the monotonic case. The model, or a priori, water column (first column from the left) is divided up into isopycnal layers, for which the individual temperature and salinity are known. This water column extends to the bottom of the sea (determined by the model topography). It is this water column[3] that supplies us with both the temperature information needed for the completion of the temperature profile, i.e. the vertical displacement (first stage of the salinity method) and the T–S relationships used for reconstructing the new, or analysed, salinity profile (second stage).

The second water column from the left in Fig. 3.2 represents the incomplete vertical profile of temperature derived from observations: it could either be the observation temperature profile itself or one processed through an assimilation error scheme, such as an OI scheme (see chapter 7). This water column only extends to 500 m in the figure, which is a typical depth for temperature measurements such as XBTs.

On the right, figure 3.2a shows the result of the whole salinity method combining its two stages. First the vertical displacement shifts the model water column in order to complete the observational water column, as discussed in section 3.2. In the schematic,

[3]Another common possible solution, that has been discussed in chapter 1, would take the T–S relationships from a temperature and salinity climatological data set.

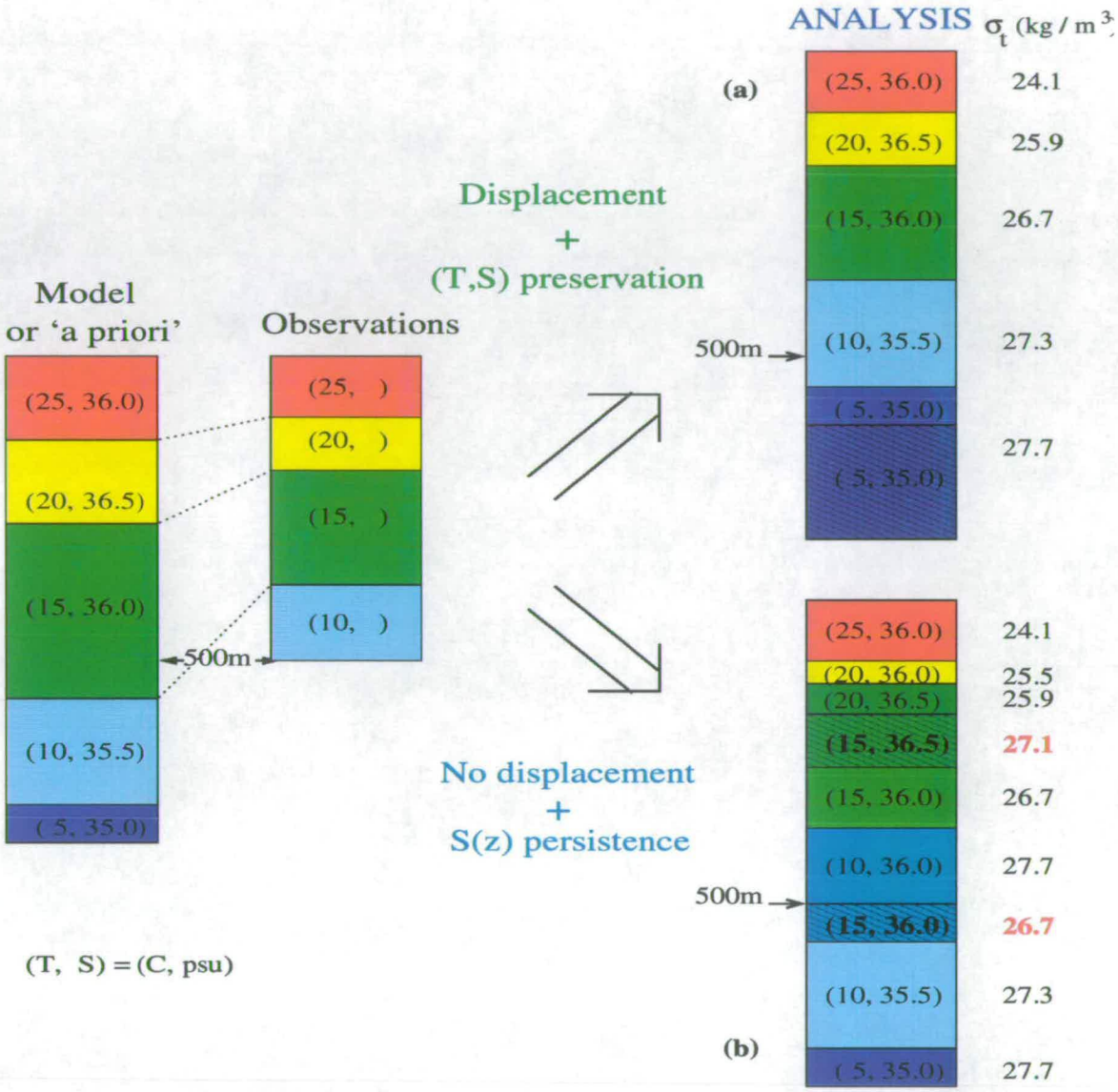


Figure 3.2: Schematic representation of the two stage analyses (right) obtained by combining 'Model' (or 'a priori') and 'Observations' water columns (left), for the monotonic case. On the right, the density anomaly (σ_t) is shown. (a): Our method: the 'Model' is displaced to match the bottom of the 'Observations' (stage 1) and the T–S preservation applied (stage 2). The blue forward hatched layer (5°C, 35 psu) highlights added water type, due to the vertical displacement. (b): Direct insertion of the 'Observations' into the top 500 m of the 'Model': the absence of a displacement causes an unstable layer (15°C, 36 psu, light blue forward hatched). Also, the unaltered S profile introduces another unstable layer (15°C, 36.5 psu, green forward hatched).

the model water column had to be lifted, thus resulting in an addition of water mass at the bottom of the column (5°C, 35 psu, blue back hatched layer). The second stage of the method associates the new salinity to the observed temperature. This new salinity is derived by assuming that the background T–S properties are preserved and are taken from the T–S relationships of the model water column on the left. The net result, i.e. the analysis, is a water column with a density stratification, in the top 500 m, which matches the thermal stratification of the observed water column. Altogether, no information other than the temperature analysis (observations in the present case) and the model T and S profiles is needed for the salinity scheme to work.

In order to show that the water column stability is preserved, the values of the density anomaly for each layer are also indicated in Fig. 3.2. The density anomaly values of the analysed water column correspond to those in the model water column, although the stratification has changed. Thus, since the model water column is statically stable, the analysed water column (Fig. 3.2a) will also be so.

For comparison, another water column analysis, that is one in which the salinity field is left unchanged and no displacement is performed, is shown in Figure 3.2b. Hitherto, this has been a common approach in data assimilation systems when temperature observations are available for assimilation. The lack of vertical displacement is reflected here in the generation of a spurious density layer just below 500 m depth (15°C, 36 psu, light blue back hatched layer). As indicated by the value of the density anomaly of this layer, $\sigma_t = 26.7$ kg m^{-3}, it is lower than that of the layer above it. Therefore the water column becomes statically unstable and, in the case of a model integration this would lead to convection with consequent generation of further spurious water masses.

Above the 500 m depth, the $S(z)$ salinity persistence yields an undesirable fragmentation of the water column. One of the problems caused by this fragmentation is that it may lead, as in our schematic, to an unstable density layer at $\sigma_t = 27.1$ kg m^{-3} (green back hatched). This unstable layer would cause the same type of problem as that just highlighted in the previous paragraph.

It should be pointed out that in this section we have neglected certain difficulties in the salinity scheme that are present even in the monotonic case. The two main problems, which are related to the T–S assumption, are that: 1) the T–S preservation may fail in the upper water column because of the presence of non-isentropic processes, and 2) we could observe a value for the temperature that is not present in the model

water column, preventing the use of the model T–S relationships. These two problems will be discussed with the more general non-monotonic case in the next subsection.

3.3.2 Temperature inversions

Although the discussion of the monotonic case in the previous section is useful to clarify the salinity method, it excludes several types of profile, i.e. those in which the temperature as a function of z has inversions. This means that in such cases the temperature profiles $T = T(z)$ are non-monotonic and, therefore, we cannot find its inverse. Further, in terms of salinity, this implies that even $S = S(T)$ is not uniquely defined either (i.e. it is not a function) and therefore the approach taken in section 3.3.1 is no longer valid. In order to take this difficulty into consideration, we adopt the solution of considering the function $S = S(T, z)$ instead of just $S = S(T)$. In other words, we introduce also the depth dependency so as to obtain a function for salinity[4]. The idea stems from the fact that vertical water column displacements do occur, because of internal waves or mesoscale features (e.g. Emery and Dewar, 1982). Normally, these processes do not modify to any great extent the water mass properties, and therefore one can distinguish between two (or more) isothermic parcels according to their depth. Salinity is then recovered from the nearest T point in depth in the background field. Also, to mimic the physical picture, an upper limit to the vertical displacement can be assigned. This limit will depend on the time lag between assimilation steps and on the location, particularly the latitude.

Furthermore, the two problems related to the T–S preservation mentioned at the end of section 3.3.1 are tackled as follows. Let us start from the second for which a simple solution is chosen. That is, if the observed temperature is outside the range of the model T profile (as may typically happen near the surface), then the model salinity is not modified. So, if for example the observed SST is larger than the model SST, then the analysed SSS is the same as the model SSS. In other words, given our ignorance about the surface fluxes, we assume that the two water columns are linked by a pure heating process with no implied change to Evaporation minus Precipitation.

The first problem is, instead, much more delicate and several solutions have been investigated and applied throughout the course of this work. One solution is to use the plain T–S relationships even near the surface (see chapters 4, 5 and 6). Amongst other

[4] A more rigorous approach should consider the density instead of the depth. That is we should consider the function $S = S(T, \sigma_t)$.

things, this solution allows one to compare this approach with the $S(z)$ persistence directly. The next solution is to leave the salinity unchanged in the top model levels (the number depends on the vertical resolution) just as in the $S(z)$ persistence. A third solution is a mixture of the previous two. In fact, in order to avoid applying the T–S relationships of near-surface water mass to deeper layers, the model T–S relationship from the upper water column, say 50 m, is used only if the corresponding observed temperature is also near the surface. Otherwise, no change is made to the model salinity, as in the $S(z)$ persistence (see chapter 7).

It must be stressed that none of these solutions represents an obviously optimal solution and that they only try to account for the fact that the available information about the surface processes, such as the fresh water budget, is scarce. In fact, if we had a better knowledge of say the Evaporation minus Precipitation budget, or even of the sea surface salinity, we could impose a further constraint that would relieve the *ad hoc* solutions discussed above.

Finally, it should be noted that even for the vertical displacement presented in section 3.2, the non-monotonicity could be a problem. However, as the deepest temperature observation, T_{ref}, is typically at 500 m depth, the part of the temperature profile below this depth is generally less affected by non-monotonicity. Nonetheless, if T_{ref} were present at more than one depth in the model temperature profile, the deepest match would be retained for the vertical displacement. Another solution could be to select the closest in depth amongst the temperatures T_{ref} in the model.

3.3.3 The salinity method at work

We will discuss now a specific example. In this example all the profiles, the T and S model profiles and the observed T profile, are taken from a model. Since the aim here is only to show how the salinity scheme works, it is not relevant to know from what model these profiles are taken or why they may have particular characteristics. Instead we will focus on the technical aspects, at this stage. The actual implementation of the salinity scheme using real and realistic observations will be presented from the next chapter.

Figure 3.3 shows the two temperature profiles used in our example. The observations profile is chosen in such a way that it extends to just below 500 m. The shapes of the two profiles are quite different: that representing the model has a regular gradient

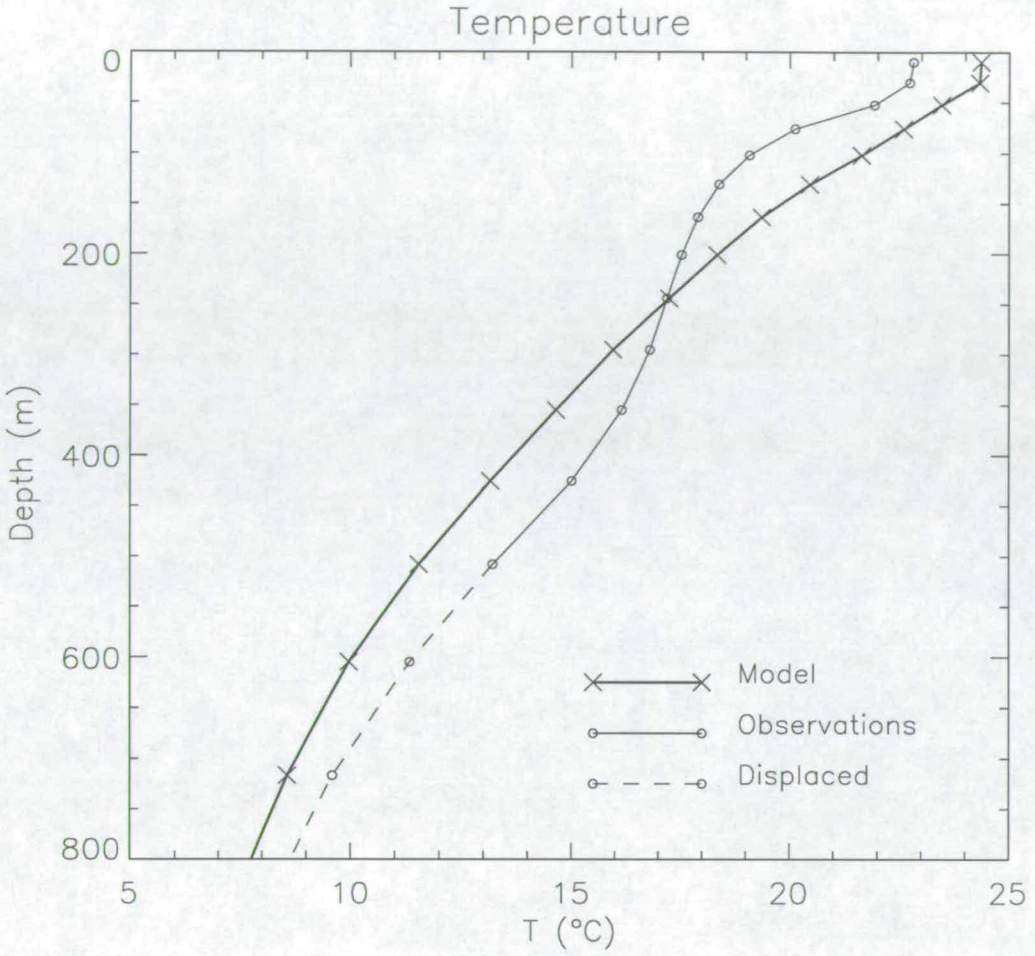


Figure 3.3: Temperature vertical profiles. The observations profile has been completed (dashed line) by shifting the model profile. In this case the model profile has been lowered of about 60 m.

throughout the water column whereas the one that represents the observations goes from a colder top water column (upper 250 m) to a warmer lower thermocline, i.e. down to 500 m, with respect to the model profile. In particular, the fact that the observations profile is warmer at 500 m implies that the vertical displacement requires the model profile to be lowered. In this case the lowering is equal to about 60 m.

The reconstruction of the salinity profile using the salinity scheme is shown in Figure 3.4. Concerning the solution near the surface, we used the T–S relationships throughout the entire water column (i.e. the first solution discussed earlier). Let us examine the shape of the analysed salinity profile. In particular, as this is derived from the model salinity profile, only the range of values of salinity present in the latter will be found in the analysed profile. In the top 250 m, the analysed salinity is obtained by lifting up the model salinity profile by amounts specified by the distance

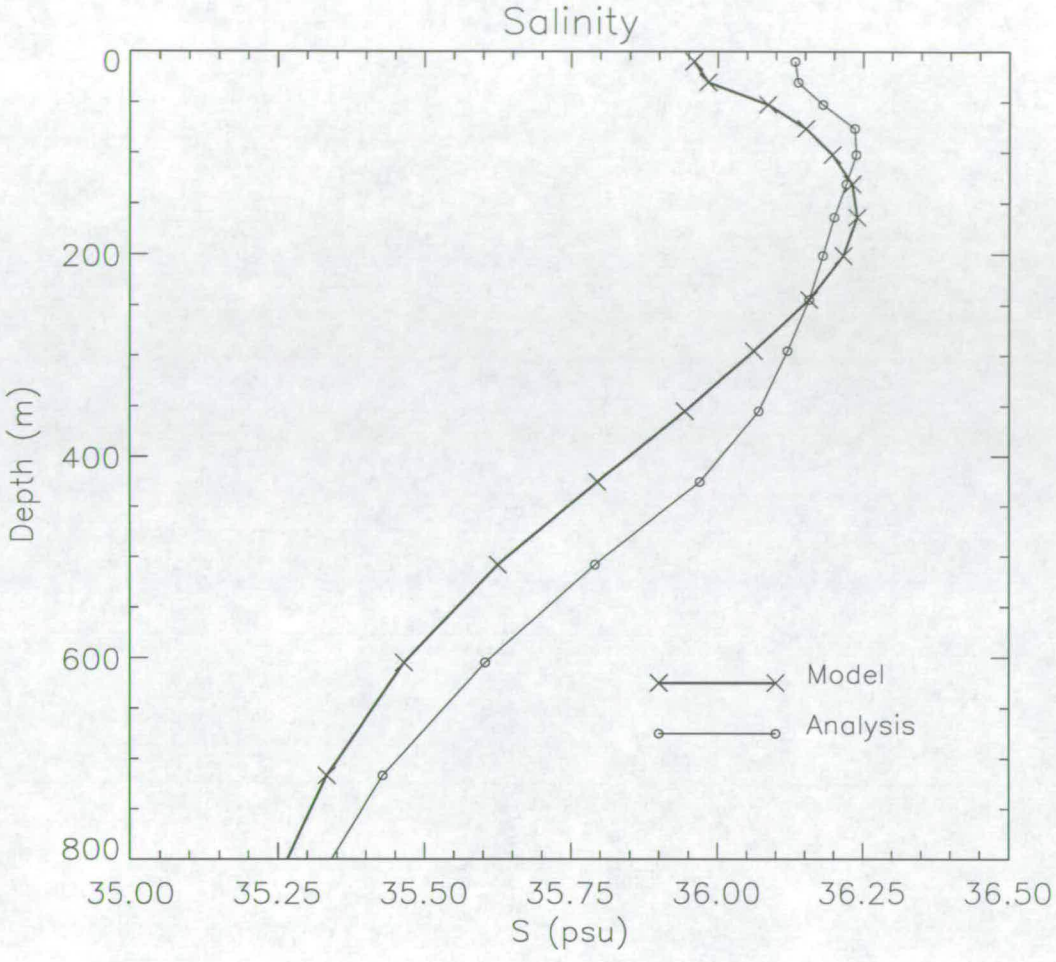


Figure 3.4: Salinity vertical profiles. The analysis profile is the reconstructed salinity profile by using the salinity scheme. This profile pairs off with the observations plus displaced profile in Fig. 3.3.

between the depths of the observed and the model temperatures. In fact, in the upper water column the temperature observation is colder than the model temperature or, stated otherwise, the model thermal structure is deeper than that of the observations. Therefore in order to maintain the same T–S relationships, the density structure of the model is lifted up, thus resulting in the shifted salinity profile. Note that at the surface, the analysed salinity has the same value as that of the model salinity at the depth of about 75 m as the observed sea surface temperature corresponds to the model temperature at 75 m depth.

Below 250 m, that is where the observed temperature is warmer than the model temperature, the analysed salinity has been obtained by lowering the model salinity profile. Because the model salinity decreases with depth below 250 m, this lowering results in a saltier analysed salinity profile with respect to the model profile.

Note that the salinity maximum present in the model at about 160 m is maintained in the analysed profile too, even though at a shallower depth (about 100 m). It must be emphasised that, even if the observation profile contains the model temperature corresponding to the salinity maximum as in the present example, this preservation is not always assured for it may depend both on the magnitude of the salinity gradient and on the model resolution in the neighbourhood of the salinity maximum. In fact, if the gradient is too large and/or the model resolution too low, the model salinity maximum could be smoothed when a vertical displacement is performed.

It is also useful to examine the results of the salinity method in a T–S diagram. Figure 3.5 shows the two T–S profiles (M for model and A for analysed), also highlighting the depth of the model levels. The two T–S curves are basically overlapping. This was evidently expected since we imposed it, through the T–S preservation, in order to get the salinity analysis. This is a confirmation that the T–S relationships are indeed preserved.

More specifically, for depths shallower than 244 m, a shift of the analysed T–S profile (the A of Fig. 3.5), over the model T–S profile (the M), towards cooler and saltier water masses can be observed. As a consequence, the range of variability in T–S for the analysed water column is more limited than in the original model water column.

Even for depths below 244 m the analysed water column present a tighter T–S curve because of its shift towards saltier, but warmer water masses. Successively, the depths for the model and the analysed water masses get closer and closer, eventually coinciding at the bottom of the water column.

Note that in this particular example the temperature observations were all found within the model temperature range. This allowed us to use the model T–S relationships with no need to make further assumptions.

Finally, in Figure 3.6 we show the complete, i.e. down to the sea bottom, temperature and salinity profiles, that is for depths deeper than the 800 m considered in Figs. 3.3 and 3.4. The two panels in Fig. 3.6 highlight the way in which the vertical displacement is accomplished. It can be observed that both the deep (displaced) temperature and analysed salinity profiles coincide with those of the model, as just noted.

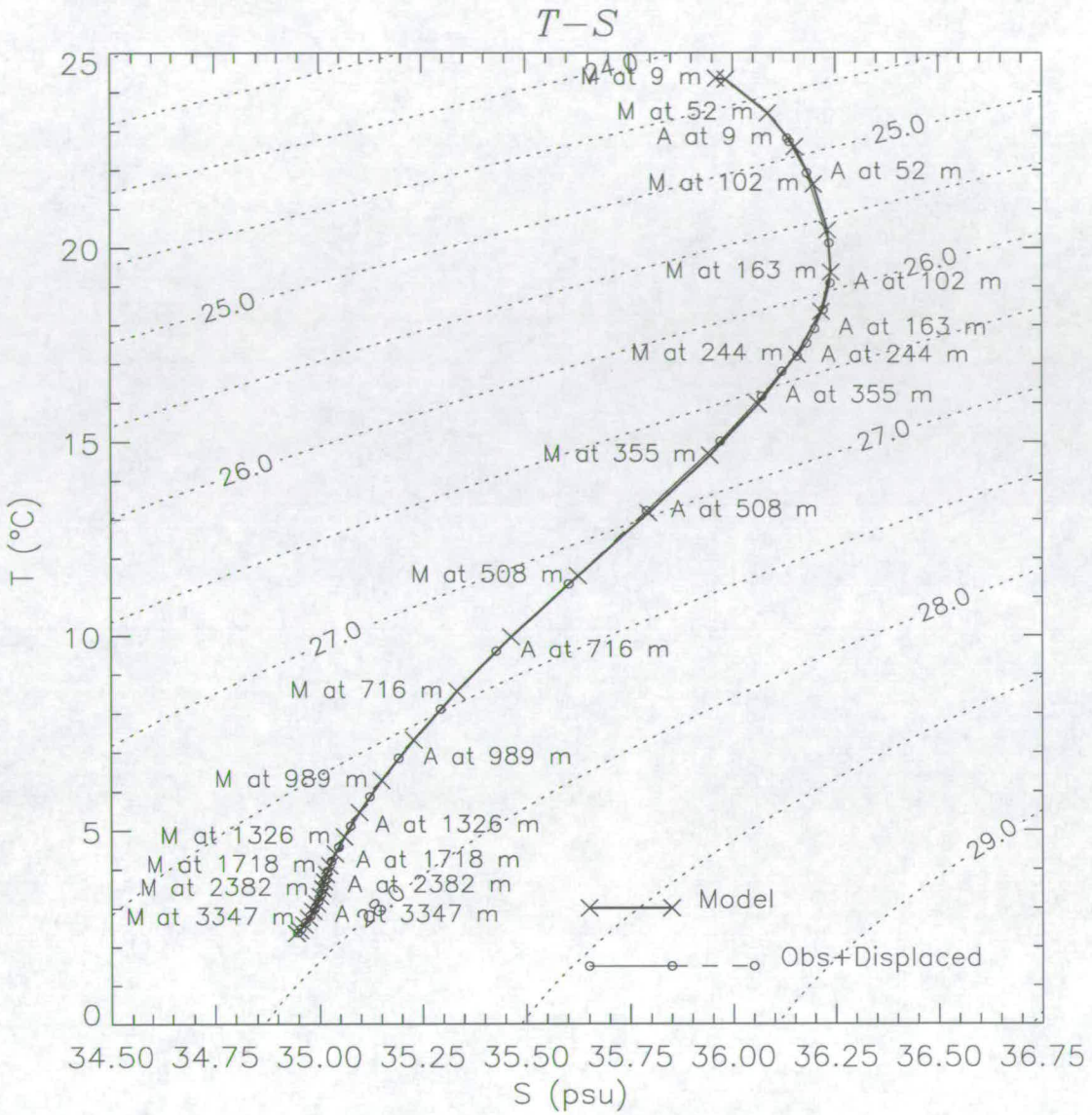


Figure 3.5: Profiles in the T–S diagram. M stands for model and A for the salinity analysis combined with the observation plus displaced temperature profile.

3.4 Enlarging the scope of the method: the inventory

Although the chief aim of a data assimilation scheme is to provide better initial conditions than just using the model fields it is also very interesting to study the changes inserted directly by the assimilation scheme itself. To this purpose, we keep account of these water mass changes in what we will call it *inventory*. This record of the action of the assimilation upon the model should lead to precious information about the physics and the dynamics of the model. In particular, we expect the inventory to supply us with insights about the physical processes not well described by the model. If, for

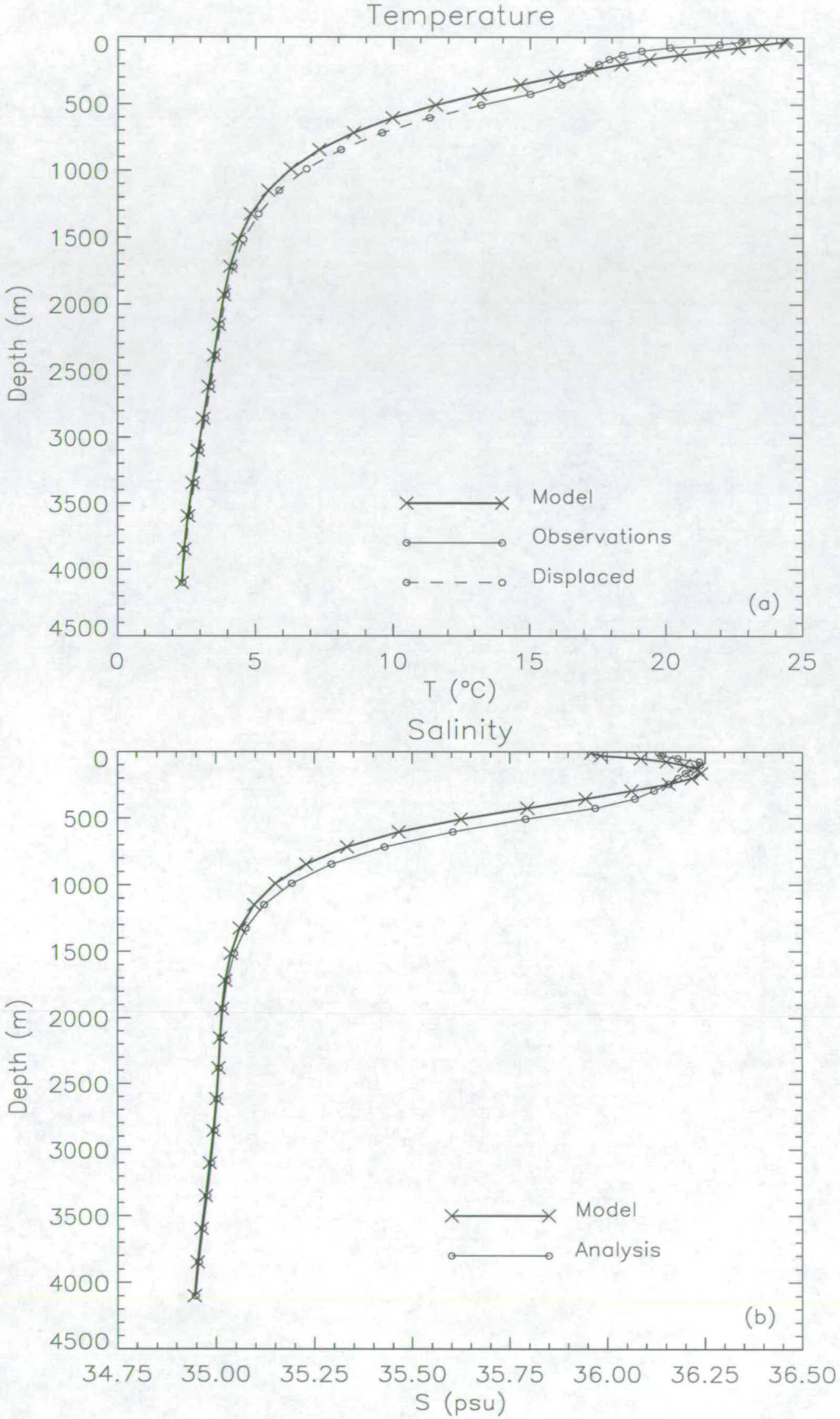


Figure 3.6: Temperature (a) and salinity (b) vertical profiles as in Figs. 3.3 and 3.4 but extended to the sea bottom.

EX BIBL. UNIV. EDINBURG

instance, a certain amount of water mass of definite T–S properties is systematically present in the inventory at each assimilation step it may imply that the model is forming water mass of the wrong values (i.e. not observed). On the other hand, a more spatially dispersed water mass may be imputed to a deficient mixing scheme.

In practice, the inventory will store the T–S properties of the modified water masses over some selected area. First, however, we examine the inventory for a single water column only in the T space, that is we take the integral of the inventory with respect to the salinity. Figure 3.7 shows the inventory in T space for the example discussed in the previous section. In other words, Fig. 3.7 shows the differences in T space between the observation plus displaced profile and the model profile according to the relation (3.4). Where the water mass difference is negative it means that the new temperature profile contains less water mass of that temperature than the model profile, e.g. for T equal to about 24°C in Figure 3.7. In more general terms, a negative sign means that an amount of the water mass of that particular temperature is removed by the assimilation scheme.

In particular, Fig. 3.7 can be divided in four parts. Let us examine them separately, commencing from the water mass with the higher temperature. The first part, $25 < T < 22.5$°C, represents the mixed layer which has a depth of the order of tens of meters. Two well defined peaks can be noticed: they simply express the mismatch between the model mixed layer temperature and the corresponding observed one. In water mass terms, this means that we have to remove the approximately 24°C water mass from the model column and replace it with the observed 22.5°C water mass. This near surface temperature discrepancy may be related to the imperfect air-sea interaction parametrisation, namely to the heat flux or to a water mass readjustment due to advection.

Below the mixed layer, the main thermocline[5] can be identified, with a temperature ranging from about 22°C to 15°C. Also for this part there are two distinct water types, even though the colder one (T centred at about 17°C) is more accentuated. Therefore, the deficit between the amount of removed water of T at about 20°C and the larger amount of added water at the lower temperature ($T \approx 17$°C) is made up partly by the removed water mass at about 24°C but mainly by the bottom water. Moreover, this

[5] In reality, this second part does not strictly represent the entire thermocline, because of our limited knowledge of the observed temperature profile.

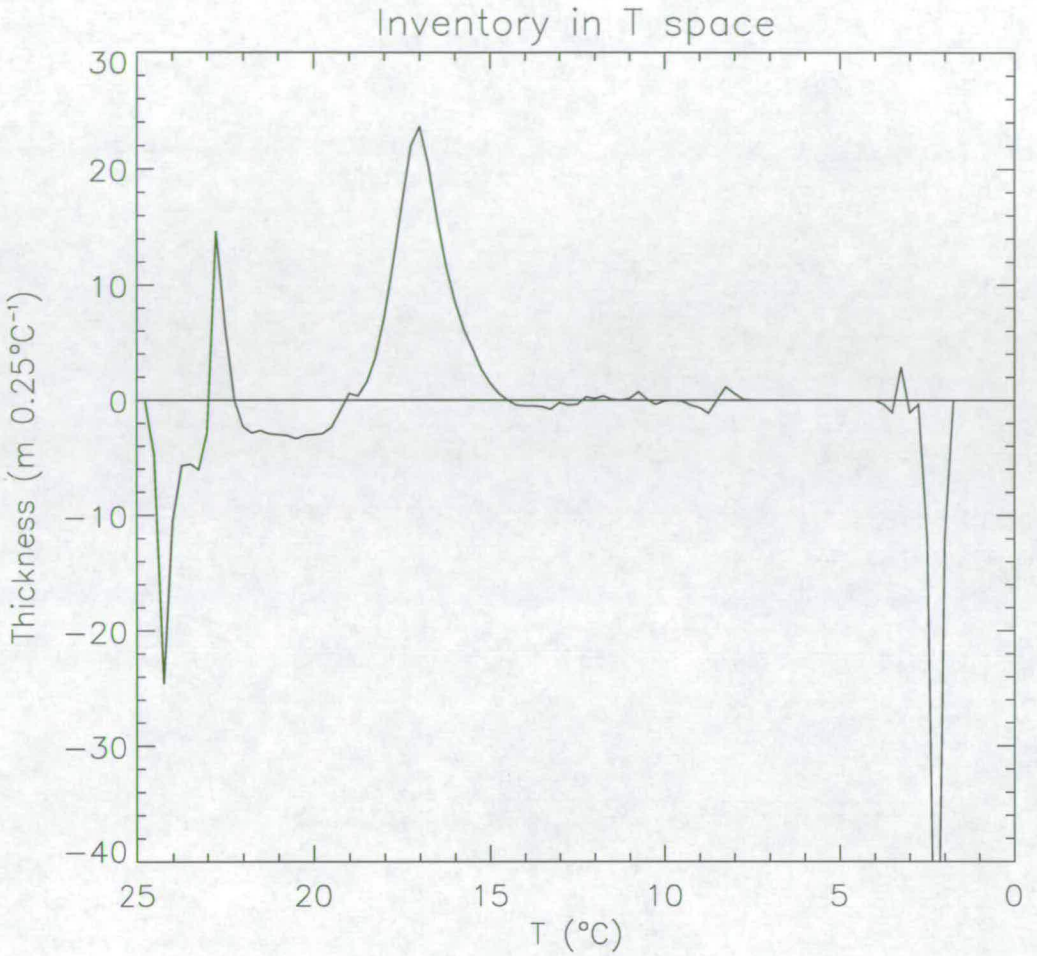


Figure 3.7: *Inventory* in the temperature space showing the difference between the observation plus displaced profile and the model profile in Fig. 3.6a according to the relation (3.4). As indicated by equation (3.2), the integral over the whole temperature range is zero. A positive value means that water mass is added in the new T and S profiles and vice-versa. The minimum is about -60 m (out of range).

deficit might indicate that the model is not able to reproduce the correct thermocline. In such a case, two possible explanations could be: a poor internal mixing scheme and/or an incorrect water mass formation. The third part of the inventory (T between 15°C and 2.75°C) is the least interesting from the analysis viewpoint. In fact, it is flat[6]. This is because between 500 m depth and the bottom the thermal structure of the two profiles is the same as implied by the assumption underlying the vertical displacement (see first stage of the vertical displacement, section 3.2). Lastly, a peak of variable temperature ($T = 2.25$°C in the current example) represents the fourth part. This negative peak is also related to the water column displacement and indicates the water mass removal at the bottom of the completed temperature profile due to the

[6]The small signal present is numerical noise.

vertical displacement procedure. Finally note that, following the equation (3.2), the integral of the inventory in T space is identically zero, i.e. the extra water mass added at $15°C < T < 19°C$ is removed at $T = 2.25°C$.

The inventory in the T space allows us to interpret the salinity scheme also from another viewpoint (it is however implicit in the discussion of the previous section). In fact, if we associate a (T, S) label to each model water type then, for a positive T inventory difference, such as between 15°C and 19°C, we will have to add a water mass with the same (T, S) value given by the model. Repeating the same procedure for each value of T we end up with the salinity analysis of Figure 3.4 or Figure 3.6b.

The complete inventory in the T–S space is shown in Figure 3.8. This contains all the information displayed in Fig. 3.7 with the addition of the salinity dependency[7]. Note that the integral of volume over all T and S is zero by definition. The integral with respect to S, therefore eliminating the S dependency, yields the function, dependent on T only, shown in Fig. 3.7.

The negative (blue) areas in Fig. 3.8 signify that a water mass has been removed during assimilation and vice-versa for the positive areas. It should be observed, however, that from the inventory it is not very easy to visually judge exactly which removed water mass matches the added water mass. What we can attain with the inventory, though, is some useful information about possible physical links between the water masses which appear in it. In other words, the inventory might represent an important tool to assess what physical processes occur from one water column realisation[8], either from model or observations, to the next, either when both T and S are known or, like in our case, when S is reconstructed. This type of assessment is similar to that performed by Bindoff and McDougall (1994). In their work, in fact, they tried to explain the changes in the subsurface water column via three different mechanisms: pure warming, pure freshening and pure heave (i.e. isopycnal displacement). To this purpose they analysed hydrographic data collected along a specific section.

Let us comment on this single water column inventory in which the salinity profile of the second water column has been derived by the salinity scheme, i.e. it is not an observation. Starting from the higher temperature, it can be observed that a warm and relatively fresh water mass has been almost entirely replaced, in the assimilation,

[7]Note that, for a better visualisation, some smoothing has been applied.

[8]An average between many water column realisations may be more appropriate, but this choice will depend on the chosen type of analysis.

by a cooler and slightly saltier water mass (the positive zone about 23°C). This is the mixed layer change noted earlier (see Fig. 3.7) where, now, salinity modifications are also included. The lower salinity in the model mixed layer might therefore be imputed either to a lower *E-P* flux or to horizontal advection from a nearby location which would hence yield a fresher water mass. Such interpretations rely however on the way the salinity profile is reconstructed. In particular, because T–S preservation is generally not a good assumption near the surface, care has to be taken in inferring model deficiencies such as the suggested forcing interpretation. Then, between about 19.5°C and 22.5°C other model water mass is removed as the observed temperature profile has, for that temperature range, a steeper vertical gradient and hence thinner inter-isothermal layers (cf. Fig. 3.3 at depths between 50 m and 100 m). Instead, for temperatures between 15°C and 17.5°C the thermal stratification of the observed profile is less accentuated (cf. Fig. 3.3 again, at depths between about 175 m and 500 m, but also Fig. 3.5 in which the distance in T–S space between the vertical grid points is smaller in the observed profile than in the model profile for this T range). This rather different value of the stratification means that the observed profile has considerably more 15°C–17.5°C water mass and this therefore yields a marked increment (the positive area) in the inventory. This 15°C–17.5°C water mass partly replaces the warmer model water mass with $19.5°C < T < 22.5°C$ (the rest will balance out the bottom water). The salinity associated with the 15°C–17.5°C water mass is in the range between 36 psu and 36.25 psu and it is mainly derived from the 200–300 m depth range of the model salinity profile, that is just below the subsurface salinity maximum (Fig. 3.4). Hence, fresher (and cooler) water mass has been added in the assimilation.

We can pass over the inventory differences between 3°C and 15°C which substantially show only numerical noise (cf. Fig 3.7 for the T inventory) and therefore indicate that the water mass structure in the two profiles is basically the same for this T–S range. This is a consequence of the vertical displacement. Instead, the inventory shows another important feature at about 34.9–35 psu and 2.25°C, namely the deep water mass removal due to the lowering of the model water column (cf. the analogous peak in Fig 3.7). This negative sign must be compensated by the extensive positive area discussed above, i.e. that between 15°C and 17.5°C. It is not straightforward to explain physically the water mass removal for a single water column. Two possible in-

terpretations for the isopycnal mismatch at about 500 m are due to: a) the dynamics, e.g. internal waves activity or b) the numerical model, i.e. the simulated thermocline is too diffuse. However, in a data assimilation experiment, one way to rule out one of the two is to consider the inventory over a large area. In a such a case, in fact, if the cause were the dynamics we would expect the inventory for deep water masses to be close to zero whereas if the model thermocline were too diffuse a larger value should be present. Further, this bottom water mass removal is a feature similar to what would be obtained by the isopycnal displacement aimed to balance the weight of two different water columns discussed by Cooper and Haines (1996).

A final comment on the inventory. The inventory, as it is defined, gives us the changes due to the assimilation procedure and it does not require any knowledge of what the true profiles are. However, the differences we obtain are not necessarily the correct changes because we have no real S observations. These changes would be true if the T–S preservation assumption were exactly met. However, and more importantly, the inventory is still useful even if the T–S are not everywhere preserved in the water column. In fact, in such a case the inventory may be very informative about the processes simulated by the model as we have pointed out with the suggested physical interpretations. It is worth noting that even real S observations may be available sometimes and these can be used to check how the S profiles are reconstructed and hence to also verify the physical interpretation of the inventory.

Although care must be taken when interpretations of the inventory are generalised to wider regions, an attentive analysis of it might reveal which mechanism of the model need a deeper inspection: the water mass formation process, the internal turbulent mixing or even the advection scheme. That these processes, especially the first two, are crucial for numerical ocean models has been pointed out in several papers. For example, in Tziperman and Speer (1994) we learn that "the model and the data analysis demonstrate the crucial role of mixing and of the seasonal cycle". An interesting and stimulating work by Tziperman (1986), based on the precursor Walin's paper (1982), shows how it is possible to relate the interior mixing to the air-sea fluxes. It is not accidental, therefore, that these papers have given a considerable boost to our work.

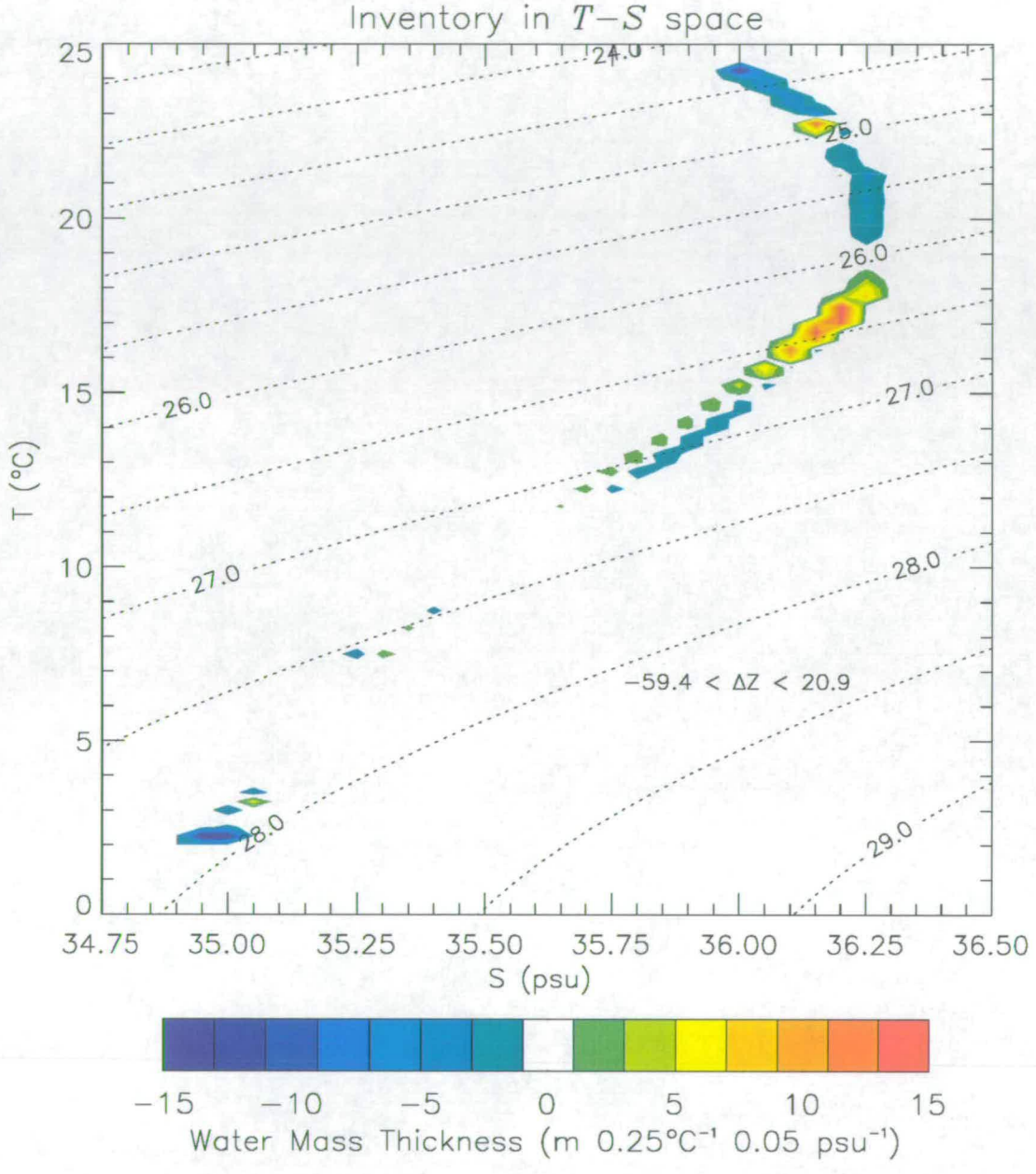


Figure 3.8: *Inventory* in the temperature-salinity space showing the water masses difference between the T and S of the analysed profiles and those of the model profiles. A positive value means that water mass is added in the analysed T and S profiles. The inventory extrema are also indicated (ΔZ is consistent with the notation in chapters 5 and 6 and it will be explained in section 5.4).

Chapter 4

Data Analysis and Test of the Method

A data analysis using conductivity-temperature-depth (CTD) measurements in the western tropical Pacific is carried out to get an estimate of the time scale over which temperature-salinity (T–S) relationships are preserved. Results show that the T–S preservation holds for periods on the order of a few weeks.

The CTD data are used to test the assimilation method by combining one profile with another. These tests recover the salinity profiles and the 0-500-m dynamic height very well (differences are smaller than 1 dyn cm). By contrast, analyses that used a climatological T–S relation did not provide a good salinity profile or dynamic height (errors were greater than 3 dyn cm). Instantaneous model realisations are also used to test the method.

4.1 Data set

The CTD data used in this study were obtained from the database maintained at the U.S. National Oceanographic Data Center (NODC) and collected as part of major campaigns. The data are located in a limited area of the western tropical Pacific between 4.5°N-4.5°S and 154°–159°E and they refer to periods between November 1992 and February 1993. The total number of CTD casts is 1252. All the casts reach a depth greater than 300 m, and 76% of them reach more than 500 m. The vertical resolution is more than 1 datum per 10 m for each profile. A map with the geographical distribution of the CTDs is shown in Fig. 4.1, from which it can be seen that the data are concentrated into three subregions: one north of the equator at 3.6°–4.4°N, 155.5°–157°E (named N) and the other two south of the equator at 2.4°–1.6°S, 154.2°–156.2°E

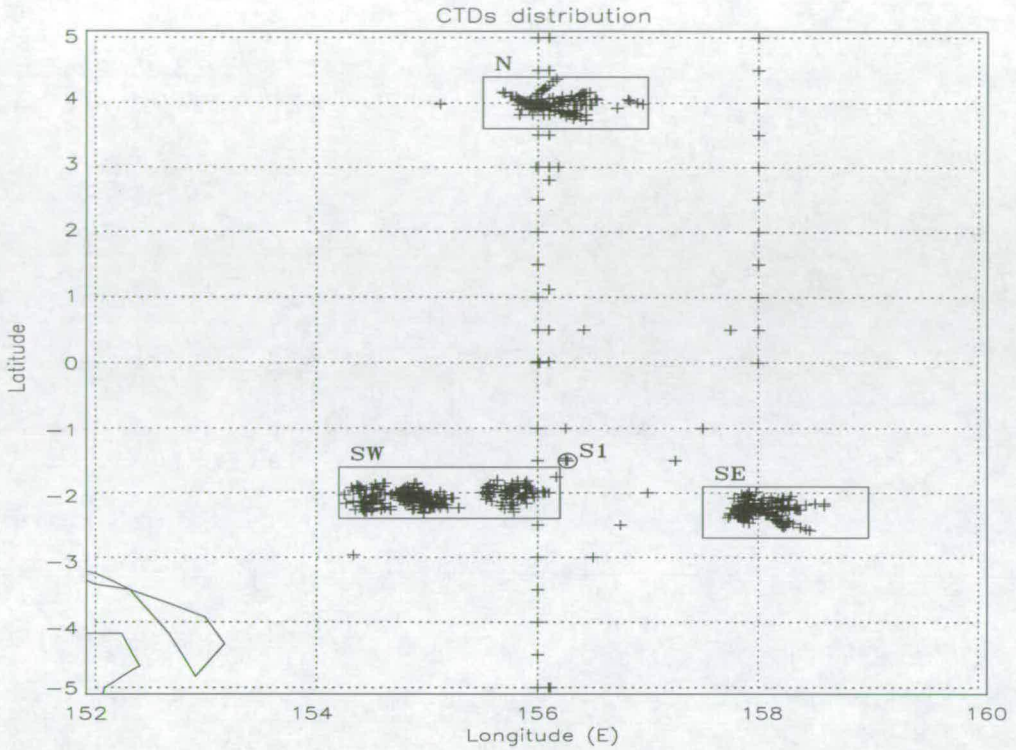


Figure 4.1: Spatial coverage of the CTD data. The three boxes (N, SW, and SE) and the single location (S1) have been highlighted.

(named SW) and 2.7°–1.9°S, 157.5°–159°E (named SE). At a single location denoted S1, 104 CTD casts have been collected within a 10-day period in November 1992. The four locations (N, SE, SW, and S1) are hereinafter treated as individual grid locations.

There are several reasons for choosing this region for study of T–S variability. The most important are the following: (a) in this period an extensive observational campaign was commissioned for which high quality data were gathered (e.g. Anderson, 1995); (b) the western tropical Pacific plays a very important role in the onset of El-Niño (Philander, 1990); (c) due to high precipitation, particularly south of the equator, important upper water column salinity features, such as the "barrier layer" (Lukas and Lindstrom, 1991, Roemmich *et al.*, 1994, Sprintall and McPhaden, 1994, Ando and McPhaden, 1997, Vialard and Delecluse, 1998a, Vialard and Delecluse, 1998b) often appear (when the mixed layer does not coincide with the isothermal layer); (d) several previous studies have analysed the western tropical Pacific, so that these can be used for reference and comparison (Emery and Dewar, 1982, Delcroix *et al.*, 1987, Donguy,

1994, Vossepoel *et al.*, 1999).

4.2 Evaluation of the T–S for deriving salinity profiles

Two approaches to deriving salinity do not require use of a T–S relation. First, climatological salinity $S_{cl}(z)$ might be assumed constant [e.g. salinity from Levitus *et al.*, 1994)], which would remove any active role for salinity in current variations. Alternatively, $S(z)$ from a numerical model being run with temperature profile assimilation could be left unaltered whenever new T data are available. This approach commonly is done because it is simple but leads to the problems already outlined.

If a T–S relation is used, the $S_{cl}(T)$ has always been used in previous works. This approach probably is acceptable when nothing better can be obtained because it is the best estimate of the long-term average (although care should be taken because most climatological data sets are not constructed with the aim of accurately representing a mean T–S relation, as pointed out by Lozier *et al.*, 1995). However, in a data assimilation context with T profile data being assimilated every week or so, it may be better to use a T–S preservation assumption, that is, to use the local T–S relation predicted by the numerical model. By keeping $S(T)$ rather than $S(z)$ fixed at assimilation time, we are assuming implicitly that a model is able to predict $S(T)$ better than $S(z)$. It will be demonstrated that this assumption is reasonable by studying the observed variability of salinity profiles on differing time scales, in both data and a numerical model.

The approach involves statistically analysing the data in the three selected boxes (N, SW, and SE) plus those in the single location S1 (1.5°S, 156.25°E), at various frequencies from daily (for S1) to weekly and seasonally (for N, SW, and SE). For the daily and weekly periods, the analysis follows a similar procedure. The variability of the single profiles [i.e. $T(z)$, $S(z)$, and $S(T)$] within the period considered is studied, focusing attention on the S variability and its correlations with T. The rms variations for $S(z)$ and $S(T)$ are compared numerically on short time scales, as discussed below. On the seasonal time scale, the discussion is essentially based on the graphical comparison between $S = S(T)$ and $S = S_{cl}(T)$ profiles, with $T = T(z)$ and $S = S(z)$ also shown.

4.2.1 High-frequency analysis of 10-day period: $S(z)$ versus $S(T)$

For this analysis, 104 CTD casts over a 10-day period in November 1992 at the same location (S1) are examined. Figures 4.2a-c show the variability of $T(z)$, $S(z)$, and the T–S relation.

In z space there is a pronounced T and S variability (Figs. 4.2a-b), which, if interpreted as vertical displacements, imply displacements as large as 40 m in the top 300 m, presumably caused by internal waves. Visually there appears to be less variability in the T–S relation in Fig. 4.2c, but it is difficult to make numerical comparisons by eye. Therefore, Fig. 4.2d provides a more consistent way of directly comparing the $S(z)$ and the $S(T)$ variability. Rms salinity variance is shown as a function of z space (solid line). The dashed line shows rms $S(T)$ variance calculated from the mean $S(T)$ relation but with the variances transformed back into z space using the mean $T(z)$ profile for the period. The tight $S(T)$ curves (Fig. 4.2c) do express the fact that on the daily time scale there is little mixing of water masses and little influence of horizontal advection, which is consistent with much of the variability being due to internal waves. Figure 4.2d shows rms variances in $S(T)$ that are several times smaller throughout much of the water column.

This high T–S correlation reflects the potential for obtaining improved S analyses from T. For instance, if one were interested in determining salinity at 100 m, the maximum uncertainty in S would be 0.35 psu using the $S = S(z)$ profiles (Fig. 4.2b), whereas, if T were known, uncertainty would be almost halved to 0.2 psu, if T–S curves are used. There are, however, depths, or temperatures, for which inference of S from T–S properties still leads to large uncertainties. These events happen, for example, in places where advective intrusions come about; the spike at about 17°C and 35 psu in Fig. 4.2c and the rms variance peak at about 200 m in Fig. 4.2d are examples. This feature is caused by inclusion of profiles from the last three days of the period. Also, use of the T–S relation does not work well where a halocline divides an isothermal layer (e.g. the 20°C water mass in Fig. 4.2c and the absolute rms variance T–S maximum in Fig. 4.2d). In spite of these problems, the $S(z)$ rms variance is almost everywhere larger than the $S(T)$ rms variance (Fig. 4.2d), and therefore $S(T)$ generally would be preferable over $S(z)$ for these data.

A feature in Fig. 4.2 worth noting is the significant S variability in the upper water

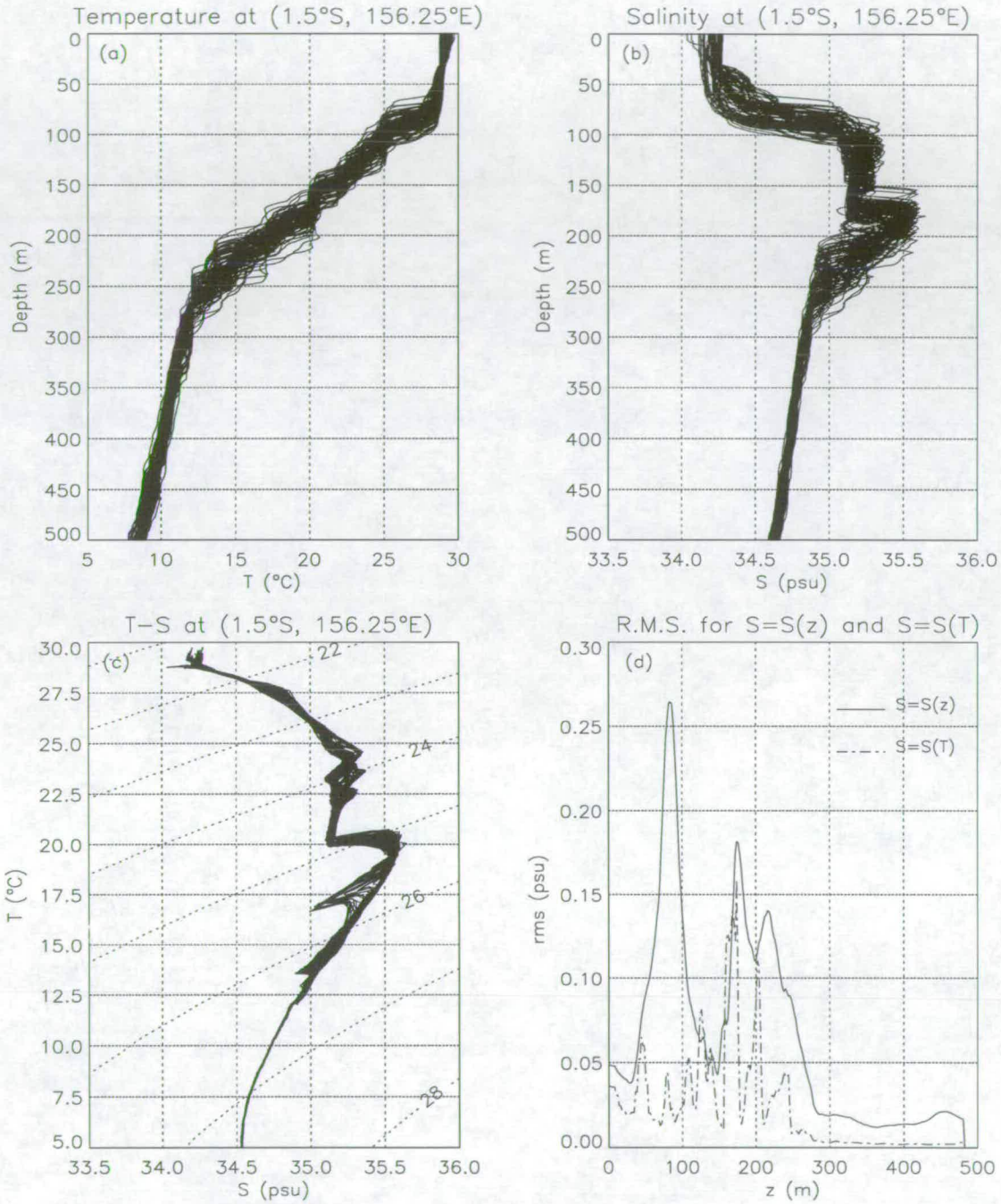


Figure 4.2: Data analysis. From the top left: (a) temperature profile, (b) salinity profile, (c) T–S diagram, and (d) $S(z)$ to $S(T)$ rms comparison for the 104 CTD casts at S1 location for a 10-day period in Nov 1992 (see Fig. 4.1). Note that to transform the $S(T)$ rms from T to z space (in d) the average temperature profile (from a) has been used.

column (e.g. 0-80 m, Fig. 4.2b), which seems to appear only in the rms variance in z space. In fact, the $S(z)$ rms variance is greater than the $S(T)$-based rms variance by a factor of 7-8 at about 80 m (Fig. 4.2d). This feature is the barrier layer, a rather common feature in the western tropical Pacific (e.g. Vialard and Delecluse, 1998a) that lies between 30 and 70 m (roughly 40-m thick). The highly stratified water column probably encourages internal wave propagation, which then preserves the T–S relation, leading to high S variability but excellent results from correlating S with T in this region of the water column.

The conclusion is that it is very useful to use an $S(T)$ relation that is derived locally on these short time scales. We would expect this result to hold almost anywhere in the global oceans. This result is not particularly surprising, considering that the 10-day period is rather short for distinct water mass variations to occur. Nonetheless, changes like the intrusion are likely to happen, even over a few days. Unfortunately, this temporal density of T data is hardly ever collected, and the scope of the analysis needs to be enlarged to longer time periods, which will permit other mechanisms to affect the S variability.

4.2.2 Weekly analysis: *S(z)* versus *S(T)*

The focus here is on the intraseasonal variability seen when comparing weekly averaged profiles. The choice of a week corresponds to the typical time between assimilation cycles for current seasonal forecasting applications and for previous ocean assimilation studies (Derber and Rosati, 1989, Rosati *et al.*, 1995, Rosati *et al.*, 1996, Carton and Hackert, 1989, Kleeman *et al.*, 1995). The representative box N is discussed (Fig. 4.3), although the results from the other boxes are similar. Nine profiles, one for each week (49-57), are shown along with the "mean" profile in bold. Table 4.1 shows the number of individual CTD profiles available for each week.

	weeks in **1992**								weeks in **1993**							
	45	46	47	48	49	50	51	52	53	54	55	56	57	58	59	60
N	(0)	9	(0)	(0)	54	46	40	42	34	12	40	36	(2)	(0)	(0)	(1)
SW	20	24	25	61	51	(2)	22	29	30	14	(1)	11	29	23	26	13
SE	(1)	70	71	17	30	16	30	52	68	42	48	4	(0)	(0)	(0)	(0)

Table 4.1: Temporal distribution of the CTD data for the selected subregions. The second line is the number of weeks (from Jan 1992, for convenience). The first column refers to the selected boxes (see Fig. 4.1). Bracketed weeks are ignored in the analysis.

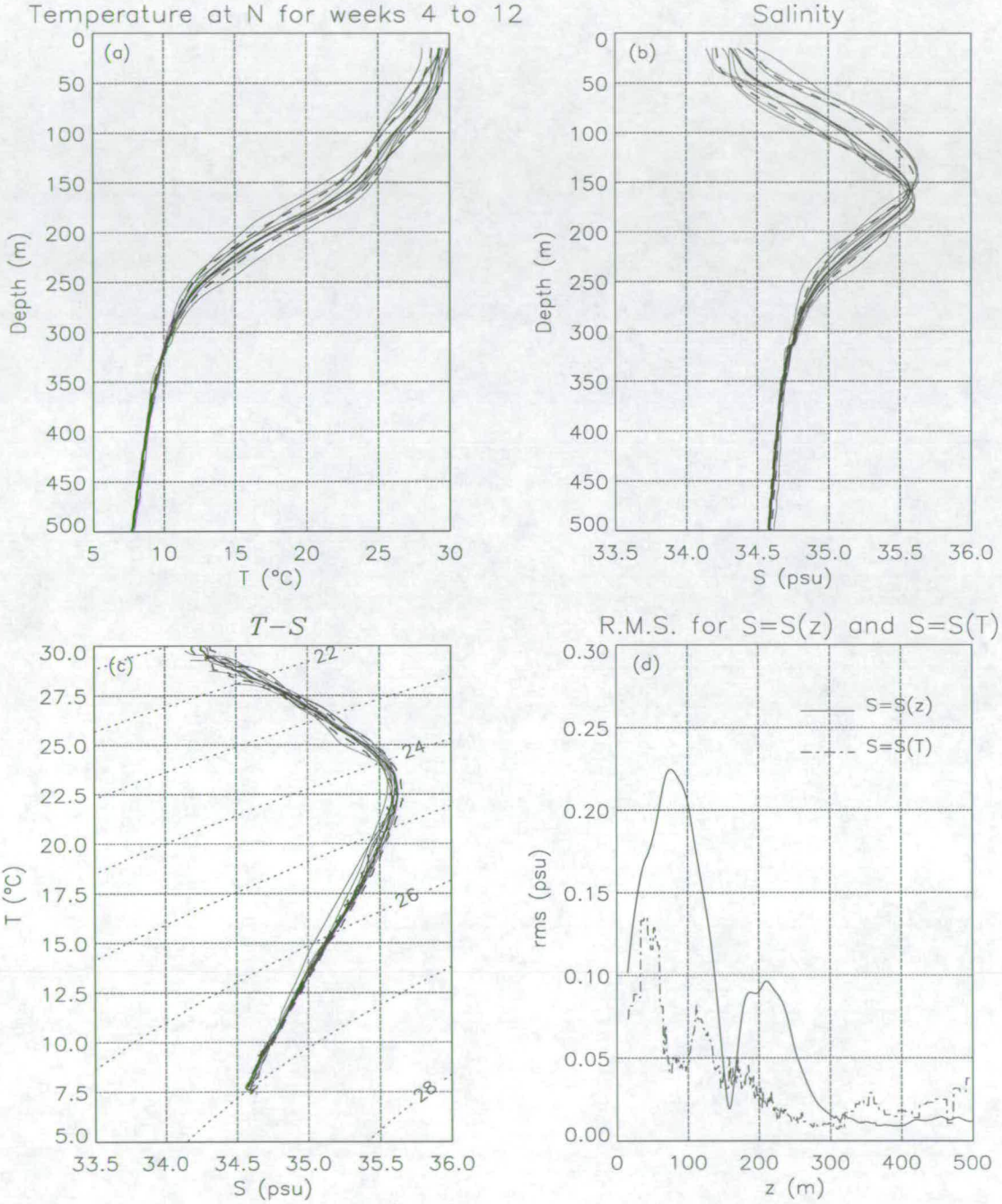


Figure 4.3: As in Fig. 4.2, but for the N box. The solid lines in (a)-(c) are the mean profiles and the dashed lines their respective rms variances. Data refer to the weeks displayed in Table 4.1.

The weekly mean T and S profiles (both in z and T spaces) were first calculated by omitting data from the first level of most casts (top 15 m), which showed inconsistencies and had to be ignored (see e.g. Ando and McPhaden, 1997).

It is evident that there are considerable differences between $S(z)$ and $S(T)$ variabilities. The latter presents a fairly compact series of profiles, suggesting that mixing and non-local dynamics play minor roles. This observation can also be read from Fig. 4.3d, which shows how the $S(T)$ rms variance almost everywhere is smaller than the $S(z)$ rms variance. At depths where this relation is not true (about 160 m and below 320 m), the $S(T)$ rms variance values are decidedly smaller than 0.05 psu and not very different to the $S(z)$ rms variance (although the former variance contains some noise caused by the data processing). The $S(z)$ rms minimum at about 160 m is peculiar. By looking at the single $S(z)$ profiles and noting the time of each profile, it is found that in the last three weeks of January 1993 there is a considerable and sudden increase in the upper layer salinity (top 150 m in Fig. 4.3b). The cause appears to be a first-mode Kelvin wave, as the respective temperature profiles also indicate, and the changes are consistent with an upward displacement of about 50 m (corresponding to an average vertical velocity of about 8.3×10^{-5} m s^{-1} over one week). The presence of a salinity maximum near this depth then gives the anomalously small S variability because the salinity at 160-m depth just happens to remain the same after the displacement.

Similar results hold for the other two boxes SW and SE (not shown), which again suggests that $S(T)$ relationships are persistent on the weekly time scale. One could compare the validity of a climatological $S_{cl}(T)$ on this time scale, but this comparison is discussed in section 4.2.3.

4.2.3 Seasonal analysis: $S(T)$ versus $S_{cl}(T)$

The results to this point have demonstrated that salinity and temperature are strongly correlated, at least on time scales of weeks in the tropical Pacific, and that this correlation supports the use of $S(T)$ functions for analysing salinity when temperature data are available. However, at some time scale, variability of the $S(T)$ relationship is likely to become important. This section compares, mostly qualitatively, the seasonally averaged $S(T)$ function from the NODC data in this chapter with $S_{cl}(T)$ from a climatological data set (e.g. Levitus). The former is obtained by averaging the individual weekly profiles discussed in section 4.2.2 (cf. also Table 4.1). Also, since

the Levitus seasonal definition and spatial grid do not coincide well with those of this study's data, linearly interpolated averages of seasonal Levitus data are used to get as close as possible to an appropriate climatological value. In Fig. 4.4, these averages are compared with the mean profiles from each of the boxes N and SW along with associated rms variability, based on the weekly variations, for the study data set (the behaviour of the SE box, not shown, is similar to the SW box).

Although the two data sets are not entirely independent (the climatological data set used all data from 1900 up to 1993, including those from this study), significant salinity differences appear in both z and T spaces. There are differences in all boxes, especially N. The $S(T)$ properties for the south differ mainly in the upper water column ($T \leq 22.5°C$, corresponding to a depth of about 160 m), whereas for the N box there is disagreement throughout the main thermocline (from about 100 to 310 m). Given the large variability in the evaporation-precipitation forcing in this region (e.g. Ando and McPhaden, 1997), it is not unexpected to find mismatches in the upper water column, but the differences in the N-box $S(T)$ properties are surprising. A plausible explanation is that this is a region of high meridional salinity gradient, especially in correspondence to the subsurface salinity maximum; therefore, a long-term average, such as that used to construct a climatology, can smooth out much of the variability.

Last, by comparing the rms variability for the $S(T)$ curves, it is observed that even a long time period, such as a specific season, is not described adequately by the climatological data set, which falls well outside the observed seasonal variability over a considerable temperature range. As a consequence, any temporally closer source of $S(T)$ information would represent a better option for inferring salinity. This is why we have chosen to seek different background $S(T)$ fields for data assimilation purposes. In the following sections some results from a numerical model are examined, and how $S(T)$ relationships vary in a modelling context is considered.

4.3 Assimilation results

The data assimilation method presented in the previous chapter is tested by combining CTD data profiles, one with another, and by combining different model realisations. It should be pointed out that, although the data analysis in the previous sections refers only to limited areas in the western Pacific Ocean, the assimilation method with model data presented in chapter 3 is not so restricted and could be applied over wide regions

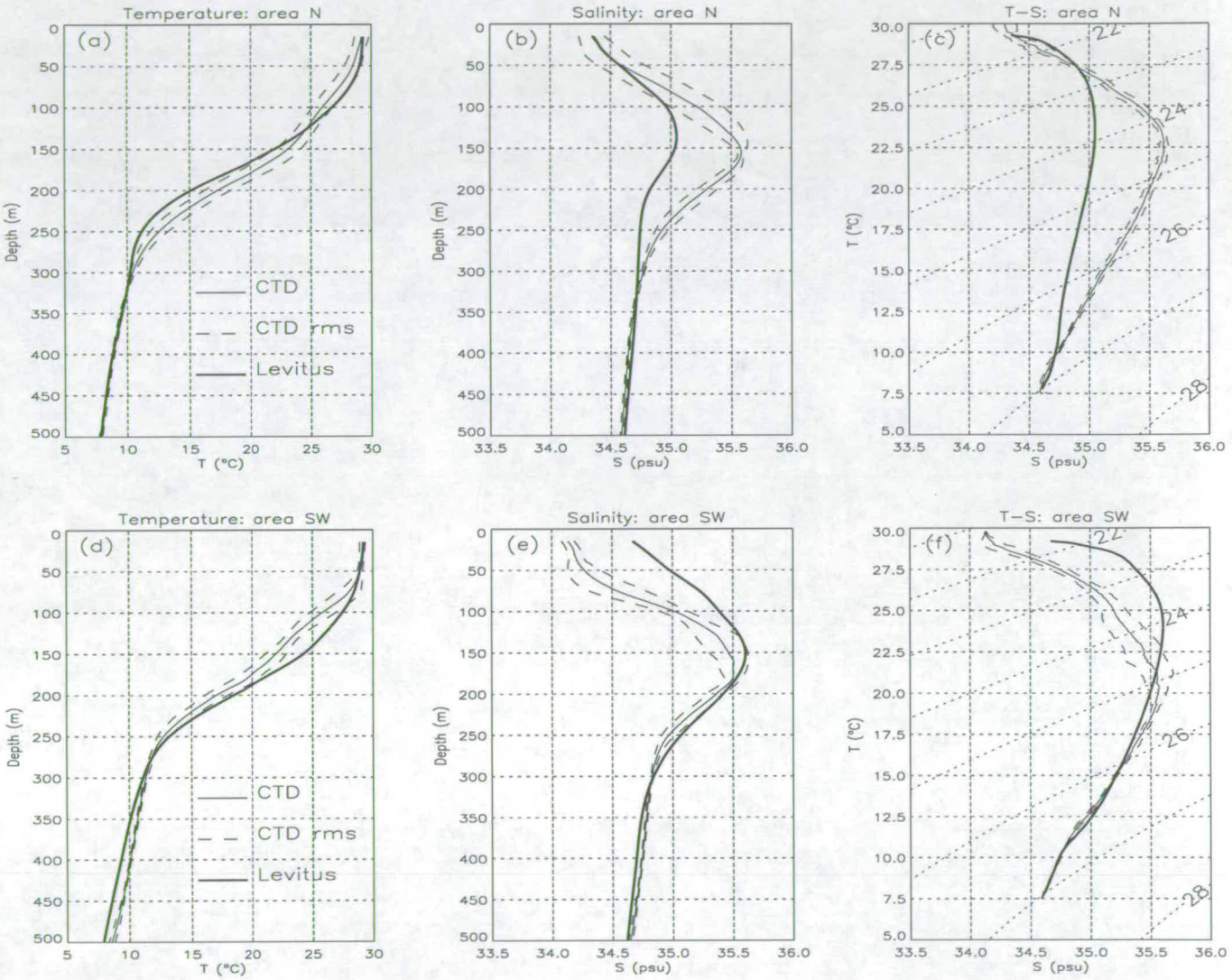


Figure 4.4: Comparison between climatological data (thick line) and seasonally averaged CTD data (lighter line) for the N (top) and SW (bottom) boxes. From left to right: (a) and (d) temperature profile, (b) and (e) salinity profile, and (c) and (f) T–S diagram.

of the oceans, including difficult areas such as those where temperature inversions are present (Emery, 1975, Emery and O'Brien, 1978). A more thorough test will be performed in the next chapters.

The procedure for the CTD data is as follows. The a priori hydrography is taken as the complete CTD T and S profile data at time t_1. Then only the upper water column (500 m) of the T field from a second CTD at a different time t_2 (e.g. a week later) is used to simulate an observed XBT at the analysis time t_2. The corresponding analysis S field is derived by vertical displacement followed by T–S property preservation based on the a priori T and S profiles. The true S field at time t_2 is available as a control field to check the accuracy of the method. The reference depth $z_{ref} = 500$ m is chosen as this depth is the normal maximum reached by XBT probes. An analogous approach is adopted later for combining numerical model fields.

There is no unique way of assessing techniques like this one. Three measures of success in reproducing fields are considered. The first is the dynamic height integral, 0-500 m, which often has been used (Emery, 1975, Emery and Dewar, 1982, Kessler and Taft, 1987, Delcroix *et al.*, 1987, Vossepoel *et al.*, 1999). However, a measure of the details of the vertical density structure also is defined by employing a 1-norm quantity defined by

$$\Delta\sigma = \sum_i [|\sigma_A(i) - \sigma_O(i)| \cdot \Delta z(i)]/z_{ref} \tag{4.1}$$

where the subscripts A and O stand for assimilation (or analysis) and observation/truth, respectively; Δz is the layer thickness; and i is the level index. Thus Eq. (4.1) supplies an estimate of the error in the density at all depths, preventing compensations that can occur in the dynamic height measure. Further, to check whether the assimilation improves the vertical S profiles, a relative assessment (in percent), using a 1 norm, is calculated:

$$\Delta S = \left(1 - \frac{\sum_i |S_A(i) - S_O(i)| \cdot \Delta z(i)}{\sum_i |S_B(i) - S_O(i)| \cdot \Delta z(i)}\right) \cdot 100 \tag{4.2}$$

where the subscript B stands for background or a priori field. According to Eq. (4.2), ΔS ranges from a maximum of 100% in the ideal case to $-\infty$ when $\sum_i |S_B(i) - S_O(i)|\Delta z(i)$ tends to zero. A negative ΔS will thus signify that the assimilation has worsened the background S profile. The assessment indices (4.1 and 4.2) are evaluated

for the part of the water column that extends from 15 to 500 m. Retaining the structure of section 4.2, that is, decreasing frequency from daily to seasonally, some of the assimilation method results are presented.

4.3.1 Daily assimilation

The first test has been carried out by selecting two CTD profiles at the S1 location (Fig. 4.1), eight days apart, that is, $t_1 \equiv$ day 0 and $t_2 \equiv$ day 8 (Fig. 4.5).

Despite a water mass intrusion that has occurred at t_2, for $\sigma \geq 26$ kg m^{-3}, the T–S curves for the two profiles very closely resemble each other (Fig. 4.5c). This resemblance suggests that a good salinity analysis is attainable by preserving the T–S relation. By contrast, the salinity in z space varies appreciably, therefore discouraging a persistence-type approach.

The actual salinity analyses are shown in Fig. 4.5b. Here S_O is the observed true profile, S_{SZ} is the a priori profile that would be preserved if salinity were unaltered, and S_{ST} is the analysis preserving the T–S relation. It is evident that the S_{ST} analysis represents the control profile very well, and this result is confirmed by the very high ΔS index (above 81%). One of the biggest $|S_O - S_{ST}|$ discrepancies is near the surface, within a shallow layer (roughly 25 m thick). The water mass intrusion at about 200 m also is not picked up by the salinity method, because the background field does not contain that water type. This failure shows up in the difference between S_O and S_{ST} at about 215 m. Last, the positive impact of the assimilation is highlighted further by the small figures of both the $\Delta\sigma$ index and the dynamic height difference ($D_O - D_{ST}$) (Fig. 4.5d).

4.3.2 Weekly assimilation

The assimilation was also applied to the weekly averaged profiles (see section 4.2.2), assimilating between weekly averaged profiles two weeks apart. The example here is from the SE box. In addition, a parallel analysis, which uses the Levitus climatological T–S for this region, was also carried out.

This study considered $t_1 \equiv$ week 53 and $t_2 \equiv$ week 55 (Fig. 4.6). As implied by the ΔS_{ST} index, the T–S background yields a 59% better analysis than does leaving $S(z)$ unmodified. A further confirmation is given by the dynamic height estimation [-1.2 dyn cm for $S(z)$ compared with 0.2 dyn cm for $S(T)$]. For the climatological data

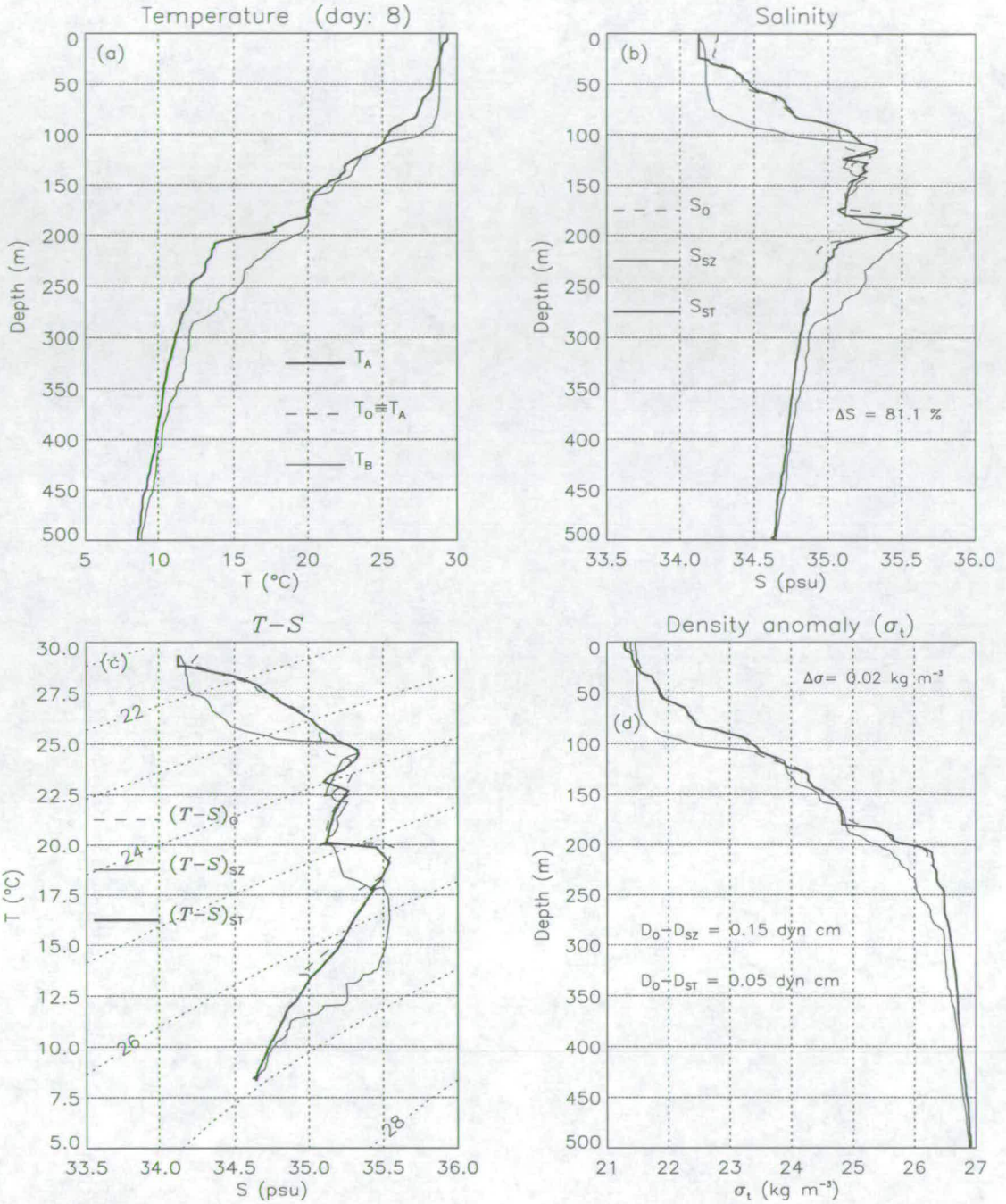


Figure 4.5: Data assimilation. From the top left: (a) temperature profile, (b) salinity profile (S_{ST} is our analysis), (c) T–S diagram, and (d) density anomaly for two profiles eight days apart at S1 location. Note that the assimilated and control T profiles are coincident, having assumed no errors in the T measurement. The ΔS figure, calculated by Eq. (4.2), is shown in (b) whereas the $\Delta\sigma$ [Eq. (4.1)] and the dynamic height differences are in (d). For consistency, $(D_O - D_{SZ})$ and $\Delta\sigma$ have been evaluated by using the T_O profile, instead of T_B.

set comparison, the two T–S dynamic heights differ substantially (i.e. $|D_O - D_{ST}| \ll |D_O - D_{STcl}|$), as do the $\Delta\sigma$ indices ($\Delta\sigma_{ST} \ll \Delta\sigma_{STcl}$) (Fig. 4.6d), mainly due to differences in the top 100 m. This result is because the climatological data set T–S curve differs considerably from the measured one (Fig. 4.6c).

To check the impact of the vertical displacement (stage 1, Fig. 3.2), the 500–1000-m dynamic height for the S_{SZ} and S_{ST} analyses was also computed. Although the displacement is not very large (16 m), it does slightly improve the description of the water column below z_{ref}.

An interesting feature in the S_{ST} salinity profile (Fig. 4.6b) is seen above 50 m depth where an isohaline layer is present. When observed temperatures are higher than any temperature in the a priori field (always near the surface), we assume that the water mass is just heated, and therefore the salinity is not changed and the whole of the warmer layer takes the salinity of the warmest water masses in the background field (cf. Figs. 4.6a-b), as also discussed in section 3.3.

4.3.3 Seasonal assimilation

Two weekly averaged profiles 10 weeks apart for the SW (Fig. 4.7) box are considered. In this case $t_1 \equiv$ week 46 and $t_2 \equiv$ week 56.

In this SW box, the background and observed $S(z)$ profiles differ substantially (Fig. 4.7b) and the corresponding T–S curves also show considerable differences (Fig. 4.7c). In particular, a water mass intrusion with σ_t between approximately 23.7 and 24.4 kg m^{-3} is present at t_2. Although this feature can not be captured by the assimilation method (cf. S_O and S_{ST} in Fig. 4.7b, between 80 and 120 m depth), the ΔS_{ST} is still over 70%, indicating a very positive impact of the assimilation scheme. This impact is also seen in the $|D_O - D_{ST}|$ index, which is equal to about 0.3 dyn cm (Fig. 4.7d). The climatological data set does not perform nearly as well, with $|D_O - D_{STcl}| \simeq 3.9$ dyn cm, even bigger than $|D_O - D_{SZ}|$.

As in the weekly assimilation, the vertical displacement (of the same magnitude, 16 m) again provides an improved 500–1000-m dynamic height.

4.3.4 Model field assimilation

We have taken the first steps toward implementing this scheme in a model. In collaboration with the ECMWF, a further test has been performed by using two instanta-

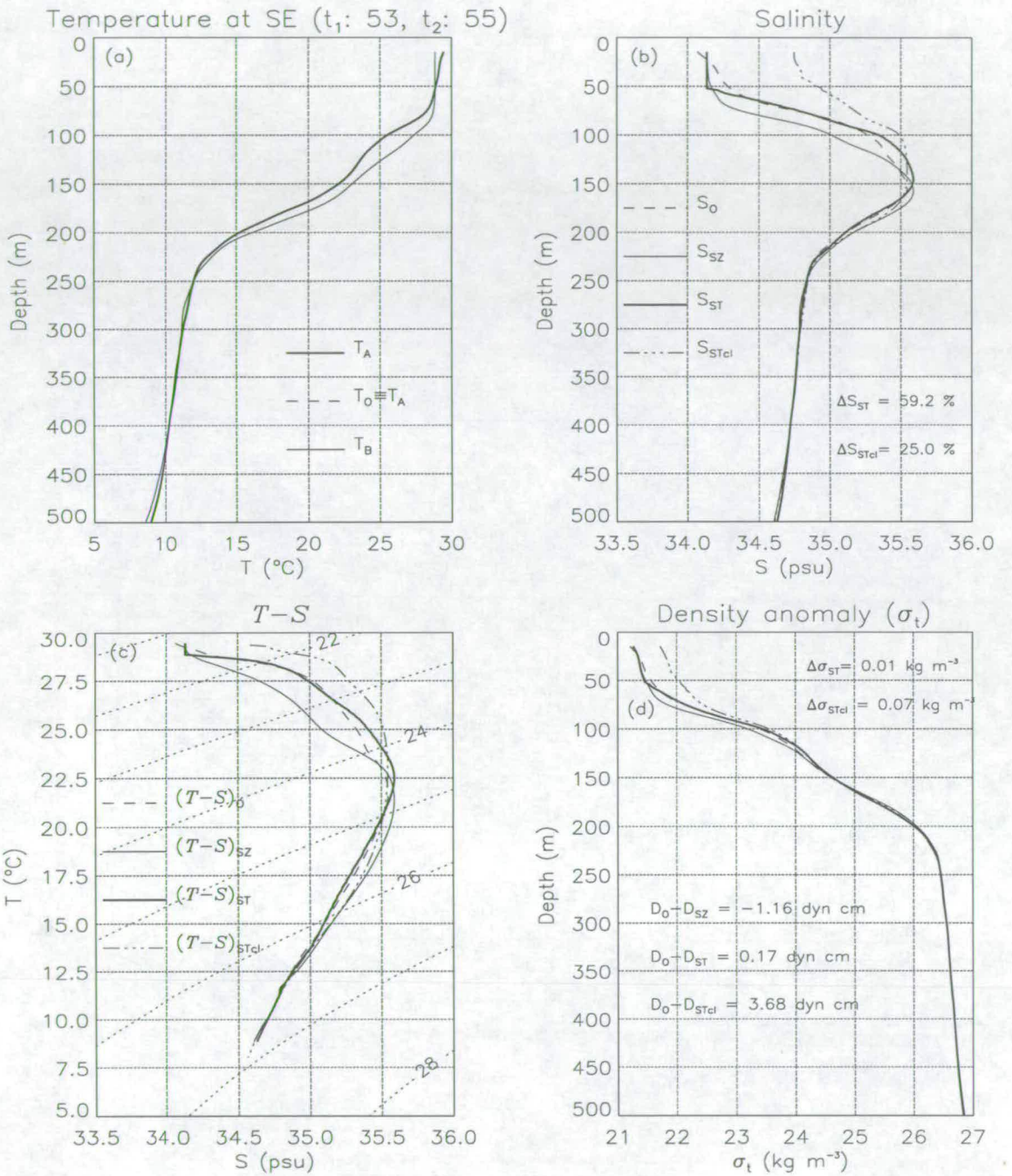


Figure 4.6: As in fig. 4.5 but for the two weekly averaged profiles two weeks apart, for the SE box. Here also the assimilation performed by using climatological T–S relations is shown (subscript "cl"). Moreover, $(D_O - D_{STcl})$ and $\Delta\sigma_{STcl}$ have been evaluated by using the T_O profile.

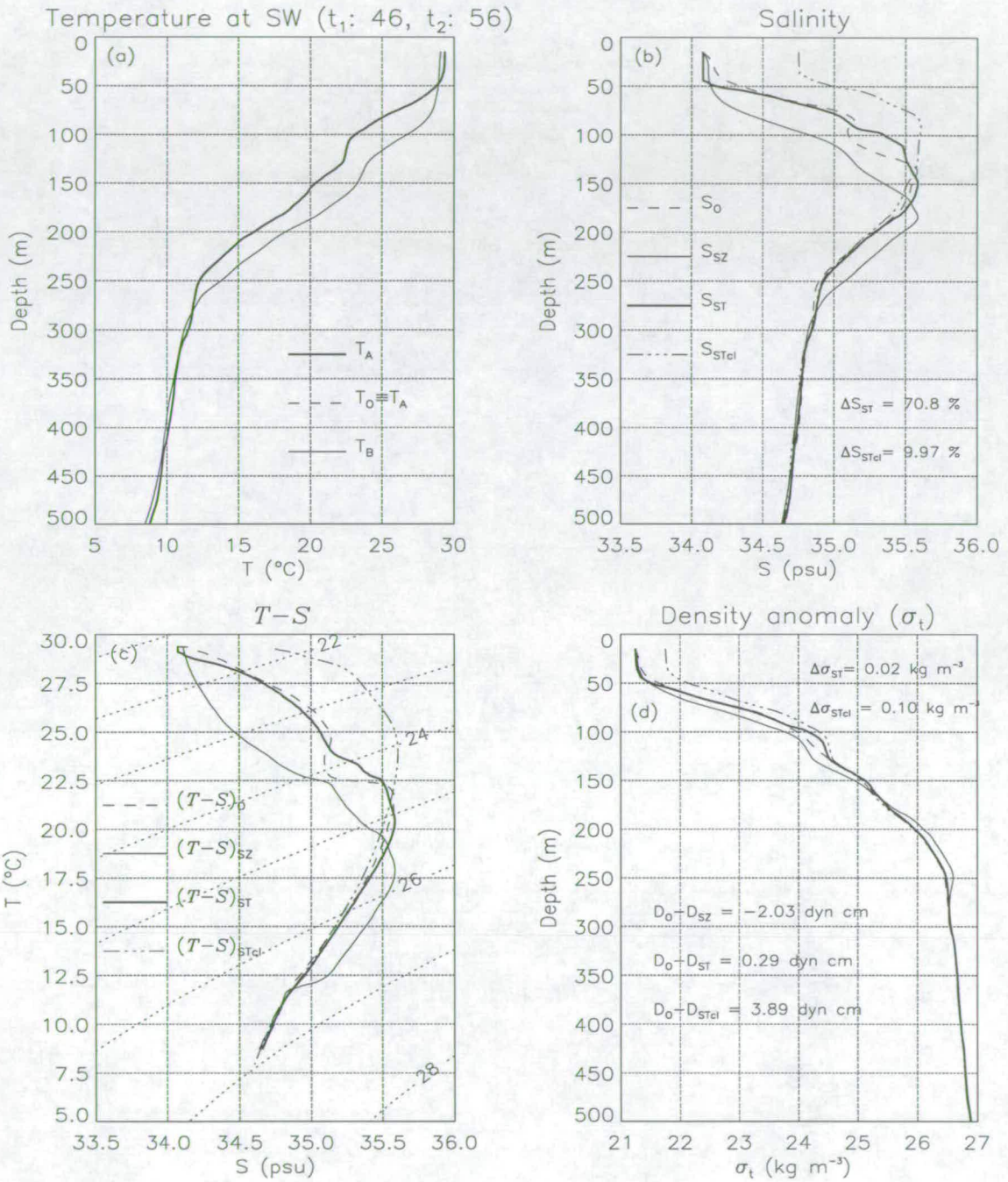


Figure 4.7: As in fig. 4.6 but for two profiles separated by 10 weeks (seasonal assimilation), and for the SW box.

neous HOPE model outputs. This ocean model is the one used as part of a coupled seasonal prediction project at ECMWF. The model is primitive-equation-based, three-dimensional, and uses z coordinates with variable surface height. Forcing is provided by surface solar heat flux, wind stress, and precipitation (see Wolff *et al.*, 1997, for a more detailed description). Only the equatorial Pacific cross section is shown here. Figure 4.8a shows the thermal field for the upper water column showing the strong stratification and an upward thermocline slope to the east. This configuration implies that vertical displacements or thickness variations of the water columns would induce large changes to the density distribution.

The two realisations discussed are initialised with the same fields but then run for three months each, using different wind stress forcing. The surface heat fluxes also will differ to the extent that they depend on the S_{ST} and wind fields. This time integration is long enough to generate large differences in the hydrography, as shown by the temperature difference section (Fig. 4.8b). The main temperature differences (as much as -1.8°C) are found east of the international date line for depths up to 200 m, where the thermocline is more pronounced in Fig. 4.8a. Large differences (about 1.8°C) are present also in the upper water column between 260° and 280°E. Salinity differences also are quite distinct as shown by the difference cross section (Fig. 4.8c), and are spread over most of the top 200 m across the basin. In particular, large values are found between 200° and 240°E, ranging from 0.45 psu in the upper water column to -0.25 psu lower down. A considerable minimum also is seen in the eastern part of the section (about -0.85 psu). The sign of the salinity differences generally is opposite to that of the temperature differences such that there is not a density compensation.

Assimilation is applied to run B (background, shown in Fig. 4.8a), using the temperature increments shown in Fig. 4.8b but maintaining the $S(T)$ relationship from run B. The salinity difference results are presented in Fig. 4.8d and show a clear improvement over most of the section. All of the extreme values present before assimilation seen in Fig. 4.8c have been reduced considerably, especially between 200° and 220°E and east of 260°E. A minor negative effect has been induced below the main thermocline between 150° and 200°E, presumably by discrepancies in the T–S relationships that develop over the 3-month period. In spite of this effect, the assimilation has led to a satisfactory ΔS index of about 23% improvement.

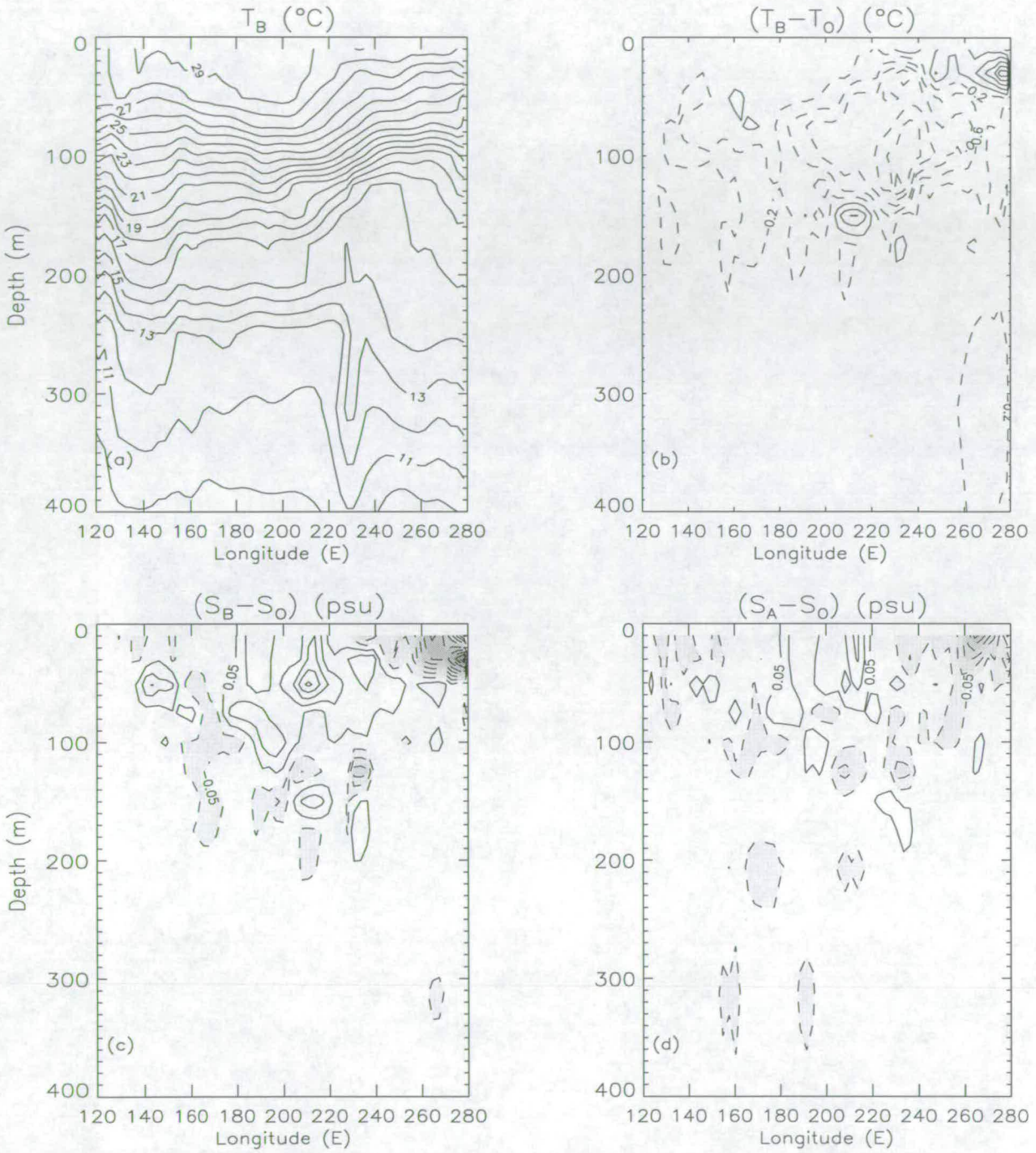


Figure 4.8: Data assimilation using HOPE model outputs along the equatorial tropical Pacific. The two 3-month runs were initialised in the same way and thereafter only the wind stress forcing was different. (a) Background temperature section after 3 months; (b) temperature difference between background and control run (contour interval is 0.4°C): this is the increment used by the assimilation scheme. Salinity difference (contour interval is 0.1 psu): (c) before and (d) after assimilation.

4.4 Summary and discussion

In this chapter, a CTD data set for a region of the western tropical Pacific was analysed and it was shown that one can use T–S relationships to link them very accurately for time periods on the order of a few weeks, except sometimes in the uppermost layer (about 50 m). The assimilation scheme is useful both for CTDs and model realisations. In the former case, values for the 15–500-m dynamic height differences (i.e. $|D_O - D_{ST}|$) rarely bigger than 2 dyn cm were obtained. Comparing this accuracy to altimetry shows that 2–3 dyn cm is a lower limit given by the satellite observational accuracy when low-frequency barotropic changes can be neglected (Katz *et al.*, 1995). It has also been shown that with assimilation performed using the climatological T–S relation, only mediocre results are obtained, with $|D_O - D_{STcl}|$ normally bigger than 3.5 dyn cm. This result indicates the inadequacy of the climatological data set in representing the water mass properties at any given time, possibly partly because of the high degree of smoothing in z space that was used. In particular, note that keeping $S(z)$ fixed sometimes leads to better dynamic height analyses than does using climatological water mass properties (e.g. Fig. 4.7d; although in this case compensations in the vertically averaged density field contribute to producing this result).

While the results shown are promising, it should be emphasised that the analysed CTD data only refer to a few limited areas, and therefore it has not been shown that this assimilation scheme will perform well globally. However, even when temperature inversions or water mass intrusions occur, the scheme still can yield positive outcomes at other levels in the water column. One of the implicit requirements of the scheme is that a sufficient stratification, that is, a wide enough T range, be present in the a priori water column. In the tropical regions this condition is met easily but problems may arise as one moves poleward, as described by Emery and Dewar (1982). Their suggested borderline at around 40°N calls for further work to examine the XBT assimilation problem in mid latitudes.

Chapter 5

Synthetic Data Experiment: Set-up and Preliminary Results

In this chapter the synthetic data assimilation experiment set-up is presented. The model configuration and the boundary conditions are relatively simple so as to focus on the impact of the assimilation method (introduced in chap. 3) on the model. We study the reference run (the "truth") and then compare it with a "corrupted" run which will be corrected by the assimilation (the "parallel"). Also, the method used for spreading the temperature data and assimilating them will be presented. The results of the data assimilation will be discussed in the next chapter (chapter 6).

5.1 Introduction

Having tested the method with CTD data, an experiment using observational data and a realistic model could be devised at this stage. Such an experiment would certainly lead to a more definite response about the usefulness of the assimilation method. Despite this being the ultimate goal in this type of study (such an experiment will be presented in chap. 7), a further intermediate step represented by simpler experiments, such as the one that will be discussed here, are normally more functional, for at least three reasons.

First, synthetic data assimilation experiments are quite useful to the extent that all the model variables are accessible and therefore one can in principle obtain a comprehensive thermodynamic and dynamical picture of the "true state" of the ocean. This is clearly not the case for the observational data assimilation experiments for which the "true state" is normally known only to a limited extent, as for example in hindcast studies. On the other hand, care must be taken when results from simplified experi-

ments are analysed: there is the risk that information may be over-interpreted, if one inadvertently disregards the nature of the experiment, especially because in these experiments one tends to simplify the model set-up and/or the data assimilation system. Secondly, these experiments might be quite useful in comparing the relative importance of the different physical processes simulated by a model (e.g. air-sea interaction, mixing parameterisation), in the sense that one could assess which process is more easily corrected by assimilating data. Therefore, this can give valuable indications on priority to be followed in correcting the physics of numerical models (this will only partly be touched upon with this work). The third reason is a practical one: it is normally much cheaper in terms of cpu time and computer resources to run synthetic experiments because of their designed simplicity.

The experiment set-up is shown in Figure 5.1. The "true state" of the ocean is here represented by the truth run (Tr). We spun up this run to a dynamical equilibrium which is reached after about 35 years, considering the kinetic energy as a proxy to the steadiness of the simulation (see Fig. 5.2). In total, the truth run is integrated for 105 years. The truth run, the parallel run (Pa) and the two assimilation runs, the first using the T–S preservation and the vertical displacement (A_{ST}) and the other using S(z) persistence and no displacement (A_{SZ}), will be discussed in section 5.2, section 5.3 and section 5.5, respectively. An overview of the adopted numerical model and its configuration is given next.

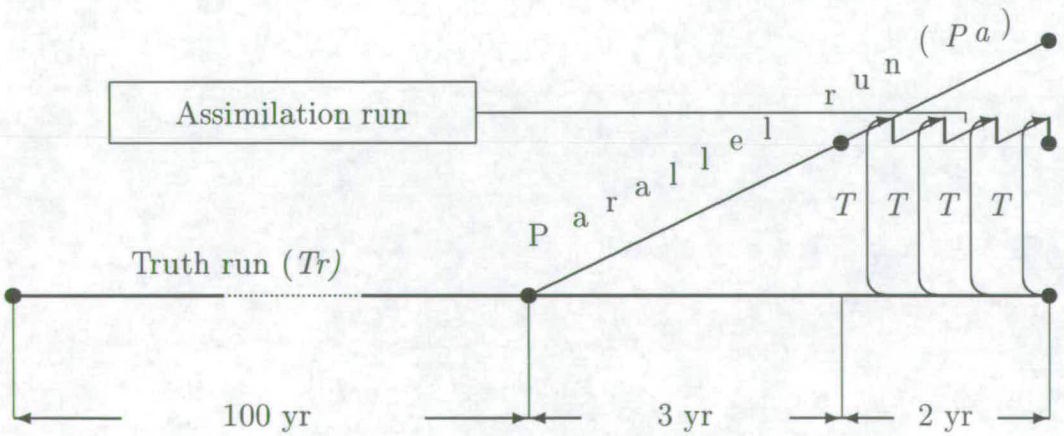


Figure 5.1: Schematic of the data assimilation experiment. After 100 yr of spin up a parallel run is generated by increasing the wind stress by 15%. At year 103 the assimilation run starts and it lasts two years. The temperature data T are taken from the truth run and assimilated every 30 days, starting at 103 yr.

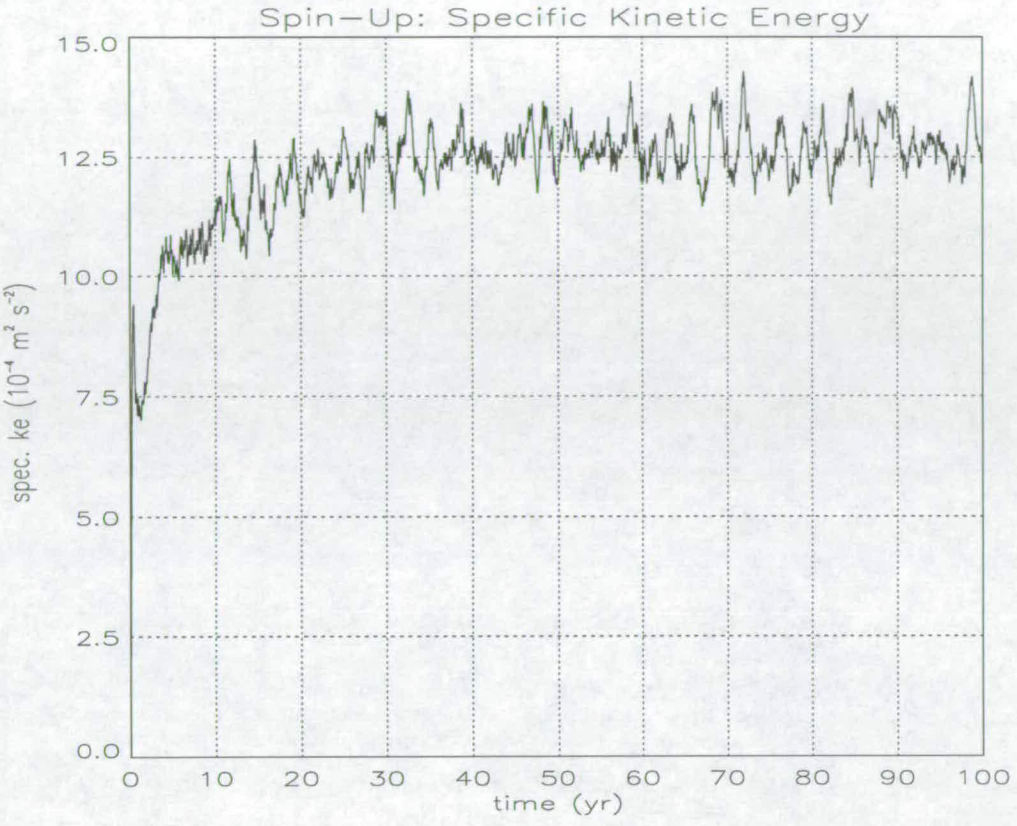


Figure 5.2: Total specific (i.e. per unit mass) kinetic energy for the first 100 years of the truth run.

5.2 Model set-up: Truth run

The model used in this work is the Modular Ocean Model - Array (MOMA), a 3-dimensional primitive equation model with z-coordinates and variable sea surface height. MOMA is a modified version of the standard GFDL MOM code (a widely utilised code in the oceanographic community), the main differences being the introduction of the Killworth *et al.* (1991) free surface scheme and of a revised horizontal advection scheme in the baroclinic momentum equation. It has also been re-organised for efficient running on array processor computers. The basic finite difference scheme used in the model is described in Bryan (1969), Semtner (1974) and Cox (1984). More detailed information about the MOMA code can be found in Webb (1993).

To mention some of its applications, MOMA is currently implemented both as a global and as a regional ocean general circulation model. In the former category falls the Ocean Circulation and Climate Advanced Modelling (OCCAM) project (e.g. Fox *et al.*, 2000a, Fox *et al.*, 2000b or Saunders *et al.*, 1999), whereas in the latter are the

Mediterranean studies by, for instance, Myers *et al.* (1998).

The model configuration is deliberately chosen to be relatively simple so as to focus on the impact of the assimilation method on the model. Given the assimilation method's portability it ought to be straightforward to adapt it to any ocean numerical model, regardless of complexity, provided salinity is treated as a prognostic variable. For instance, Alan Fox, Keith Haines and Paul Myers (personal communication) have implemented it in the 1/4 degree global version of the OCCAM model.

The choice of the model configuration is essentially based on the work by Cox (1985), which in turn is a modification of the model used by Cox and Bryan (1984). The configuration adopted for this study is summarised in Table 5.1. The region considered extends from 0° to 60°N and is 50.4° in longitude. It is a closed basin which embodies a land mass and a continental shelf along the western boundary to roughly approximate the topography of the North Atlantic (for simplicity, North Atlantic terminology, such as Gulf Stream, will be espoused hereafter). Moreover, in order to enhance the baroclinity of the flow field, compared to a flat-bottomed basin, a rough topography, as described in Böning (1989), is adopted. Such a topography is a random field, with an isotropic spectrum that resembles the observed abyssal topography (Bell, 1975). In addition, it also has a stabilising effect on eddies, that maintain their identity for a longer period than in the flat bottom case (Böning, 1989). Cooper and Haines (1996) also used the same model as Böning (1989) for their altimeter twin assimilation experiment. The model domain is depicted in Fig. 5.3, showing also a 2-year average of the sea surface height (the continental shelf, that deepens to the bottom within 4° longitude, is not clearly visible). The horizontal resolution is 0.5° meridionally (that corresponds to 56 km at 0° and to 44 km at 37°, the latter corresponding to the latitude of the model Gulf Stream) and 0.6° zonally.

A legitimate question would be why the selected model domain is quite different from the tropical region considered for the data analysis in chapter 4. There are several reasons for this choice but the main one is that here we aim at studying the assimilation effect on a wider latitudinal domain including extra-tropics and sub-polar regions, as in our view it would have been too restrictive to circumscribe our investigation to low latitude regions. Further, since Emery and Dewar (1982) showed that T–S preservation is more suspect at high latitudes (north of 40° in the boreal hemisphere), the chosen set up is useful to test high latitude assimilation.

Model configuration parameters	
Meridional resolution (extent)	0.5° (0° – 60°N)
Zonal resolution (extent)	0.6° (50.4°)
Vertical resolution (maximum depth)	20–550 m (4175 m)
Number of levels	23 (13 ≡ 525 m)
Baroclinic timestep (baroclinic/barotropic ratio)	120 min (80)
Horizontal biharmonic eddy viscosity: A_{MH}	2.0×10^{19} cm^4 s^{-1}
Vertical eddy viscosity: A_{MV}	1.5 cm^2 s^{-1}
Horizontal biharmonic eddy diffusivity: A_{TH}	3.0×10^{19} cm^4 s^{-1}
Vertical eddy diffusivity: A_{TV}	0.1 cm^2 s^{-1}
Bottom drag	0.01
Relaxation time for T and S	30 days
Area basin	29.3×10^6 km^2
Volume basin	10.5×10^7 km^3
Average depth: Volume/Area	3.6 km
Run conventions	
1 yr ≡ 360 d	
1 mth ≡ 30 d	

Table 5.1: Parameters for the box model.

From Fig. 5.3 the presence of some mesoscale eddies along the Gulf Stream can be seen (they are generated by baroclinic instabilities e.g. Mellor, 1996 and are also referred to as "rings", e.g. Pickard and Emery, 1992). More eddies can be seen in instantaneous sea surface height model fields (not shown). Eddies are quite important in the ocean circulation as their kinetic energy is generally an order of magnitude bigger than that of the mean flow, with the exception of strong current regions where the ratio falls to around two (Wyrtki *et al.*, 1976). The size of mesoscale eddies is normally related to the internal Rossby radius of deformation (R_I) considered a natural scale for the ocean (Gill, 1982), where R_I can be defined as (e.g. Cushman-Roisin, 1994):

$$R_I = \frac{NH}{f} \approx \sqrt{\frac{g\Delta\rho}{\rho_0 H}}\frac{H}{f} = \frac{\sqrt{g'H}}{f} \tag{5.1}$$

where N is the Brunt-Väisälä frequency, a basic measure of stratification, H is a characteristic depth scale, g' is the reduced gravity acceleration and f is the Coriolis parameter (or frequency) equal to $f = 1.47 \times 10^{-4} \sin\phi$ s^{-1}, where ϕ is the latitude. Thus, the relation (5.1), which represents the horizontal length scale at which rotation and stratification effects equilibrate, supplies an estimation of the eddy size. Typical values at mid latitudes are 50-100 km. With the chosen resolution it is therefore possible to resolve eddies, although it is not sufficiently high for the model to be

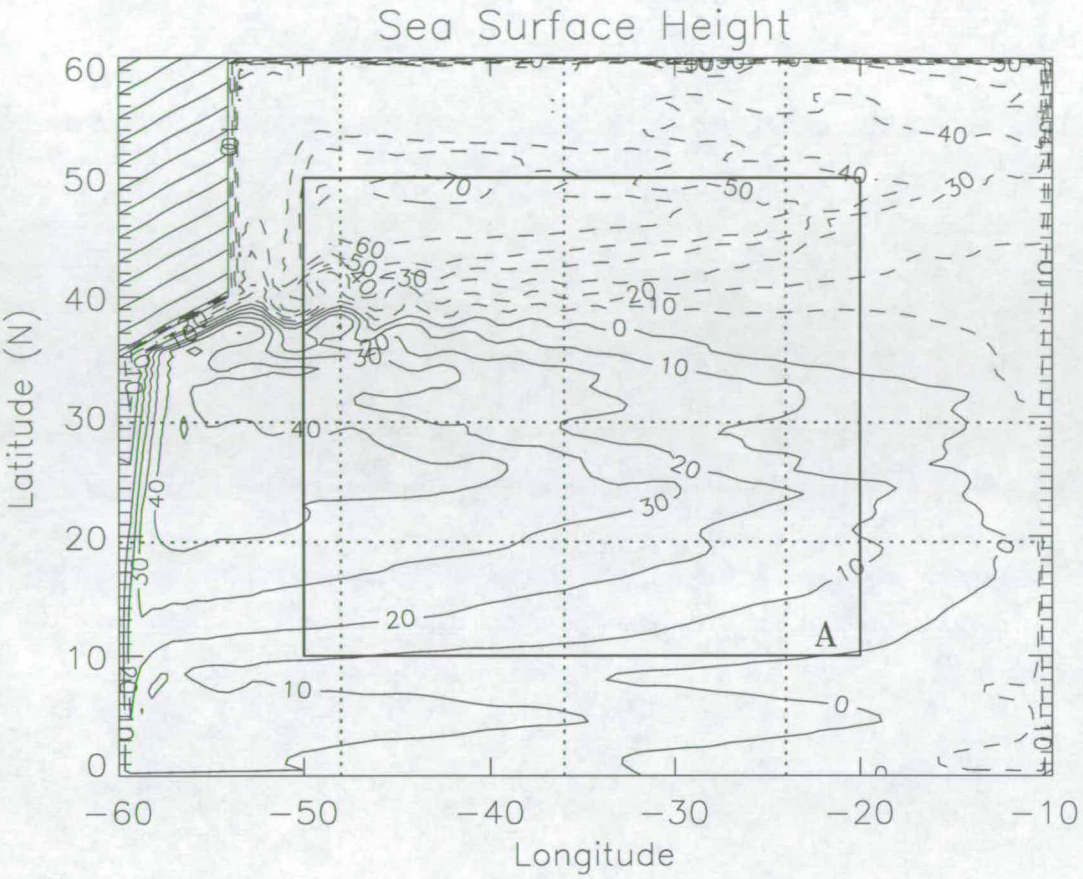


Figure 5.3: Sea surface height for the *Tr* run averaged over 2 years (from year 103 to year 104). Contour interval is 10 cm and dashed lines indicate negative values. Clearly discernible are the anti-cyclonic sub-tropical gyre and the cyclonic subpolar gyre. The oblique lines mark the land mass. The highlighted area A (solid line) and the five sections (dotted lines) are for later reference.

considered fully eddy-resolving. For this type of study, however, eddies are not essential as the assimilation method can be used for climate models as well, which normally have lower resolutions. Furthermore, the eddy activity is also regulated by the eddy viscosity and diffusivity coefficients. Their values are given in Table 5.1.

In the vertical there are 23 levels with a resolution that varies between 20 m at the surface and 550 m at depth. In order to resolve the thermocline well, thirteen levels are allocated in the upper 525 m (this is also the deepest depth used in the data assimilation experiment). The maximum depth is 4175 m.

Restoring conditions are applied at the surface for temperature and salinity. They have only a meridional dependence, their values being derived from a representative section in the middle of the North Atlantic (40.5°W) of the Levitus and Boyer (1994)

and Levitus *et al.* (1994) climatologies (hereafter referred to as Levitus). These climatological values (Fig. 5.4) are interpolated using polynomial functions shown as solid lines (second order for T and third order for S). The relaxation time scale for both T and S is 30 days (acting on a top layer of 20 m thickness), as for instance in Hasumi and Suginohara (1999).

Wind stress data are also climatological values dependent only on the latitude and are taken from the Trenberth *et al.* (1989) data set for the 41.25°W section (Fig. 5.5). For convenience, only the zonal component of the wind stress (τ_x) is considered (i.e. $\tau_y = 0$ N m^{-2} for all model grid points). However, to get the vertical component of the wind stress curl, $(\nabla \times \boldsymbol{\tau})_z$, as close as possible to the climatological one (Fig. 5.5b), τ_x is shifted southward by 7-8° latitude to compensate for the null τ_y, similarly to Cox (1985). Also, to reduce unrealistic features in the proximity of the southern and northern boundaries, the wind stress is chosen such that its curl is nearly zero here. In fact, because it is the wind stress curl (vertical component) that is directly related to the horizontal velocity field, one finds that the transport, $\boldsymbol{M} = \left(\int_{-H}^{0} u\, dz\,,\ \int_{-H}^{0} v\, dz\right)$, is zero when $(\nabla \times \boldsymbol{\tau})_z$ is zero. This choice of the wind stress is normally referred to as a "double gyre" configuration as it generates a circulation with two main gyres (cf. Fig. 5.3).

The truth run is spun up from a stationary state with simplified temperature and salinity fields for 100 years. Its integration is then continued for a further 5 years to have a reference run with which the parallel and the assimilation runs can be compared.

In order to check whether the model reasonably reproduces the T and S fields, a section from the middle of the basin (36°W) is picked and compared, in a purely qualitative way, with an analogous North Atlantic section from Levitus, Fig. 5.6 (the derived density anomaly is in Fig. 5.7). Note however that the former section is averaged over only a 2-year time period, much shorter than that used for deriving Levitus (more than 40 years). The model T and S means in Fig. 5.6 are calculated by averaging 24 realisations, one for each month, of the respective fields. The σ_t mean has been derived for the averages thus obtained. A better way of calculating the average for σ_t would have been to consider the σ_t field for each realisation, but because the present discussion is merely qualitative, that would have been a superfluous complication. However, this more elaborate procedure will be executed for fields like potential vorticity on isopycnals and for T–S diagrams (in the next chapter, sections 6.5.1 and

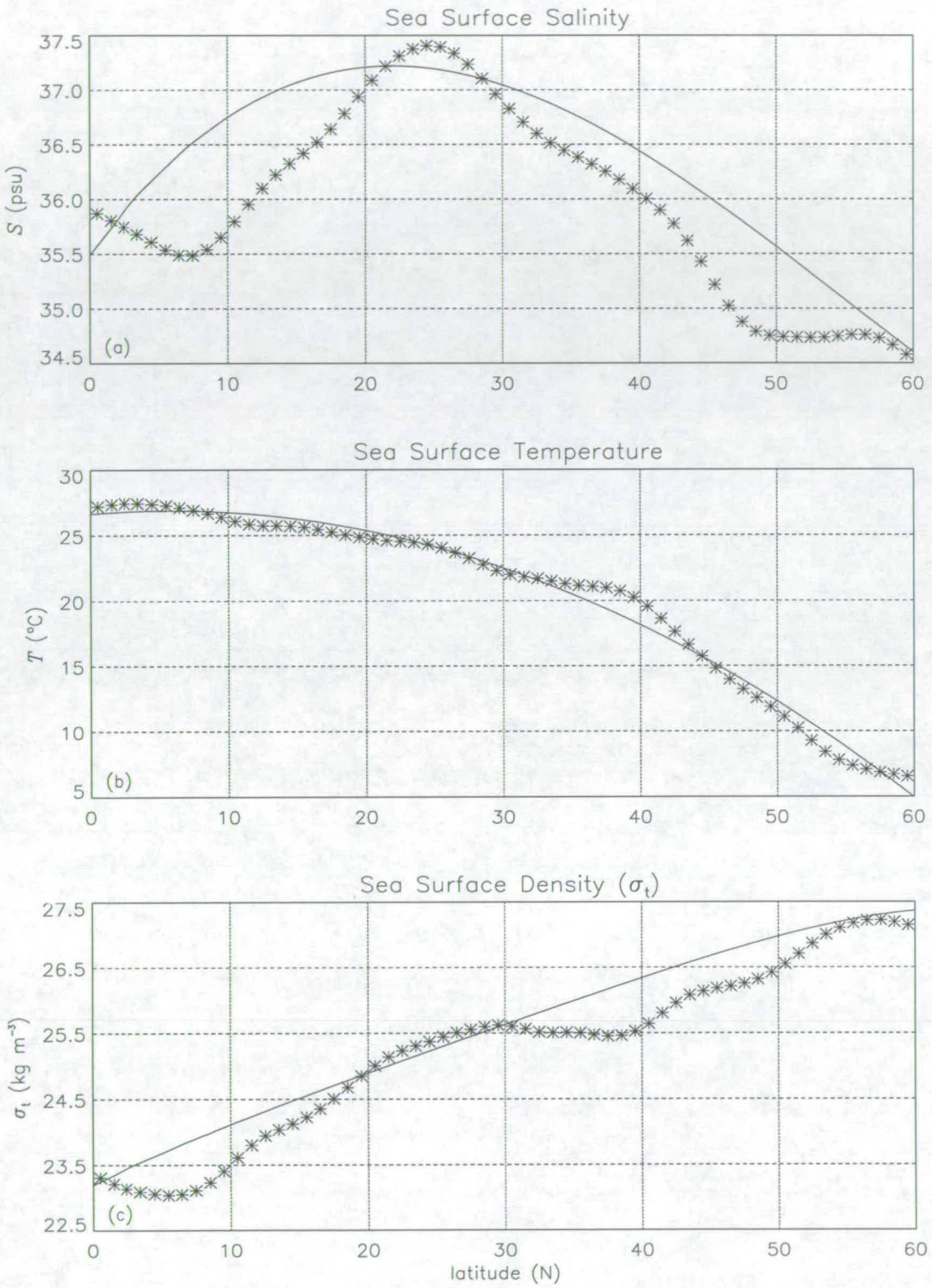


Figure 5.4: Surface boundary conditions for salinity (a) and for temperature (b). Stars denote Levitus values for the 40.5°W section whereas the solid lines are the interpolated polynomial functions used by the model. The values for the density anomaly σ_t (c) are derived from (a) and (b), for the Levitus and the interpolated curves respectively.

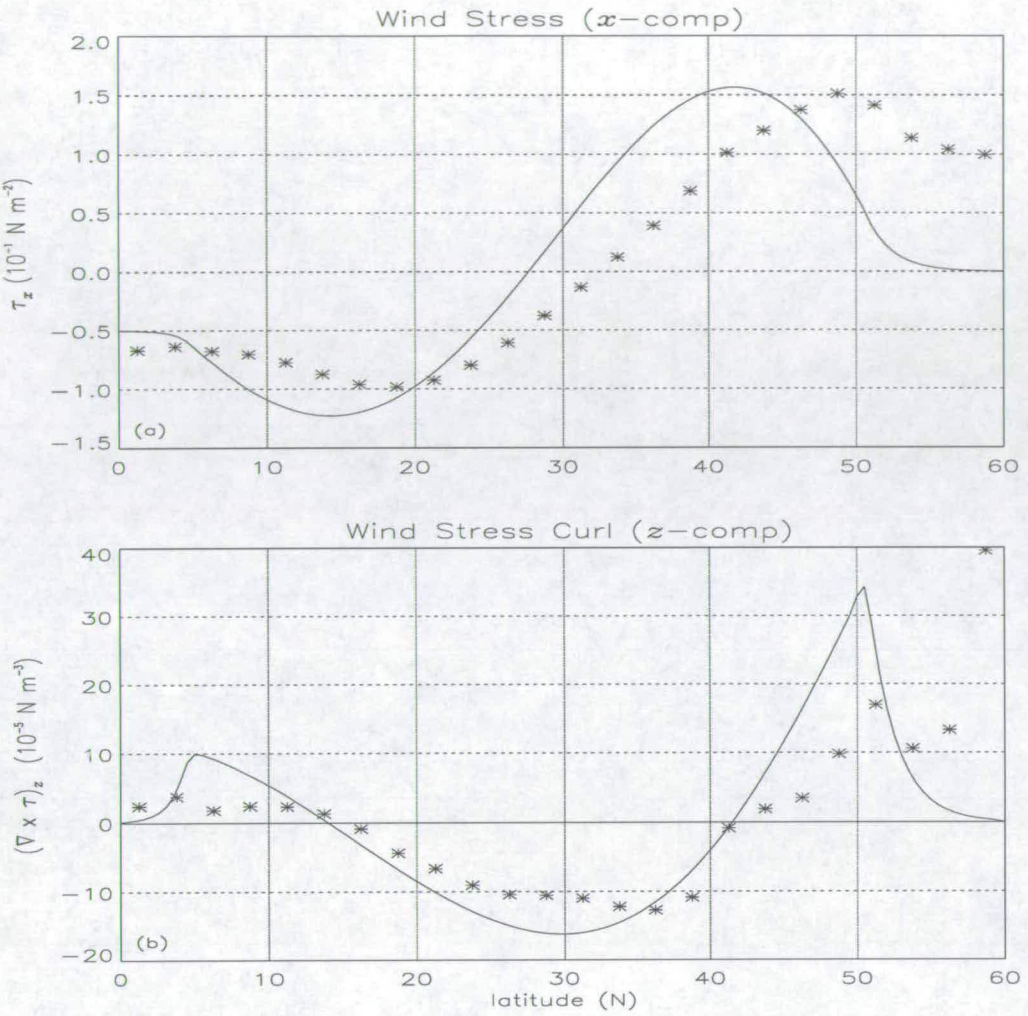


Figure 5.5: Surface boundary conditions for the zonal component of the wind stress (a). Stars denote climatological values for the 41.25°W section whereas the solid line is the modified interpolated function used by the model. The derived wind stress curl (vertical component) is represented by the solid line in (b) and it is compared to the climatological one (*).

section 6.5.2, respectively), that is when more accurate analyses are carried out, although it is applied for consistency also for a more qualitative description in Fig. 5.9.

Because of the simplified model configuration, we are only concerned with simulating the main oceanic features. Therefore, the main conclusion that can be drawn from the comparisons in Fig. 5.6 and 5.7 is that the model does a reasonably good job between 10° and 50°N, although the 18°C isotherm, for example, is deeper than its climatological counter-part (i.e. deeper thermocline) and also the outcropping region centred at around 38°N is narrower in the model (i.e. frontal region with steeper density gradients), suggesting a more intense sub-tropical gyre circulation and Gulf Stream

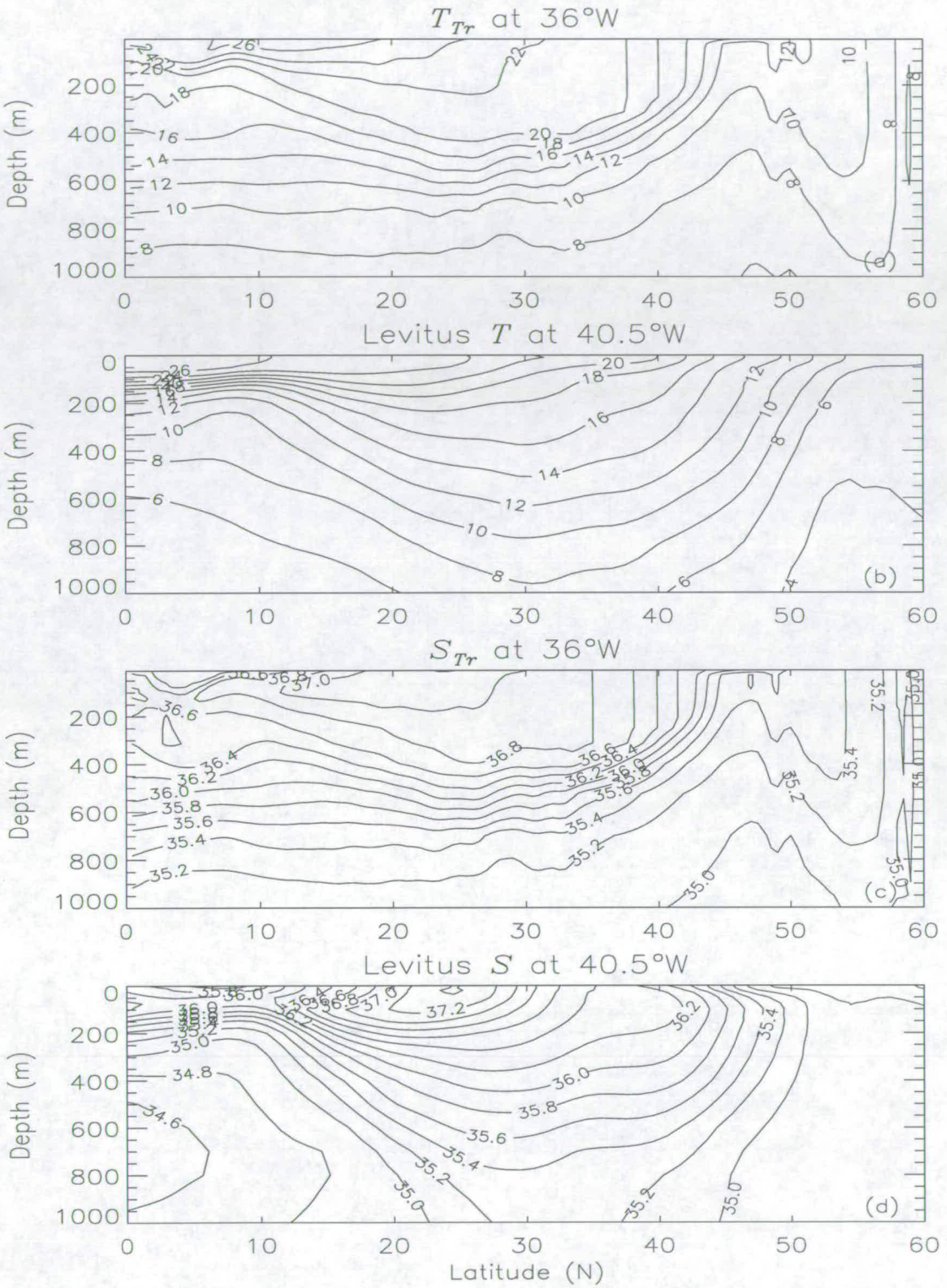


Figure 5.6: Comparison between a model cross section and its analogous Levitus section. The model data are averaged over a 2-year time period. Note that the longitude in the model plots (i.e. 36°W) is only indicative, the section being chosen far from the lateral boundaries. Temperature section (a) from the model and (b) from Levitus (contour interval 2.0°C) Salinity section (c) from the model and (d) from Levitus (contour interval is 0.2 psu).

in the model. However, it is a known problem that in the Levitus climatology (i.e. averaging in z-space rather than in the density space) features like this are generally too smooth (see Lozier *et al.*, 1995). Yet, it is also true that taking a longer time mean for our model would reduce this gradient. Besides, regions with big gradients like this will possibly render things more difficult for the assimilation experiment, as for instance when temperature data are spread in such areas. Outside that range (10°–50°N), mainly because of the closed boundaries, the model does not bear much resemblance to the climatology. For instance, the model thermocline and halocline south of 10°N are much too diffuse. For this reason, where relevant, subsequent analyses will neglect the regions near the zonal boundaries. For similar reasons, also areas within about 10° from the lateral boundaries should be examined with care.

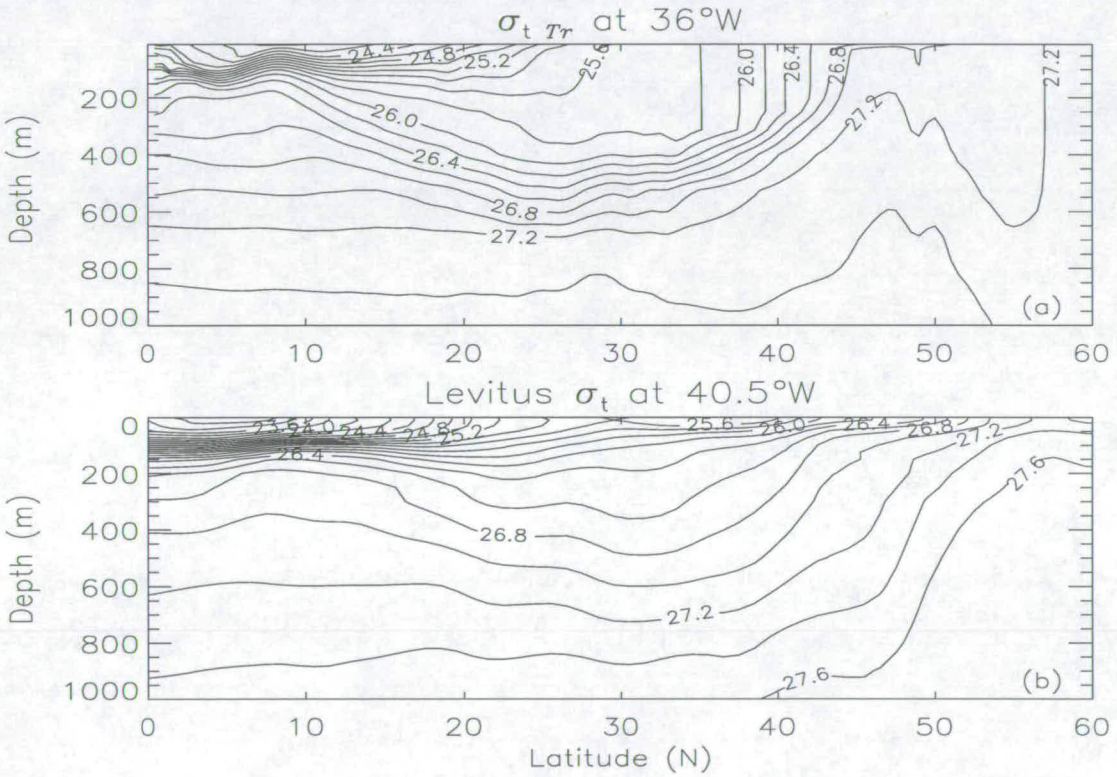


Figure 5.7: As in Fig. 5.6 for density anomaly (contour interval is 0.2 kg m^{-3}).

The sea surface temperature (SST) and the sea surface salinity (SSS) for the truth run averaged over the 2-year assimilation experiment (24 realisations) are shown in Fig. 5.8. The zonal structure in both fields, essentially determined by the zonally constant surface forcing, is apparent. Also, the T and S values in Fig. 5.8 closely reflect the values of their respective forcing (see Fig 5.4a-b), the only exception being

at the more intense - western - end of the Gulf Stream. These two fields, SST and SSS, will be a useful reference for our subsequent analyses.

As a further model validation, we compared the potential vorticity fields at $\sigma_t = 26.0$ kg m^{-3} from the fine grid case run in Cox (1985) (i.e. his Fig. 5d) and from our truth run (Figure 5.9). The potential vorticity considered here is its simplified linear version, namely equation (2.19) $[q = -f\,(\partial\rho/\partial z)]$ (see section 2.4 for a more detailed treatment of q). Here we just recall that the importance of q stems from the fact that for an inviscid adiabatic fluid q is a conserved quantity in a Lagrangian sense. At the same time, given its definition, q is an indicator of the local (in z-space) stratification (or, roughly, of the inverse of the inter-isopycnal thickness). So, at constant latitude, a higher value of q is associated to a more pronounced stratification.

The temporal average in Fig. 5.9a has been obtained by first calculating the PV for each month of the 2-year integration and then averaging the 24 potential vorticity realisations. Such a procedure is aimed to avoid undesirable smoothing that could be introduced by first temporally averaging in z-space and then calculating the PV. From Fig. 5.9 it can be seen that both experiments present the same general features: two principal sources of high q, one at the eastern boundary (called the shadow zone) and the other at the western boundary (where the northward flow in the sub-tropical gyre meets the land mass, and called the pool region). These two sources are separated by a region of nearly homogeneous q, resulting from the eddy activity which removes q gradients (PV homogenisation, see Cox, 1985).

5.2.1 Time scales

It is interesting to estimate what the main time scales for our model are. We will compare the results with the time scales found by Cox (1985), whose model, as already noted, is essentially the same as the one used in the present work, but with a flat bottom. He found three primary time scales: a 50-day period associated with mesoscale variability, a 1.1-year period due to energy transfer from the first baroclinic mode into the barotropic mode and a 4-year period identified as due to first baroclinic mode Rossby waves.

It is useful to have an idea of the main periodicities involved in the model circulation as these may become relevant if they are comparable to the time scale chosen for the assimilation experiment. To this end, we consider the specific kinetic energy as a

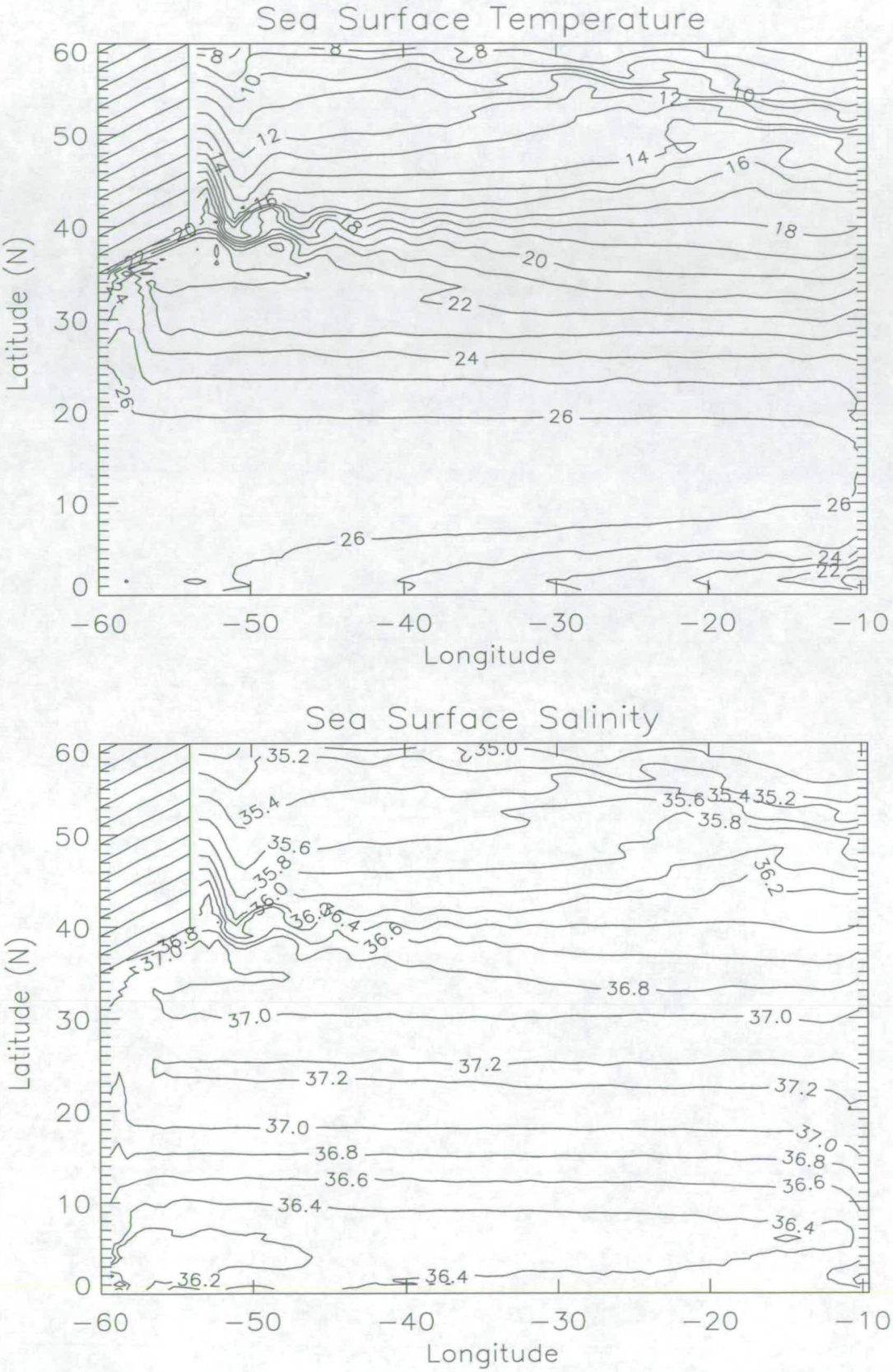


Figure 5.8: As in Fig. 5.3 but for sea surface temperature (top, contour interval 1°C) and sea surface salinity (bottom, contour interval 0.2 psu).

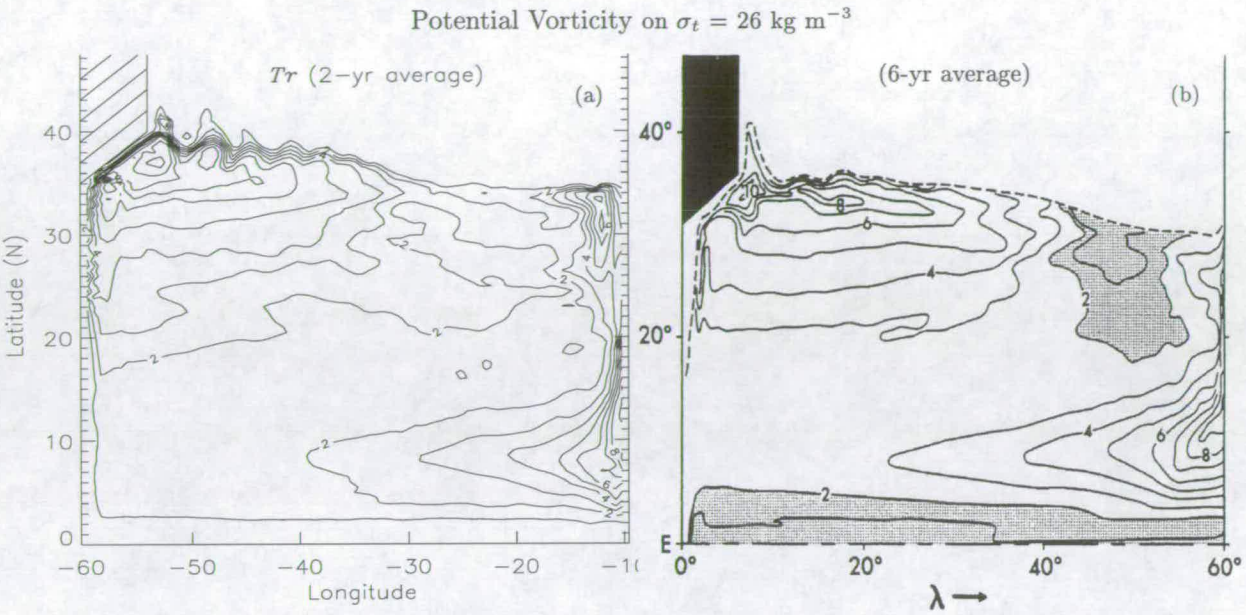


Figure 5.9: Potential vorticity in units of 10^{-7} m^{-1} s^{-1} for (a) 2-yr average of the truth run and (b) the 6-yr average from Cox (1985) (his Fig. 5d).

proxy for the system (cf. Fig. 5.2) and assume its time series can be described by the following function, i.e. a Fourier expansion:

$$K_t = \bar{K} + \sum_{j=1}^{\lfloor N/2 \rfloor} [A_j \cos(2\pi f_j\, t) + B_j \sin(2\pi f_j\, t)]\,, \qquad t = 1, 2, ..., N. \tag{5.2}$$

where f_j is the jth standard (or Fourier) frequency, defined by $f_j \equiv j/N$. Note that both time and frequency are discrete. In particular, our time interval is equal to 5 days. It can be shown that the spectrum of the variable K_t is given by the relation:

$$S_j = \frac{A_j^2 + B_j^2}{2} \tag{5.3}$$

and we therefore need to work out what the A_j's and B_j's are. By multiplying both sides of equation (5.2) by $\cos(2\pi f_j\, t)$ $[\sin(2\pi f_j\, t)]$ and summing over t, one finds the A_j's $[B_j$'s]:

$$A_j = \frac{2}{N} \sum_{t=1}^{N} K_t \cos(2\pi f_j t) \qquad\qquad B_j = \frac{2}{N} \sum_{t=1}^{N} K_t \sin(2\pi f_j t) \tag{5.4}$$

For a complete derivation see for example Percival and Walden (1998).

The spectrum calculated from a 55-year period (from year 50, to avoid the initial transients, to year 104) of the truth run is shown in Fig. 5.10[1]. The dominant time scale

[1]Because S_j has the dimensions of K^2, $\log_{10}(S_j)$ has to interpreted as $\log_{10}(S_j/S_0)$, with S_0 constant. The $\log_{10}(S_j)$ is used, instead of just S_j, because for the former the variance is approximately the same for all f_j's. Besides, 10 $\log_{10}(S_j)$ is equivalent to a decibel (dB).

in our model is at around 4.3-year period (maximum at 2.3×10^{-1} yr^{-1}), close therefore to the 4-year period found by Cox (1987). From Fig. 5.10 other relative maxima can be observed in the kinetic energy spectrum, which are pronounced at frequencies higher than 1.0 yr^{-1} (i.e. for periods shorter than 1 yr), even if they have a much lower intensity than the absolute maximum. In decreasing order, they have periods of 11.3, 9.7, 8.0, and 6.5 months. In particular, the time scale at 1.1 yr found by Cox (1987) emerges only partly, with a relative maximum at 8.3×10^{-1} yr^{-1} corresponding to a 1.2-year period. The 50-day time scale is not represented by Fig. 5.10 (minimum period is 6 mth). Note that the zero frequency term, corresponding to $\bar{K}$, is not shown. $\bar{K}$ is equal to 12.9×10^{-4} m^2 s^{-2}.

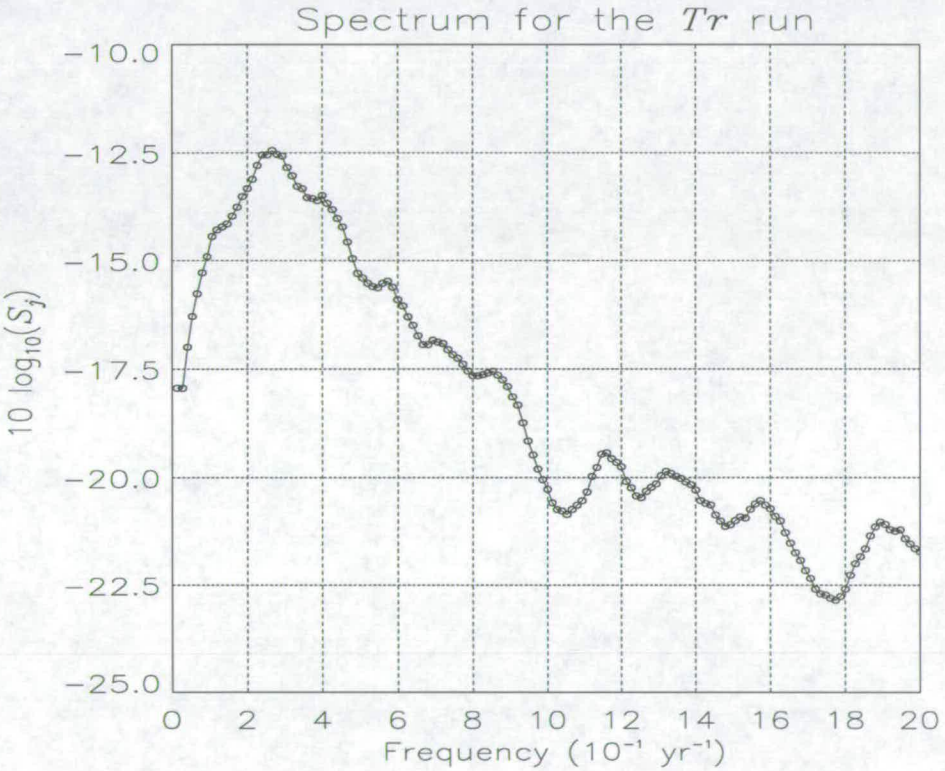


Figure 5.10: Specific kinetic energy spectrum for the truth run calculated over a 55-yr period (from year 50, to avoid the initial spin-up transients, to year 104).

5.3 Parallel run

The parallel run is a 'degraded' version of the truth run. Its purpose is to provide us with a model run similar to the truth, but with some "deficiencies", to simulate the analogy between the real state of the ocean (our truth run) and any numerical

model used to reproduce it (our parallel run). Different ways of altering the truth run could be opted for, essentially by mimicking the likely physical and/or numerical flaws of models. Commonly, internal turbulent mixing parameterisation, air-sea interaction (wind stress, heat and fresh water fluxes are often in error due both to uncertainties in their values and the way they are numerically represented in the mixed layer) and advection schemes are the weakest features in a model. Note that we need to introduce this model 'disturbance' because this is not an *identical* twin experiment. In fact, as discussed in chapter 1, for an *identical* twin exactly the same model would be used both for truth and parallel runs from which two distinct integration times would be selected as their initial conditions.

Several alternatives are possible in setting-up the experiment. Though, taking into consideration that: 1) our model is forced by time-independent climatological forcings and therefore a limited internal variability is allowed; 2) we need to generate modifications in the water mass structure (otherwise too optimistic results would be achieved, in principle) in a reasonable amount of integration time; 3) it would be preferable for the parallel run to attain a dynamic equilibrium, so that transient effects are reduced to a minimum; 4) surface forcings might be subject to large uncertainties (for instance, Böning *et al.*, 1991 compared two wind stress climatologies for the North Atlantic, one by Hellerman and Rosenstein, 1983 and the other by Isemer and Hasse, 1987, and found differences as large as 25% in the zonal component of the annual mean); 5) a simple alteration would be preferable so as to attain a more straightforward analysis of the results.

A choice that accounts for the listed points is given by a modification of the wind stress. In particular, we opted for increasing the wind stress in the parallel run by 15% at all latitudes, so that the two peaks become (1.80, -1.41) $\times 10^{-1}$ N m^{-2} instead of (1.56 ,-1.23) $\times 10^{-1}$ N m^{-2}, cf. Fig. 5.5. It is important to note that the wind stress modification will also affect the sea surface fluxes (heat and fresh water) as they are not prescribed. Furthermore, the increased wind stress will induce a more intense double-gyre circulation and, as hinted at in section 5.2, this should make things more difficult for the assimilation experiment.

The parallel run reaches a new dynamical equilibrium in about 3 years (this is what emerges by looking at the kinetic energy of a 10-year integration of Pa, not shown). The average specific kinetic energy for Pa for the period 103-104 yr (to have a direct

comparison later with the assimilation runs) is equal to 15.5×10^{-4} m^2 s^{-2} (see Fig. 6.1 in the next chapter), that is 24% higher than the truth run (its average for the selected period is 12.6×10^{-4} m^2 s^{-2}).

5.4 Truth and parallel runs comparison

In this section we discuss the differences between truth and parallel runs in terms of water mass properties, using T-S diagrams and potential vorticity differences. The former is an integral quantity calculated over the area A (which constitutes 45% of the whole domain, see Fig. 5.3) whereas the latter is a local measure of stratification, at pre-defined density levels, as a function of the geographical location.

With the T-S diagrams, our objective is to show that, in terms of water mass properties, the 3-year Pa-Tr divergence is sufficient to generate significant discrepancies in the Pa run relative to the Tr run (e.g. $|Tr(t_1) - Tr(t_2)| < |Tr(t_1) - Pa(t_2)|$, with $t_1 = 100$ yr and $t_2 = 103$ yr. In fact, even if the truth run has reached a dynamical steady state its water mass properties are still subject to non negligible temporal variability. Therefore, by verifying that the above inequality holds, we would prove that the data assimilation experiment is well posed, in the sense that the error introduced by the extra wind stress is capable of developing quite distinct differences, so as to have new initial conditions, from which the assimilation runs will be started. It is important to observe how this systematic error can be detected through the study of the water mass properties and how data assimilation can correct for it.

The variations of the water mass properties for the Tr and Pa runs during the 3-year period, 100-102 yr, for the area A are shown in Fig. 5.11. The T-S diagrams are constructed as follows. For each water column, the thickness differences (ΔZ_{mn}, with $\Delta Z = \Delta Z(S, T, \lambda, \phi)$) are allocated into the T-S space whose granularity is equal to $\Delta T = 0.25$°C and $\Delta S = 0.05$ psu. The differences are then weighted by the area of its grid location (i.e. depending on its latitude). The sum of all the differences thus obtained are divided by the sum of the area weighting factors (i.e. weighted average):

$$\Delta Z(S,T) = \frac{\sum_m \sum_n \Delta Z_{mn}(S,T,\lambda_m,\phi_n) A_u \cos(\phi_n)}{\sum_m \sum_n A_u \cos(\phi_n)} \tag{5.5}$$

where λ and ϕ are the longitude and the latitude, respectively; $A_u \cos(\phi_n)$ is the area of the grid at longitude λ_m and latitude ϕ_n. Thus, these T–S diagrams are to be interpreted as layer thickness differences between water masses of each type.

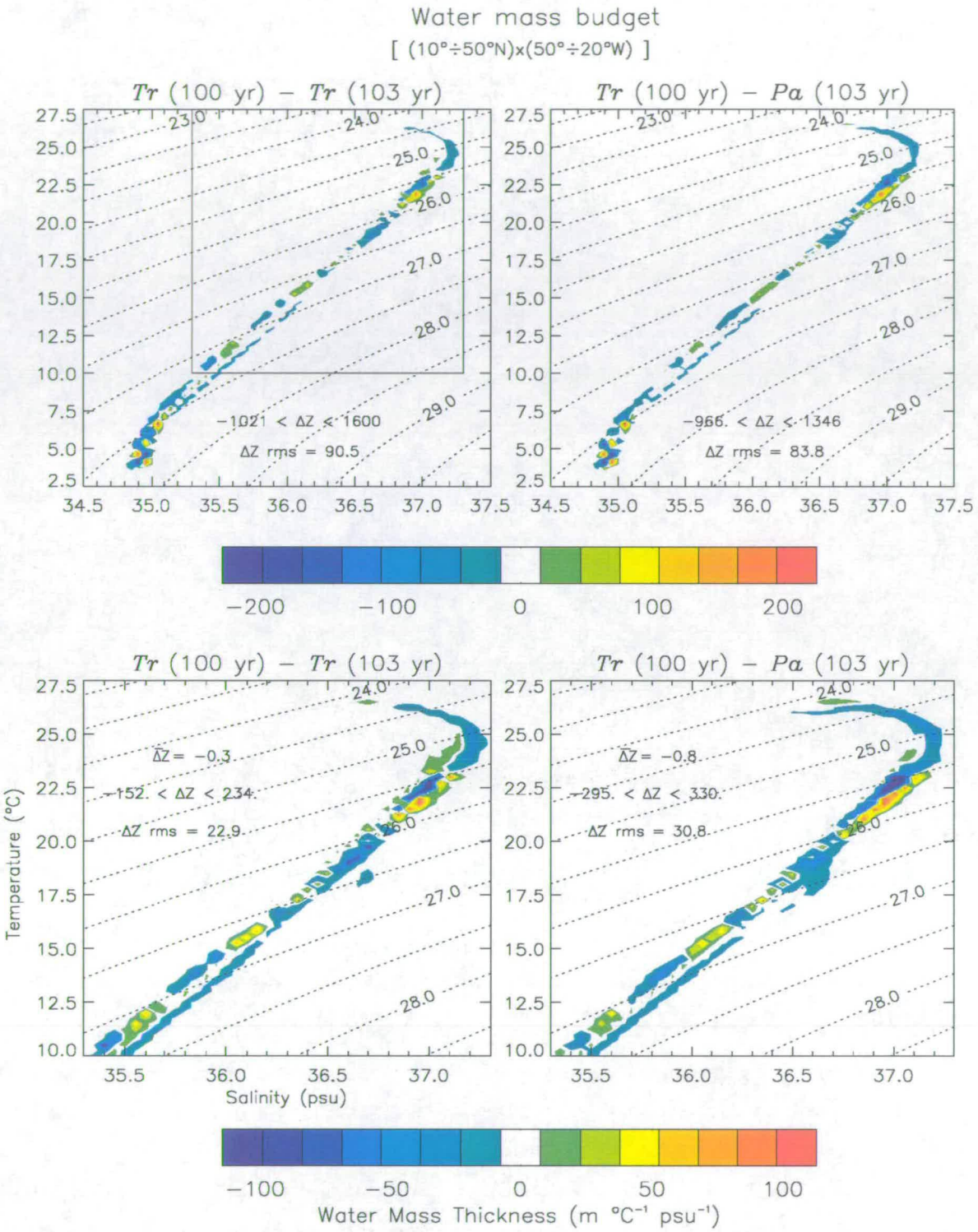


Figure 5.11: T-S diagrams showing the difference between the truth run at year 100 and (left) the truth run (right) the parallel run both at year 103 for the area A highlighted in Fig. 5.3. Water columns are weighted according to relation (5.5). Superimposed are the σ_t dotted curves. Top left panel displays the portion of the T-S diagram utilised for the bottom panels. Averages, extrema and rms are indicated (the former only for the bottom panels as for the top ones averages are zero by definition). Note also the different scales for top and bottom panels.

Top panels in Fig. 5.11 show the complete T–S diagrams for the two differences (i.e. Tr(100 yr)–Tr(103 yr) and Tr(100 yr)–Pa(103 yr)). Although, in both cases, there are differences along most of the T–S "curve", they are mainly concentrated in two intervals, that is for σ_t smaller than about 26.4 kg m^{-3} and for σ_t bigger than about 27.4 kg m^{-3}. Some of the variability in the latter interval is caused by small temporal variations of the water masses being formed at high latitudes. More evident is the variability in the range 27.5–27.6 kg m^{-3}, whose T and S values are $5 < T < 7$°C and $34.9 < S < 35.1$ psu, which correspond in fact to the high latitude T and S surface boundary conditions (cf. Fig. 5.4) and which characterise the T and S properties of this deep water mass. Even for $\sigma_t > 27.6$ kg m^{-3} there are significant differences, but there are more similarities between the two cases.

A further confirmation of this different water mass formation rate is given by the $\bar{\Delta Z}$ values for $T < 10$°C and $S < 35.3$ psu, which are equal and opposite to those given in the lower panels, that is 0.3 m °C^{-1} psu^{-1} for the truth run and 0.8 m °C^{-1} psu^{-1} for the parallel run (this is because $\bar{\Delta Z}$ is identically zero, by definition, when calculated over the whole T–S diagram). Therefore in the parallel run less deep water mass than in the truth run is produced during this 3-year integration.

Because the assimilation mainly affects the upper water column, we will proceed now to the more important discussion of the bottom panels in Fig. 5.11, which are zooms of the top ones (see top left panel), that is for the range 10°C–27.5°C and 35.3–37.3 psu. Differences are decidedly bigger in the Tr(100 yr)–Pa(103 yr) case compared to the Tr(100 yr)–Tr(103 yr) case, as is indicated by the extrema in the bottom panels of Fig. 5.11: (-152; 234) m °C^{-1} psu^{-1} against (-295; 330) m °C^{-1} psu^{-1}. Moreover, there is a surplus of water mass in the chosen density range in the parallel run, with respect to the truth, as shown by the values of $\bar{\Delta Z}$.

In the lighter end of the range, i.e. $\sigma_t < 26$ kg m^{-3}, the parallel run generally produces lighter water mass than the truth run. In fact, there is a predominance of negative (blue) areas over the positive ones in the right panel. In particular, the main differences are concentrated in the temperature range 20–23°C and salinity between 36.75 and 37.15 psu. Within this range, a lighter water mass is being formed at a higher rate in the parallel run, as shown by the wider negative blue zone. Accordingly, the positive zone is also more accentuated in the parallel run, since it counterbalances the larger amount of lighter water mass (blue zone). Also, these T and S water mass

properties can be traced to the surface (see the boundary conditions in Fig. 5.4a-b) and, in particular, to the latitudinal range 28-36°N. At those latitudes the density anomalies range between about 25.5 and 26.0 kg m^{-3} (Fig. 5.4c), in agreement with the range in Fig. 5.11 (bottom right). Additionally, it can be seen from Fig. 5.7a that at those latitudes isopycnals indeed outcrop. Another perspective to this interpretation in terms of water mass formation will be also given by the potential vorticity analysis in the next chapter. To sum up, the analysis now presented suggests that the increased circulation, induced by the stronger wind stress, produces a larger amount of water mass formation in the northern part of the sub-tropical gyre.

Despite the larger magnitude of the difference in the case of the parallel run with respect to the truth run, that is the bottom right panel compared to the bottom left panel in Fig. 5.11, the pattern of the differences is similar in both runs. In a dynamical steady state the water mass budget oscillates, just like the kinetic energy in Fig. 5.2. To prove this point, we have calculated the water mass budget for longer time intervals (not shown). Therefore, part of the reason why the two plots have a similar pattern is that the 3-year period considered is less than the dominant variability time scale of our model, at least for the truth run (4.3 yr, section 5.2.1). For longer time periods, we would in general expect different patterns for the two runs, taking the same reference state as in our case.

Lastly, it should also pointed out that, because of possible sign compensations between water masses with the same properties but at different locations, this type of analysis could hide important features. Possible solutions could be: to select several smaller regions or, alternatively, consider the same area but taking for each water column the modulus of the difference (i.e. $|\Delta Z_{mn}|$). Both approaches have been carried out and the results (not shown) are substantially the same as in the case presented above.

5.5 Data assimilation experiment

Two runs will be conducted as part of the temperature data assimilation experiment. The first, and more important, is the one that is aimed at testing the assimilation method introduced with this work (abbreviated by A_{ST}). The second, which will be used as a comparison with the first one, uses a salinity persistence approach (i.e. not modifying $S = S(z)$ at assimilation time and abbreviated by A_{SZ}). Because the latter

has been widely used hitherto, it is one of our principal goals (see chapter 6) to check whether our method performs better.

The initial conditions for these runs are taken from the end of the third year of the parallel run (i.e. year 103, see Fig. 5.1). For file storing convenience, the actual data assimilation only starts after a further month of integration (namely at 103 yr and 1 mth).

In these experiments only the upper part of the vertical profiles of temperature are assimilated. This is to simulate an XBT assimilation. In fact, most of the available oceanographic temperature data are normally collected by means of XBTs and they typically reach a depth of 500 m. Due to model constraints, the maximum depth chosen for the assimilated data is equal to 525 m (level 13 out of 23).

5.5.1 Sections selection

Five fixed sections are chosen to provide data for the assimilation experiment (19.5°N, 29.5°N, 48°W, 36°W and 24°W, see dotted lines in Fig. 5.3). The two zonal sections allow us to study the assimilation impact on the sub-tropical gyre, whereas the three meridional ones cover more diverse physical characteristics, ranging from the rather tight thermocline of the sub-tropical gyre, to the strong currents in the Gulf Stream region, to the weaker stratification of the sub-polar gyre. The selection of their shape and location is also based upon the disposition of the real measurements (typically XBTs). In fact, data are usually collected along straight lines that could be derived either from merchant ship tracks or from research cruises.

Malanotte-Rizzoli and Holland (1986) addressed the question of which data sections are more efficacious in driving the assimilation run towards the truth run and found that it is better to assimilate along meridional sections, which are long and located at a distance from the western boundary. In a successive paper, Malanotte-Rizzoli and Holland (1988), they suggest this is because westward propagation of the long Rossby waves is quite effective in transporting the assimilated information and hence for sections closer to the western boundary information would be soon reflected as short waves that would propagate at much lower speed and hence information would be confined in a more spatially limited area. Yet, further inspection of Figure 6 of Malanotte-Rizzoli and Holland (1986), which shows the impact of assimilated data along a zonal section in their southern gyre, seems to imply an overall beneficial effect, for instance

comparable to the meridional section of their Fig. 4 in the same paper. Therefore, it appears as though some zonal sections may be as influential as some meridional sections in the propagation of information. Also, for their investigation, they used a steady, weakly non-linear, highly frictional quasi-geostrophic model, therefore neglecting advective and eddy propagation effects, which are really very important in general. However, in their later work (Malanotte-Rizzoli and Holland, 1988), using the same model but in a time-dependent, fully eddy-resolving configuration (much more similar to the one used in this work) they found that, over time scales of the order of 100 days, all their chosen (now only meridional) sections where equally ineffective in driving the assimilation run towards the truth state, regardless of their position and length and that a much longer time period is needed to obtain some benefit. In addition, they argued that information propagated by the long Rossby waves is also more important (at least one order of magnitude) than propagation by non-linear advection in highly energetic regions such as the Gulf Stream. Thus, it will be interesting to observe in the next chapter how and to what extent our sections are affecting the assimilation outcome.

In the real world XBT lines are generally not repeated periodically, ergo, a question arises as to whether it is preferable to adopt, for assimilation purposes, fixed sections or ones that are variable in time. If one is to attain a better convergence between assimilated and truth runs, the latter would probably be more efficient, because of the greater difference in water types processed during assimilation. However, if the main aim is to analyse the impact of the assimilation method, as it is here, fixed sections are arguably a better option, as they allow, amongst other things, a more systematic study of temporal variations of physical quantities such as density fields, currents and so on.

5.5.2 Temperature analysis

The temperature data used by the two assimilation runs are taken from the truth run along the five sections every 30 days. In order to use the data along these lines in a more efficient way (instead of just inserting them directly), the temperature information is spread over the surrounding area. In fact, a measurement taken at a certain location is representative, to some extent, of its neighbourhood. How large this neighbourhood is will depend mainly upon the deformation radius, i.e. on the local density structure

and the geographical location (this information is contained in the decorrelation scale). Yet, here we will consider only the geographical dependency. The scheme adopted here is essentially the same as the one used by Moore *et al.* (1987) and Moore and Anderson (1989) - its description follows.

The model background (or forecast) temperature, T_B, is combined with the temperature observations, T_O, at each assimilation step by taking their difference (i.e. $T_O - T_B$). This difference (or increment) is then spread ellipsoidally over the neighbourhood of the data location by means of an imposed correlation function, with correlation length scales a_x (zonal) and a_y (meridional). The new model temperature, namely the analysis, T_A, is then given by adding to the background value the increment obtained from the correlation function, through a weighted average procedure. Thus:

$$T_A = T_B + \frac{\sum_k \alpha_k (T_{Ok} - T_{Bk})}{\alpha_p + \sum_k \alpha_k} \tag{5.6}$$

for each model grid point and where k runs over all the grid points; α_p is an empirical weight that formally diminishes the influence of T_O on T_A. The weighting factors α_k, or decorrelation scales, are given by:

$$\alpha_k = a \cdot \exp - \left\{ \left[\left(\frac{dx}{a_x} \right)^2 + \left(\frac{dy}{a_y} \right)^2 \right] \frac{1}{\cos\phi} \right\} \quad \text{For} \quad |dx| < 2.5\, a_x \ , \quad \text{and} \quad |dy| < 2.5\, a_y \tag{5.7}$$

$$\alpha_k = 0 \qquad \text{Otherwise} \tag{5.8}$$

Here a is a constant, a=100, but it could be taken to be dependent on stratification, i.e. $a = a(z)$, see Behringer *et al.* (1998); dx and dy are the distances from the grid point considered. The correlation length scales are taken equal to be $a_x = 70$ km and $a_y = 30$ km. The $\cos\phi$ term acts as a latitudinal scale selector, filtering out larger scale features at higher latitudes (see Derber and Rosati, 1989). An example of the spreading procedure for six selected points along the sections is presented in Fig. 5.12. The increments $(T_O - T_B)$ are the same for all the six points and equal to 2°C, so the effect of the $\cos\phi$ term can be picked out.

To have an idea of the spatial impact on the model grid points, the chosen sections directly affect about 5.5% of the whole model domain whereas after applying the function (5.6) the percentage rises to about 20%. Clearly, not all of the grid points involved will have the same influence on the salinity analyses given by the assimilation

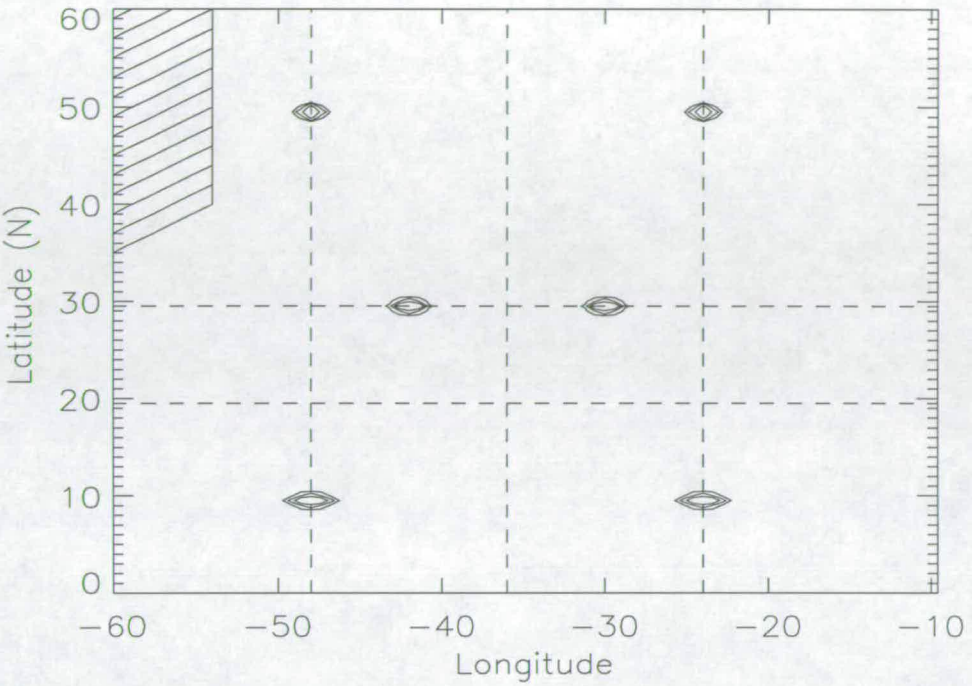


Figure 5.12: Example of temperature analysis using the horizontal correlation function 5.6. The initial temperature increments are equal to 2°C for all six cases, so to highlight the $\cos\phi$ term effect. Contour lines are 0.1, 0.5 and 1.5°C.

method, as the temperature increment may not be large enough away from the sections to produce a noticeable salinity update.

In this experiment the spreading is done on z levels, regardless of the location of the data. Yet, in regions of strong horizontal density gradients, such as along the Gulf Stream, a more appropriate way would be to propagate thickness increments on temperature levels (see Lozier *et al.*, 1994 and Redi, 1982). However, although conceptually straightforward, it is quite difficult to write a numerical code that yields satisfactory results, at least for a z-coordinate model.

5.5.3 Salinity analysis

The increments obtained by the spreading procedure in section 5.5.2 are then used by our assimilation scheme to obtain the salinity analysis for the A_{ST} run (the discussion in this paragraph applies only to this run, not to the A_{SZ} one). However, due to both numerical and physical problems, a few requirements have to be met for the method to be applied. In fact, mainly near the boundaries and especially along the shelf, the

numerics may give rise to abnormal vertical temperature gradients. Because this is a confined and limited problem, we do not attempt to correct it but rather we introduce a gradient limiter so as to avoid processing through the assimilation scheme these few water columns. As far as physical problems are concerned, they arise because the stratification may be too weak, such as at high latitudes. In these circumstances the water masses in the background water column may be quite different from those present at the assimilation step, for instance because of the enhanced convective activity. An empirical criterion is therefore employed according to which the salinity is left unchanged (i.e. just as in the A_{SZ} run) if the vertical temperature gradient is everywhere in the column smaller than 10^{-2}°C m^{-1}. In practice, in our model this typically occurs above 50-52°N, and hence only over a small portion of the model domain. This approach is also supported by the data analysis executed by Emery and Dewar (1982) who found that in certain areas of the North Atlantic, approximately above 40°N, the $S = S(z)$ varies less than $S = S(T)$ (i.e. the rms is smaller in the former case).

In addition, to allow for measurement-like errors, the assimilation scheme is not activated when the maximum difference between the observed and the background (assimilation runs) temperature is smaller than 0.1°C. Although this is a typical instrumental error (e.g. from XBTs, see Bailey *et al.*, 1994), one should also consider depth errors (due to calibration) which may cause temperature errors as big as 2°C at thermocline depths (Carton *et al.*, 1996). This is not done here, though.

A further difference between the two assimilation runs (A_{ST} and A_{SZ}) is the use of the vertical displacement in the A_{ST} run (see section 3.2). As a consequence, the A_{SZ} may exhibit acute convective instabilities that in turn could give rise to abnormal water masses. On the other hand, the vertical displacement, whilst avoiding convective problems, could modify marginally the weight of the water column (by removing or inserting water mass at the bottom) and hence bottom pressures and currents. We shall discuss the issue of the bottom current variations in more detail in the next chapter.

The four runs introduced in this chapter (Tr, Pa, A_{ST} and A_{SZ}) are summarised in Table 5.2.

	Run	period (yr)	wind stress (x/Tr)	vert. displ.
Tr	truth	0–104	1	–
Pa	parallel	100–104	1.15	–
A_{ST}	T–S preservation	103–104	1.15	Y
A_{SZ}	persistence	103–104	1.15	N

Table 5.2: Description of the four runs. The wind stress is expressed as a ratio with respect to the truth run. Vert. displ. stands for vertical displacement.

5.5.4 Velocity analysis

At each assimilation step the velocity field could be updated, for instance, by means of geostrophy (at least to within a few degrees of the equator). However, according to Philander *et al.* (1987), the model should be capable of generating the currents consistent with the new density field, when the potential energy is bigger than the kinetic energy (that is generally when geostrophy holds). Also, Malanotte-Rizzoli *et al.* (1989) found that severely unbalanced initialisation fields are required to produce strong internal gravity wave shocks in ocean models. Otherwise, in places like the Gulf Stream, an imposed geostrophic adjustment (after inserting the new density field) would not be the appropriate solution. For these reasons we have opted for leaving the velocity field unmodified when the assimilation is performed.

Chapter 6

Synthetic Data Experiment: Assimilation Results

In this chapter the results of the synthetic data assimilation experiment are discussed. Not only will the typical tools for assessing the success of an assimilation method (e.g. T and S rms) be adopted, but also a more physical analysis of the model modifications, due to the assimilation, will be carried out. This will be achieved by studying the water mass modifications induced by the data insertion and also by looking at specific fields such as dynamic height differences and potential vorticity on constant density surfaces. The chapter ends with the analysis of the data assimilation inventory.

6.1 Aims of our experiment

Ultimately, the chief aim of a data assimilation system is the error reduction of the assimilation run compared to the real world (the truth run in our case). However, it is also useful to study how the assimilation method interacts with the model, as this may be helpful for improving both the model and the assimilation system. Therefore, in this chapter we will first show the performance of the data assimilation by looking at field differences between the runs considered for our experiment, as described in chapter 5 (see Table 5.2), and then we will analyse in more detail how the data insertion modifies the water mass properties and, in turn, the circulation.

Other authors have previously addressed the issue of data assimilation-model interaction: for instance, as discussed in section 5.5.1, Malanotte-Rizzoli and Holland (1988) studied the effect of the data insertion process on a model, though using a quasi-geostrophic model, as opposed to a primitive equation model. They found that although sections which are meridional, long and located at a distance from the western

boundary are ineffective over time scales of about 100 days, the assimilated information had an appreciable contribution to the basin circulation on long time scales (about 10 years). Their main conclusion is that a single data section is too localised for a clear improvement to be observed, even assimilating at each model integration step, as they did. This result will thus represent a useful reference for our work, even though their focus was different from ours in that their main interest was in the dynamics of the data propagation, by looking at the way in which the streamlines were modified around the data sections. Here, the principal approach is from a water budget perspective, therefore highlighting the density field role rather than that of the velocity field.

The main aims of this chapter are the following:

1. to assess the method performance at each assimilation step (e.g. how the salinity profile is re-constructed when only temperature is assimilated);

2. to analyse the model response to the new density profiles (i.e. the impact of the method on the model);

3. to assess whether the assimilation method is effective at controlling the model drift, i.e. to compare A_{ST} to Pa (because of the 'wrong' forcing the A_{ST} run would tend to diverge from the Tr run, just as the Pa run does);

4. to evaluate whether the A_{ST} run yields better results than the Pa run and/or the A_{SZ} run? (the latter being the most common way to assimilate vertical profiles of temperature).

To this end, several diagnostics tools will be adopted: section snapshots, salinity rms errors, dynamic height differences, potential vorticity on constant density surfaces and water mass budgets. The first three are used to check whether the method itself is effective (these are the tests normally employed when assessing data assimilation experiments). The rest of the tools are more useful to probe the impact of the assimilation on the model - as discussed above, in data assimilation contexts this type of analysis is not usually carried out.

6.2 A global evaluation

We start evaluating the assimilation method from a global perspective by considering the specific kinetic energy, the T rms and the S rms for the entire basin. In the

following sections we will also include local analyses.

Figure 6.1 shows the specific kinetic energy for the whole domain and for the four runs considered in our experiment (Table 5.2) relative to the 2-year period 103-104 yr. The initial kinetic energy for the two assimilation runs (A_{ST} and A_{SZ}), which is the same as that of the parallel run, is decidedly bigger (about 20%) than for the truth run. Successively, the kinetic energy of A_{ST} and A_{SZ}, which remains similar in both cases, does not vary much: the average over the assimilation period is 14.6 $\times$ 10^{-4} m^2 s^{-2} for both, hence even smaller than their starting value of 14.8 $\times$ 10^{-4} m^2 s^{-2}. On the other hand, the increase in both the Pa and Tr runs is evident (in the latter, it is especially true in the last 6 months) and their averages are 12.6 and 15.5 $\times$ 10^{-4} m^2 s^{-2}, respectively, therefore bigger than their initial values (12.3 $\times$ 10^{-4} m^2 s^{-2} for the Tr). Thus, a first conclusion that can be drawn from Fig. 6.1 is that both assimilation runs are capable of restraining or slightly reducing the kinetic energy despite having the same forcing as the parallel run. The fact that the A_{ST} and A_{SZ} behave similarly, as far as the kinetic energy is concerned, may be symptomatic of a predominance of the temperature over the salinity in controlling the density, and hence the currents, in the assimilation analyses (the temperature analyses are very similar for both runs as we will see shortly).

It is useful to remind ourselves that the five chosen sections along which data are assimilated cover only 5.5% of the entire model domain, even though the complete assimilation is carried out over almost 20% of the domain, as a consequence of the temperature spreading (see section 5.5.2). Hence, it is quite encouraging to see that the kinetic energy improvement is about 31% on average (note that this evaluation is slightly biased because the Pa and assimilation runs have the same initial conditions). In fact, a local constraint of the thermal field does not assure an error reduction in the velocity field because the density field may be: a) quite different from that of the truth run (due to salinity differences) and b) not in equilibrium with the adjacent density field at assimilation time.

The rms errors are calculated with respect to the truth run, i.e. in general terms: $X\ rms = 1/N \left\{\sum_{n=1}^{N} [X(n) - X_{Tr}(n)]^2\right\}^{1/2}$, where X is a generic field (e.g. T), X_{Tr} is the field for Tr and N is the number of grid points. The temperature rms errors are shown in Figure 6.2. They are area and depth averages, where the area average is performed over the whole model domain and the depth average is done over the

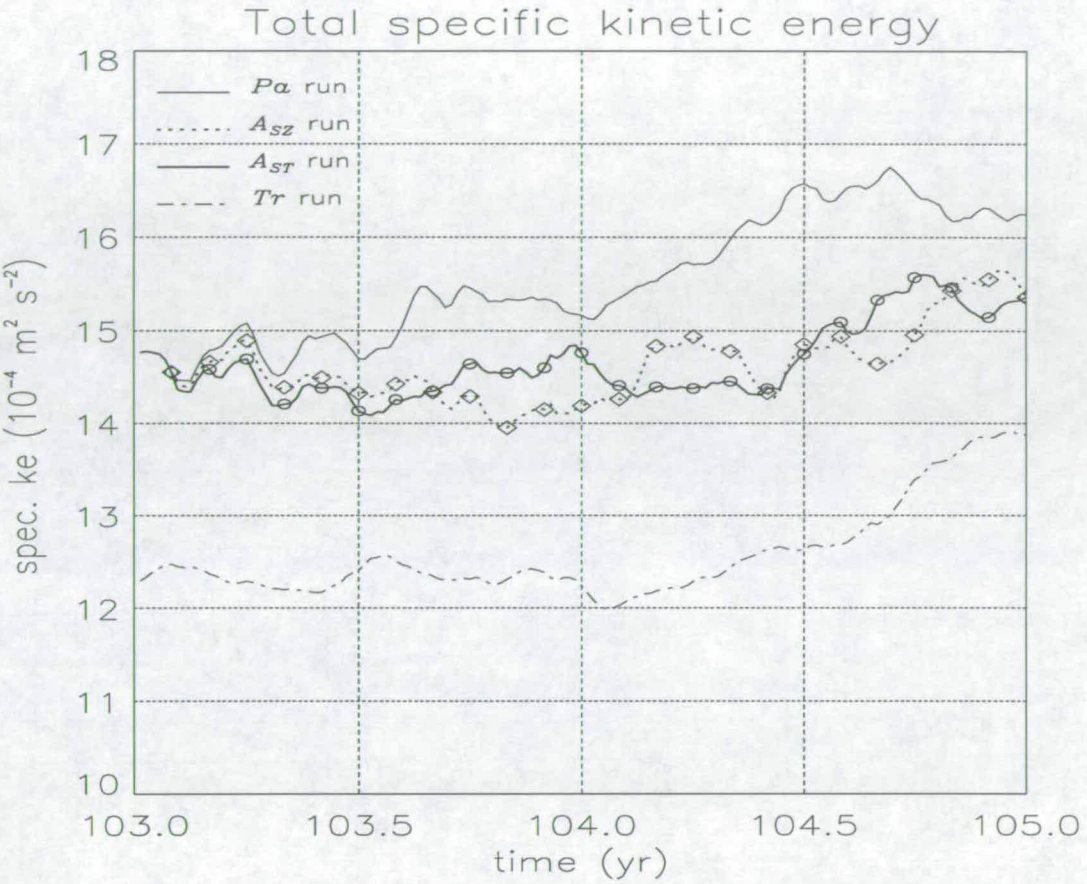


Figure 6.1: Total specific kinetic energy for the assimilation period for the four runs: Tr, Pa, A_{ST} and A_{SZ}. Circles and diamonds indicate assimilation steps.

assimilation depth (525 m). The latter average is weighted with weighs given by the thickness of each vertical level (this same weighting procedure is adopted for subsequent similar rms evaluations).

Figure 6.2 shows a distinct increasing trend for the T rms error for the parallel run: its slope is about 0.1°C yr^{-1} for the 2-year experiment, although it shows a tendency to decrease towards the end of year 104. However, here we are more interested in relative values, i.e. whether the A_{ST} is closer to the truth run than is the parallel run. Fig. 6.2 shows that, for the T rms error, this is indeed the case. In particular, both assimilation runs (A_{ST} and A_{SZ}) present only a marginal increase from their initial values and almost overlap each other, except for the last few assimilation steps when the A_{ST} errors are slightly smaller, although this does not look significant. Also, the magnitude of the error differences before and after assimilation (the Δ highlighted at the bottom of Fig. 6.2) is analogous for both assimilation runs. Of course, this similarity might

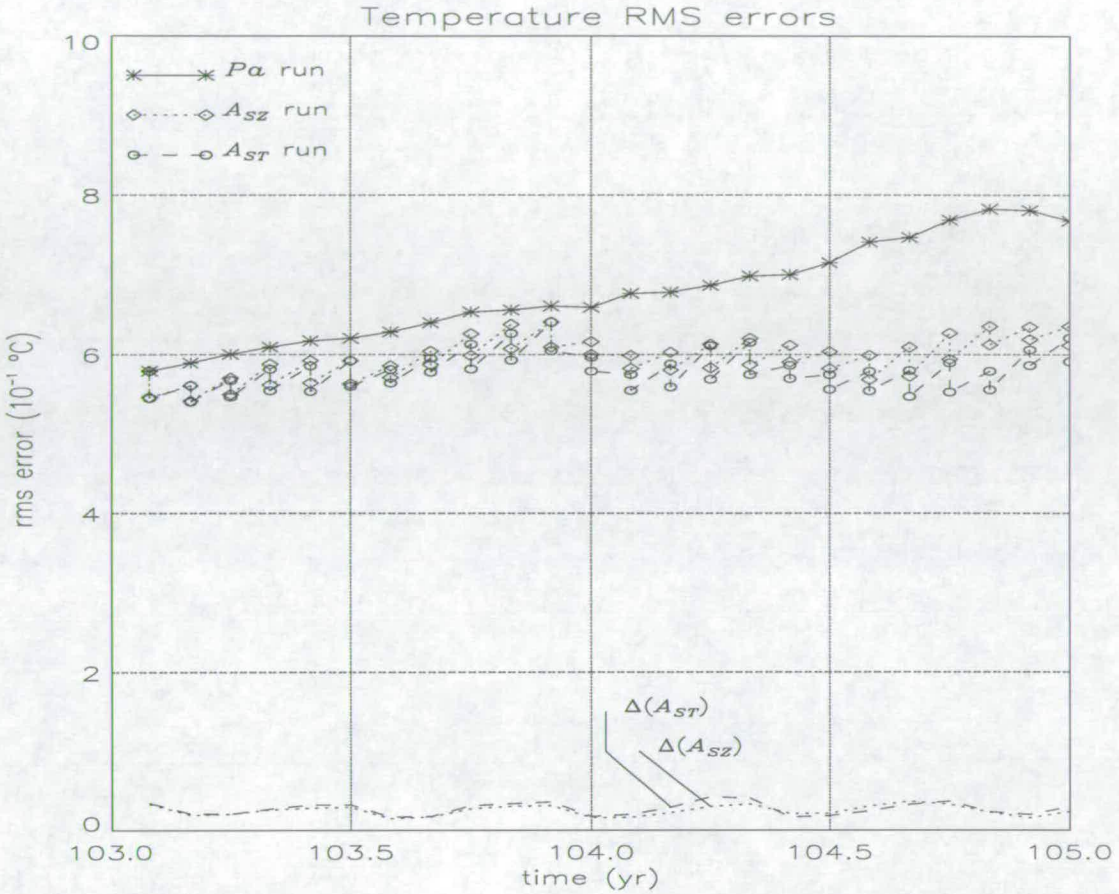


Figure 6.2: Temperature rms errors (with respect to the truth run) averaged over the whole model domain down to the assimilation depth (525 m). The depth average is weighted with the level thicknesses. Note that for the A_{ST} and A_{SZ} runs errors before and after each assimilation step are plotted and their differences (Δ (A_{ST}) and Δ (A_{SZ})) are represented at the bottom.

have been expected since both runs adopt the same spreading scheme for temperature increments (see section 5.5.2) and, more importantly, the strong surface relaxation combined with the 30-day assimilation period does not allow the two runs to diverge significantly in T.

It is interesting to note that these error differences ($\Delta(A_{ST})$ and $\Delta(A_{ST})$) clearly vary with time (note that they represent instantaneous values). They undergo a wave-like behaviour with period of roughly 10 months. Analyses of the separated T rms errors for the zonal and meridional sections indicate that this oscillation is independent of location of the section (not shown). Further, a similar period is observed in the kinetic energy for the A_{ST} and A_{SZ} runs, whereas for the truth and parallel runs such a periodicity is less manifest (cf. Fig. 6.1). Therefore, it can be deduced that these

"oscillations" are amplified by the data assimilation itself. Qualitatively, in fact, the assimilation of data can be viewed as an additional dynamical forcing, to the equations of motion, which varies both temporally and spatially.

Globally, the temperature improvement over the two-year assimilation period is almost equal to 25% (i.e. the rms reduction from the parallel run of A_{ST} or A_{SZ}, Fig. 6.2). However, this improvement appears to be dependent on the assimilation frequency for the temperature errors tend to diverge after each assimilation, as shown by the zigzagging lines. Although these zigzags are normal in sequential assimilations, the magnitude appears to be relatively large for our experiment. A possible cause for this anomalous zigzagging is that the temperature increments introduced by the assimilation are not completely retained between assimilation steps (as we will see shortly, this feature is also present in the salinity rms errors). Therefore, we studied the temporal evolution of the temperature fields along and across the assimilation sections soon after the assimilation was performed. It was noted that even where large T differences were introduced by the assimilation, they would be smoothed out with a time scale of order of a few days, thus partially decreasing the value of the input data. This is an important issue for data assimilation in general, as one would like to retain the assimilated information as much as possible, although this also depends on the model used and also on the chosen decorrelation scale (see section 5.5.2). However, no modifications to the experimental set-up are made because, as we will see, it is possible to discern the impact of the salinity scheme, which is what we are mainly interested in.

The global salinity rms errors are shown in Figure 6.3. Overall they show an encouraging trend for the A_{ST} run (it increases only by about 6% in two years) with an improvement higher than 15% with respect to the A_{SZ} run (and even bigger with respect to the Pa run) at the end of the 2-year assimilation. This is quite surprising if we consider that the S corrections introduced by the assimilation scheme are relatively small (bottom of Fig. 6.3). This suggests that these corrections, even if smoothed out as discussed above, are still kept by the model, to a certain degree.

The different dynamics between A_{ST} and A_{SZ}, induced by the different density fields, also play an important role (we will see how the water masses are considerably changed by the S persistence in the A_{SZ}). Note for instance how, at the turn of year 104, A_{ST} shows a marked improvement both in the T and S rms errors (Figs. 6.2 and

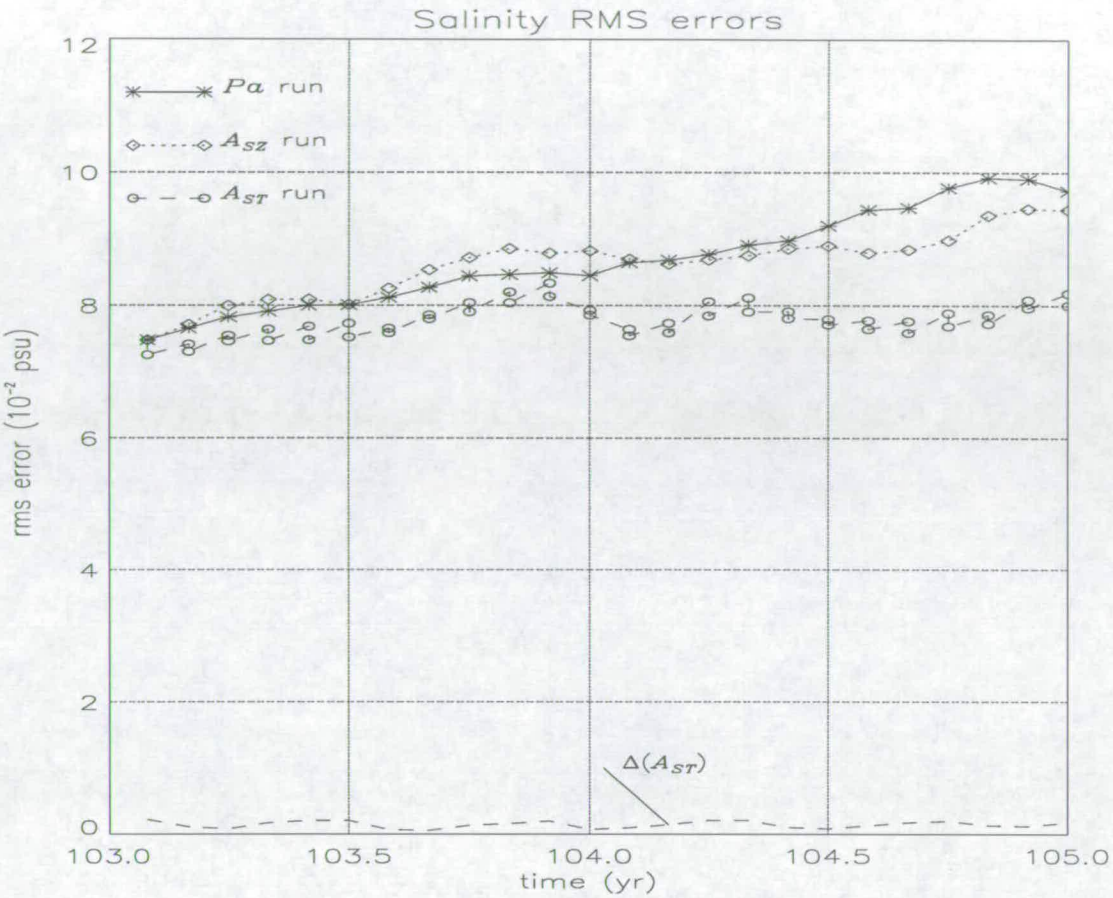


Figure 6.3: As in Fig. 6.2 for salinity rms errors. Note that for the A_{SZ} run the errors before and after assimilation coincide.

6.3). The A_{SZ} also has a similar temperature improvement (Fig. 6.2), yet, such a sign is not present in the S rms error.

As for the temperature rms errors differences (i.e. the Δ), even the corresponding values for salinity (now only for A_{ST}) show some oscillatory behaviour. The actual S rms errors also oscillate with almost the same period, but in phase opposition (i.e. bigger rms error where the improvement is larger), indicating a dynamical delay in the salinity correction. Roughly, a maximum in the T and S rms errors differences (bottom of Figs. 6.2 and 6.3) precedes the descending trend of the rms errors.

Further, the fact that the values of the S rms error for A_{ST} depart from those of A_{SZ} and Pa, even if slowly, shows another sign of the positive impact of the salinity scheme. In order to analyse in more detail the performance of the assimilation scheme, the behaviour of the model closer to the five selected sections will be considered next.

6.3 A closer look at the method performance

In this section we will assess the local impact of the assimilation scheme on the salinity, temperature and density fields. We have shown, in the previous section, some tools that enabled us to measure the distance (or error) between the A_{ST} run and the truth run, namely the specific kinetic energy and the rms errors for T and S. On a basin average, we have seen that A_{ST} performs generally better than both Pa and A_{SZ}. But what is the vertical structure of the salinity field before and after assimilation? Is the salinity rms error improved at all depths? Are we able to attain a better density field in the A_{ST} than in the A_{SZ}?

6.3.1 First assimilation step

We start addressing these questions by considering the first assimilation step along the meridional section at 48°W (i.e. one of the five chosen sections). Figure 6.4a shows the upper 1000 m of the instantaneous thermal field along this section for A_{ST} and from which diverse features can be observed. Near the equator a thermocline is present in the upper 220 m, even though it is not as tight as in reality for two reasons: the model is too diffusive and because of the vicinity of the closed boundary at the equator (cf. discussion in section 5.2). Between 15°N and 30°N, the region of highest vertical temperature gradient is situated between 400 and 700 m. Then, at around the latitude where the curl of wind stress changes sign (about 42°N), the horizontal temperature gradient is quite large. Finally, in the subpolar gyre the stratification is very weak, with temperature gradients normally smaller than 10^{-2} °C m^{-1} (i.e. smaller than the threshold chosen for the assimilation, see section 5.5.3). One could therefore predict a better method performance, for this section, between 10° and 38°N, that is where there is sufficient temperature stratification. North of this band, the non-linearities and strong mixing associated with the Gulf Stream are likely to modify the T–S properties on short time scales. Given these characteristics, we consider the analysis of this section to be a stringent test for the assimilation method. Note also that the evaluation of the first assimilation step will be model independent, if we set aside issues related to the vertical resolution.

For completeness, the salinity field along 48°W for A_{ST} at year 103 and 1 month is shown in Figure 6.4b. Features very similar to the T field appear in the S field too.

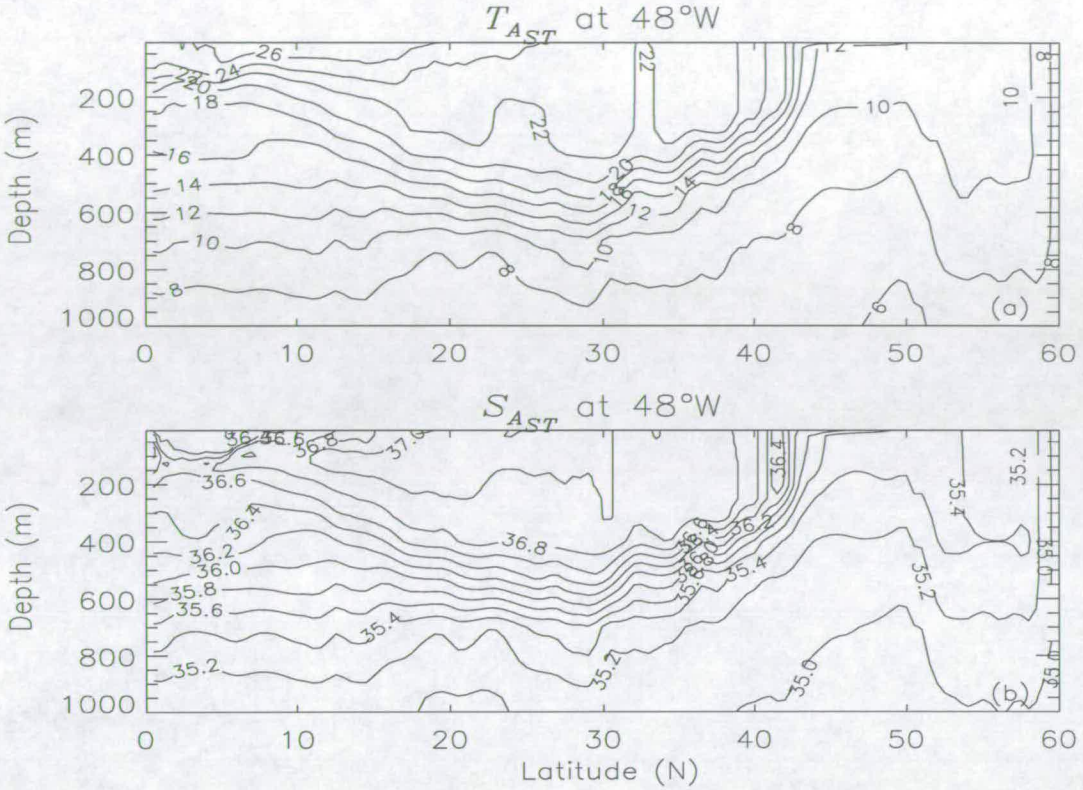


Figure 6.4: Longitudinal sections at 48°W for A_{ST} at 103 yr 1 mth before assimilation for (a) temperature and (b) salinity.

The main difference is the presence of subsurface maxima, especially at low latitudes, i.e. south of 25°N.

The temperature differences between the truth and the A_{ST} run after 3 years and 1 month (i.e. before the first assimilation step; A_{ST} is equivalent to Pa up to this time) are shown in Figure 6.5a. They are as large as ± 2.5°C between 29°N and 46°N and, as expected, they are larger in correspondence with steeper horizontal T gradients. The temperature analysis is shown in Fig. 6.5b. This is the result of applying the equation (5.6) to A_{ST}. The top 500 m confirms that the differences between Tr and A_{ST} are within ± 0.5°C. More interesting is the error reduction below the deepest assimilation level: only errors equal to about ± 0.5°C, that is noticeably smaller than those prior to assimilation, are present after the displacement is applied. For example the differences between 22° and 40°N present in Fig. 6.5a have been removed or considerably reduced (Fig. 6.5b). This is the effect of the vertical displacement presented in chapter 3 and it might imply that during the 3-year integration the thermal structure has basically undergone an adiabatic vertical movement, quite possibly preserving its

T–S relationships too (i.e. negligible salt diffusion).

The salinity differences before assimilation are shown in Fig. 6.5c, and they show a pattern similar to that of T (Fig. 6.5a), with values larger than $\pm$ 0.25 psu especially in the band 29°–46°N, but also near the surface at low latitudes. Note that, for this first assimilation step, these errors coincide with those of Tr minus A_{SZ}, therefore the following discussion can be viewed as a comparison between our scheme and the $S(z)$ persistence approach, as well as between the Tr and our scheme.

The results of the salinity scheme, in terms of the difference (or errors) between Tr and A_{ST}, are shown in Fig. 6.5d. They indicate a remarkable improvement of the S field, especially below the isothermal layer, where the T–S relationships are better preserved. Improvements as large as 0.3 psu are discernible almost everywhere and mainly between 100 m and 525 m. As expected, the assimilation scheme has little impact in the upper water column of the Gulf Stream (i.e. the top 200 m in the 38°–42°N band), where the T–S preservation time scale is short, although a noticeable, even if small, positive change is present there too. North of 52°N, the errors are unchanged as the stratification is below the chosen threshold for the assimilation scheme to get activated. Even below the deepest assimilation level, where salinity differences are solely due to the vertical displacement, errors are noticeably reduced. This would confirm the statement made above that, at depth, processes preserve T–S relationships well.

6.3.2 Temperature rms errors

Similarly to what has been done in section 6.2, we analyse now the T rms errors for the three runs: Pa, A_{ST} and A_{SZ} (Figure 6.6). This time, however, we restrict the area over which the calculation is done, as we aim to assess the impact of the assimilation method more closely. In particular, we calculate the errors along the bands given by the five sections plus one grid point either side. These bands cover about 15% of the whole model domain. We do not consider all the area influenced by the assimilation (equal to about 20%) as the increments are small outside the band considered. Note that the scales of the axis in Fig. 6.6 are the same as in Fig. 6.2.

The rms errors in Fig. 6.6 are essentially the same as those for the global average (Fig. 6.2). For the parallel run, the rms errors again increase monotonically throughout most of the 2-year integration, with a linear trend equal to about 0.16°C per year, that

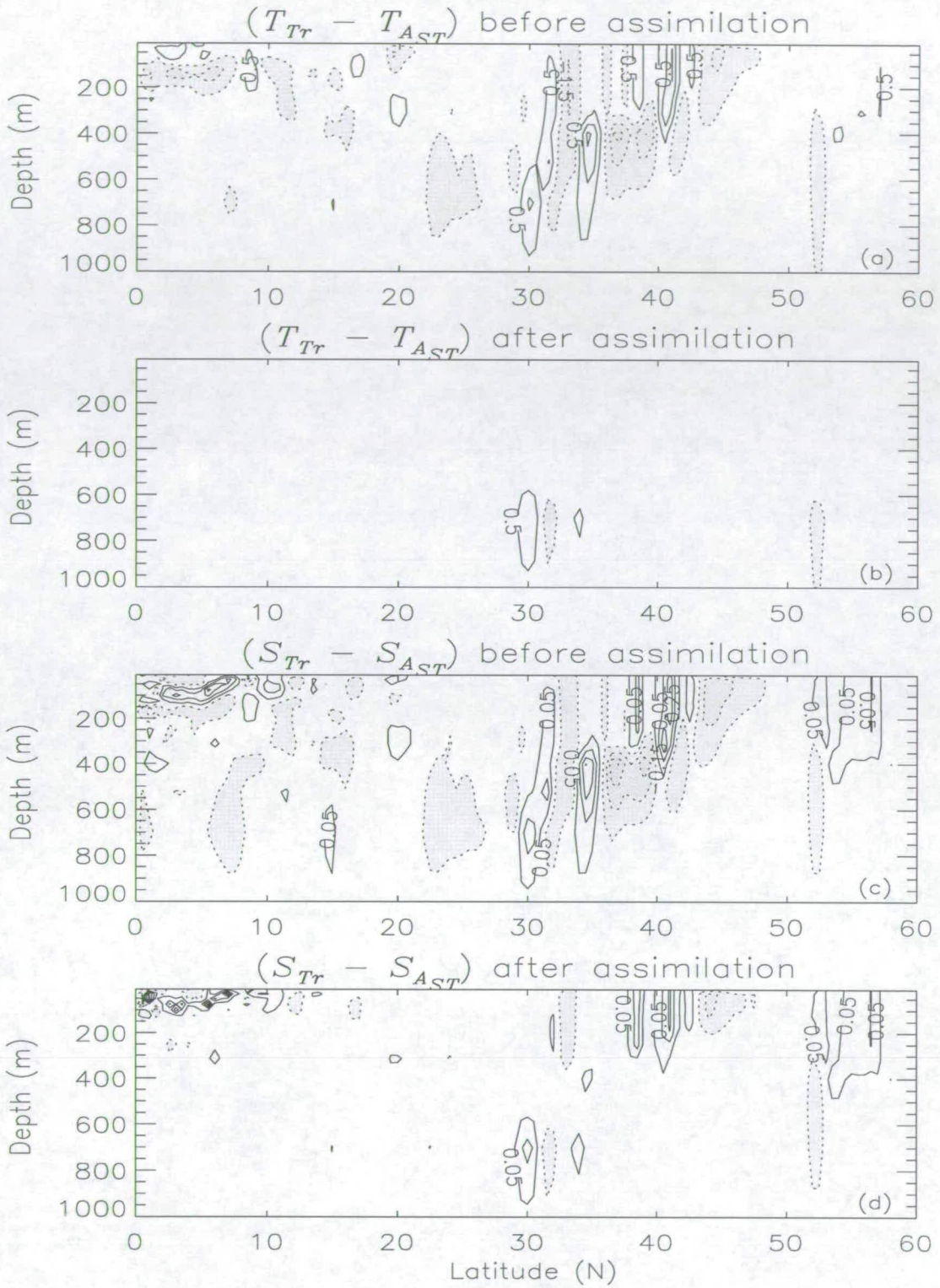


Figure 6.5: Longitudinal cross sections at 48°W. Temperature difference between Tr and A_{ST} (contour interval is 1.0°C, dashed line and shading for negative): (a) after diverging 3 yr 1 mth (i.e. A_{ST} is equivalent to Pa, up to this time step), this is the increment used by the first assimilation step; (b) after the first assimilation step. Salinity difference (contour interval is 0.1 psu): (c) before and (d) after first assimilation step.

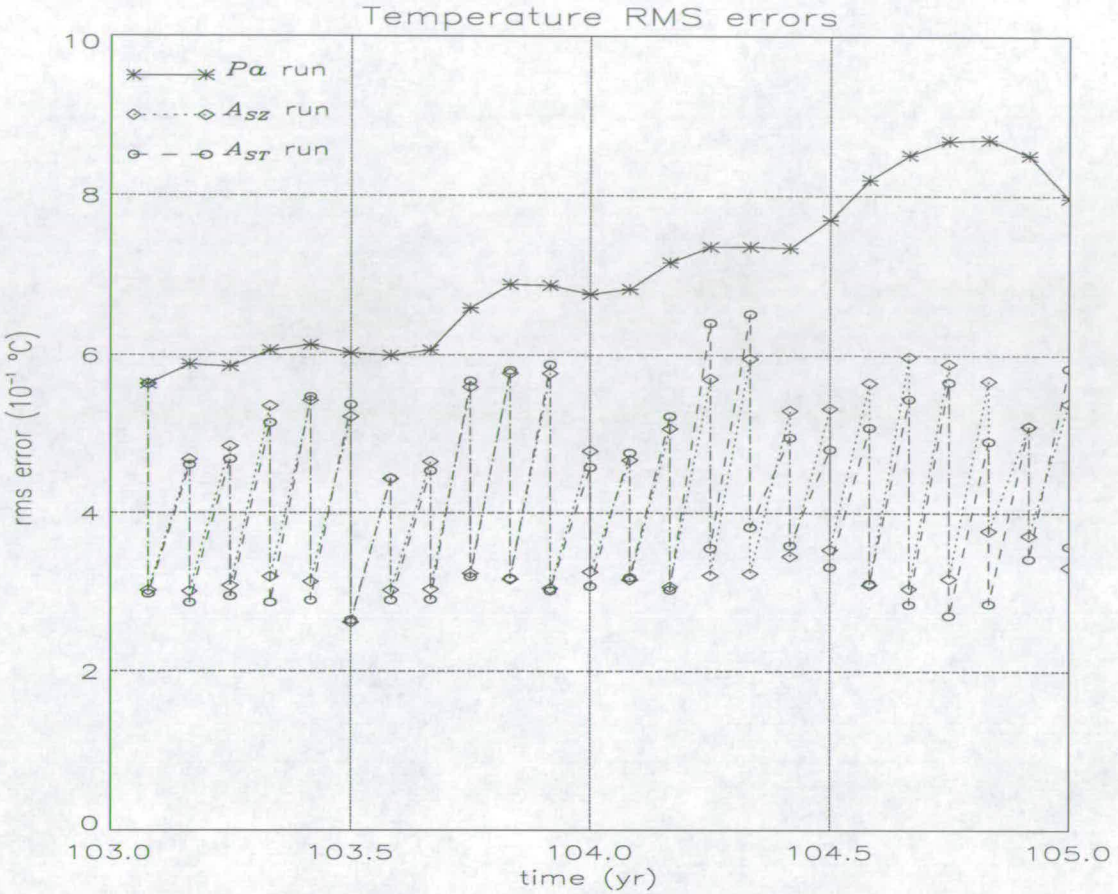


Figure 6.6: Temperature rms errors averaged over the assimilation depth (525 m) and over the grid points along and adjacent (one either side) the chosen sections (ca. 15% of the model grid points). For the A_{ST} and A_{SZ} runs the errors before each assimilation step are also plotted.

is only slightly bigger than in the global case, and about 8 times bigger than A_{ST} or A_{SZ}. Also, the rms errors for both A_{ST} and A_{SZ} are close to each other, with an error reduction at the first assimilation step equal to 0.26°C (from 0.56°C to 0.3°C), i.e. proportional to that in the global case, 0.04°C, in the ratio 100 to 15. Yet, an apparent feature of Fig. 6.6 is the pronounced behaviour of the zigzags, which are obviously more accentuated in the present case, as the local effect of the temperature analysis is now averaged over less grid points. Of course, zigzags are a normal feature in such assimilation experiments, because of advection and/or wave propagation, and in fact they are more evident in the meridional sections, and especially in the one closest to the western boundary. However, these zigzags again highlight the fact that assimilation increments are not retained by the model for long.

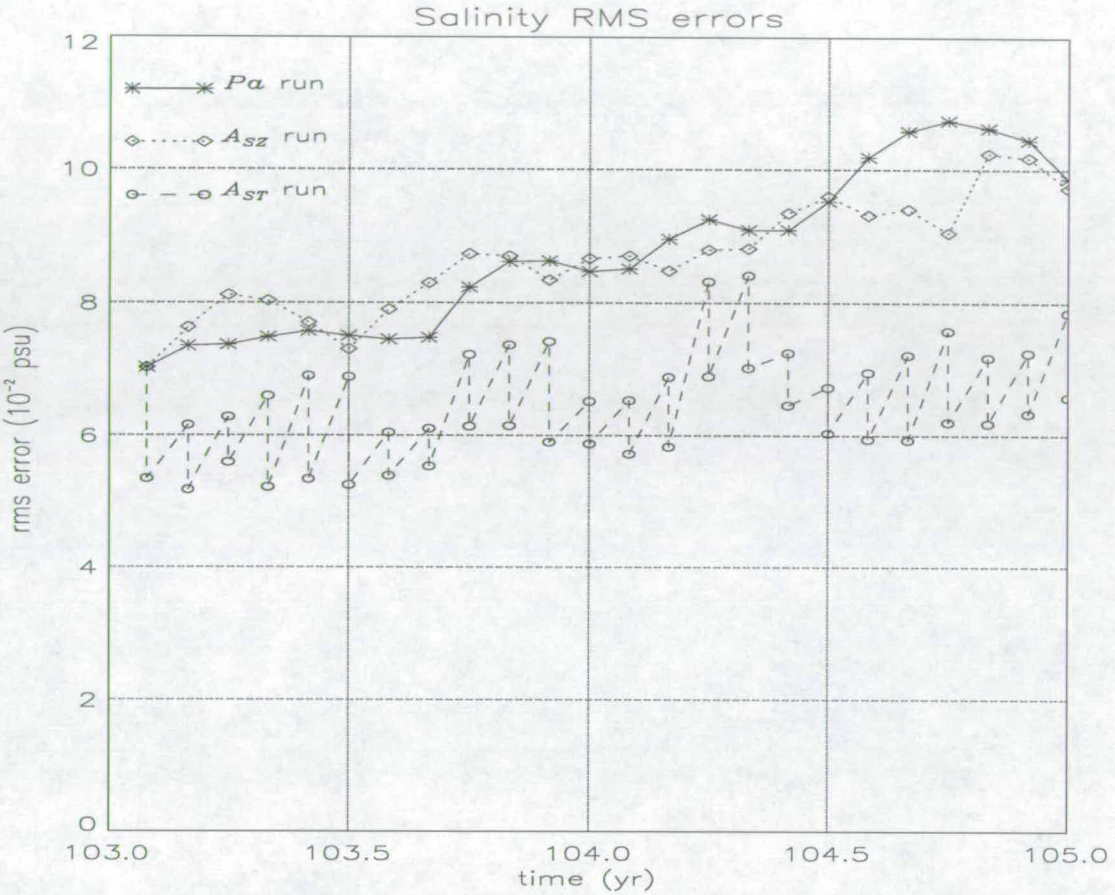


Figure 6.7: As in Fig. 6.6 but for salinity. For the A_{SZ} run, the errors before and after each assimilation step coincide.

6.3.3 Salinity rms errors

In this section we will look at the salinity rms errors as a function of both time (as done up to now, Fig. 6.7) and depth (Fig. 6.8). In both cases they are averaged over the same grid points as in the previous subsection.

The rms errors as a function of time in Fig. 6.7 show that our salinity scheme introduces a 1.7×10^{-2} psu improvement in the first assimilation step, which corresponds to an error reduction of about 24% with respect to the parallel and A_{SZ} runs. In all assimilation steps, the error reduction in A_{ST} is positive and ranges between 1.7×10^{-2} psu at the first step and 0.6×10^{-2} psu at the eighth step. Also, the rms errors in A_{ST} are always smaller than both A_{SZ} and Pa, both before and after assimilation. In particular, a linear interpolation for A_{ST} leads to an average increase of the error of 0.6×10^{-2} psu yr^{-1}, which is more than 2 times smaller than the analogous

trends for A_{SZ} and, more so, for Pa.

Another positive result comes from the comparison between this linear trend for A_{ST} and that corresponding for the global case. In fact, the latter, 0.2×10^{-2} psu yr^{-1}, is 3 times smaller than the former, which indicates that the corrections introduced with our salinity scheme are partly advected away from the five sections and, thereafter, kept by the model (the same ratio is equal to about 1.6 for both A_{SZ} and Pa). This is an important result if the assimilation is aimed at improving the ocean forecast, as it would imply that assimilation need not be performed too frequently, that is tens of days is a good choice. If one is more concerned with salinity observations though, this result shows that the salinity drift, which is more pronounced in Pa and A_{SZ}, is contained well. Therefore, generalising, if the initial salinity field for an assimilation run is close to reality, then it would remain considerably closer than preserving $S(z)$.

In order to gain more insights into the error distribution, we now remove a constraint in the averaging procedure and look at the depth dependency of the salinity rms errors in Figure 6.8 for three selected assimilation steps (1, 12, and 24). The A_{ST} rms errors are compared only to the A_{SZ} ones, so as to verify whether our method performs better than persistence.

In the upper water column, about 100 m, it can be seen that the rms errors for the two runs are similar to each other, although A_{ST} is at times worse than A_{SZ} as for instance at the first time step at 50 m depth. In particular, the rms values for A_{ST} are higher than their corresponding depth averages (step 1: 5.3×10^{-2}, step 12: 5.9×10^{-2}, step 24: 6.6×10^{-2} psu, cf. Fig. 6.7). Note, that the lowest values are attained at the first model vertical level (this holds true for A_{SZ} as well). This is because all the runs have the same T and S restoring forces at the surface and their relaxation time is relatively short (30 days).

Below the top 100 m, the assimilation scheme produces analyses which are remarkably better than $S(z)$ persistence, with rms magnitudes that generally diminish with depth, down to the assimilation level of 525 m. The fact that errors decrease with depth is something that could have been expected, since T–S relationships tends to be better preserved as one moves downward in the water column (e.g. Emery and Dewar, 1982). Still, it is encouraging to be able to produce such a marked difference with respect to A_{SZ}.

The plot does not show the corresponding rms errors for Pa. Suffice to say that they

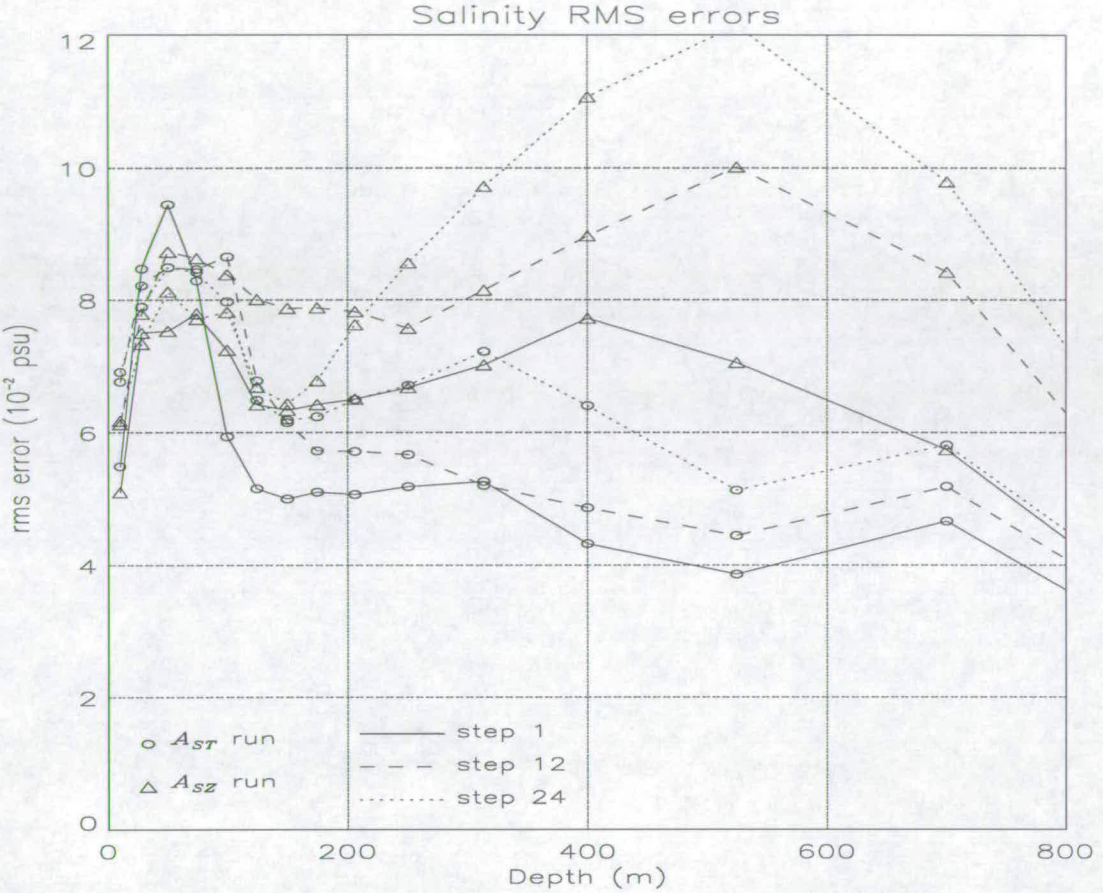


Figure 6.8: Salinity rms errors for the A_{ST} and the A_{SZ} run, averaged over the grid points along and adjacent (one either side) the chosen sections, as a function of depth for three assimilation steps (1, 12 and 24). In order to keep the same vertical scale, one point (12.1×10^{-2} psu) falls outside the range.

are normally larger than A_{SZ} down to 400 m but vice-versa below it, the difference being more pronounced between 400 and 525 m (see Table 6.1 for errors at 525 m). In fact, A_{SZ} rms errors are quite large below 400 m and this is due to the fact that the $S(z)$ persistence induces spuriously enhanced vertical mixing. In other terms, the combination of the analysed temperature with the background salinity makes the water column (nearly) unstable therefore inducing an unphysical mixing (see section 3.3.1). Because of the structure of the density field, which is less stratified below 600 m (cf. Fig. 5.7), this effect is more pronounced only down to about 800 m. We will discuss in more detail this effect in chapter 7, where the assimilation into a global model is discussed.

Note that in Fig. 6.8 the depth goes intentionally down below the deepest assimila-

	S rms at **525 m** (10^{-2} psu)			S rms at **700 m** (10^{-2} psu)		
Experiment	step 1	step 12	step 24	step 1	step 12	step 24
A_{ST}	3.9	4.3	5.1	4.7	5.2	5.8
A_{ST} no v.d.	3.9	4.2	5.2	5.7	7.1	7.6
A_{SZ}	7.0	10.0	12.1	5.7	8.4	9.8
Pa	7.0	9.8	11.0	5.7	8.1	9.0

Table 6.1: Salinity rms errors at 525 m and 700 m at assimilation steps 1, 12 and 24 for A_{ST}, A_{ST} with no vertical displacement (v.d.), A_{SZ}, and Pa.

tion level, namely to 800 m: this is done to highlight the effect of the vertical displacement. In fact, the rms errors below 525 m, and especially at the next level (700 m), are considerably smaller than in an experiment where no displacement was performed (i.e. as for A_{ST} but with no displacement). In particular, in this latter experiment the rms error at 700 m is at least 20% larger than for A_{ST} (Table 6.1). At the first assimilation step, for instance, the two rms errors are 5.7×10^{-2} and 4.7×10^{-2} psu, respectively, and their difference increases thereafter up to nearly 2.0×10^{-2} psu. At the same time, though, the experiment with no displacement yields better rms errors than A_{SZ}. This is because the T–S preservation prevents the enhanced mixing from happening at depths where assimilation is performed (i.e. down to 525 m), which are instead present in A_{SZ}. These effects are such that the rms errors at 700 m for A_{SZ} are notably worse than Pa too.

Another remarkable feature for A_{ST} in Fig. 6.8 is that, as already noted for Fig. 6.7, rms errors do not vary much with time: only up to about 2.1×10^{-2} psu at 400 m between step 1 and step 24, compared to 5.1×10^{-2} psu at 525 m, which is the maximum excursion for A_{SZ}. On the other hand, the trend of the rms errors for A_{SZ} steadily increase with time, which also confirms what is seen in Fig. 6.7. Again, this is the reflection of the fact that once the assimilation has started, it is capable of restoring the water mass properties that would otherwise drift away, as is the case for A_{SZ}.

6.3.4 Dynamic height rms errors

To complete the analysis of the rms errors, we consider now the 0–525-m dynamic height averaged along and adjacent to (one either side) the chosen sections (Fig. 6.9). Because of the way dynamic height is defined, we expect to see close similarities between Fig. 6.9 and the analogous for temperature and salinity (Figs. 6.6 and 6.7).

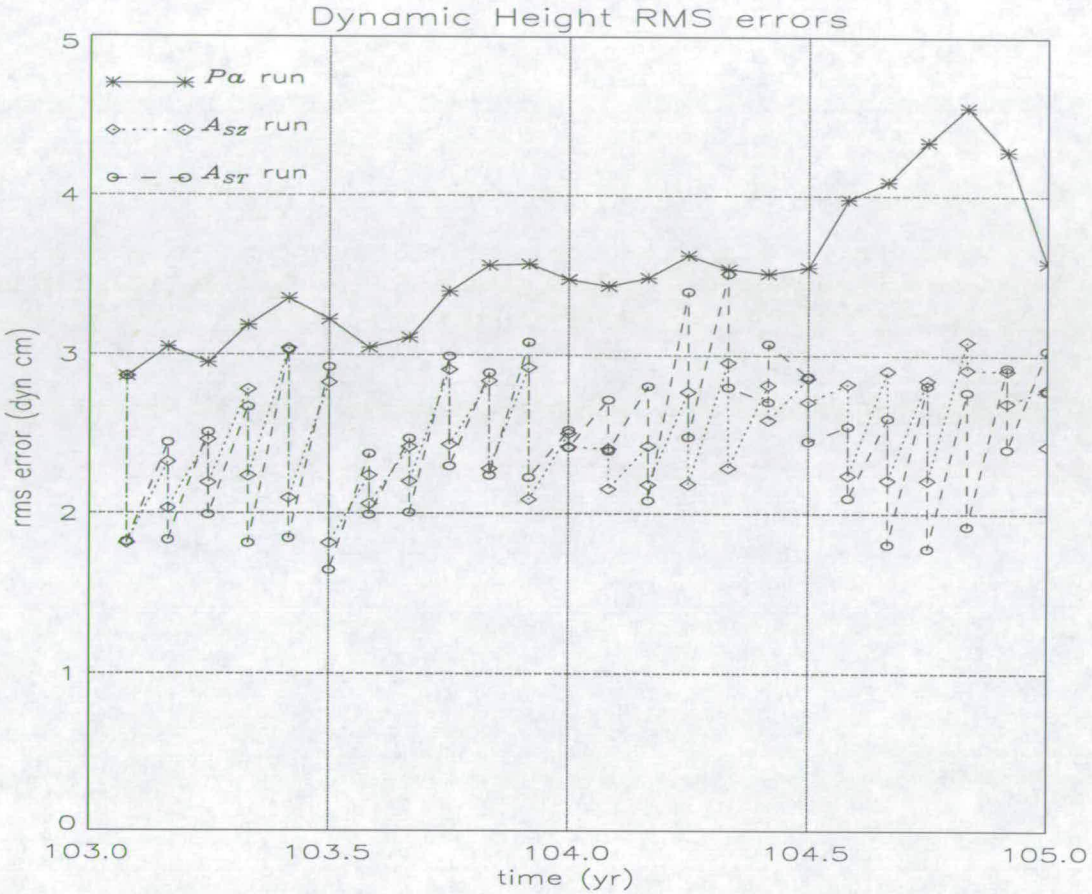


Figure 6.9: 0–525-m dynamic height rms errors averaged over the grid points along and adjacent (one either side) the chosen sections. For A_{ST} and A_{SZ} the errors before each assimilation step are also plotted.

In particular, such a comparison will also give us some indication about the relative influence weights of T and S on the dynamic height.

The rms errors for the parallel run reflect the behaviour of their corresponding T and S rms errors and have an increasing trend of about 0.6 dyn cm per year. On the other hand, the rms errors for A_{ST} and A_{SZ}, after assimilation, have smaller increase rates, equal to about 0.1 and 0.2 dyn cm per year, respectively.

The values of the rms errors for A_{ST} and A_{SZ} are very close to each other, both before and after assimilation, which seems to suggest that the role of the temperature generally prevails that of salinity in the dynamic height (besides, the same assertion was made from the analysis of the specific kinetic energy, Fig. 6.1). If we consider that a ΔT= -1°C or a ΔS= 0.25 psu yield the same density variation (section 2.1), we can have an estimate of the predominance of T from Figs. 6.5a and c. In fact, this

figure shows that for each degree of temperature variation the corresponding salinity variation is a little more than 0.1 psu, that is the temperature bears almost twice as much weight as salinity.

Large differences between before and after assimilation are present also for the dynamic height rms errors, both for A_{ST} and A_{SZ} (the zigzags). In particular, for A_{ST}, differences are as large as 1.3 dyn cm (step 6), and the rms errors after assimilation are often smaller than those for A_{SZ}. There are six cases where the opposite is true, that is at steps 11, 13, 15, 16, 17 and 24. Amongst these, step 17 represents a pathological case in that the assimilation worsen the rms error for A_{ST} by about 0.37 dyn cm. We investigated this behaviour in more detail and found that the major contribution to this worsening comes mostly from salinity in the top 100 m of the grid points adjacent to the sections (the effect is much weaker for the grid points along the sections), and especially those for the meridional section close to the western boundary and near the Gulf Stream region (between 30° and 45°N). This is because the way in which the temperature spreading is done is not optimal for regions with large horizontal temperature gradients such as the Gulf Stream. Hence, the salinity analysis is affected by the temperature analysis. To have a rough estimate, a ΔS= 0.1 psu over a depth of 100 m reflects on a dynamic height variation of about 0.72 dyn cm. The T and S errors that cause such a dynamic height difference are however hidden in Figs. 6.6 and 6.7 (the corresponding errors do not worsen) due to the averaging procedure.

6.3.5 Dynamic height

In order to understand better what the spatial distribution of errors is, we consider the dynamic height as a function of the geographical location. We have chosen this quantity for, as it has already been remarked, the dynamic height is closely related to the sea surface height, which is a relatively abundant observational datum. Dynamic height constitutes therefore a good way of validating assimilation experiments such as ours.

The left panels of Figure 6.10 show the 0–525-m dynamic height difference between the A_{ST} run and the truth run for three - after - assimilation steps (1, 12 and 24: top, middle and bottom panels, respectively). For comparison, the analogous plots for the A_{SZ} run are presented on the right panels. At the first assimilation step (Fig. 6.10, top panels), the positive impact of the assimilation along the five sections is evident.

In fact, differences between Tr and either A_{ST} or A_{SZ} are very small (they are mostly white), except in places like the branch of the Gulf Stream near the western boundary for which errors reach large values (about 5 dyn cm along the section). Because the two top panels are very close to each other, it is difficult to discern what impact the salinity method has. Hence, for the first assimilation step, it appears as though we have the confirmation that the temperature plays a major role in the assimilation procedure, that is the salinity is a second order correction to the density field. In order to draw this conclusion more firmly, we also calculated a map like that in Fig. 6.10 but for the 0–100-m dynamic height (not shown) so as to check the influence of the vertical structure of salinity. This is because we have seen in Fig. 6.8 that even at the first assimilation step A_{ST} is generally worse than A_{SZ} in the top 100 m whereas there is a marked reduction of the salinity rms below 100 m in A_{ST} with respect to A_{SZ}. However, the 0–100-m dynamic height difference between the truth run and the assimilation runs did not show any substantial difference between A_{ST} and A_{SZ}.

After 12 assimilation steps (middle panels), some differences between Tr-A_{ST} and Tr-A_{SZ} have developed, manifestly also away from the sections, although it is difficult to spot significant differences. Perhaps more evident is the improvement in A_{ST}, with respect to A_{SZ}, in the box (55°–45°W, 35°–45°N). Otherwise the differences are rather marginal. At the end of the assimilation experiment (i.e. the 24th assimilation steps, Fig. 6.10, bottom panels) the positive impact of the salinity scheme is generally more clear for example downstream of the Gulf Stream, in the region between 45°–20°W, and north of 30°N. Yet the results for A_{ST} are occasionally worse than for A_{SZ}, as for instance in the portion of the sub-tropical gyre close to the land mass (accidentally for this assimilation step the dynamic height rms error for A_{ST} is notably larger than that for A_{SZ}, as shown in Fig. 6.9).

The large dynamic height errors present in both assimilation runs across the 48°W section between 30° and 45°N are difficult to reduce through data assimilation because this is a very energetic area and also because of the numerical problems caused by the vicinity to the continental shelf, as hinted at in section 5.5.3.

6.3.6 Last assimilation step

We examine now the performance of the last assimilation step along the same section (48°W), considered for the first assimilation step in section 6.3.1. Figure 6.11 shows the

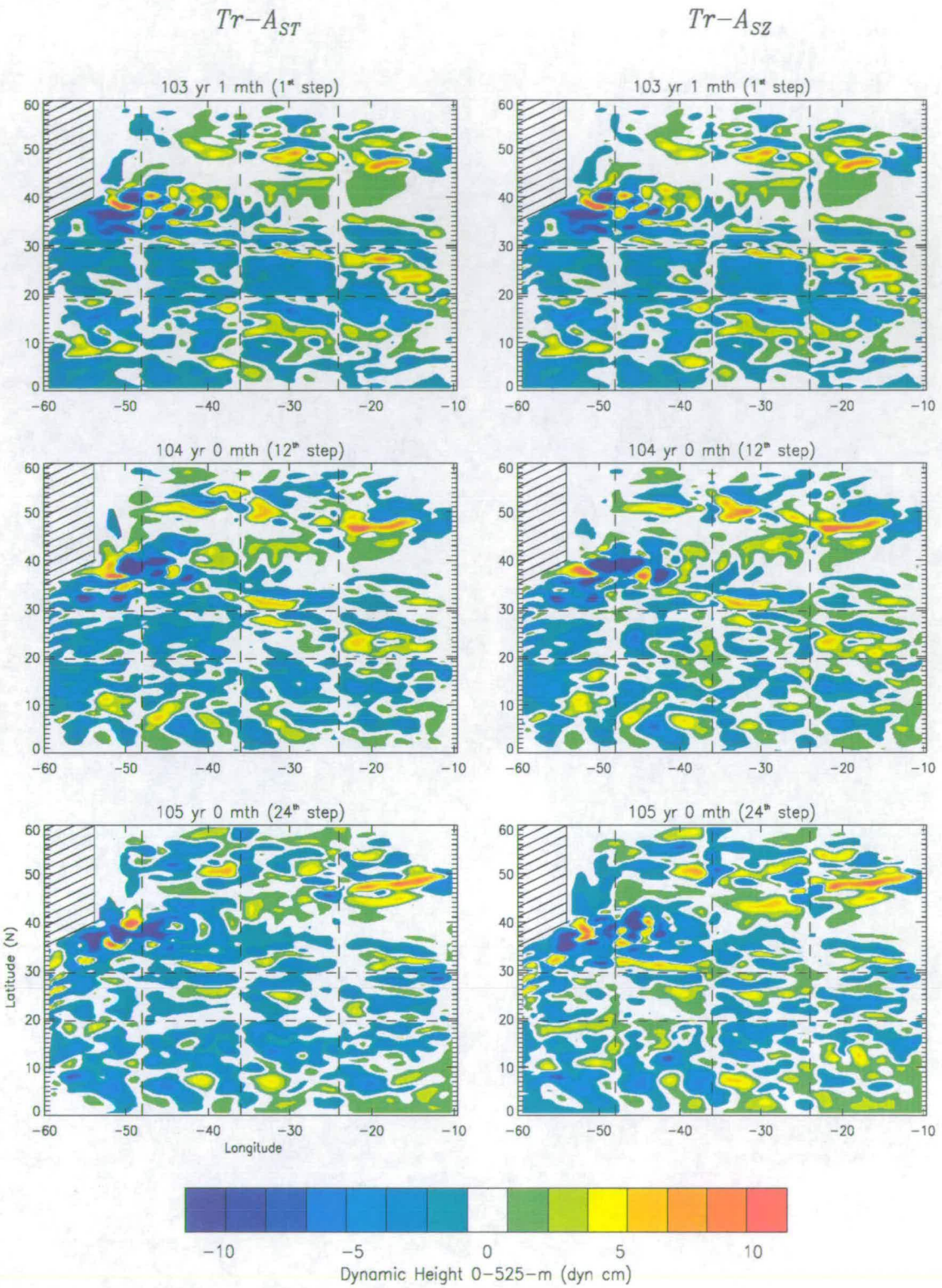


Figure 6.10: 0–525-m dynamic height differences between the truth run and A_{ST} (left) and truth run and A_{SZ} (right), at three assimilation steps (1, 12 and 24).

temperature and salinity differences between Tr and A_{ST} along 48°W before and after the last assimilation, as in Fig. 6.5 but with larger contour intervals: 1.5°C instead of 1°C and 0.2 psu instead of 0.1 psu.

The main temperature differences before the assimilation are between 35° and 42°N, with a peak of more than 6.75°C (Fig. 6.11a). These differences are almost eliminated by the temperature spreading procedure, even though a confined 0.75°C is still present because of the large horizontal temperature gradients (Fig. 6.11b). The pattern of the salinity differences before the assimilation reflects that of the temperature, with a peak of more than 0.9 psu corresponding to the maximum T difference (Fig. 6.11c). From Fig. 6.11d we can see that the salinity scheme generally reduces the differences between Tr and A_{ST} in this last assimilation step too, even if during the 2 year integration the T–S relationships are further modified both by the action of the systematic error given by the stronger wind stress and also by the data assimilation itself, which, inevitably, introduces errors. The magnitude of these errors will be discussed in section 6.5, where the assimilation is analysed in terms of water mass properties.

For comparison, we also show the salinity differences at the end of the assimilation experiments between truth and parallel (Fig. 6.12a) and truth and A_{SZ} (Fig. 6.12b). For the parallel run this is clearly the salinity error after 5 years of divergence between the truth and the parallel runs, which compared to that after 3 years (Fig. 6.5c, though the contour interval is doubled here) is generally increased, though only moderately. Fig. 6.12b shows that the salinity field for A_{SZ} is worse than that for A_{ST}, compared to Tr (see the large areas in the range 10°–25°N and cf. Fig. 6.11d), except in the Gulf Stream region (37°–42°N).

6.4 How is the velocity field modified?

In this section we will show some features of the velocity field so as to appreciate, mostly qualitatively, firstly how the salinity scheme affects the upper water column (section 6.4.1) and secondly to check the effect of the vertical displacement part of the assimilation scheme on the abyssal circulation (section 6.4.2). In both sub-sections we will consider temporal averages of the velocity field: these are calculated like the T and S fields in Fig. 5.6.

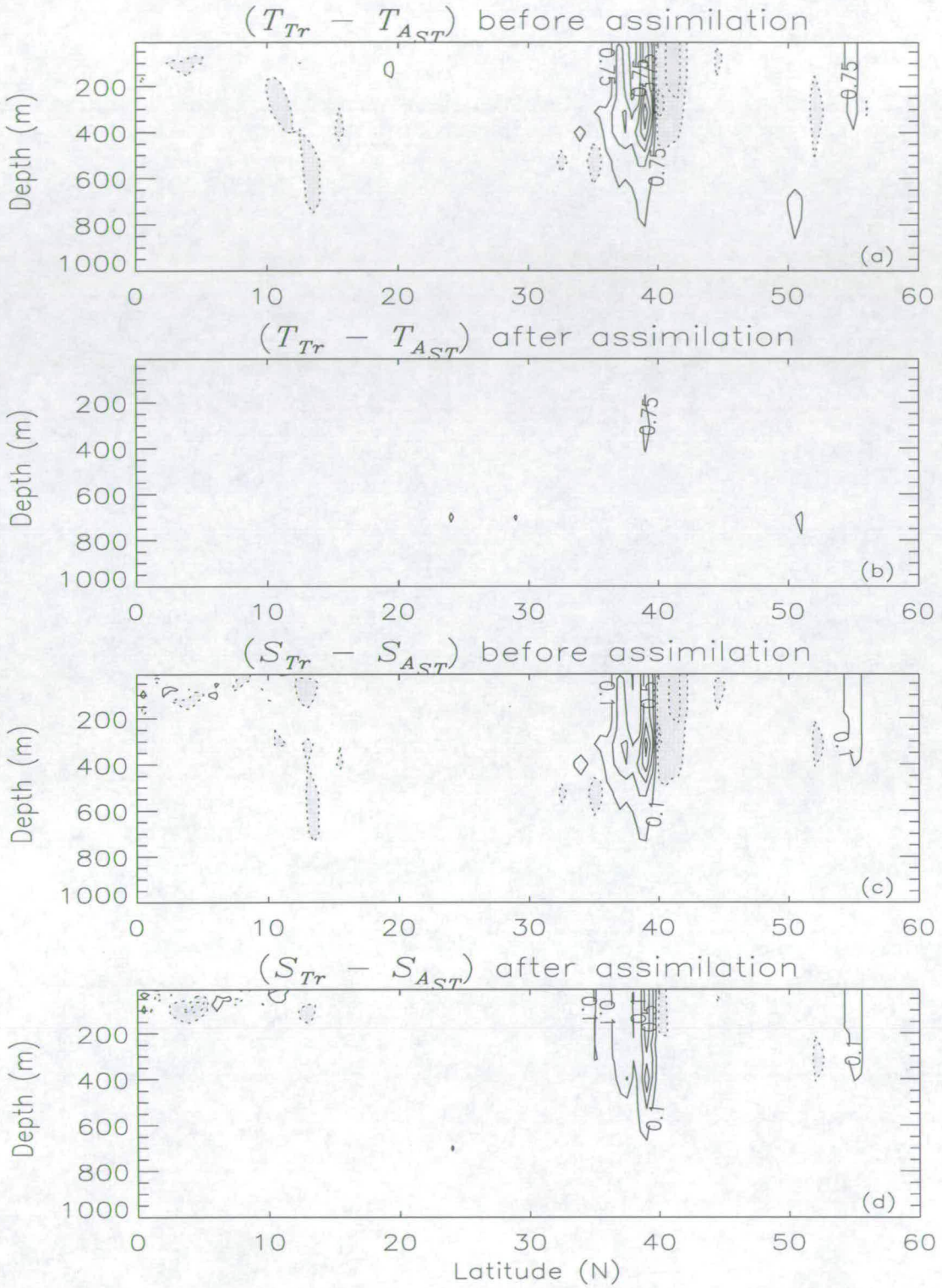


Figure 6.11: Longitudinal cross sections at 48°W at the end of year 104. Temperature difference between truth and A_{ST} runs (contour interval is 1.5°C, dashed line for negative): (a) before and (b) after the last assimilation step. (c) and (d) corresponding salinity difference (contour interval is 0.2 psu).

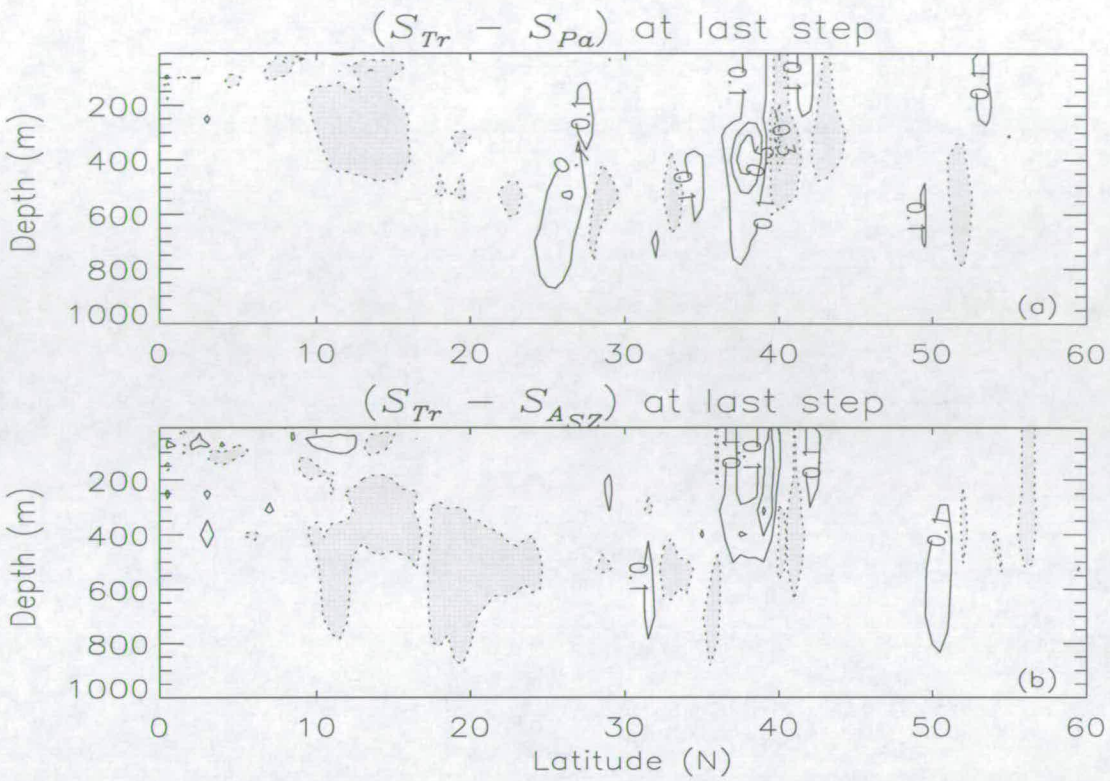


Figure 6.12: Longitudinal cross sections at 48°W at the end of year 104. Salinity difference between truth and (a) parallel and (b) A_{SZ} (contour interval is 0.2 psu).

6.4.1 Zonal velocity

For the first case, we consider the mean zonal velocity, averaged over the whole assimilation experiment period, along 42°W, Fig. 6.13. Since this section is located between the two assimilation sections 48°W and 36°W, it can be considered as showing the effects of the data assimilation from the 48°W section for the positive, or eastward, velocity and from the 36°W section for the negative, or westward, velocity. In Figure 6.13 this mean zonal velocity is shown for the four runs: Tr, Pa, A_{ST} and A_{SZ} (from top to bottom). Note that, for clarity of presentation, the band 0°– 10°N has been omitted, as there the representation of the circulation is not very realistic given the vicinity of the southern closed boundary. The comparison between Tr and Pa (Fig. 6.13a-b) shows that the parallel run has generally higher absolute values than the truth run, especially near the surface, even though the differences are not very marked. For instance, the eastward currents at around 44°N and in the 25°–28°N band are more intense in Pa. Also, in correspondence of the Gulf Stream region, i.e. between 35° and 45°N, i.e. the region where the two main gyres merge, the zonal velocity is slightly more intense and

certainly more spread in Pa. One place where the opposite is true, that is where the westward current is notably reduced in Pa compared to Tr, is at around 32°N. On the whole, however, the larger velocity values yield a more energetic circulation for Pa, which agrees with the global evaluation of the kinetic energy in Fig. 6.1.

For the assimilation runs, the analogous plots (Fig. 6.13c-d, for A_{ST} and A_{SZ}, respectively) show that both are generally closer to Tr than Pa, as for example the eastward current between 33° and 49°N (which have values closer to Tr even near the surface), or the eastward current between 25° and 28°N, as well as the westward current between 20° and 25°N. Localised exceptions are present, as in the band 28°–32°N, where Pa is a bit closer to Tr than either of the assimilation runs.

It is more difficult to determine which of the two assimilation runs performs better. In fact, although A_{ST} is somewhat closer to Tr than A_{SZ} between 28° and 49°N, A_{SZ} is more similar to Tr between 16° and 25°N. Therefore this zonal velocity analysis, though partial, is a further confirmation that whilst temperature analyses have a first-order effect for the circulation, the salinity analyses are second-order.

6.4.2 Abyssal circulation

Since in our assimilation scheme no constraint to the way the bottom pressure can change with assimilation is applied, spurious bottom pressure gradients might be introduced, which in turn may give rise to spurious bottom currents. In particular, we recall that our assimilation scheme consists of both a vertical displacement of the isopycnals below the deepest assimilation levels, and the T–S preservation for the whole water column. Therefore, the bottom pressure could vary either because of the vertical displacement or the insertion of the analysed temperature and salinity profiles. The common assumption in this case would be to impose a zero bottom pressure change, e.g. Cooper and Haines (1996). Yet, there is no compelling reason for doing this in our case, as i) our scheme, unlike for example statistical approaches, tries to reproduce the physical processes that can modify the water column as well as possible and therefore this can be a way to estimate how the bottom circulation should change (although the method by Cooper and Haines, 1996 is physical too, the no change in bottom pressure is imposed there as a pre-requisite), and ii) there is no firm evidence that the change in bottom pressure should be exactly zero, although a change, such as that imposed in our assimilation, is in general not realistic as we do not control or constrain it. A pos-

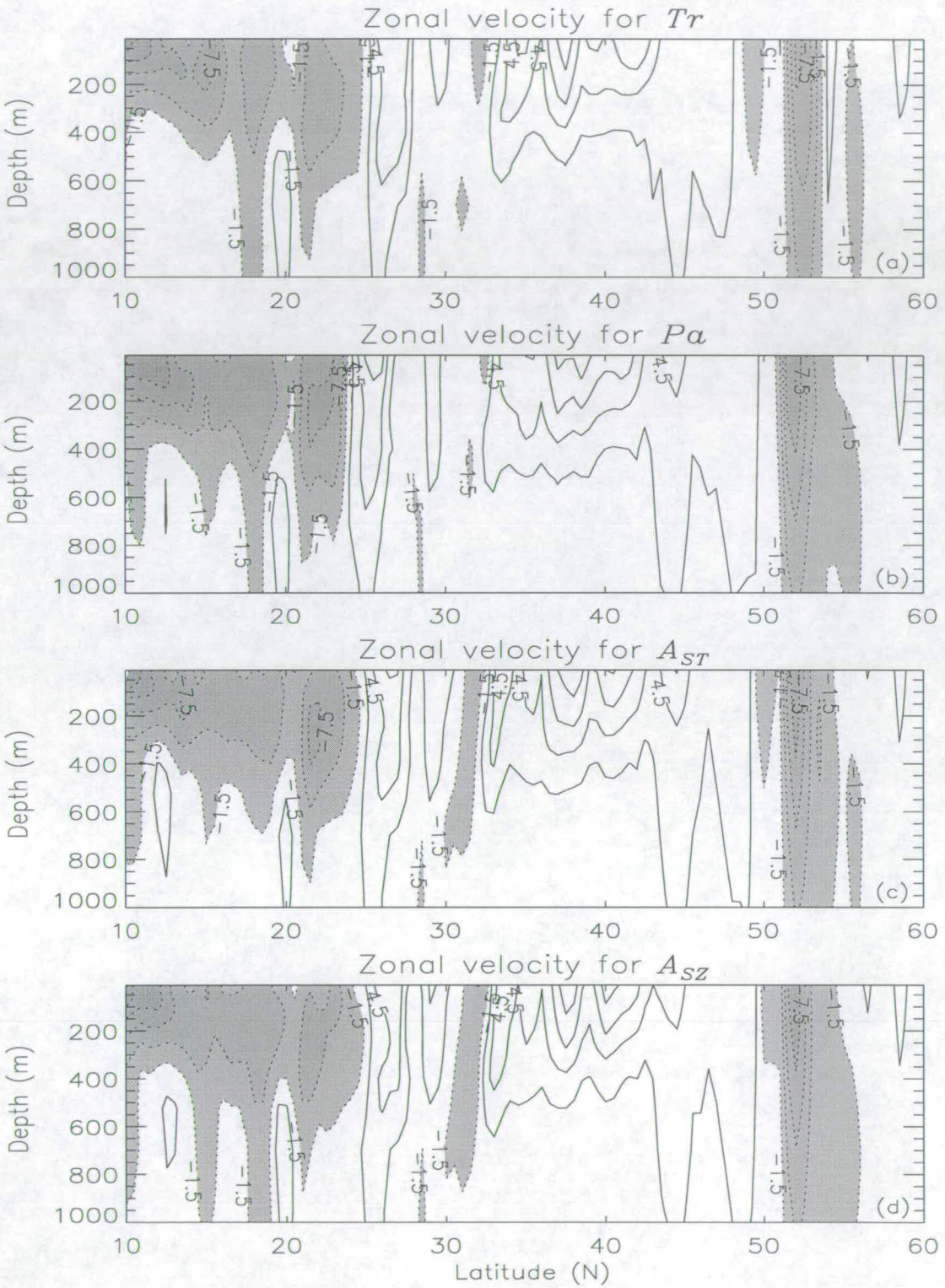


Figure 6.13: Zonal velocity along 42°W averaged over the two-year assimilation integration for (a) Tr, (b) Pa, (c) A_{ST} and (d) A_{SZ} (contour interval is 3 cm·s^{-1}, dotted line and shading for negative). Note that the latitudinal band 0°– 10°N has been omitted.

teriori, if we realised that this imposed change in bottom pressure caused unrealistic deep circulation modifications, we could add a further constraint to the assimilation scheme (as we will shortly see, in the present experiment it is more difficult to discern this effect as the observations are taken from the model itself). Besides, such a constraint could be useful in supplying further information on the salinity in the upper water column, i.e. on the weight of the upper water column. At this stage this is pure speculation as no tests have been made, but it is a possibility that could be explored. For instance, still speculating, one could find that there is some correlation between the amount of dense water mass which is to be inserted at each assimilation step, as a consequence to the lifting of the isopycnals, and the weight of the upper water column.

In order to check how the deep circulation behaves, we show in Figure 6.14 the velocity field at the depth of 3425 m, which corresponds to model level 21, averaged over the two-year assimilation integration. Strictly, level 23 (i.e. the deepest level) should be considered but, given the rough topography, we would observe the effect of the vertical displacement only for a limited number of grid points. We should also note that even A_{SZ} suffers from the problem of possible spurious bottom pressure changes induced by the modifications in the upper water column due to the assimilation.

Figure 6.14a shows that the circulation at 3425 m for Tr is mainly concentrated in two regions, between 18° and 32°N, corresponding to the sub-tropical gyre, and north of 48°N, corresponding to the subpolar gyre. In particular, in the former region the circulation is organised in small gyres, whereas in the northern region a westward current is predominant. A similar structure is present for the other three runs: Pa (Fig. 6.14b), A_{ST} (Fig. 6.14c) and A_{SZ} (Fig. 6.14d). It should be observed, though, that part of this circulation is determined by the topography, hence it is bound to be similar in all four runs.

In the parallel run, the circulation in the subpolar region is strengthened with respect to Tr, with a stronger and more defined westward jet. In the sub-tropical region, instead, differences are less definite, although the truth run appears to have a generally stronger circulation there, as for instance, in the anti-cyclonic current, dominated by a northward jet, by the shelf and centred at 22°N or, though less so, in the cyclonic structure between 50° and 35°W. Altogether, however, these differences do not seem to be very significant.

Even the assimilation runs, which looks very close to each other, show basically the

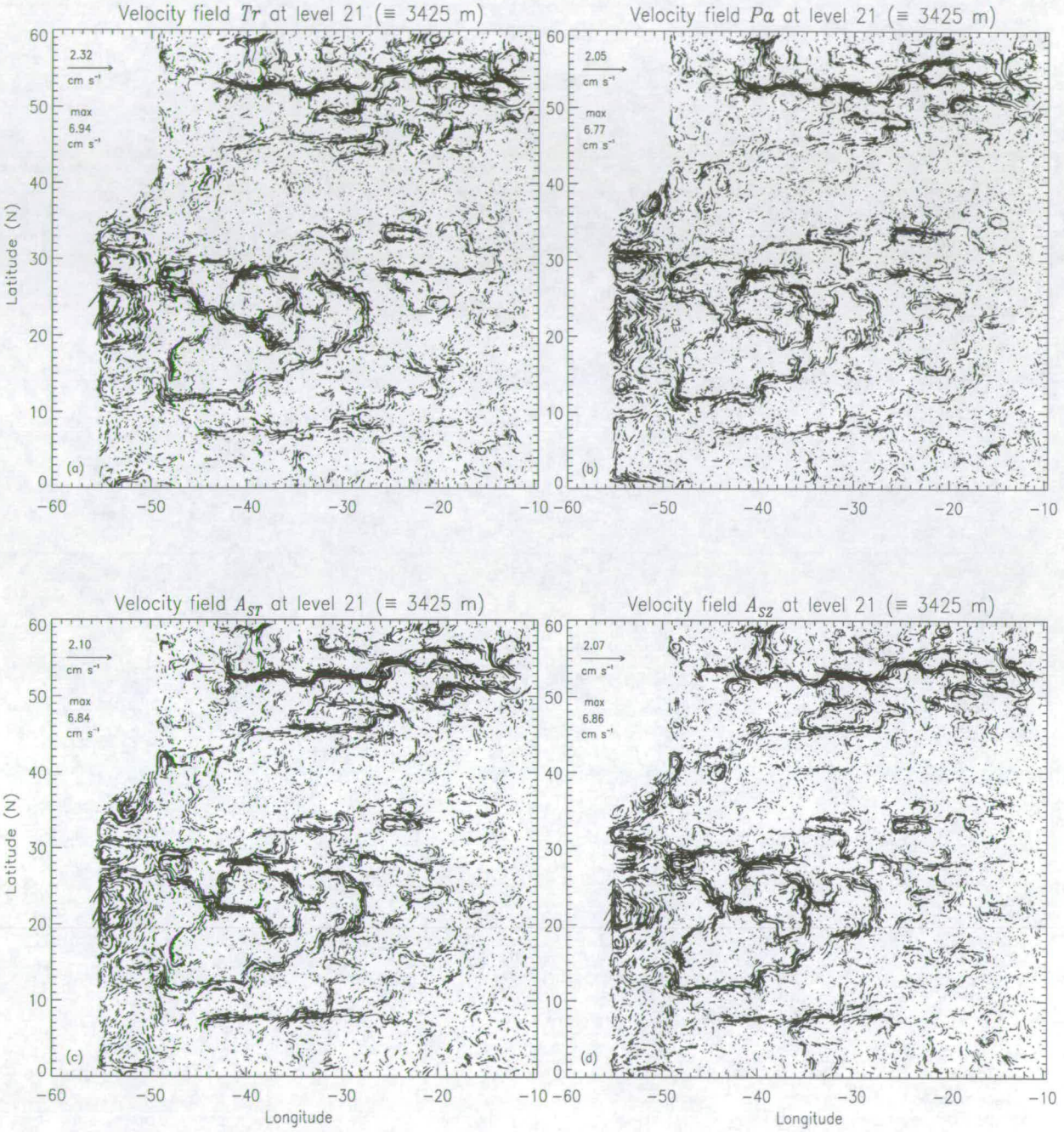


Figure 6.14: Velocity field at 3425 m depth, averaged over the two-year assimilation integration for (a) Tr, (b) Pa, (c) A_{ST} and (d) A_{SZ}. The value of the maximum velocity is shown at the top left of each plot.

same patterns as in Tr and Pa. Some marginal improvement of A_{ST} with respect to Pa and A_{SZ} can be observed for the small gyres by the western shelf between 18° and 33°N. It is more debatable whether A_{ST} has improved the larger cyclonic circulation in the sub-tropical gyre. Anyhow, this analysis shows that the deep circulation is very little affected by the increased wind stress and by the data assimilation. We can conclude therefore that to first order it appears as though the bottom pressure changes is not an important issue, at least for this particular (synthetic) experiment.

6.5 Water mass structure

In the previous sections we have analysed the assimilation experiment using typical validation tools (rms errors, section snapshots, dynamic height and velocity field) which constitute a salient first step in the assessment of an assimilation method. From these tools, it has emerged that the salinity scheme generally yields positive results. Nonetheless, to understand better the impact of the assimilation on the model, and in particular on its water mass properties, we now first analyse the potential vorticity on chosen density levels (in section 6.5.1) and then we consider the T–S relationships averaged over a limited area (in section 6.5.2). The temporal averages considered in this section are calculated as for Fig. 5.9a.

6.5.1 Potential vorticity

A useful way to analyse how two runs differ from each other is by means of differences between potential vorticity on an isopycnal. The appeal of this type of analysis is that it can also be interpreted in terms of abundance of different water masses, of one run with respect to the other, and in turn in terms of water mass production. This PV analysis also constitutes a useful intermediate step towards the model analysis in terms of water mass properties in the T–S diagram (next section).

We consider now the potential vorticity difference between the Tr and the Pa for the 2-year average (103-104-yr period) as a function of location. In Figure 6.15 the potential vorticity on six σ_t levels (i.e. derived at a point) are considered (top left panel for the lighter σ_t level and bottom right for the heavier one). Figure 5.7a provides a useful reference to locate the approximate depth of these σ_t levels. In the top two panels we find major differences mainly in the high q production areas: the shadow zone (eastern boundary) and in the pool region (western boundary). Differences are

also associated with the ventilated zone (northern part of the sub-tropical gyre and between longitudes -40° and -15°), especially for the 25.2 kg m^{-3} level. In particular, positive values signify a higher q for the Tr run, which means higher stratification and, in turn, less water mass of that type for the Tr run. Thus, in terms of water mass production, a higher q implies a lower production of water mass of that type[1]. The level 26.0 kg m^{-3} presents similar features to the previous two, even though differences are smaller. Levels 26.4 and 26.8 kg m^{-3} show major differences near outcropping regions, probably signalling a different rate of water mass formation. In particular, the positive and very high difference in the denser level is associated with an (anomalously) high q region. Finally, the last level (27.2 kg m^{-3}) shows only small differences, but, as we shall see later in this section, this level will be affected by the assimilation runs.

Now we want to see whether, with the insertion of the data, the description of the assimilation runs in terms of potential vorticity has improved. In Figure 6.16 the potential vorticity difference between the truth run and A_{ST} averaged over the 2-year assimilation experiment for six density levels is shown. The same plot, but for A_{SZ}, is shown in Figure 6.17. Let us discuss Fig. 6.16 first. For density smaller than 27.2 kg m^{-3}, the comparison between this figure and that for the parallel run (Fig. 6.15) indicates a marked improvement, with errors reduced basically for each density level, except for the negative difference along the Gulf Stream at level 26.0 kg m^{-3}. This negative sign means that less 26.0 kg m^{-3} water mass is produced by A_{ST} with respect to Tr and, by comparing Fig. 6.16 with Fig. 6.15, to Pa too. Besides, evidence of large errors in this region has already been found in the analysis of the dynamic height (Fig. 6.10). This is therefore a further confirmation that this highly energetic region is a problematic region to tackle through temperature data assimilation (velocity data would certainly represent a helpful complementary piece of information). Also, since large potential vorticity gradients are present in this region large differences between Tr and A_{ST} are likely to occur (see Fig. 5.9). However apart from some worsening at level 26.0 kg m^{-3}, differences are notably reduced in A_{ST}, compared to Pa, and they are almost exclusively left only along the Gulf Stream (see for example the clear reduction for the two levels $\sigma_t = 26.4$ and 26.8 kg m^{-3}) and close to the eastern boundary, which is also a region of strong PV gradient. These differences are mainly found for the

[1]Because q is defined only locally, the algebraic sum of the six plots does not yield zero. In any case this would be an approximation because not all the density levels are considered here.

lighter water masses, i.e. $\sigma_t = 25.2$ and 25.6 kg m^{-3}. Finally, we observe that the PV difference for the deepest level, $\sigma_t = 27.2$ kg m^{-3}, has been reduced by A_{ST} along the western boundary, but it has slightly worsened at high latitudes. This, however, is a region where the salinity scheme is not active, because of the low stratification (see section 5.5.3). Therefore this difference is to be attributed to the $S(z)$ persistence, hence preserving the T–S relationships at those latitudes, does not improve the PV description either (as we will see shortly, the PV analysis for A_{SZ} further corroborates this conclusion).

Even in the other assimilation run, A_{SZ}, the PV differences with respect to Tr (Fig. 6.17) have been generally reduced considerably, when compared to those for the Pa (Fig. 6.15). Furthermore, Fig. 6.17, for A_{SZ}, looks generally more similar to Fig. 6.16, for A_{ST}, than to Fig. 6.15, for Pa, as in the case of the large differences along the Gulf Stream on the density levels 26.0 and 26.8 kg m^{-3} (the blue and the red patches, respectively). Yet, despite this similarity in the difference pattern, the differences appear more accentuated in the A_{SZ} experiment. Observe, for example, the differences near the western boundary close to the land mass as well as those along the Gulf Stream for all density levels. One of the few exceptions is represented by the more spread negative (blue) difference at level 26.8 kg m^{-3} at around (28°W, 48°N). By contrast, A_{SZ} is markedly worse than A_{ST} at level 27.2 kg m^{-3} south of 50°N, i.e. below the latitude (about 52°N) at which our method is not active. Note that in the band 45°–50°N the stratification is not pronounced (see Fig. 6.4), but it is just sufficient for our method to work. Therefore what we see in the lower right panel of Fig. 6.17 is basically the effect of not updating salinity. In particular, for latitudes north of about 40°, that is where the 27.2 kg m^{-3} isopycnal is shallower than 525 m, only the $S(z)$ persistence effect is observed, whereas for latitudes south of about 40°, that is where the 27.2 kg m^{-3} isopycnal is deeper than 525 m, the combined effect of $S(z)$ persistence with the lack of vertical displacement is seen. The main differences (blue patches in the subpolar gyre and yellow-green patches in the sub-tropical one) are, in fact, concentrated across the assimilation sections, especially for those at 48° and 36°W.

Overall, the potential vorticity analysis has shown that most of the error generally occurs in places where the potential vorticity gradient is large, hence where there are likely to be large differences between one run and another. In particular, we have

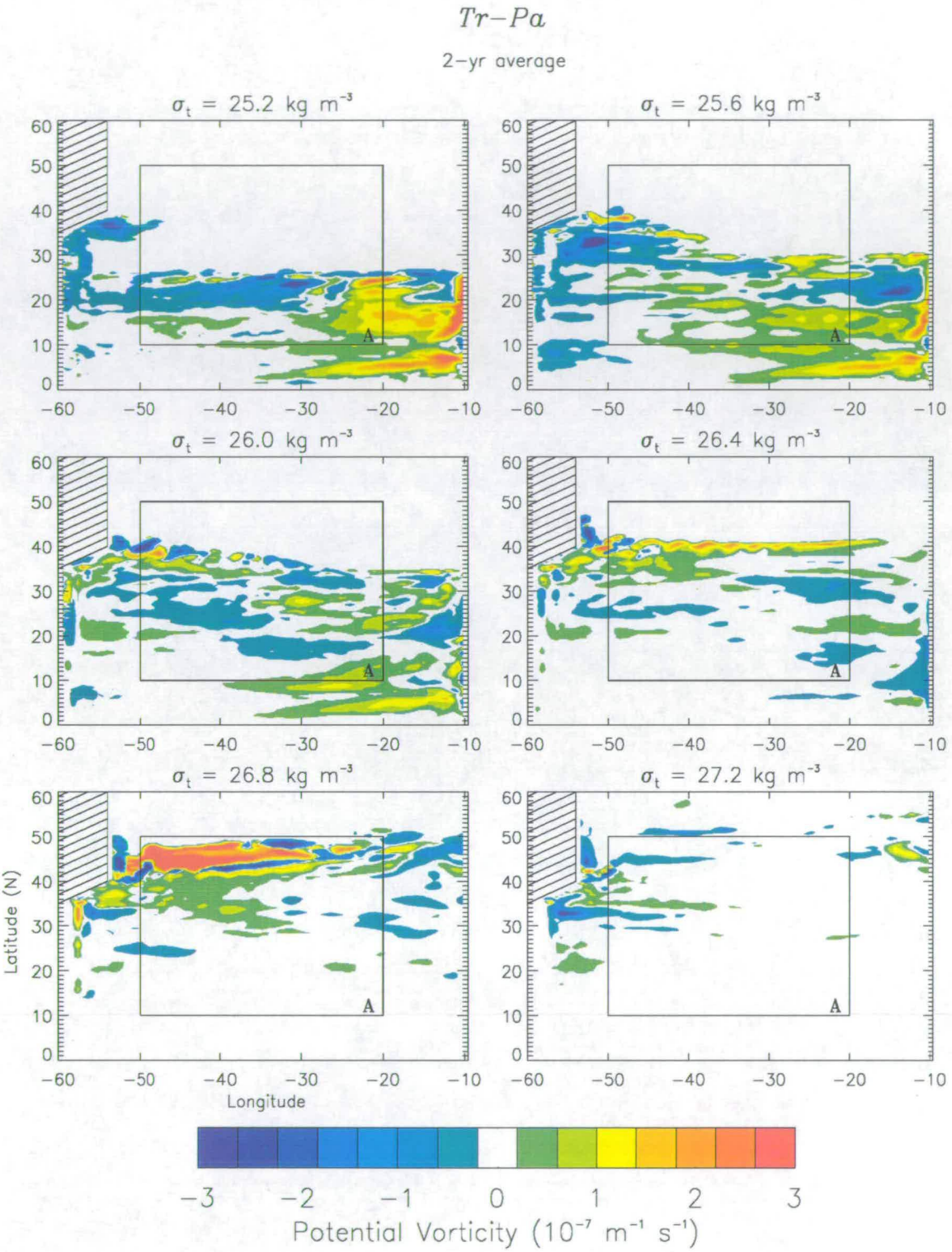


Figure 6.15: Potential vorticity difference between Tr and Pa for six density levels averaged over the 2-year period 103-104 yr. This figure is also useful to identify outcropping regions. Area A is highlighted for later reference.

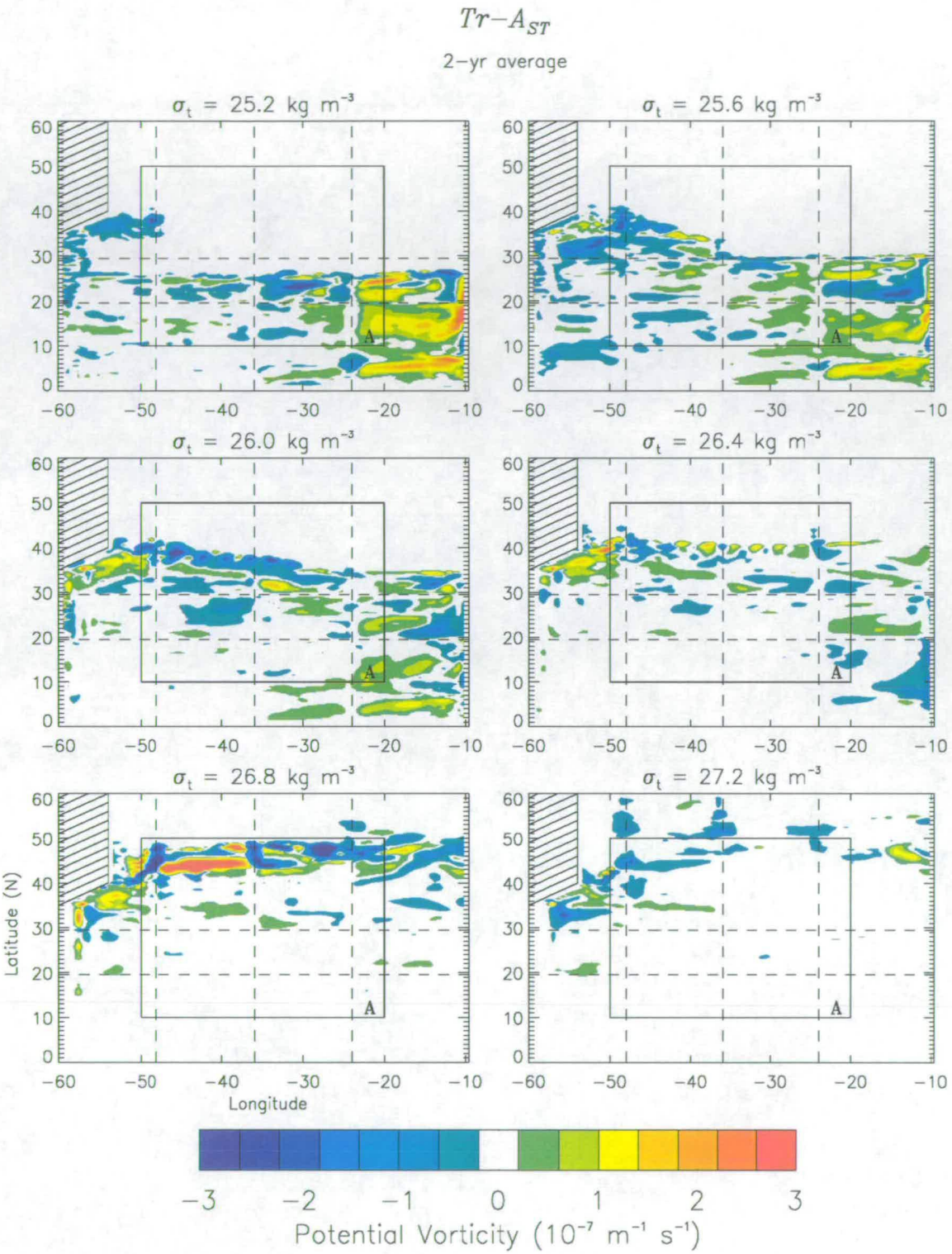


Figure 6.16: As in Fig. 6.15 but for A_{ST}. The assimilation sections have also been highlighted.

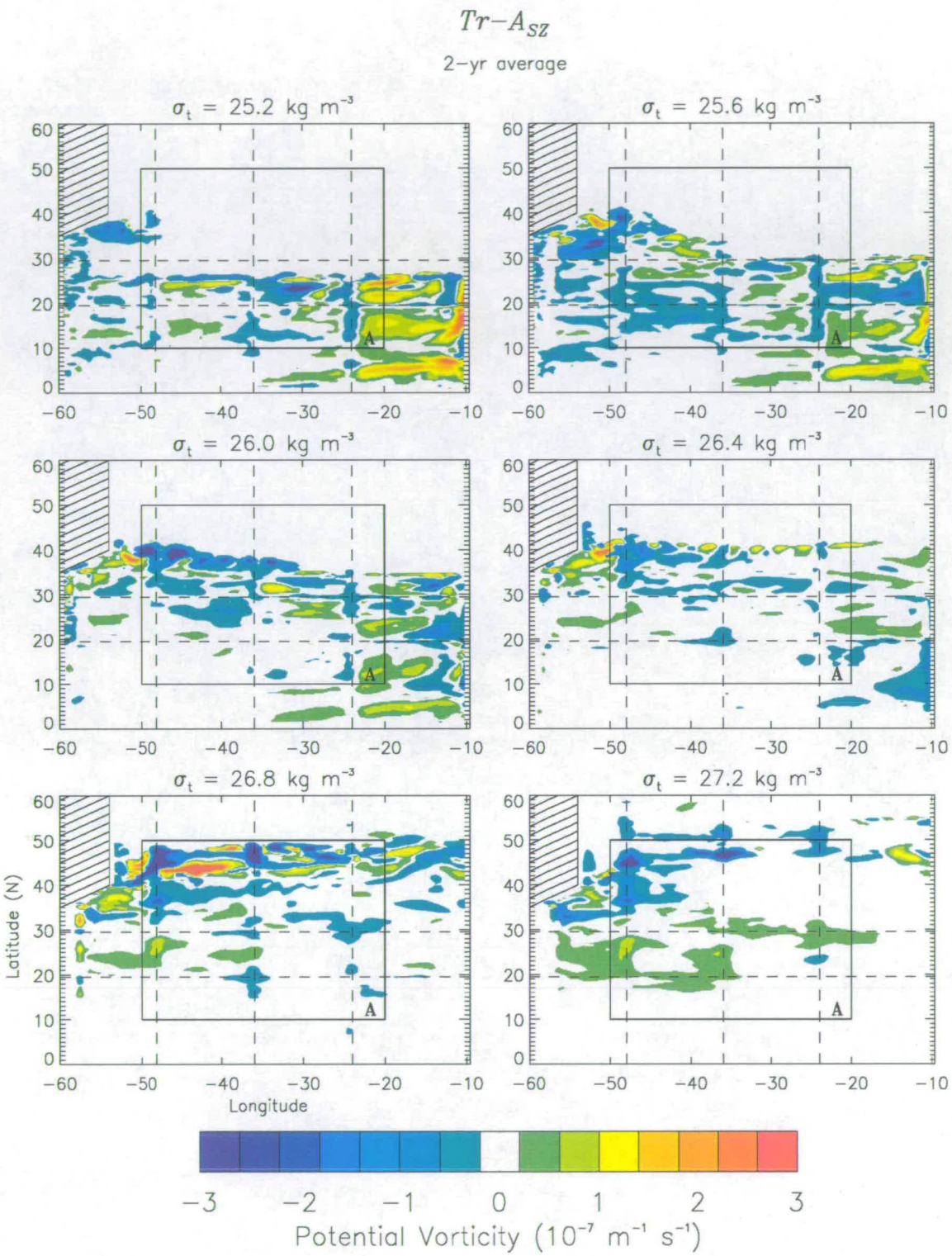


Figure 6.17: As in Fig. 6.16 but for A_{SZ}.

seen that these regions are mainly in the shadow zone (eastern boundary) and in the outcropping regions, especially along the Gulf Stream. In this latter region, any attempt of improvement would also be curbed by the high natural variability. In a way, it looks like this PV analysis has not added much information to the analyses in the previous sections. However, as already pointed out, this information can also be interpreted in terms of water mass production. So, for example, the large negative difference at $\sigma_t = 26.0$ kg m^{-3} in Figs. 6.16 and 6.17 can be seen as a deficit of water mass of that density in A_{ST} and A_{SZ}. Another, somewhat complementary, way of visualising these differences is by means of T–S diagrams.

6.5.2 *T*–*S* relationships

The T–S diagrams considered in this section are all similar to those presented in section 5.4 (Fig. 5.11). As in Fig. 5.11, they refer to the area A highlighted in Fig. 6.15 (here, as in the right panels of Fig. 5.11, we only show the most interesting part of the T–S diagram, that is between 10°C and 27.5°C and 35.3 psu and 37.3 psu). As a reminder, the main reason for choosing the area A is that it is safer not to get too near the boundaries, which are normally not very realistically simulated in our model configuration. Also, as a mnemonic rule, a plus sign in the PV analysis goes with a minus sign in the water mass budget and vice-versa, or, more simply, red with blue and vice-versa.

Figure 6.18 shows the water mass budget for the three runs with respect to Tr, i.e. the difference of the water mass properties between Tr and Pa (Fig. 6.18a), Tr and A_{ST} (Fig. 6.18b), Tr and A_{SZ} (Fig. 6.18c), for the area A and for the first assimilation step, that is immediately after the assimilation for A_{ST} and A_{SZ}. The budget at the first step for the parallel run (Fig. 6.18a) is the difference between the bottom panels in Fig. 5.11 and it has already been partly discussed in section 5.4. Note that it also corresponds to the water mass budgets for A_{ST} and A_{SZ} just before the first assimilation step and this is a useful reference for the discussions of the other two panels in Fig. 6.18, i.e. Figs. 6.18b-c.

We shall interpret now the water mass budget differences in terms of physical and dynamical processes. For convenience, we will also consider three density ranges: $\sigma_t <$ 25.5 kg m^{-3}, 25.5 $< \sigma_t <$ 26.4 kg m^{-3} and $\sigma_t >$ 26.4 kg m^{-3}. From Fig. 6.18a we can see that the parallel run has more water masses with $\sigma_t <$ 25.5 kg m^{-3},

i.e. in the lighter range, than the truth run because the negative area dominates the positive area. These lighter water masses are associated to a more pronounced Ekman advection in Pa, especially in the southern and the eastern parts of the sub-tropical gyre, but also to Ekman pumping, as in the eastern part of the sub-tropical gyre (cf. the PV differences in the top left panel of Fig. 6.15 which also gives an indication of the different circulation pattern). This increased circulation is clearly due to the larger wind stress applied to Pa. In particular, within the interval $\sigma_t < 25.5$ kg m^{-3} we can distinguish between the warmest water mass with $T > 25$°C and water mass with lower T. The warmer water mass is also fresher. In fact, the origin of this water mass can be traced to the south of the sub-tropical gyre, i.e. between 10° and 22°N, that is where the relaxation T is larger than 25°C (see Fig. 5.4b). This water mass is transported northward through Ekman advection and, because the salinity is at a maximum at about 22°N (Fig. 5.4a), the additional advected water mass in Pa is fresher than in Tr. In addition, these water mass changes between Tr and Pa (Fig. 6.18a) mostly affects the upper water column (top 200 m) as can be deduced from Fig. 5.7a.

Other major differences in Fig. 6.18a are in the density range 25.5–26.4 kg m^{-3}. The largest differences for these water masses are mainly associated with the northern part of the sub-tropical gyre, i.e. latitudes higher than about 25°N, as can be derived from the relaxation T and S (Figs. 5.4a-b) and the T and S values for the density range considered, i.e. $T < 23$°C and $S < 37.1$ psu (Fig. 6.18a). Also, the Gulf Stream, i.e. 38°–41°N, can be taken as the northern boundary for these water masses (see Fig. 5.7a). The increased recirculation along the western boundary and Ekman advection along the Gulf Stream in Pa are mainly responsible for the differences between Tr and Pa (an indication is given by the relative panels in Fig. 6.15, but further evidence will be shown by the surface flux differences in Fig. 6.25). In particular, the increased southward Ekman advection in Pa transports more fresh and cool water than in Tr, as can be observed from the two distinct bands of positive and negative signs in Fig. 6.18a, for the density range considered. The effect of the increased recirculation along the western boundary is instead to advect saltier and warmer water masses northward (e.g. see Fig. 5.8). These water masses are located in the band 30°–40°N (see Fig. 6.15) and have temperatures between 18°C and 23°C and salinities between 36.5 psu and 37.0 psu (Figs. 5.4a-b). An example of such a water mass difference is seen across the 25.5 kg m^{-3} sigma level in Fig. 6.18a where a positive difference is found at lower

salinity and temperature than the corresponding negative difference, which represents an excess of this water mass in Pa with respect to Tr. Even for this density range the water mass differences between Tr and Pa are likely to be in the upper water column as can be inferred from the density structure in Fig. 5.7a.

For density larger than 26.4 kg m^{-3} the differences between Tr and Pa are smaller (Fig. 6.18a) than those referring to lighter density. Now, latitudes north of the Gulf Stream (about 41°N) are also included in the water mass budget (see Fig. 5.7a), although most of the error is present south of the Gulf Stream (see bottom panels in Fig. 6.15). Therefore, part of these differences occur even in the main thermocline in the sub-tropical gyre (cf. again Fig. 5.7a). This means that the 3-year divergence of Pa is sufficiently long to induce modifications to the ventilation of water mass layers in this density range. It is not easy, however, to determine the correspondence between negative and positive differences in Fig. 6.18a for this density range, for these water masses attain to diverse locations within the area A. Moreover, given the low stratification in the sub-polar region the temperature resolution chosen for the T–S diagram, i.e. $\Delta T = 0.25$°C, may not be sufficient (cf. Fig. 5.6a). However, an exception is represented by the sub-range 26.5–27.0 kg m^{-3} for which the water mass budget shows a pattern according to which Pa is cooler and fresher than Tr, probably as a result of the ventilation in the sub-tropical gyre region.

The effect of the A_{ST} data assimilation for the area A immediately after the first step can be seen by comparing Fig. 6.18b with Fig. 6.18a. This comparison shows some improvement of A_{ST} over Pa in the first ($\sigma_t < 25.5$ kg m^{-3}) and third ($\sigma_t > 26.4$ kg m^{-3}) density ranges, whereas it is generally worse in the second density range, as for instance on the 26.0 kg m^{-3} sigma level for which both positive and negative differences are larger in A_{ST}. The extrema[2] indicated in the two panels show that differences with respect to the Tr are reduced by A_{ST} from (-167; 282) m °C^{-1} psu^{-1} before assimilation to (-106; 198) m °C^{-1} psu^{-1} after assimilation. Further, if we consider the rms deviation from Tr as a more reliable measure of the success of a run, then A_{ST} is better than Pa, with a rms equal to 17.4 m °C^{-1} psu^{-1} against 19.6 m °C^{-1} psu^{-1}. Note that, because the assimilation area along the tracks only affects about 30% of the whole area A, the water mass changes due to the data assimilation may be visually not so evident.

[2]Although this measure is not highly significant it supplies a useful first indication.

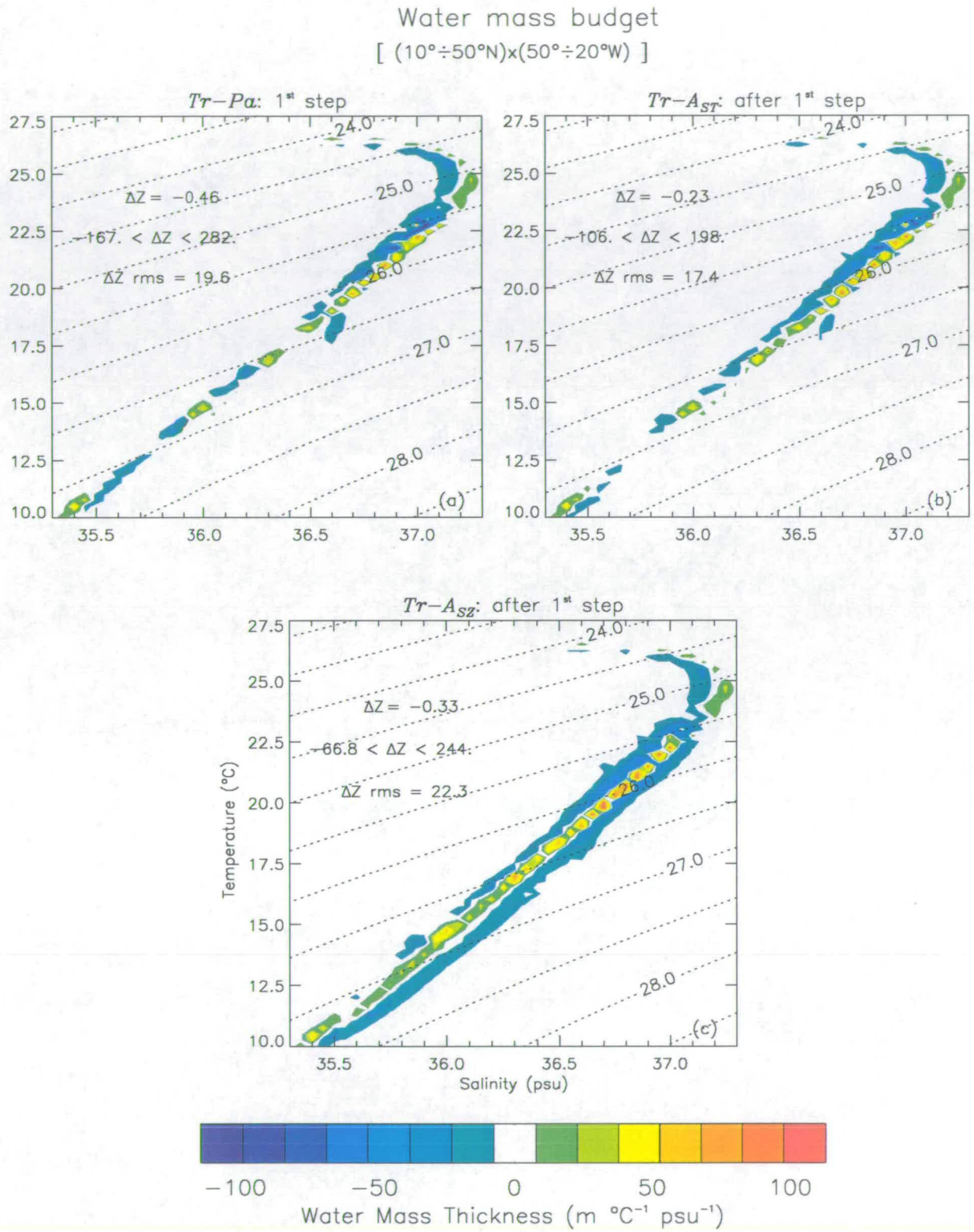


Figure 6.18: T-S diagrams showing the difference between the truth run and the three runs (a) Pa, (b) A_{ST} and (c) A_{SZ} at year 103 and 1 month (i.e. first assimilation step) for the area A indicated beneath the title plot and highlighted in Fig. 6.15. Superimposed are the σ_t dotted curves. Averages, extrema and rms are indicated.

The impact of the data assimilation is much more evident in the case of A_{SZ}, as shown by Fig. 6.18c (again, it refers to immediately after the first assimilation step), especially for density larger than 25.5 kg m^{-3}. It is clear that persisting $S(z)$, and not performing the vertical displacement, leads to the formation of spurious, water masses which are not consistent with those of the model. The enhanced positive difference and the appearance of a new negative difference in Fig. 6.18c are manifestations of this process. Even the apparent positive effect such as the reduction of the minimum from -167 m °C^{-1} psu^{-1} to -67 m °C^{-1} psu^{-1} is explained by the formation of these spurious water masses. Fig. 6.18a shows in fact that at about (37 psu, 23°C), on the σ_t = 25.5 kg m^{-3} isopycnal, the truth minus Pa is locally at a maximum and this maximum is incidentally close to the absolute minimum (-167 m °C^{-1} psu^{-1}). In A_{SZ} then, the assimilation of this locally warmer temperature combines with the saltier background giving rise to a denser water mass and the difference minimum is thus reduced. It is clear therefore that the A_{SZ} assimilation run is bound to introduce spuriously dense water masses which are likely to be statically unstable, as is schematically indicated by Fig. 3.2b, which is certainly not a desirable feature in a data assimilation system. Only in the first density range the differences between A_{SZ} and Tr are basically unchanged from before the assimilation (cf. Fig. 6.18c with Fig. 6.18a) as for these near surface water masses the $S(z)$ persistence is an acceptable solution (see Fig. 6.8 for depths shallower than about 100 m). Overall, though, the ΔZ rms, 22.3 m °C^{-1} psu^{-1}, shows a worsening with respect to both Pa and A_{ST}.

Figure 6.19 shows the water mass budget for the three runs as in Fig. 6.18 but for the average over the 2-year experiment calculated at the time of assimilation (immediately after for A_{ST} and A_{SZ}) and it therefore consists of the average of 24 fields. This figure essentially shows the same pattern as that in Fig. 6.18, only now the differences are perhaps slightly smoother.

It is interesting to relate these differences to the previous PV analyses. Let us consider the Tr minus Pa first (the PV analysis is in Fig. 6.15). For example, the dipole difference (positive-negative) at $\sigma_t < 25.2$ kg m^{-3} in Fig. 6.19a corresponds to the differences in the top left panel in Fig. 6.15. In particular, the saltier and slightly warmer water mass in Tr (green area in Fig. 6.19a) corresponds to the negative region within the area A in Fig. 6.15, whereas the fresher negative difference in Fig. 6.19a matches the positive difference in the eastern part of area A in Fig. 6.15. To this purpose a

useful reference, especially for the values of salinity, is given by the surface maps in Fig. 5.8, even if the level $\sigma_t = 25.2$ kg m^{-3} outcrops at about 24°N. Another example is at $\sigma_t < 26.8$ kg m^{-3} for which the negative difference in the T–S diagram, with S that ranges between 35.8 psu and 35.9 psu and T between 13°C and 14°C, matches the pronounced positive difference in the bottom left panel of Fig. 6.15. Although this pronounced difference must be interpreted with care as at the outcrop the PV values are quite high and so small variations in the two runs may imply large PV differences, it shows that the parallel run is forming more water of that type, as indicated by the smaller PV than in Tr.

It is not obvious that both Fig. 6.18a and Fig. 6.19a should show the same features. The fact that this is the case implies therefore a certain correlation between the water mass formed in the two runs over the 2-year integration. An indirect indication of this is given for instance by the kinetic energy behaviour in Fig 6.1 according to which Tr and Pa are basically in phase. A possible reason for the correlation between Fig. 6.18a and Fig. 6.19a is that the 2-year integration is shorter than the dominant time scale of our model, which is equal to 4.3 yr (see section 5.2.1).

The situation of A_{ST} is slightly worse than that for Pa for the 2-year average for $\sigma_t > 25.5$kg m^{-3}, as can be seen by comparing Fig. 6.19b with Fig. 6.19a. For example, the separation between the positive and negative differences between 25.6 and 26.0 kg m^{-3} is considerably increased in A_{ST} with respect to the parallel run. In particular, the positive (red) difference in A_{ST} is notably worse than in Pa and this is in agreement with the PV analysis, which showed a marked worsening in the A_{ST} for the density level 26.0 kg m^{-3} (the blue zones in the left middle panel of Fig. 6.16). The reason for the worsening of the T–S properties of the water mass layers in the middle density range, 25.5–26.4 kg m^{-3}, is related to the errors introduced by the assimilation upstream of the Gulf Stream, that is especially on the 48°W assimilation section and for the upper water column (cf. Figs. 6.11c-d and Fig. 6.12a). In fact, rms calculations like those in Figs. 6.7 and 6.8 but only for the 48°W assimilation section (not shown) indicate that the salinity rms errors are markedly larger than those for the average over the five assimilation sections. These errors thereafter remain in A_{ST} as they are advected by the Gulf Stream and, eventually, influence the different water properties for the water masses formed along the Gulf Stream, as discussed above, and which normally fall in the middle range, 25.5–26.4 kg m^{-3} (cf. Fig. 5.7a).

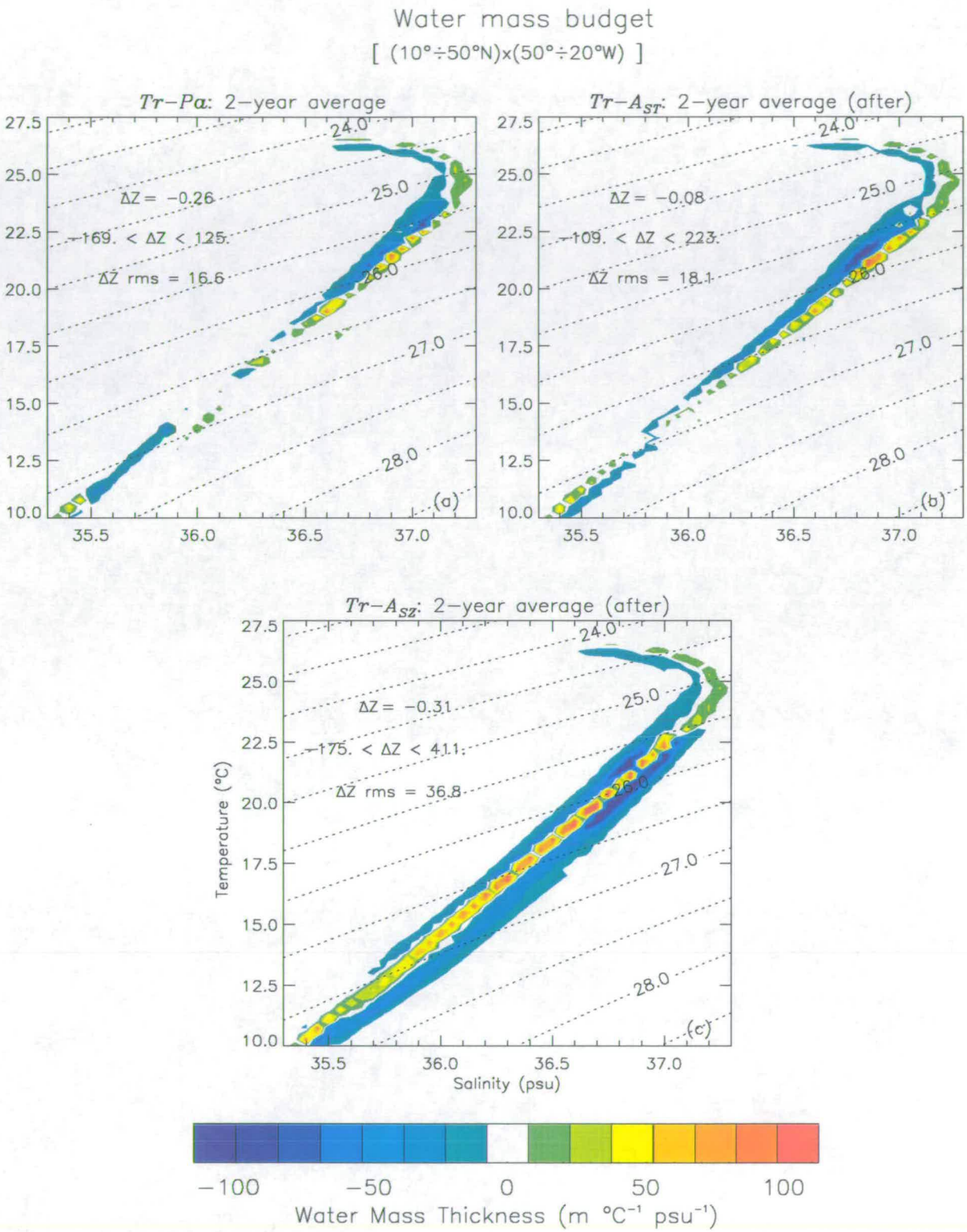


Figure 6.19: As in Fig. 6.18 but for the 2-year average.

However, some improvement of A_{ST} is also apparent. For example, on the density level 26.8 kg m^{-3} the difference between Tr and A_{ST} has been reduced as can be observed by comparing Fig. 6.19b with Fig. 6.19a. This reduction is also in agreement with the reduction in the PV difference on the same density level and which has been highlighted in the PV analysis for Pa (Fig. 6.15). This is also backed up by the PV differences reduction discussed with Fig. 6.16. Further, even in the lighter density range the differences in the water mass budget are generally reduced by A_{ST}. Observe for example those on the $\sigma_t = 25.2$ kg m^{-3} which matches the improvement shown by the PV analysis for the corresponding density level (Fig. 6.16). Overall, in terms of rms deviations, we have for the A_{ST} 2-year average a value of 18.1 m °C^{-1} psu^{-1}, that is larger than that after the first assimilation step (17.4 m °C^{-1} psu^{-1}) but also than the one for the Pa 2-year average, which is equal to 16.6 m °C^{-1} psu^{-1}.

Fig. 6.19c confirms the negative impact of the $S(z)$ persistence approach in A_{SZ}. This is also made manifest by the values of the extrema, (175; 411) m °C^{-1} psu^{-1} for the 2-year average, and the rms deviation, which goes from 22.3 m °C^{-1} psu^{-1} for the first assimilation step in Fig. 6.18c to 36.8 m °C^{-1} psu^{-1} for the 2-year average in Fig. 6.19c.

In both assimilation runs (Figs. 6.19b-c), the positive - green - area at around (37.25 psu, 24°C) has not improved much through the assimilation (see Figs. 6.18 and 6.19). This was to be expected for, in the truth run, the salinity of this water mass is greater than any salinity found in Pa, A_{ST} and A_{SZ}, and therefore it can not be captured by the salinity scheme because it is not present in the background salinity field at assimilation time. Moreover, some errors might also be introduced by the method numerics which would then contribute to worsen the A_{ST} description, thus further enhancing the differences between Tr and A_{ST} with respect to those between Tr and Pa. However, it is encouraging that the differences present in A_{ST} (Figs. 6.18b and 6.19b) are far smaller than those in A_{SZ} (Figs. 6.18c and 6.19c).

Figure 6.20 shows the water mass budget for the three runs as in Figs. 6.18 and 6.19 but for the last, 24th, assimilation step. In other terms, Fig. 6.20 shows how much the three runs differ at the end of the 2-year experiment in terms of T–S water mass properties. This figure essentially shows the same pattern as that in Fig. 6.19 for the 2-year average, only that now the differences are larger (note the different colour scale). This augmented difference was to be expected, at least for the parallel run, as

the increased 'wrong' wind stress acts throughout the duration of the experiment in such a way as to make the parallel and assimilation runs diverge from the truth run. Given the close similarity with the previous water mass budgets in Fig. 6.18 and 6.19 we will not discuss Fig. 6.20 any further. Yet, this figure will be relevant when the inventory, accumulated over the whole 2-year assimilation experiment, is discussed in the next section.

Finally, it is useful to note that, integrating the function represented graphically by the T–S diagrams with respect to S (i.e. $\Delta Z(T) = \int \Delta Z(S,T)dS$, therefore eliminating the S dependency), one obtains the information about the temperature data assimilated, that is the difference between the assimilated and the truth run temperatures (cf. section 3.4). Likewise, for the integration with respect to T (i.e. $\Delta Z(S) = \int \Delta Z(S,T)dT$) one can see the salinity modifications introduced by the data assimilation method (i.e. by our method in the case of A_{ST}, whereas the S integral is equal to zero for A_{SZ}, by definition). These integrations will not be shown explicitly.

6.6 The Inventory

What we have analysed so far, using the synthetic experiment formulation, has taken for granted that the true state of the ocean is completely known. This is manifestly not true for a real data assimilation experiment, for which only sparse observations are normally available. It should therefore be interesting to analyse a quantity that can be derived for any assimilation experiment, i.e. even non-synthetic ones, that is the accumulation of the modifications inserted directly by the assimilation, at each assimilation step, which we will call the *inventory*. In the case of our synthetic data assimilation experiment, we can also relate this information to the previous analyses. However, because truth comparisons cannot be applied to any data assimilation experiment, we will also discuss how the inventory could be utilised and interpreted in the case of real experiments. Note that in the following T–S diagrams, the water mass differences, in this case the inventory, are weighted using the same area as that used for the water mass budgets (Figs. 5.11, 6.18, 6.19 and 6.20) so as to allow a direct numerical comparison and hence to better appreciate the impact of the inventory on the water mass budgets.

Figure 6.21 shows the inventory for A_{ST} at the first assimilation step (top panels) and for the 2-year accumulated (i.e. the sum over the 24 assimilation steps, bottom

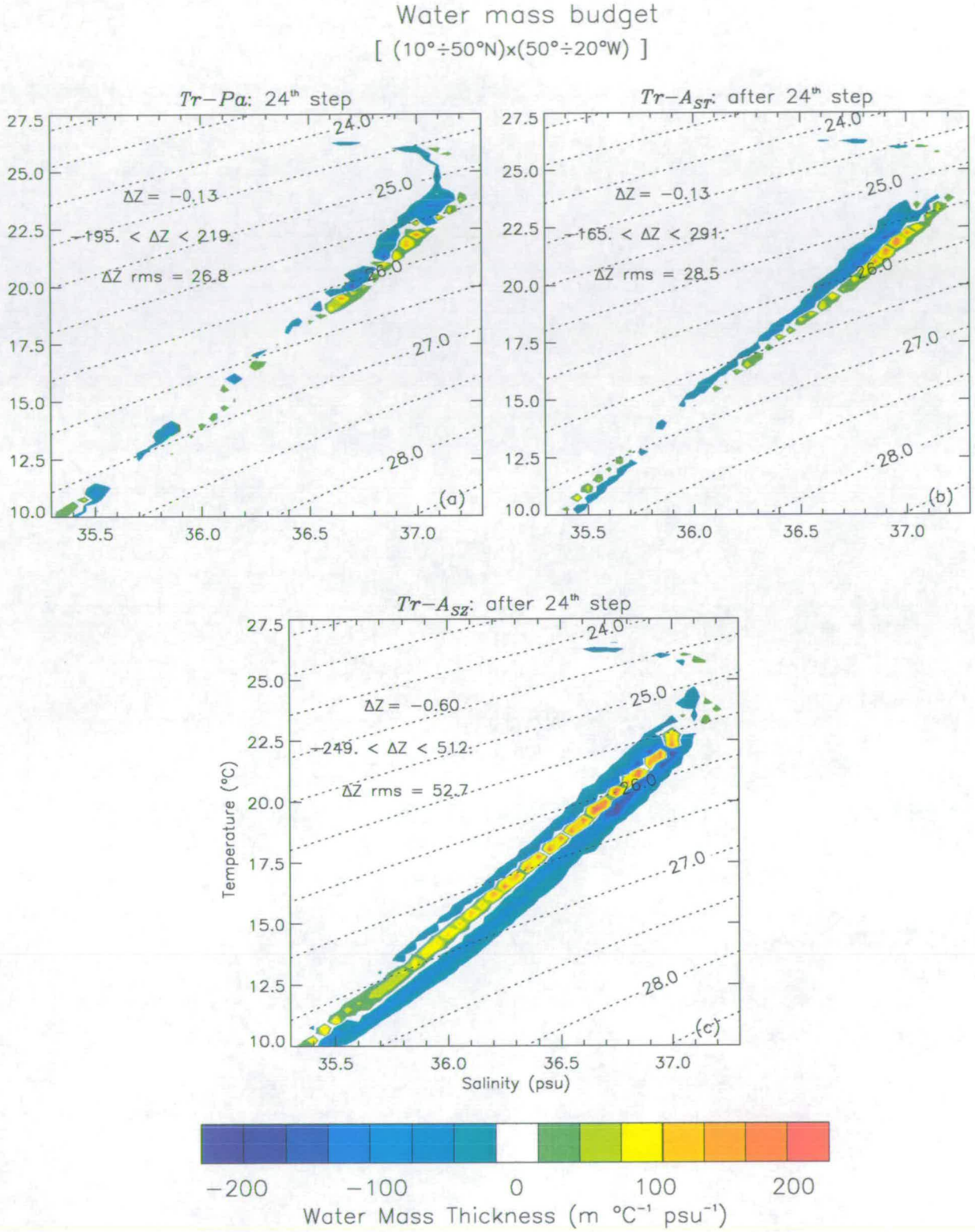


Figure 6.20: As in Fig. 6.18 but for the last assimilation step (i.e. the 24th).

panels; note the different colour scale). In other words, this is what has been added, positive, and removed, negative, with the assimilation (cf. section 3.4 and Fig 3.8). The complete versions of the T–S diagrams, which aim to highlight the role of the data assimilation, and especially that of the vertical displacement on the deep water, are shown on the left panels. Let us start from these bottom water masses then. The water mass changes at these depths are characterised by a dipole structure with a positive denser water mass at about (34.9 psu, 4°C) and a corresponding negative lighter water mass. These two water masses have different origin, even though they can be attributed to the same cause. The former is an inserted water mass, through the displacement part of the salinity scheme, due to the fact that in Pa the sub-tropical anti-cyclonic circulation has been strengthened by the stronger winds and therefore the thermocline in Pa is deeper than in Tr and needs to be corrected in A_{ST}. The latter, the lighter water mass, which instead is a removed water mass, again through the displacement procedure, is due to the increased cyclonic circulation in the sub-polar region which causes the thermal structure in Pa to rise with respect to Tr. Again this is being corrected for in A_{ST}. As expected, this dipole feature is present in the 2-year accumulated inventory too (bottom left of Fig. 6.21). Note that the vertical displacement yields an overall addition of deep water mass, as can be deduced by the sign of the mean ΔZ_{mn}, $\bar{\Delta Z}$ for this portion of the T–S diagram. The sign is in fact positive, even though its value is rather minute: 0.2 m $^{\circ}C^{-1}$ psu^{-1} for the first time step and 1.0 m $^{\circ}C^{-1}$ psu^{-1} for the 2-year accumulated.

Let us now focus on the right panels of Fig. 6.21, the zooms. Ideally, to perfectly reproduce the truth run, the T–S inventory plot at the first step (top right panel) should have the same pattern (and same colours) as that in Fig. 6.18a (note that Fig 6.18b is the difference between Fig. 6.18a and the top right panel of Fig. 6.21). Most of the changes introduced by the assimilation in A_{ST} are for water masses heavier than $\sigma_t = 25.5$ kg m^{-3}, but especially for water masses in the middle density range, i.e. 25.5–26.4 kg m^{-3}, in both the first step (top panel) and 2-year accumulated (bottom panel). Even the pattern of the inventory is very similar in both cases, therefore we can discuss them together. The more evident feature for these inventories, especially between 25.5 and 26.4 kg m^{-3}, is the presence of a bipolar band, whereby the added water masses (positive sign) overlie the removed water masses (negative sign). It is not very easy to determine exactly which old water masses (negative values) have been replaced by

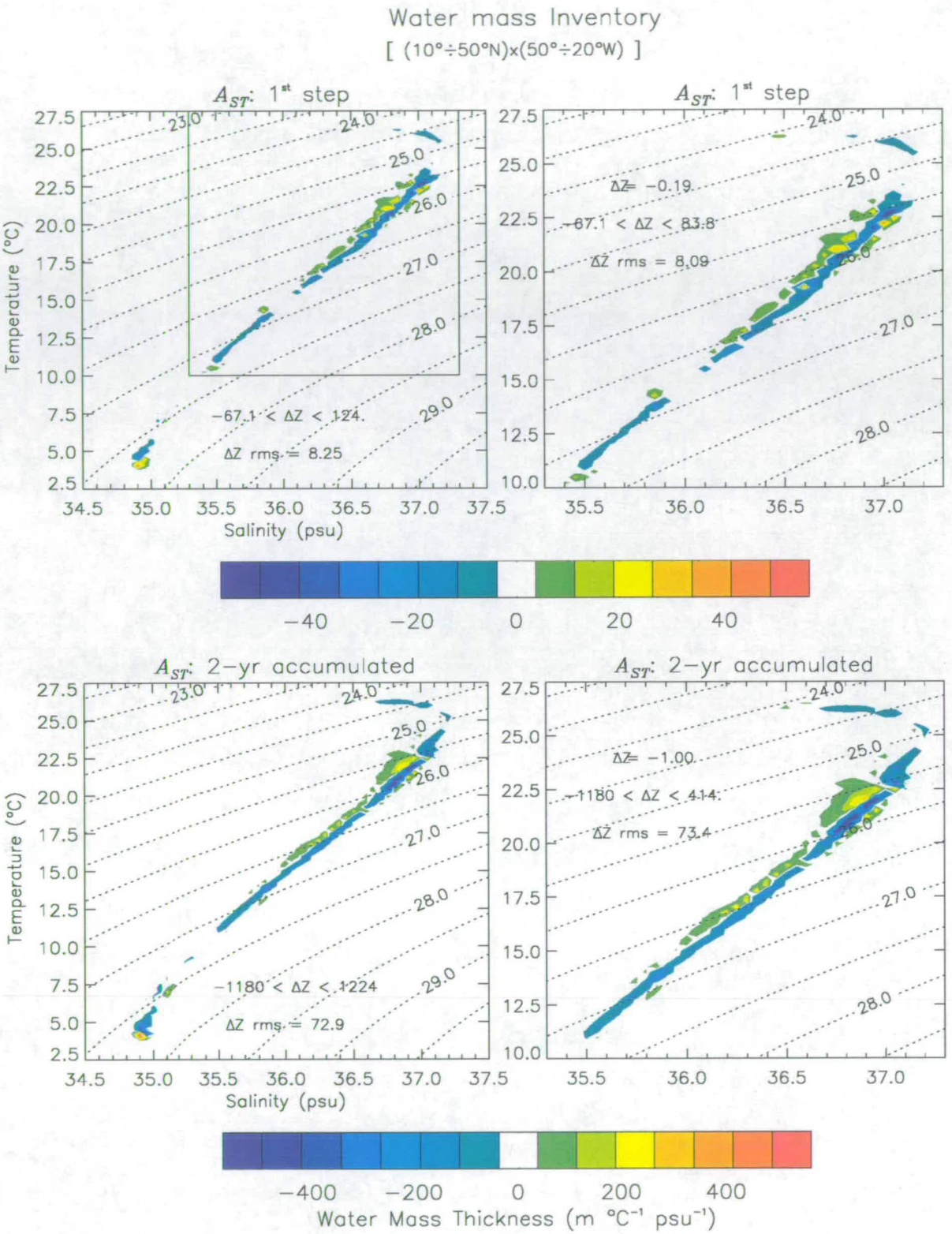


Figure 6.21: T-S diagrams showing the water mass inventory for the A_{ST} run at the first step (top) and for the 2-year accumulated (bottom) for the area indicated beneath the title plot (area A). Superimposed are the σ_t dotted curves. Averages, extrema and rms are indicated (the former only for the right panels as for the left ones averages are zero by definition). Note the different scales for top and bottom.

the new ones (positive values), even if we have the temperature information. However, if we interpret the positive part of the bipolar band, the added water, as vertically shifted towards larger temperature in T–S space, this implies that the assimilation has added warm water mass but the salinity has been less affected than temperature in the assimilation. Of course, we know that, for density larger than 25.5 kg m^{-3}, the water mass gets generally warmer because we assimilated the temperature data (see the water mass budget analyses in the previous section). Nonetheless, we do not have a precise way to assess whether the salinity of the water masses added in the assimilation and shown by the inventory yields water masses which are closer to those of the truth run. A practicable approach is outlined later in the section and uses the idea that useful information is obtainable through integrals of ΔZ. For the moment, we keep focusing attention only on the density interval with $\sigma_t > 25.5$ kg m^{-3}, and especially the middle density range. For these density values, we know from the water mass budget analyses that the truth run is generally warmer than Pa, as we supposed above with the vertical shift, but also saltier than Pa. We just recall that this was due to the different Ekman advection in the northern part of the sub-tropical gyre. Therefore, in order for A_{ST} to get closer to the truth run, even in terms of salinity, the inventory should show a partial shift towards higher salinity of the added water masses. The shift is only partial because not all the changes shown by the inventory have the wrong salinity for otherwise we would not have observed a beneficial effect of the salinity scheme throughout this chapter. For instance, the inventory does show a water mass that is added and which has a relatively high salinity, that is the water mass across the $\sigma_t = 26.0$ kg m^{-3}, below the negative part of the bipolar band.

Of course, we know that this systematic fresh water mass addition introduced by the assimilation is wrong because we have analysed the water mass budget in the previous sections, where we assumed that we knew all the T–S water properties of the truth run. On the other hand, if we did not know anything about the truth run, and hence we could not perform most of the diagnostics presented in this chapter, from the inventory we could only infer that, for example, we systematically add warmer and fresher water mass in the middle density range which would erroneously lead one to think that the model (i.e. the assimilation or, in general, the parallel run) is producing too much of a cold and salty water mass, in the middle density range, with respect to the truth run (the "real world"). Therefore, it is in general not possible to draw firm

conclusions solely by looking at the inventory because of errors which the assimilation method might introduce, such as the freshening discussed above. In order to interpret better the inventory we would need some other constraint or information. For example, if we also knew that the transport of a water mass responsible for the temperature mismatch comes from a region where we can have a reasonably good estimate of the salinity, we could also infer something about how good the salinity analysis is. In particular, this could be the case for which the temperature difference derives from an enhanced/decreased water mass formation at a certain site or region and for which we also know the value of the sea surface salinity. In reality, these SSS observations are presently not widely available, but they may start to be observed on a routine basis by satellite (Lagerloef *et al.*, 1995).

More reliable information could be obtained from the inventory, though, even when the salinity for the truth run is not available. For example, we could analyse the inventory in T space, as done in section 3.4 (Fig. 3.7), for we know the temperature for the truth run, at least along the sections. The inventory in T space would be constructed by integrating $\Delta Z(S,T)$ with respect to S, as also explained in section 3.4 and represented in Fig. 3.7. It is not explicitly shown here for a fairly good idea can be obtained by visually integrating the T–S diagrams. Another useful piece of information is the amount of heat or salt that has been added in the assimilation. These are calculated through the following integrals, respectively: $\int T[\int \Delta Z(S,T)\, dS]\, dT$ expressed in (m °C) and $\int S[\int \Delta Z(S,T)\, dT]\, dS$ expressed in (m psu). When the integration is extended over the whole T–S diagram they yield about -20 $\times$ 10^3 m °C and -3 $\times$ 10^3 m psu, respectively, for the 2-year accumulated inventories and for the whole of area A (for the inventory at the first step the integrals are about 10 times smaller in both cases). This means that overall the assimilation cools and freshen the water masses within area A. More specifically these figures tell us that, on average over area A, the temperature in the upper 1000 m, say, has been lowered by less than 1°C and that the amount of salt removed is about 3 $\times$ 10^{15} Kg, taking an average for each step (the area A is equal to about 1.3 $\times$ 10^{13} m^2). It is also useful to compare these figures with those obtained from the water mass budget. For instance, for the average over the 24 assimilation steps, the same calculation for Pa (Fig. 6.18a, but for the whole T–S diagram) also yields negative numbers (-5.7$\times$ 10^3 m °C and -5 $\times$ 10^2, respectively), meaning that the truth run is cooler and fresher than A_{ST}. In turn, this

means that the assimilation is improving on average not only the heat content of A_{ST}, as seen in the inventory in Fig. 6.21, but also, and encouragingly, the salt content. This result does not contradict the fact that for limited ranges of T and S values, or indeed σ_t values, the integral can yield the opposite result, that is the truth run may produce locally, in T–S space, saltier water masses than in Pa. To this purpose, the integrals above could also be calculated for limited ranges of T and S, although in these cases the fact the integral of the water mass thicknesses over the chosen range may not be zero must also be taken into account.

Figure 6.22 is analogous to Fig. 6.21 but for A_{SZ}. Note that, by definition of $S(z)$ persistence, the integral $\Delta Z(S) = \int \Delta Z(S,T)\, dT$ is equal to zero, whereas $\Delta Z(T) = \int \Delta Z(S,T)\, dS$ is very close to that for A_{ST}, as they adopt the same temperature analysis procedure. The left panels in Fig. 6.22 highlight some modification of the bottom water mass (T <7°C). However, these differences are to be interpreted with care as there is no vertical displacement in A_{SZ}, so the water mass structure must be basically unaltered below the deepest assimilation level (525 m) and T = 7°C is generally below this level for the area A. Moreover, on average, there is no significant imbalance between added and removed deep water masses as can be ascertained from the value of $\bar{\Delta Z}$ for the bottom water masses, which are basically zero both at the first step and for the 2-year accumulated inventories (i.e. they are 0.004 m $^{\circ}C^{-1}$ psu^{-1} and 0.09 m $^{\circ}C^{-1}$ psu^{-1}, respectively). These fictitious differences in Fig. 6.22 are an artifact of the spline procedure which, unlike in the A_{ST} case, here it has to deal also with anomalous temperature profiles, due to the lack of vertical displacement (see the schematic in Fig. 3.2b).

The right panels in Fig. 6.22 (the zooms) reflect well the respective water mass budgets presented in Figs. 6.18c and 6.20c. As for A_{ST}, we can discuss these two panels in Fig. 6.22 together as they carry the same information. From these two panels it emerges that a relatively salty water mass, i.e. the denser positive difference, exists in the background field, that is in the assimilation (or parallel) run, because the salinity does not change at assimilation time in A_{SZ}. In particular, in the middle density range, that is where the main changes are seen, the added water mass is generally warmer than that removed (the negative deep blue band extends to lower temperatures than do the positive deep red bands), in agreement with the inventory for A_{ST}. This warmer water mass then combines with the unmodified background

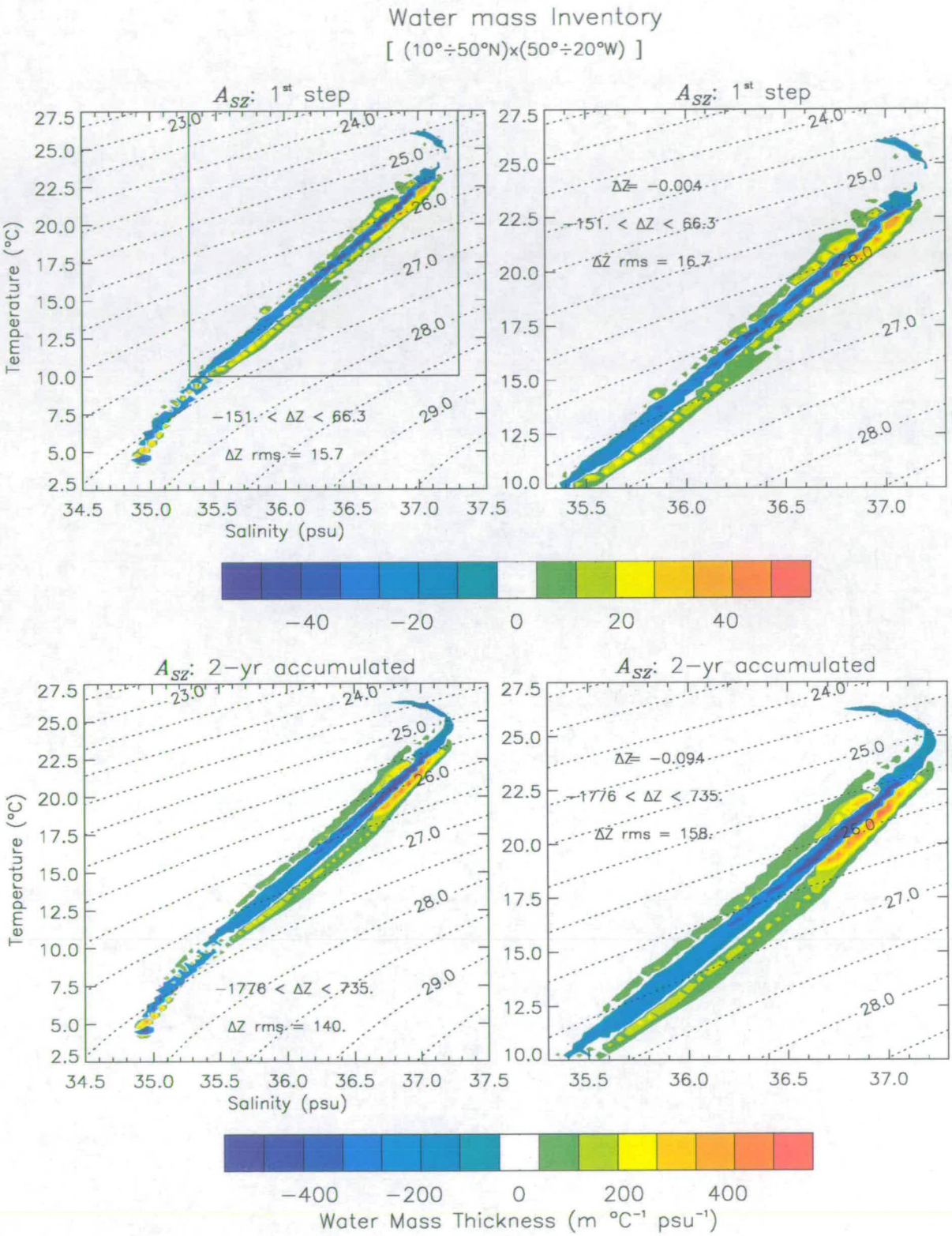


Figure 6.22: As in Fig. 6.21 but for A_{SZ}.

salinity giving rise to two positive bands, either side of the removed blue water mass, that is one saltier and one fresher than the pre-existing water mass. For heavier water masses, $\sigma_t > 25.5$ kg m^{-3} it appears that the opposite situation is present, whereby cooler water masses replace warmer ones. Even in this case, however, the combination of the assimilated temperature generates the two positive bands.

The comparison between the inventory for the two assimilation runs contributes to give useful insights about the way the salinity scheme works. In fact, when a colder water mass is assimilated in A_{ST}, the salinity scheme seeks the new salinity along the T–S curve, which is more like that in Fig. 6.18b or Fig. 6.20b, therefore yielding a lower value for salinity than the background, as shown by the heavier positive band in Fig. 6.22. On the other hand, the lighter positive band seems to be responsible for the persistent error in A_{ST} (see Fig. 6.20b). In this case, in fact, the background salinity is lower than that in the truth run, hence the salinity scheme cannot reproduce it correctly.

Finally, it is interesting to note that the magnitude of the 2-year accumulated inventory (bottom right panels in Figs. 6.21 and 6.22) is markedly larger than the changes observed in the water mass budget in the 2-year integration for both assimilation runs (Figs. 6.20b-c, respectively). This may be due to the fact that the assimilation introduces water masses which are different from the state preferred by the 'wrong' forcings of Pa. This therefore would result in a systematic insertion of the same water masses at each assimilation step. The smoothing that intervenes soon after the assimilation might also contribute to worsen this situation. A gradual insertion of the data and/or a larger decorrelation length scale could reduce this effect.

6.6.1 Inventory evolution

We shall study now the temporal evolution of the inventory. There is not a unique way to do this: here we consider the evolution of the rms deviations as a proxy of the inventory evolution. These are the rms deviations of the inventory functions discussed in the previous section (see Figs. 6.21 and 6.22). Fig. 6.23 shows the temporal evolution of these rms deviations, that is the inventory rms for each of the 24 assimilation steps for both A_{ST} and A_{SZ}. Also, the rms deviations are calculated only for the zoom portion of the inventory T–S diagrams, i.e. for $S > 35.3$ psu and $T > 10$°C (their behaviour does not vary appreciably if we include the rest of the T–S range).

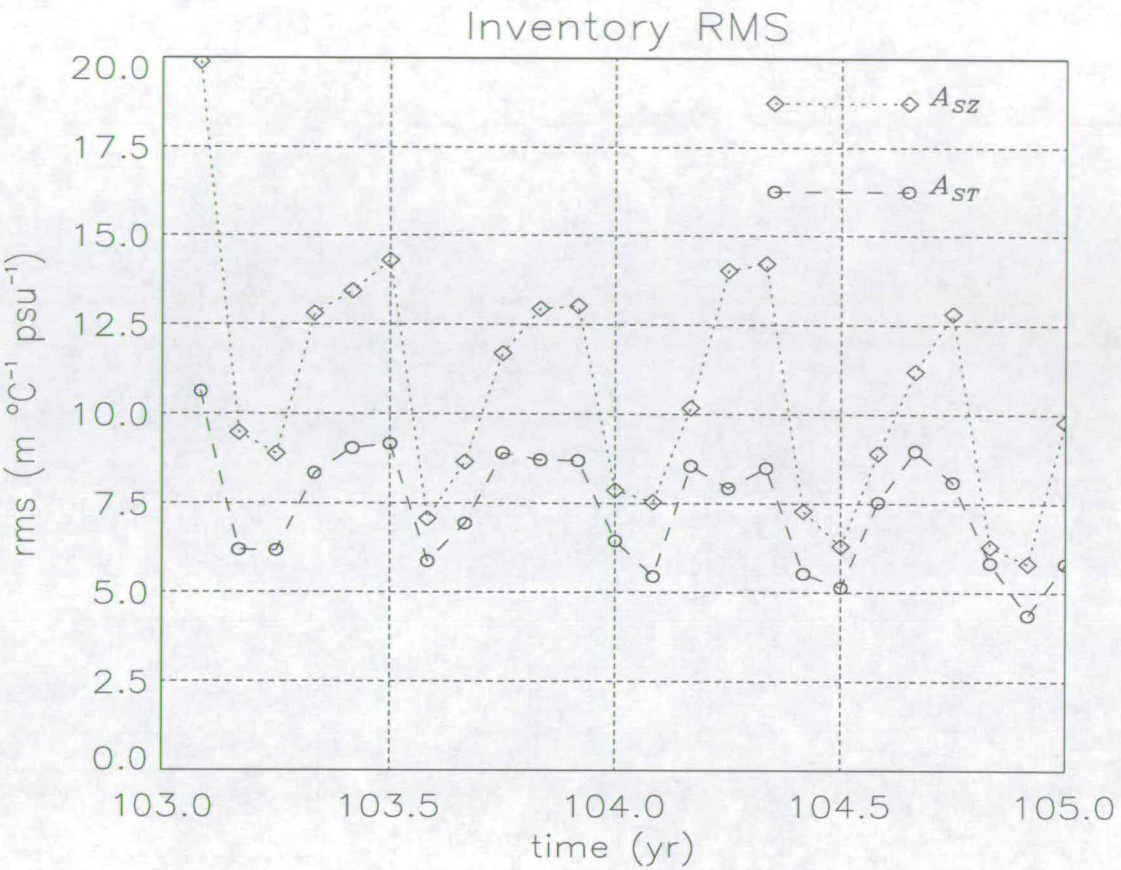


Figure 6.23: Temporal evolution of the inventory rms for A_{ST} and A_{SZ} calculated for $S > 35.3$ psu and $T > 10°C$.

The main difference between the two runs is the magnitude of the rms, with the A_{SZ} rms larger, up to twice as much, than those of A_{ST}. Note also that the rms deviations for both A_{ST} and A_{SZ} undergo an oscillation very similar to that observed, for instance, in the case of the S rms in Fig. 6.7. However, the most important feature of this rms evolution is that there is a decreasing trend, which is more evident in the A_{ST} case (what follows refers mainly to this run). This decreasing trend, in fact, signifies that the information introduced by the assimilation decreases with time. On the one hand this is good news because it means that the information inserted at assimilation time is retained after the assimilation. On the other hand, it signals that the assimilation becomes less and less active as time goes by, for adding the same amount of data (the five sections) their impact diminishes. At the same time, we know from the water mass budget analyses that this reduction of the rms is not accompanied by a decrease in the difference between Tr and A_{ST} (more so for A_{SZ}). Therefore, it

looks like a longer data assimilation experiment would not benefit much from further data insertions. And the lower bound for the difference between Tr and A_{ST} (or A_{SZ}) is given by the error in the initial conditions (see Fig. 6.18a).

Two suggested ways to obtain further benefit from the data assimilation are 1) to diversify the sections along which temperature data are assimilated and 2) to "observe" salinity and therefore to reduce the T–S error between Tr and the assimilation run so as to have better T–S background relationships. Both of these, however, rely upon observations that, in reality, may not be available, even though the first solution may be more practicable than the second, for it would only need temperature observations rather than both T and S.

6.7 Surface flux modifications

Following the ideas of Walin (1982) and Tziperman (1986), according to which it is possible to relate the fluxes at the surface (total heat and fresh water) with the interior water masses in an ocean that has reached a steady state and in which the role of mixing is negligible, we will now discuss rather summarily the differences in the surface fluxes in the four runs that constitute our experiment. This analysis could supply suggestions for further work.

In Figure 6.24 we show the surface total heat flux and the Evaporation-Precipitation (E-P) flux for the truth run, averaged over the 2-year assimilation experiment. These fluxes have been presented in section 2.5, and have been calculated here using the difference between the relaxation and the first model level temperatures and salinities, as follows:

$$Q = \gamma_T \times C_p \times \rho_0 \times (T^* - T_1) \tag{6.1}$$

$$E - P = \gamma_S \times t_y \times (S^* - S_1)/S_0 \tag{6.2}$$

where γ_T and γ_S, in s^{-1}, are the relaxation constants for the temperature and salinity, respectively and t_y is equal to one year expressed in seconds. C_p is the heat capacity of water taken equal to 3994 J kg^{-1} K^{-1}, ρ_0 is a reference density taken equal to 1025 kg m^{-3} and S_0 is a reference salinity taken equal to 36 psu. T^* and S^* are the relaxation values for T and S and T_1 and S_1 are the T and S at the first model level. To have an idea of the relation between the numerical values of the fluxes and the corresponding values of the T and S variations, a difference in $T^* - T_1$ equal to about

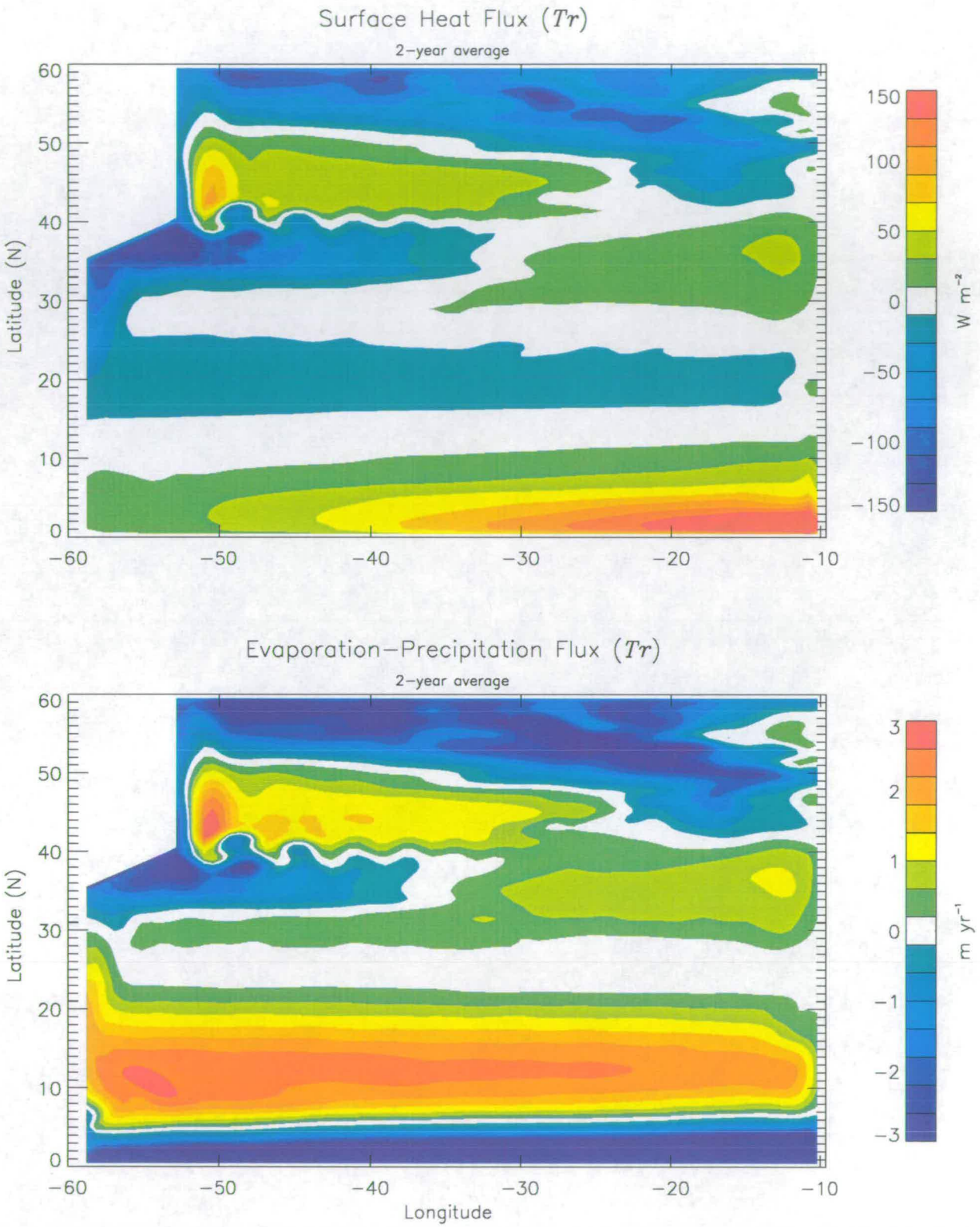


Figure 6.24: Surface fluxes averaged over the 2-year assimilation experiment for Tr. Total heat flux (top, positive downward) and Evaporation-Precipitation (bottom).

3°C yields an increase in Q of 100 W m^{-2} and a difference in $S^* - S_1$ equal to 0.15 psu yields an increase in E-P of 1 m yr^{-1}. To calculate the averages of both fields, Q and E-P, they have been stored at each model time step.

In the truth run, heat is gained by the ocean (positive values) at low latitudes whereas the ocean releases heat (negative values) to the atmosphere at high latitudes (Fig. 6.24, top). Furthermore, the Gulf Stream divides a southern negative region, where heat is released to the atmosphere, from a northern positive one, where heat is gained by the ocean. A similar pattern is present for the E-P salt flux, with some discrepancies at low latitudes (Fig. 6.24, bottom). Near the equator, an excess of precipitation is present (negative blue area), whereas evaporation is dominant further north (positive red area, between 6° and 22°N). North of 30°, the excess of precipitation (the negative areas south of Gulf Stream and near the northern border) is accompanied by a heat flux towards the atmosphere (i.e. freshening and cooling), and vice-versa for the evaporative red area north of the Gulf Stream (i.e. increasing salinity and warming).

We shall now consider the difference, in terms of total heat and E-P fluxes, between the truth run and the other three runs, that is parallel, A_{ST} and A_{SZ}, respectively. Figure 6.25 shows this difference for the parallel run. The area A is also highlighted so as to facilitate the comparison of this figure with the water mass budget analysis of section 6.5.2. The positive sign in the surface heat flux difference (top of Fig. 6.25) essentially means that the SST of Pa is higher than that of Tr (cf. Eq. 6.1), and vice-versa for the negative sign. Analogously, the positive sign in the E-P flux (bottom of Fig. 6.25) means that the SSS of Pa is higher than that of Tr (cf. Eq. 6.2), and vice-versa for the negative sign. Therefore, the differences present within the area A in Fig. 6.25, show that Tr is generally saltier and warmer than Pa (the negative blue regions) and this is agreement with the water mass budget analyses for the density range 25.5–26.4 kg m^{-3} (see subsection 6.5.2 and Fig. 6.19a).

The differences between Tr and A_{ST} are shown in Fig. 6.26. They are generally reduced, with respect to Pa, as expected, especially those in the heat flux field, because of the assimilated temperature data. One exception is represented by the positive difference along the Gulf Stream, which is in agreement with the the PV analysis on the level $\sigma_t = 26.0$ kg m^{-3} discussed in subsection 6.5.1 (Fig. 6.16).

The E-P analysis is particularly useful for it allows us to check how the salinity

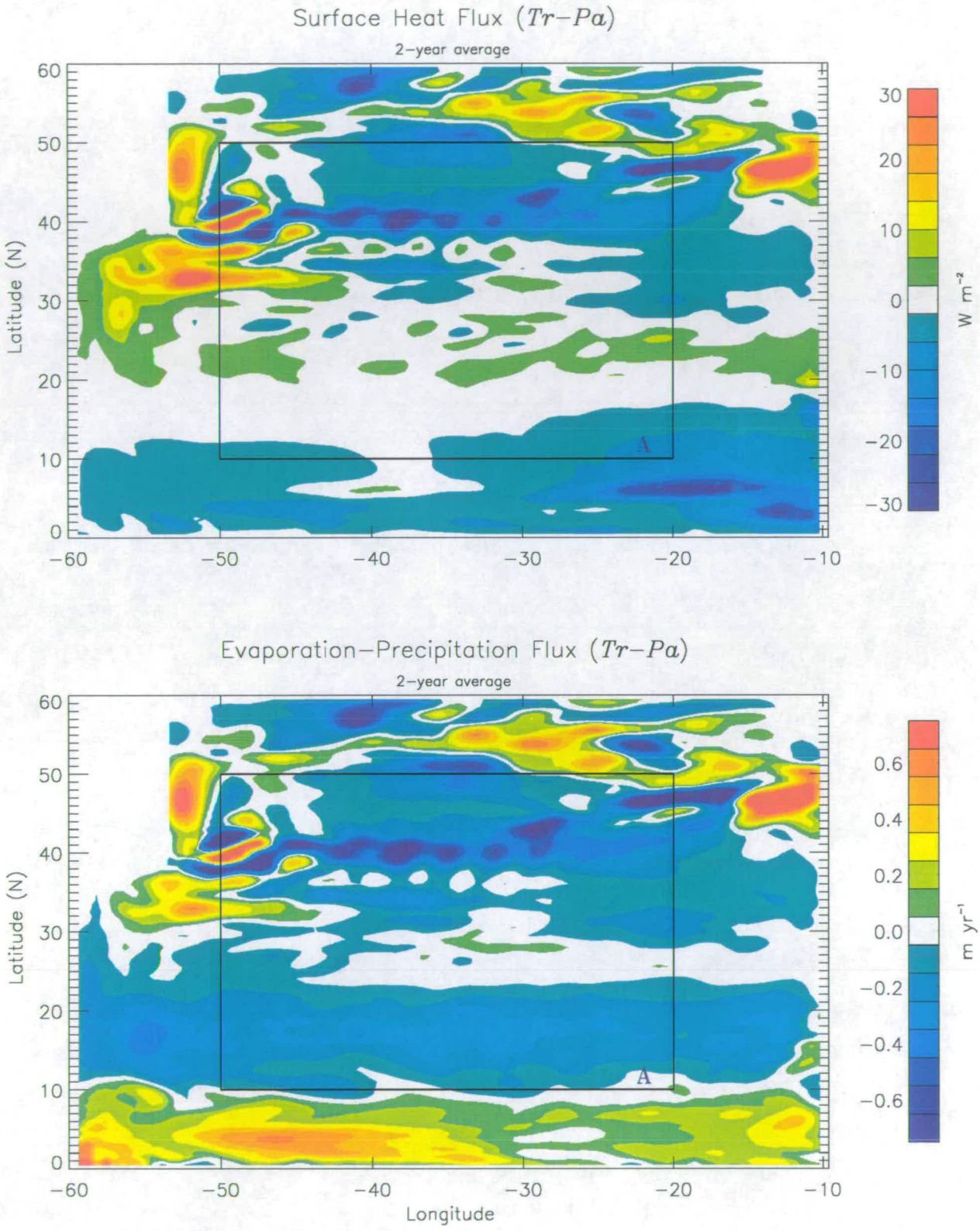


Figure 6.25: As in Fig. 6.24 but for Tr–Pa. Area A is highlighted.

at the surface is reproduced by the salinity scheme. Yet, a proper comparison has to be carried between A_{ST} and A_{SZ}, because they use the same temperature analysis but a different salinity analysis. Let us introduce the differences between Tr and A_{SZ} then: they are shown in Fig. 6.27. The total heat flux difference (top panel) is, not surprisingly, very similar to that for A_{ST}. Discrepancies are instead more evident in the E-P field. In particular, A_{ST} has smaller differences with respect to Tr than A_{SZ} almost everywhere, with the major exception on the north-eastern edge of area A (the more pronounced negative difference). The fact that there are improvements in the E-P flux, i.e. in the SSS, in A_{ST} compared to A_{SZ}, is quite encouraging because the near surface salinity is a weak point in the salinity scheme.

6.8 Summary and discussion

The method for updating the salinity field during the assimilation of temperature data has been tested in a synthetic data assimilation experiment framework. Four runs were considered: the truth, the parallel and two assimilation runs, one in which our method is applied (A_{ST}) and the other in which salinity is left unmodified during the temperature assimilation (A_{SZ}). The two assimilation runs were started from different initial conditions with respect to the truth run and were also forced by a wind stress 15% larger than Tr (as in Pa). This was therefore a more severe test than the more common identical twin experiments, in which only the initial conditions differ. Vertical temperature profiles down to a depth of 525 m were taken as synthetic data from Tr and assimilated along 5 sections (3 meridional and 2 zonal, which after spreading the data either side of these sections covered about a sixth of the whole model domain) every 30 days and for two years into A_{ST} and A_{SZ}.

The salinity method has proven to be effective in reconstructing the salinity profiles. In terms of salinity rms errors, A_{ST} is globally 15% better than A_{SZ} (and even better with respect to Pa). A study of the vertical structure of the rms errors has shown that, while the T–S preservation is considerably better than $S(z)$ persistence below 100 m, above this depth the results of A_{ST} and A_{SZ} are comparable, but with A_{SZ} slightly better. In fact, near the surface it is known that the T–S preservation is generally not appropriate. However, a good representation of the SSS, or indeed, the use of observed SSS (which should become available in the near future, e.g. through the Argo floats or the SMOS satellite mission), will certainly improve the upper part of the vertical

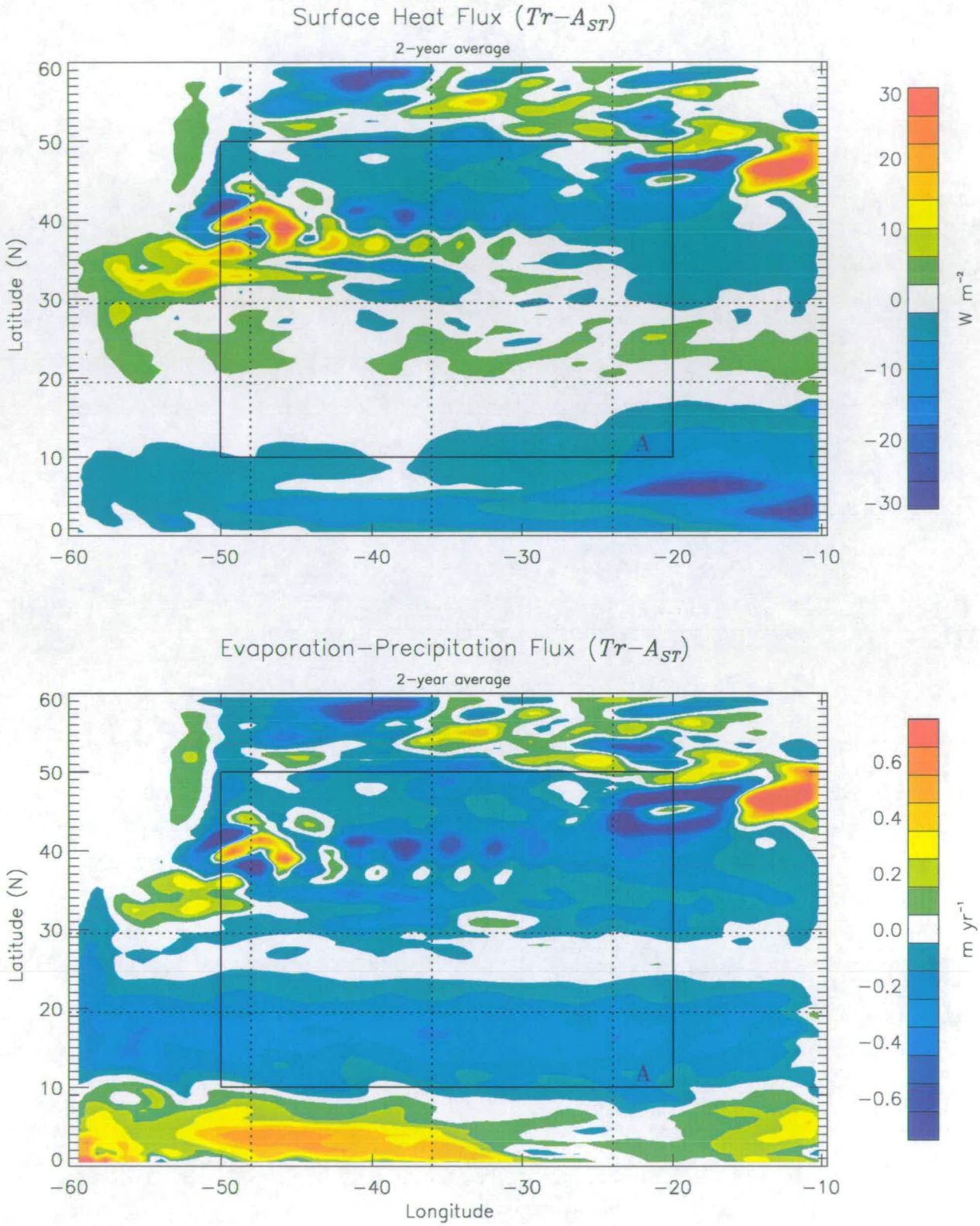


Figure 6.26: As in Fig. 6.25 but for $Tr-A_{ST}$. The 5 assimilation sections are highlighted.

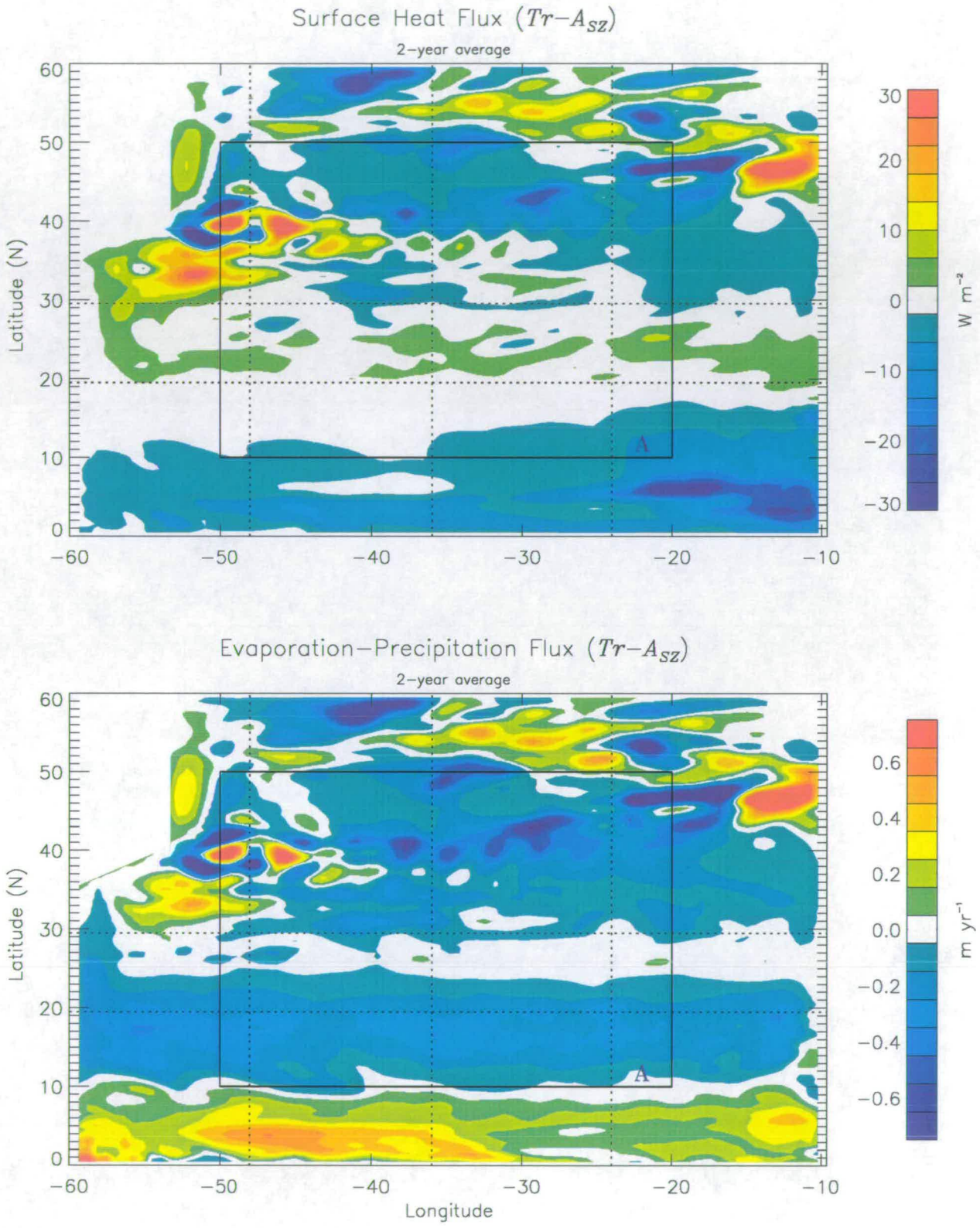


Figure 6.27: As in Fig. 6.26 but for $Tr-A_{SZ}$.

salinity profiles.

Even if the results of applying the salinity scheme are quite encouraging, there appears to be a lower bound to the improvement of A_{ST} and this is determined by the difference in the initial condition between A_{ST} and the truth run. Because the assimilation method uses the model background for its analysis, it is not possible in principle to reduce this distance, given that in A_{ST} the different wind forcing keeps forming water masses which are in error with respect to the truth run. Further, in the experimental configuration chosen, it was even more difficult for A_{ST} to recover the right salinity in certain locations, such as in the northern part of the sub-tropical gyre, because there the truth run was systematically forming saltier and warmer water masses which could not be found in the water column in A_{ST}. It is possible that reversing the order of the Tr and Pa better salinity profile reconstructions could be achieved by the salinity scheme.

We have also noted that the changes introduced by the data assimilation are partly smoothed out. This is due to the relatively small decorrelation radius adopted in this study but also to the the fact that the 'wrong' forcings tend to diminish the benefit of the changes inserted in the assimilation through air-sea flux exchange. This was confirmed by the analyses of two very useful quantities: the water mass budget, i.e. the difference in T–S space between two runs, and the *inventory*, i.e. the collection of changes inserted directly by the assimilation. In particular, we noted a mismatch between the water mass budget difference immediately after the last assimilation step (i.e. Tr–A_{ST}) and the 2-year accumulated inventory for A_{ST}. The latter was, in fact, considerably larger than the water mass budget, indicating that part of the changes inserted in the assimilation were not retained by the ocean model. A similar behaviour held true for the other assimilation run, A_{SZ}. Possible solutions can be represented by the use of a larger decorrelation length and/or the insertion of the T and S analyses in a more continuous manner, i.e. dividing the increments introduced in one single step over a larger time period (an example of this is given with the assimilation experiment in chapter 7). The latter would have the advantage of reducing abrupt density changes at assimilation time.

Furthermore, it has been shown that the changes introduced by the assimilation decrease with time, therefore in order to make the data assimilation more effective one could consider assimilating along different sections (instead of keeping them fixed,

as we did) or introducing episodically and locally salinity information from the truth run. The latter would certainly be a more satisfactory solution but, in reality, this depends upon the availability of new observations, that is of temperature observations in the former case and temperature plus salinity observations in the latter. Of course, it is more likely that only temperature observations will be available but the benefit of updating the salinity directly would be undoubtedly greater.

Chapter 7

Assimilation in a Global Ocean Model

In this chapter we evaluate the role of salinity in the framework of temperature data assimilation in a global ocean model that is used to initialise seasonal climate forecasts. It is shown that even in this case the univariate assimilation of temperature profiles, without attempting to correct salinity, can induce first order errors in the subsurface temperature field. The salinity scheme is then used to improve the salinity field.
Two data assimilation experiments are performed for the 9-year period 1990-1998. These show that the salinity scheme is effective at maintaining the halocline and thermocline structures especially in tropical regions. In addition to the improvement of the mean state, the scheme allows more temporal variability than relaxation to climatological data. Some limitations of the scheme are on occasion apparent, however. These limitations might be reduced in the future by use of altimeter sea level or sea surface salinity observations from satellite.

7.1 Introduction

A currently-used strategy to produce ocean analyses from which to begin seasonal forecasts is to force an ocean model with the recent history of wind stress, heat fluxes and precipitation minus evaporation fields, and then use the analysed ocean state as initial conditions in a coupled ocean-atmosphere model. It is mainly the subsurface structure of the temperature fields which provides predictive skill on the time scale of a few months, at least in the tropics. The analysed ocean states are not perfect, however, as both forcing fields and ocean models contain errors. Ocean temperature data assimilation has proven to be capable of improving the simulated upper ocean

temperature structure in such a way as to be beneficial for seasonal climate forecasting (e.g. Alves *et al.*, 1999, Ji *et al.*, 1998, Fischer *et al.*, 1997, Rosati *et al.*, 1997). The seasonal forecasting system at the European Centre for Medium-Range Weather Forecasts (ECMWF) uses an ocean analysis in which in situ temperature data have been assimilated.

Not much attention has been given to salinity in the context of temperature data assimilation for seasonal climate forecasts. Salinity observations in the western equatorial Pacific revealed large interannual variations of salinity at subsurface levels (Kessler, 1999, Ji *et al.*, 2000). The physical causes for the observed anomalies are not fully explored yet, and it is therefore not clear to what extent the ocean analyses at ECMWF, in which salinity is treated as a prognostic tracer, can reproduce the observed changes. In this chapter we study the salinity role in the HOPE model and evaluate the impact of the salinity scheme on it. This work was carried out by the author, in collaboration with the Seasonal forecasting group, whilst working at ECMWF.

The chapter is organised as follows. In section 7.2 the ocean model, the data assimilation system and the experiments are described. Results from the latter are presented in section 7.3. A discussion is provided in section 7.4.

7.2 Experimental set-up

This section presents the experimental set-up adopted in this chapter. The set-up chosen is slightly different from that used in the operational mode at ECMWF in that some parameters have been changed for this study. In particular, we use manually quality controlled data so guaranteeing that the same temperature data are used in both experiments. Further, the maximum depth to which data are assimilated is reduced from 1050 m to 425 m, to match the bottom of the TAO mooring observation profiles. Finally, a 3-day window is used in our experiments instead of a 10-day window in the operational set-up, thus giving more weight to the temperature observations in our experiments. In the following, a brief description of the ocean model is given first. Then the data assimilation system is described and, finally, the two experiments to test the salinity scheme are outlined.

7.2.1 Ocean model

The ocean model used in this chapter is the Hamburg Ocean Primitive Equation (HOPE) model (Wolff *et al.*, 1997) modified by the Seasonal Forecast Project at the ECMWF and utilised for seasonal forecasting in coupled mode (e.g. Stockdale *et al.*, 1998, Alves *et al.*, 1999). Here we only describe its main features. It is a 3-D primitive equation model using z-coordinates and a variable sea surface height in a global domain. The model uses an E grid with a horizontal resolution of 2.8° x 2.8° (longitude/latitude), plus an equatorial refinement: the meridional resolution is 0.5° within 10° of the equator, and increases smoothly from 0.5° to 2.8° between 10 and 30 degrees. In the vertical there are 20 levels, 12 of which are in the upper 425 m. The parameterisation of the vertical mixing uses a Richardson number dependent K-scheme, a modification of that of Pacanowski and Philander (1981). The K-value is increased mainly within the mixed layer, which is diagnosed as the depth-range in which temperatures differ by less than 0.5°C from the Sea Surface Temperature (SST). In order to avoid numerical problems with static instability, an *ad hoc* convection scheme is included, which mixes two adjacent model levels if $d\rho_\theta/dz > 0$ locally, where ρ_θ is the potential density.

The model is forced by daily average momentum, heat and fresh water fluxes taken from the ECMWF atmospheric analysis system. In order to avoid unrealistic drifts, additional weak restoring terms (time scale of 1 year) are applied to the 3-dimensional T and S fields by using annual climatological values from Levitus and Boyer (1994) and Levitus *et al.* (1994) (hereafter referred to as Levitus). An additional weak relaxation (time scale of 1 year) is applied to the Levitus surface S implying a damping time of 6 months for the surface salinity. A strong relaxation (time scale of 3 days) is applied to the surface temperature using weekly observational data (Reynolds and Smith, 1995).

7.2.2 Data assimilation system

The data assimilation method used in this study is an Optimal Interpolation (OI) derived from Smith *et al.* (1991). The observations utilised are subsurface temperature measurements, obtained mainly from the United States National Oceanographic Data Center through the GTSPP (Global Temperature Salinity Pilot Project) data distribution network. The main components of the observing system are the XBTs and TAO moorings in the equatorial Pacific. TAO-type moorings in the tropical Atlantic

from the developing Pirata array and PALACE float data distributed through the GTS are also used, even though these data types are much more recent and only impact towards the end of the experiments. The OI method is used to map these subsurface temperature observations onto the model background. The observed T profiles are first interpolated onto the model levels, which are treated independently from each other in the OI. The OI of the temperature field (with the model T used as a background) is performed every 3 days, using observations grouped in 3-day bins in the TAO region and 10-day bins elsewhere. The data outside the TAO region are thus used more than once. Following Smith *et al.* (1991), the background is given the same weight as an individual observation. The background errors are expressed as anisotropic and inhomogeneous gaussian functions whose correlation length scales near the equator are 1500 km zonally and 200 km meridionally. In all the experiments described in this chapter the assimilation is done over the levels from 2 to 12 (i.e. between 30 and 425 m depth). For further detail on the OI implementation in the HOPE model see Alves *et al.* (1999).

In order to obtain the updated vertical salinity profiles (i.e. the salinity analyses), the temperature profiles obtained by the OI are processed through a slightly modified version of the salinity scheme. In fact, in order to avoid applying the T–S relationships of near-surface water masses to deeper layers, the model T–S relationship from the upper 50 m of the water column is used only if the corresponding OI temperature is also near the surface. Otherwise, no change is made to the model salinity (see discussion in section 3.3.2).

In addition, a latitudinal filter has been applied to the salinity increments such that the whole salinity increment is applied only within 30 degrees of the equator. Outside this region, the weight given to the salinity analysis diminishes linearly to zero at latitudes poleward of 60 degrees. This is done to avoid implementing the salinity scheme in areas where the stratification is weak and $S(z)$ persistence is more appropriate (see Emery and Dewar, 1982).

7.2.3 Description of the experiments

Three experiments, listed in Table 7.1, are run to test the salinity scheme. They all use the ocean model set-up described in section 7.2.1. The initial conditions are taken from a spin-up run which has been relaxed with a 10-day time scale to the Levitus

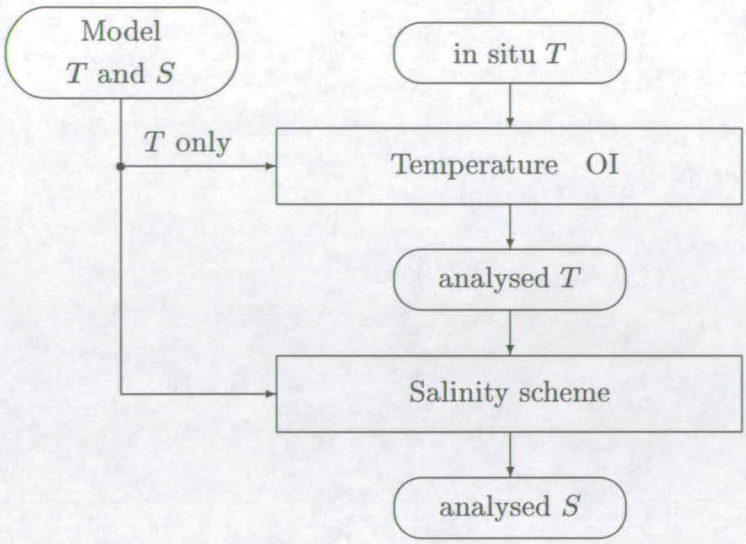


Figure 7.1: Schematic of the data assimilation system.

climatology at all depths. The experiments are run for the period 1990 to 1998.

Experiment	Period (yr)	Assimilation
CNT	1990–1998	none
TOI	1990–1998	OI
TOIS	1990–1998	OI+SS

Table 7.1: The three experiments. OI stands for Optimal Interpolation (temperature data only) and SS for the salinity scheme.

To assess the impact of the salinity scheme on the OI analysis, two experiments are considered: one in which the salinity scheme is added to the OI (*TOIS*) and the other in which only the OI is used (*TOI*). In both experiments the temperature observations are presented to the OI procedure first. In *TOIS* the salinity scheme is applied locally as a second step at each model grid point, as described in section 7.2.2. The T and S increments thus calculated are then uniformly added to the model background over a 3-day period, in order to allow the model to gradually adjust to the analysed density field. For reference, a run with no data assimilation is also performed (*CNT*), which will be mainly used to check how the data assimilation affects systematic model errors.

7.3 Assimilation results

In this section we analyse the impact of the salinity scheme, by comparing the two runs *TOIS* and *TOI* with observations (e.g. Levitus climatology) and the experiment *CNT*. We first analyse the 9-year mean in section 7.3.1 and then we investigate the salinity and the sea level variability in sections 7.3.2 and 7.3.3, respectively.

7.3.1 Analysis of the 9-year means

To investigate whether the salinity scheme can improve the mean state, we examine time-averaged fields from the entire run (i.e. the 9-year mean 1990-1998). We first consider the equatorial section through the Pacific and Atlantic oceans. The equatorial Pacific is an area relatively rich in T data and it is also a very important for seasonal forecasting.

Figure 7.2 and Figure 7.3 show temperature and salinity sections along the equator for the Pacific and Atlantic ocean. In each figure, panel (a) shows the climatological average from Levitus and panels (b-d) show the differences between *CNT*, *TOI*, *TOIS* and Levitus. Although we will use Levitus as a measure of climatology, it should be born in mind that it is not an absolute measure of the mean state of the oceans. For example the TAO thermal data have a somewhat different climatology in the west Pacific, either because of a different averaging period or a better data coverage during the TAO period. We will first discuss temperature. The dominant feature in Figure 7.2a is the sloping thermocline, which is an important feature of these two oceans. The *CNT* experiment shows substantial deviations of up to 3°C at the depth of the thermocline. The *CNT* experiment is warmer than Levitus in the eastern Pacific and in the Atlantic ocean, and colder in the western Pacific. The warmer temperatures in the Atlantic and eastern Pacific ocean are due to systematic bias in the *CNT* experiment. This bias is linked to a too diffuse thermocline in the model, possibly due to limitations of the mixing scheme combined with a poor vertical resolution. The assimilation of temperature profiles helps to control these errors. Figures 7.2c and 7.2d show that the errors are substantially reduced in *TOI* and *TOIS*, as a result of temperature assimilation. The differences between the assimilation experiments and Levitus in the western Pacific are likely to indicate differences between the Levitus and TAO climatologies. Levitus is based on data from 1900 to 1993 whereas the

experiments span the 1990-1998 period. We compared the Levitus climatology with the TAO climatology from Yu and McPhaden (1999). and found that TAO was colder by about 2°C around 150 m depth in the western Pacific. Since the long-term mean of *CNT* is already consistent with the TAO data, the assimilation of temperature data does not change the thermal structure of *CNT* in the subsurface western Pacific very much.

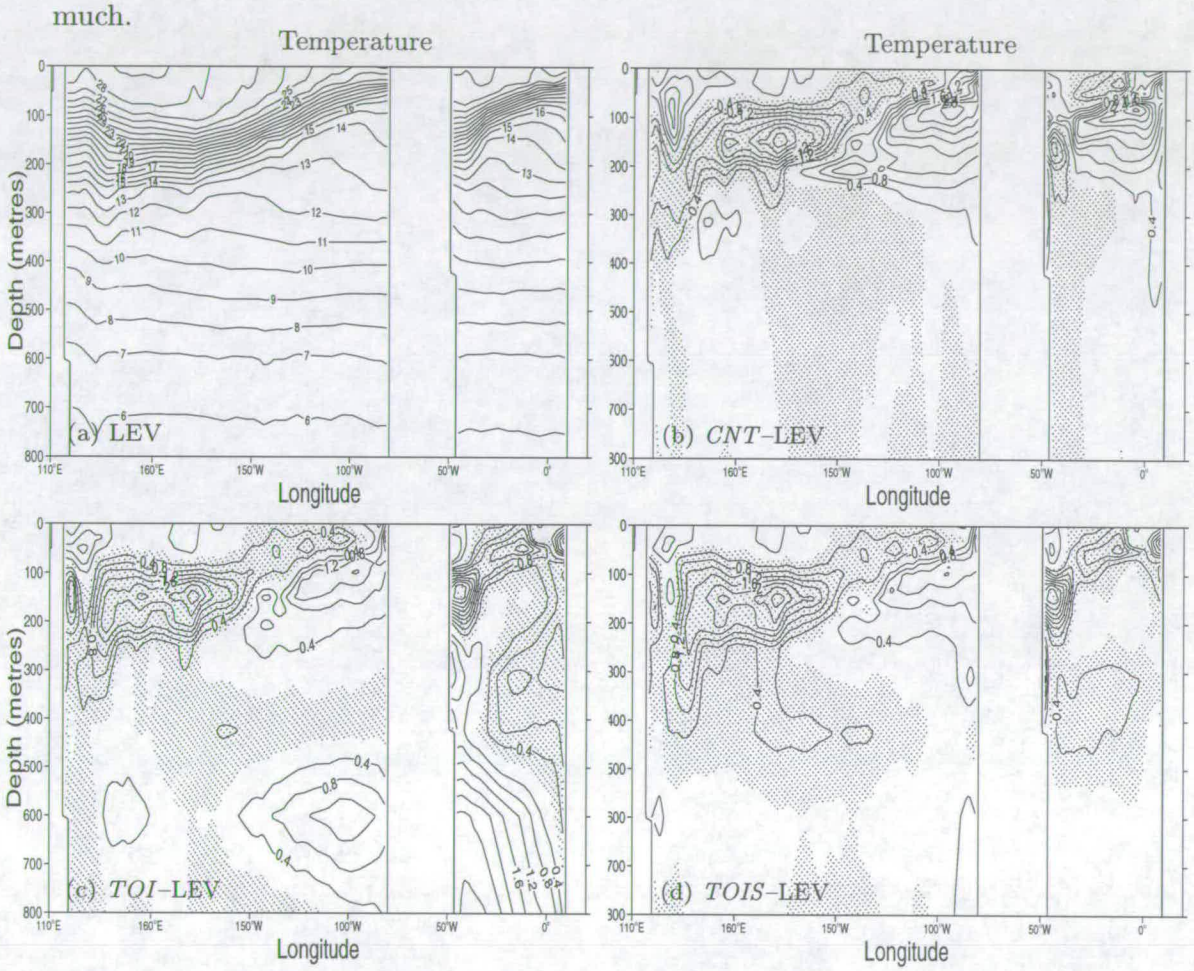


Figure 7.2: Equatorial sections of temperature. (a) Annual mean Levitus climatology; (b) the difference between the exp. *CNT* and Levitus averaged over the 9-year mean (1990-1998), (c) as for (b) but for the exp. *TOI* and (d) as for (c) but the exp. *TOIS*. Negative values are shaded.

Both the *TOI* and *TOIS* experiments improve the thermal state of the model at the thermocline level. Below the thermocline, however, significant differences with respect to Levitus, appear in *TOI* which is 1°C colder than Levitus around 300m and more than 2°C warmer than Levitus below 500 m in the Atlantic ocean. It is 1.2°C warmer than Levitus below 500 m in the eastern Pacific ocean. It must be noted that this corresponds to a vertical displacement of the isotherms on the order of 100 to

200 m at these depths. The differences between *TOI* and Levitus are thus quite large. These spurious differences are not present in *CNT* and must therefore be induced by the assimilation. They disappear in *TOIS* showing that the salinity scheme helps to improve the deep ocean thermal structure in the assimilation. A discussion about the possible causes of the differences in the two experiments *TOI* and *TOIS* is deferred to later in this section, after introducing the salinity fields.

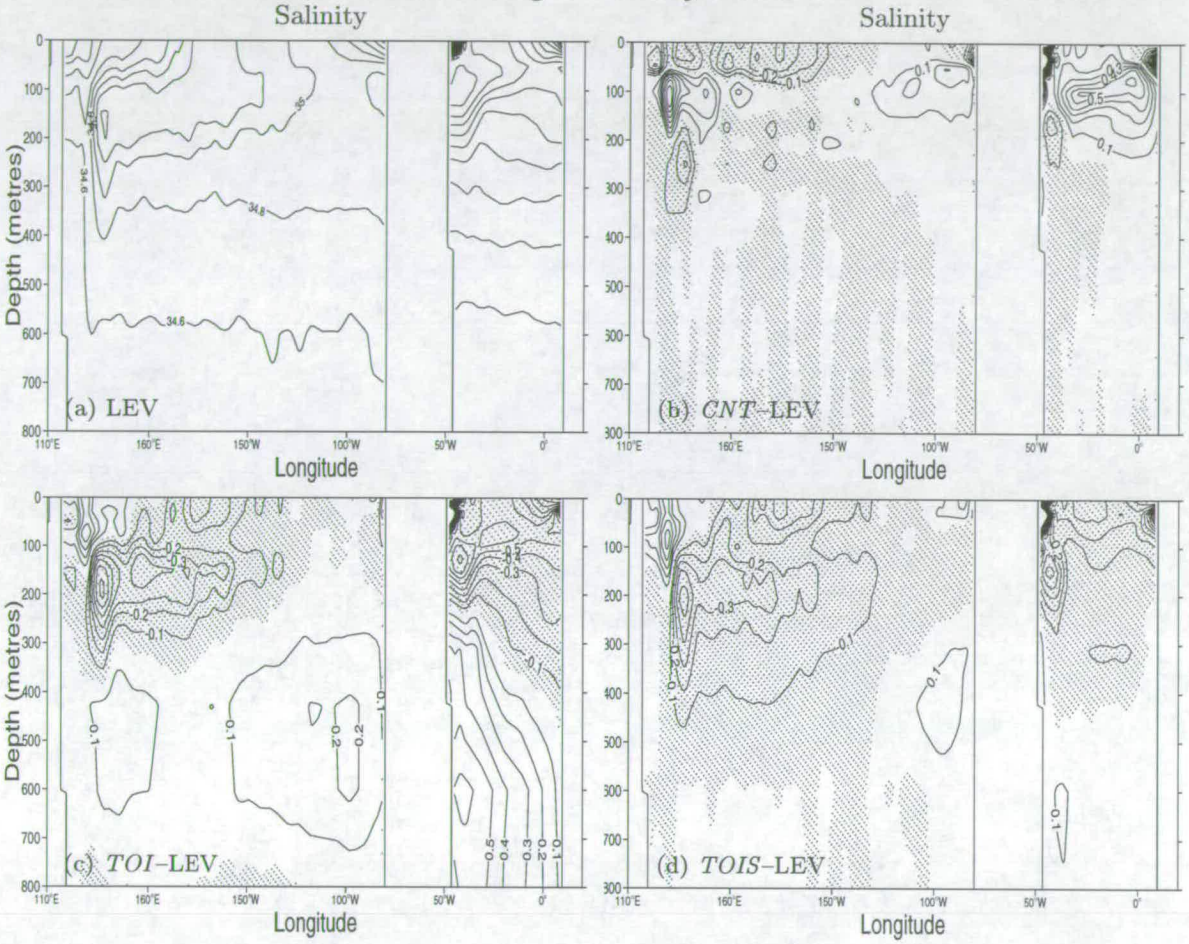


Figure 7.3: As in Fig. 7.2 but for salinity.

Figure 7.3 shows the salinity sections corresponding to the temperature sections from Figure 7.2. The Levitus climatology (Figure 7.3a) is characterised by relatively fresh water mass close to the surface, an intermediate salinity maximum around the depth of the thermocline, and monotonically decreasing salinity below. Low surface salinities are present at both the eastern and western boundaries in both oceans due to strong precipitation and/or river runoff. The subsurface salinity maximum is most pronounced in the western part of the basins. Because of errors in the specified surface freshwater flux and in the model formulation, *CNT* is different from Levitus (Fig-

ure 7.3b). It is fresher near the boundaries in the surface layer, and saltier around the subsurface salinity maximum. However, for the section shown, the departure from climatology is small below 200 m.

Figure 7.3c shows that the assimilation of temperature data in experiment *TOI* introduces large changes in the salinity field in the subsurface. In particular, salinity is lower than Levitus at around 200 m (by up to 0.8 psu in both the western Pacific and Atlantic). Below 300 m, salinity is higher than Levitus (by up to 0.2 psu in the Pacific and 0.6 psu in the western Atlantic). This indicates an export of salt from intermediate to deeper layers, as will be discussed later. The additional correction of salinity in experiment *TOIS* (Figure 7.3d) results in smaller differences with respect to Levitus salinity. The large differences with Levitus that were present below 300 m in experiment *TOI* essentially disappear. At the thermocline level, they are significantly diminished in the Atlantic ocean. In the Pacific, the maximum deviations from Levitus are halved. All in all, below the depth of 50 m, *TOIS* shows a promising improvement over *TOI* when compared to Levitus. The behaviour of all three experiments is very consistent in the surface layer, but as mentioned earlier, we do not expect the salinity scheme to improve surface layer salinity.

We can now start discussing possible causes of the differences between *TOI* and *TOIS*. Figure 7.4 shows meridional sections along 30°W of climatological temperature and of an instantaneous model output from *TOI*. After only three months, the temperature structure reveals large errors in the equatorial region. The isotherms between 5°N and 5°S have been displaced downwards in an unrealistic way in *TOI*. This is most likely caused by strong vertical mixing or convection in *TOI*. Very weakly stratified or unstable water columns can be created as the result of temperature assimilation in regions where there is a subsurface salinity maximum. Below this maximum, S decreases with depth and static stability is ensured by the temperature stratification. If the temperature increments given by the OI scheme in *TOI* are such as to decrease the vertical T stratification in these regions, (while S is left unchanged) the water column may become statically unstable. The model mixing scheme then responds by spuriously increasing the vertical mixing. This is strongly reduced by the salinity scheme in *TOIS*: the scheme adjusts the salinity profile in order to preserve T–S characteristics and thus mainly ensures static stability.

The spuriously increased mixing is most likely to occur where the salinity maximum

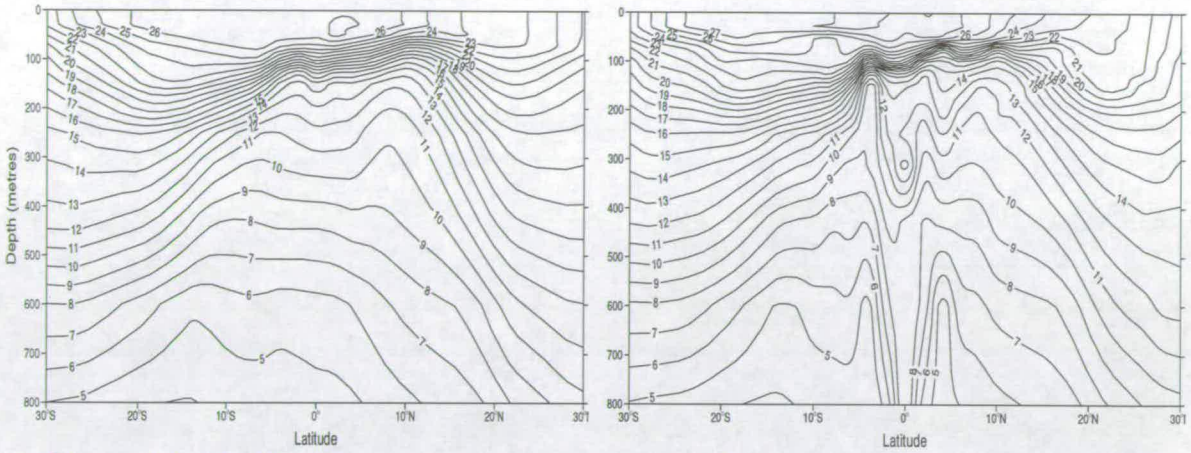


Figure 7.4: Meridional temperature section at 30°W. Left: initial conditions (i.e. climatology). Right: instantaneous field after a 3-month model integration with an Optimal Interpolation temperature assimilation (experiment *TOI*).

in the main thermocline is relatively prominent or, more generally, when the salinity gradient below the S maximum is large. This explains why differences between *TOI* and *TOIS* are more pronounced in the equatorial Atlantic where the subsurface S maximum is stronger than in the Pacific.

An objective way of identifying those areas most likely to be affected by the enhanced mixing is provided by the following analysis. The stability of the water column can be expressed as the derivative of $\rho_\theta = \rho_\theta(\Theta, S)$ with respect to depth (z positive upward):

$$\frac{d\rho_\theta}{dz}(\Theta, S) = \left(\frac{\partial \rho_\theta}{\partial \Theta}\right)_S \frac{d\Theta}{dz} + \left(\frac{\partial \rho_\theta}{\partial S}\right)_\Theta \frac{dS}{dz} = -\alpha\, \rho_\theta\, \frac{d\Theta}{dz} + \beta\, \rho_\theta\, \frac{dS}{dz} \tag{7.1}$$

where ρ_θ is the potential density, θ the potential temperature α and β the thermal and haline expansion coefficients. In a statically stable water column $d\rho_\theta/dz$ is negative. In *TOI* the temperature profile is changed while the S profile is retained. If dS/dz is positive, this can lead to a statically unstable profile if temperatures are reduced at that depth by the OI. The critical value of the temperature stratification $(d\Theta/dz)_U$, which would cause convection to begin (when $d\rho_\theta/dz$ is zero) is given by:

$$\left(\frac{d\Theta}{dz}\right)_U = \frac{\beta}{\alpha}\, \frac{dS}{dz} = \gamma\, \frac{dS}{dz} \tag{7.2}$$

where $\gamma = \gamma(\Theta, S) > 0$.

If we assume that temperature variability in the thermocline occurs mostly through vertical displacements of the water masses, it is possible to compute the minimum vertical displacement of the water column for which this will happen. The smaller this

value, the greater the risk of spurious convection. Figure 7.5 shows the results of such evaluation with the temperature and salinity fields taken from the Levitus climatology along the equatorial section (left) and the 30°W meridional section (right). The solid lines show the minimum displacement, while the dashed line gives the depth at which instability occurs. The plot on the left shows that the Atlantic sector (between 50° W and 10° E) is more prone to instability than the Pacific sector. In the Atlantic, upward shifts of the temperature profile of between 15 m and 60 m (solid line) are generally sufficient to make the water column unstable at depths that vary between 90 m and 240 m (dashed line). In the Pacific these displacements are always more than 70 m and generally well over 100 m.

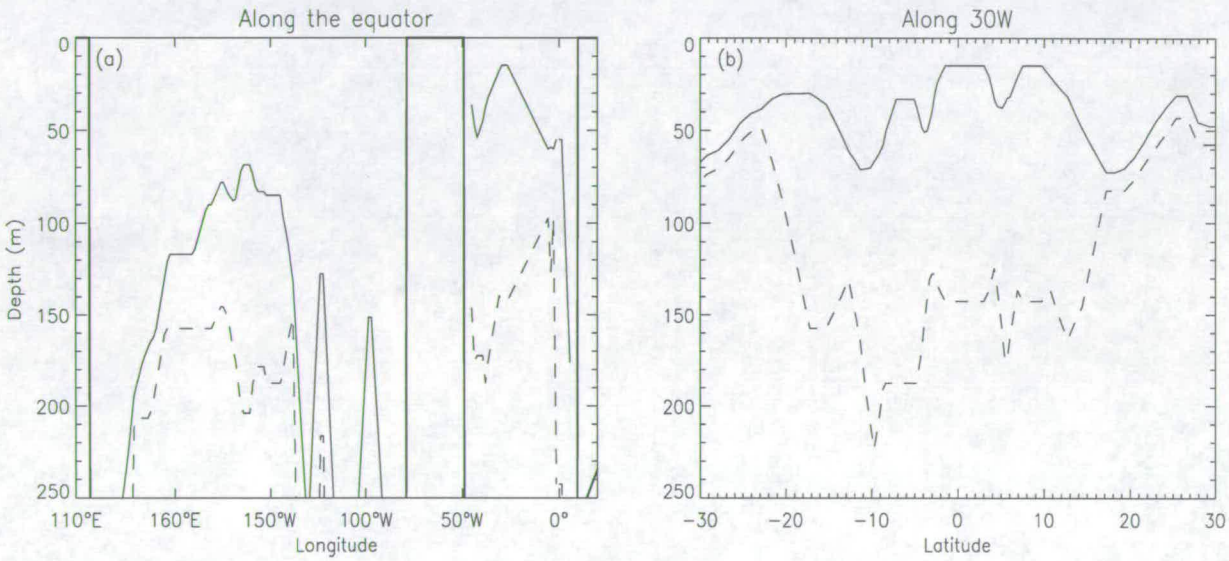


Figure 7.5: Minimum vertical displacement which would destabilise the water column (solid line) and depth of the corresponding level (dashed line). Along the equatorial section (a) and Atlantic meridional section at 30°W (b).

The above analysis yields a more rigorous confirmation of what could have been deduced from the climatological S in Fig. 7.3a: the S maximum in the Atlantic is up to 1 psu larger than in the Pacific, but the S values at depth are very close in the two oceans.

The smaller amount of temperature data collected in the Atlantic is another contributing factor as to why the T differences between *TOI* and *TOIS* are more pronounced in the equatorial Atlantic than in the Pacific, in particular in the thermocline. In the Atlantic during 1990-98 the main source of T profiles are XBT casts along ship tracks, so that observations at one location are only made a few times per year. Some

of these will tend to generate spurious mixing and to erode both the temperature and salinity stratification. The only opposing effect to these damages to the T and S fields will be the relaxation to climatology which acts on the slow time scale of 1 year. On the other hand, in the Pacific ocean there are frequently repeated observations at the same location from the TAO array. Once the salinity gradients have been eroded, the following temperature observations can constrain the temperature field without generating any spurious mixing or convection. The temperature field is thus very well constrained whereas the salinity field is still in error.

Note that in *TOI*, the assimilation makes no temperature increments below 425 m depth. This is an extreme "data sparsity" problem, and means that if the analysis starts to go wrong, there is nothing to bring it back other than the very slow relaxation to climatology. Thus, once a warm column begins to develop at these depths, it may be hard to stop. Extending the temperature analysis to lower depths might reduce this problem, or at least push it down deeper. In the experiments presented here, we chose 425 m instead of the operationally used 1050 m in order to match the depth to which TAO observations extend. It is mainly XBT observations that extend to greater depth. It might also be possible to formulate a bottom boundary condition of some sort to the temperature increments to help ensure stability. It is clear, however, that the present formulation of *TOI* has severe problems in maintaining the thermocline in the equatorial Atlantic.

To further study the impact of the salinity scheme, we consider now a meridional section at the same location as for Figure 7.4 (30°W) but now for the nine year mean of the experiment. Figures 7.6a-d show the T and S fields for both *TOI* and *TOIS* and the difference between the two experiments (Figs. 7.6e-f). The T field is characterised by a tight thermocline between 8°S and 13 °N, whereas the S field presents two salinity maxima, and corresponding haloclines, one at about 17°S and the other at about 24°N. In Figs. 7.6a-b, starting at the base of the main thermocline, an anomalous warm and salty water column is seen in *TOI* in the neighbourhood of the equator. Such a feature is not present in the Levitus climatology: it is a manifestation of the spurious mixing activity discussed previously. On the other hand, the T and S fields of *TOIS* look more realistic (Figs. 7.6c-d), with only a slight bulge in the salinity field on the 34.6 psu isohaline near the equator and a corresponding though smaller bulge in the T field (5 and 6°C isotherms). This suggests that some strong mixing may still be

occurring intermittently in the *TOIS* experiment, probably due to the fact that the assimilation does not take into account the actual depth of each observation profile (the deepest assimilation level is fixed, at 425 m). The difference between *TOI* and *TOIS* along this section (Figs. 7.6e-f) shows large discrepancies in T and S, especially in the 7°S - 8°N band, where the stability analysis (Fig. 7.5b) shows that instabilities are most likely.

We are now going to investigate the effect of the differences in T and S between *TOI* and *TOIS* on the density field. Fig. 7.7a shows an equatorial section of density and Figures 7.7b-c of temperature and salinity, respectively. In both oceans *TOI* is lighter than *TOIS* at the pycnocline level (around 150 m) and denser below. In the Pacific ocean, T differences between the two experiments are small (Fig. 7.7b). The density differences are thus mainly linked to the salinity (e.g. saltier water mass in *TOI* below the pycnocline results in denser water mass). In the Atlantic ocean, there is a competing effect of T and S on the density field (e.g. with *TOI* warmer and saltier below the thermocline). However, the salinity effect is once again dominating.

It is interesting to see the effect of these density differences between the two experiments in term of sea level. Because of the compensating effects of T and S differences, and because of vertical compensation between denser water mass in *TOI* below the pycnocline and lighter water mass above, the overall difference in sea level is generally small. Along the equator in the Pacific and in the Atlantic, *TOIS* has a higher sea level than *TOI*, but the difference does not exceed 2 cm for the nine-year average (not shown).

7.3.2 Salinity variability

In the previous section we have shown that the use of the salinity scheme generally improves the mean state of the ocean. However, for seasonal climate forecast initialisation, the variability is also of concern. In this section we will examine how the salinity scheme affects the salinity variability both by looking at differences between the time varying salinity fields in *TOI* and in *TOIS* and by comparing them with other modelling and observational results. Comparisons with CTD observations will also be made. In the next section we will compare the simulated sea level with Topex/Poseidon (T/P) sea level observations.

We focus attention on the tropical western Pacific ocean because subsurface salinity

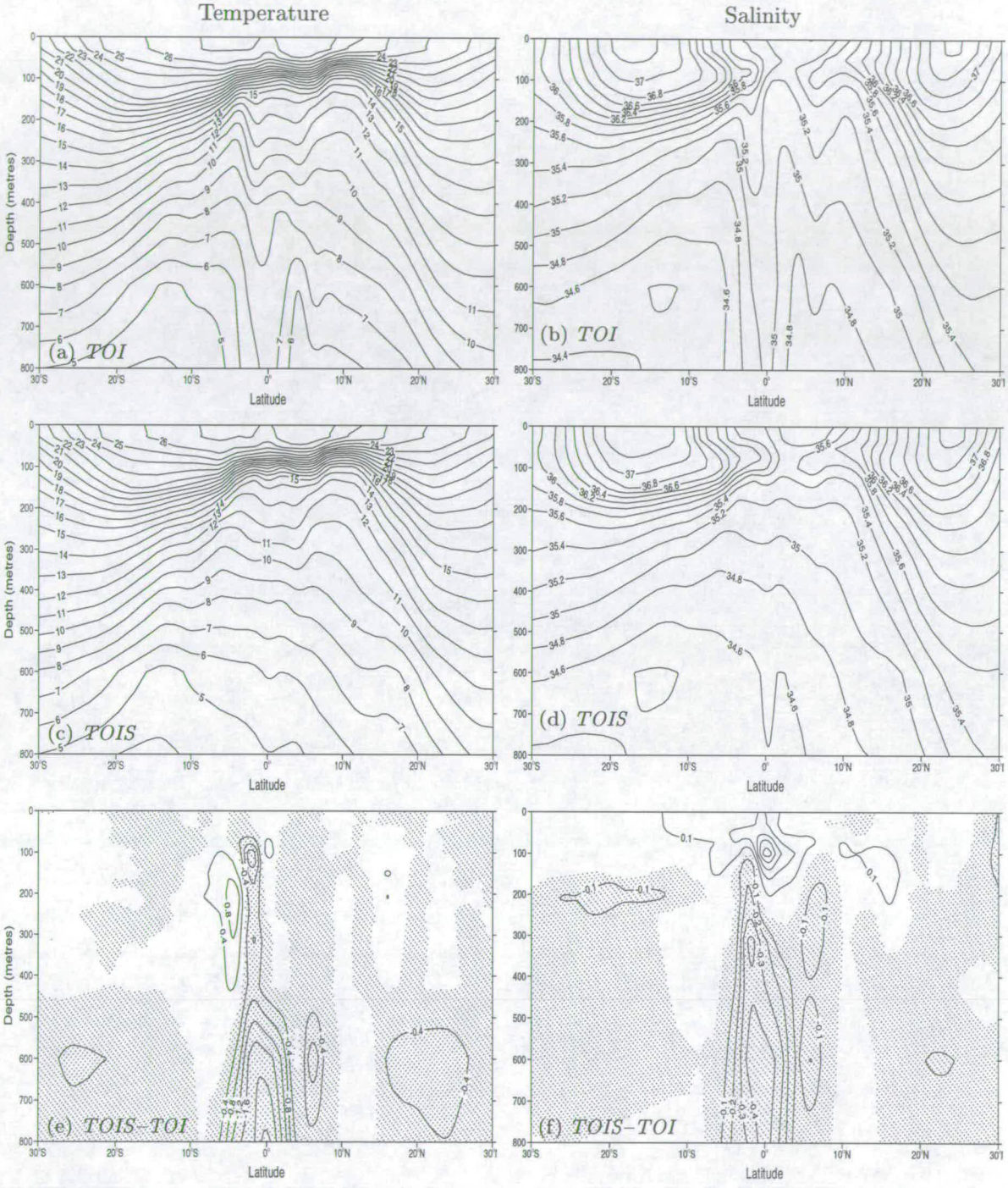


Figure 7.6: Meridional sections at 30°W of the 9-year mean (1990-1998). Temperature (a) and salinity (b) for the OI-only run (exp. *TOI*); Temperature (c) and salinity (d) for the OI plus salinity scheme run (exp. *TOIS*); *TOIS–TOI* temperature difference (e) and *TOIS–TOI* salinity difference (f). Negative values are shaded. The enhanced vertical mixing is evident in *TOI* between 7°S and 8°N (a-b). This causes large differences both in T and S between *TOIS* and *TOI* (e-f).

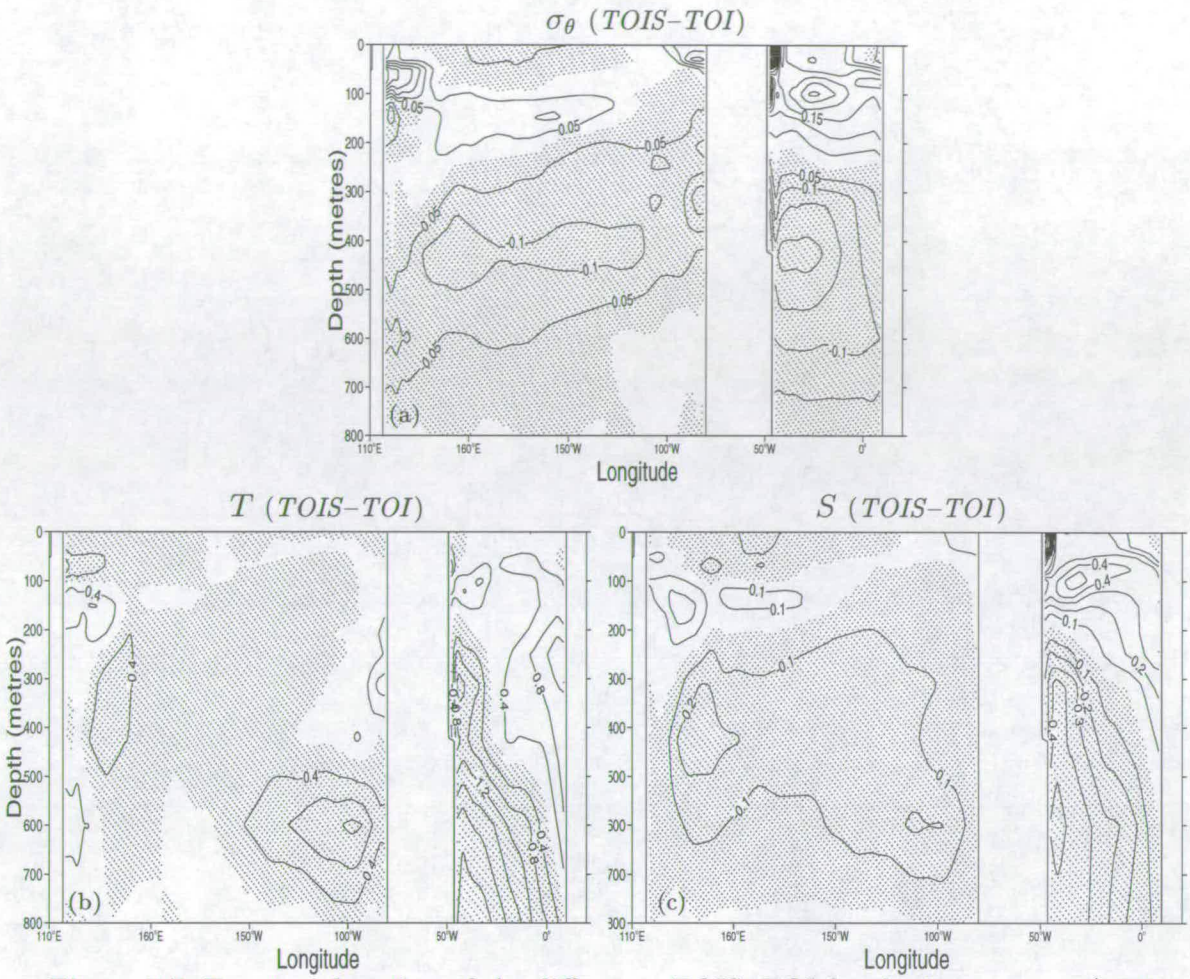


Figure 7.7: Equatorial section of the difference *TOIS–TOI* for the 9-year mean (1990-1998) for (a) σ_θ, (b) temperature and (c) salinity. Negative values are shaded.

observations are relatively abundant in this region throughout the 1990–1998 period. The section along 165°E is one of the best observed but even here data coverage is poor. The most thorough analysis of the temporal variability of salinity along the 165°E section is that of Kessler (1999) (hereafter K99). We will compare results from our model assimilations with K99's analysis, though direct comparison is not easy, since Kessler had to fill data gaps and smooth the results. Sometimes the section is occupied only twice in a year and then only at a couple of stations. Figure 1 from K99 illustrates this point very well.

Figure 7.8a shows the temporal evolution of the salinity maximum at 165°E, averaged over 3°S to 5°S for both *TOI* (dashed) and *TOIS* (solid). K99's interpolated values are shown by the heavy curve. We use the S maximum from the model and compare it with the equivalent observed quantity which has been recalculated for us by Kessler (priv. comm.), rather than the value of S on $\sigma_\theta = 24.5$ kg m^{-3} as in K99.

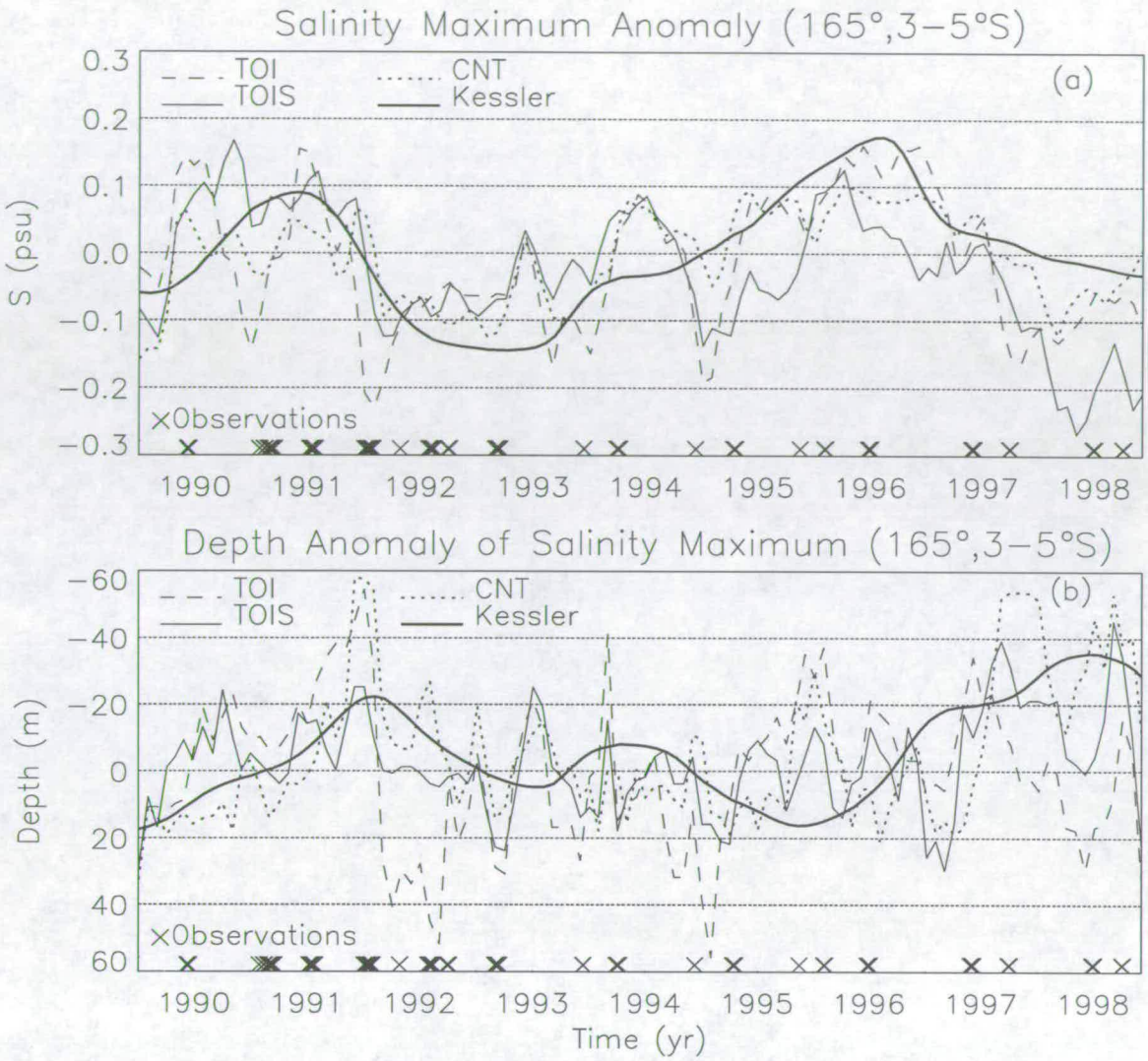


Figure 7.8: Temporal evolution at (165°E, 3-5°S) of the salinity maximum (a) and its depth (b) for *TOI* (dashed), *TOIS* (solid), *CNT* (dotted) and Kessler (1999) data (heavy line) with respect to their own 1990-1996 mean. The times of observations are shown by the crosses on the time axis.

The times of observations are shown by the crosses on the time axis. Only anomalies are plotted, relative to a mean spanning the years 1990-1996. The mean value salinity for K99 is 35.83 psu. The model mean values are all fresher than this. The difference is largest for *TOI*, 0.24 psu, somewhat smaller but still sizeable in the case of *TOIS*, 0.19 psu, and smallest in the case of the control, 0.11 psu. It should be noted, though, that these smaller values are partly due to the model vertical resolution which is much lower than that of CTDs.

With respect to the variability, the two assimilation experiments capture the low frequency signal seen in the data quite well, with high values in 1990–91, low values

in 1992–93 and then increasing until 1996. This rising trend already discussed in K99 is not maintained after 1996 and salinity values drop in 1997. The extension of K99's analysis, to include later values after 1996, confirms the drop in salinity (Fig. 7.8a). Although the *TOI* values do not reach as low as those in *TOIS*, the drop from the peak in 1997 is just as large. The control integration *CNT* does not show such a large drop as either of the assimilation experiment and indeed agrees better with K99. We will return to this point later.

The model results all show more variability than the K99 curve, which is however a heavily smoothed interpretation of the data. It is difficult to say how appropriate the model variability is, but we note that both *TOI* and *TOIS* have larger fluctuations than *CNT*, and so there is a possibility that the data assimilation is introducing noise into the salinity field.

Still, it is not clear from this figure if *TOIS* is better than *TOI* or not. In Figure 7.8b, the anomalous depth of the salinity maximum is shown for the two experiments. The analysed depth from K99 is also shown, again heavily smoothed. This figure shows less obvious agreement between the model values and K99's analyses. What is obvious is that *TOI* has much wilder excursions than is the case for *TOIS*. These large excursions are related to the spurious mixing events in *TOI* discussed earlier. Although they are most acute at the equator, they can also occur off the equator as this figure shows. In terms of mean values, *TOIS* is closest to K99's data: 158 m for *TOIS* against 166 m for the latter. The mean values for *TOI* and *CNT* are 150 m and 144 m, respectively.

We now look at specific profiles and consider the event emphasised by Ji *et al.* (2000), for which salinity seems to play an important role in the density structure. Ji et al.'s two assimilation experiments, one with only T data and the other with T plus altimeter data, yielded a large sea level difference (up to 9 cm), spanning several degrees of latitude around the equator between 140°E and 140°W, starting early in 1995 and peaking in mid-1996. In order to try to explain the cause of this sea level discrepancy, they examined the observed salinity difference taken from two CTD profiles at (165°E, 2°S), one at the beginning of the episode (2 May 1995, hereafter CTD95) and the other near its peak (10 July 1996, hereafter CTD96). In particular, the CTD95 salinity profile is fresher than the CTD96, down to a depth of about 180 m. Ji et al. argue that the interannual S variation would account for about 5 to 10 dyn cm difference comparable with the estimate of Maes and Behringer (2000).

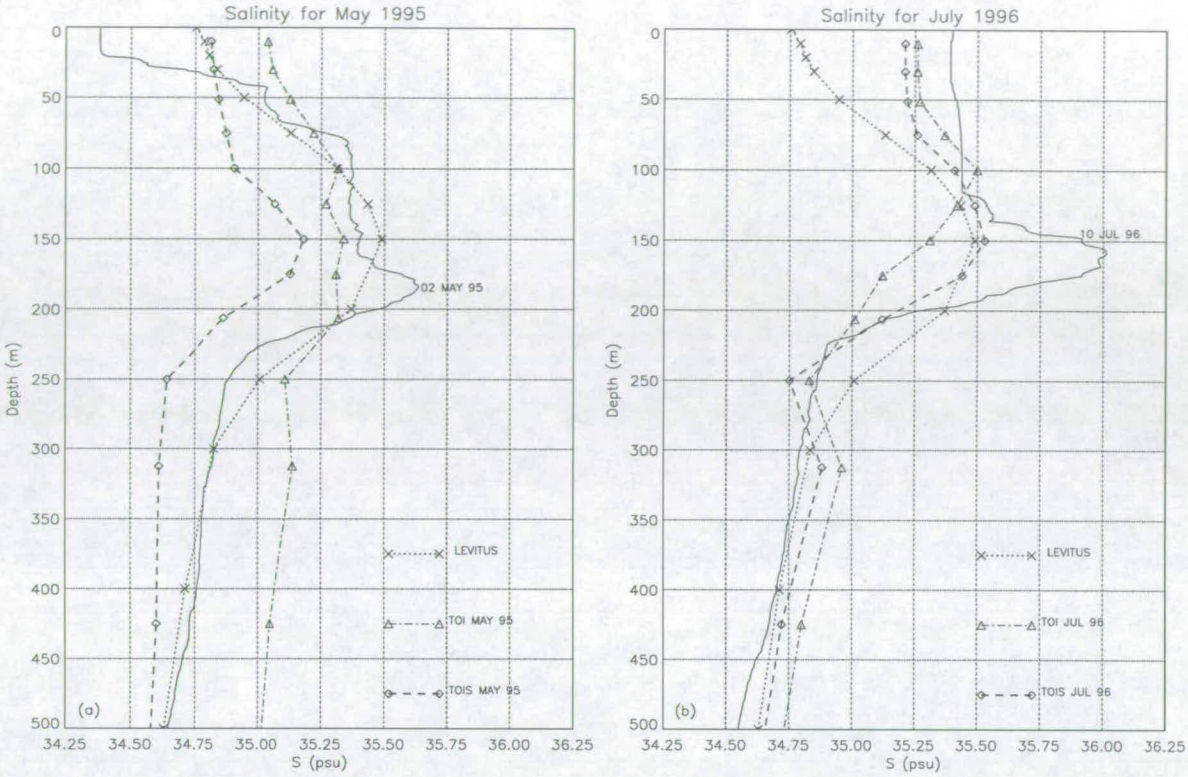


Figure 7.9: Salinity profiles at (165°E, 2°S) from instantaneous CTD data (solid lines) and monthly averages for *TOI* (dash-dotted) and *TOIS* (dashed) for May 1995 (a) and July 1996 (b). Also plotted is the annual Levitus salinity profile (dotted) to which *TOI* and *TOIS* are relaxed.

In Figures 7.9a-b we consider the same two CTD profiles and compare them respectively with the May 1995 and July 1996 monthly average profiles for *TOI* and *TOIS*. These comparisons will not be exactly equivalent because there is only one CTD profile available for each month at the chosen location, thus precluding a temporal average. [On a time scale of order one month, the CTD rms variability could be as large as 0.2 psu in the thermocline and even larger closer to the surface (cf. Fig. 4.2 for the 10-day period).] As a reference, the Levitus annual salinity profile at (165°E, 2°S), to which *TOI* and *TOIS* are relaxed, is also plotted in Figs. 7.9a-b.

The agreement of the S profile for May 1995 for *TOI* and *TOIS* with CTD95 is not particularly good (Fig. 7.9a). However, while the salinity maximum in *TOI* is marginally closer to CTD95, the shape of the profile in *TOIS* is more realistic both at the surface and at depth. As a consequence of the enhanced mixing, the S profile in *TOI* is almost homogeneous: S varies by only about 0.3 psu in the top 500 m, about half that of *TOIS*.

The observed salinity maximum in CTD96 of about 36 psu is not reached by either *TOI* or *TOIS* (Fig. 7.9b). However, *TOIS* agrees generally better than *TOI* with the observed profile, CTD96. In particular, the depth of the S maximum for *TOIS* is closer to that of CTD96. Both model profiles present a peculiar inversion at 250 m to 300 m depth. Since this is present in both *TOI* and *TOIS* we conclude that it is not a feature of the salinity scheme. As it is not present in *CNT*, it must be caused by the OI procedure, and may be related to the fact that the T assimilation is done level by level.

Vossepoel and Behringer (2000) (hereafter VB) compare their model results with CTD casts also, using casts close to those shown in Fig 7.9. Ji *et al.* (2000) do not show model salinity profiles so we can not compare with their results. The fit to CTD96 in the top 250 m in Fig. 16 of VB is also poor, and worse than in *TOIS* by up to 50%: near the surface the difference with CTD96 is 0.25 psu compared to 0.17 psu in *TOIS*, and at the depth of the S maximum it is 0.75 psu compared to 0.5 psu in *TOIS*. Yet, below 250 m the fit to CTD96 in VB is very good, better than in either of our assimilation runs or in our control run. This may arise in part from the time scale used to relax the salinity to climatology: we have a relaxation constant of 1 year, whereas they use a value of 50 days. However, it is generally not easy to compare the results of two assimilation methods. The VB method is active only in the upper hundred meters or so. In our approach, there is no such restriction.

Whilst one would expect a better fit at depth (as in Fig. 16 of VB, or indeed between Levitus and CTD96 in Fig 7.9b), it should also be noted that some salinity variability is still present even below 250 m. For example, Fig. 2 in Vossepoel *et al.* (1999) shows a standard deviation of 0.1 psu at around 300 m, even though a much more local analysis yielded a value of 0.02 psu (Fig. 4.2). In any case, this salinity variability indicates that a strong feedback to climatology is not necessarily desirable.

The salinity variability is further analysed by means of a Hovmoller plot of $S(z)$ at (165°E, 2°S) for *TOI* (Fig. 7.10a) and *TOIS* (Fig. 7.10b). The episodic and extended flooding of the deeper layers with high salinity water mass (more than 35 psu, i.e. unshaded regions) is clearly visible in *TOI*, as for instance in the 1993-95 period. This is the effect of the strong vertical mixing discussed in section 7.3.1 and it does not appear in *TOIS* (Fig. 7.10b).

The interannual S variability in the *TOIS* run looks generally plausible. Several

features of the variability seem to correspond with K99's data from Figure 7.8, although the location of the data is slightly further south than the area plotted here. Note that the persistent salinity maximum (S larger than 35.4 psu), from the beginning of 1990 to the second half of 1991, as well as the salinity up-lifting, corresponding to the 1991-1992 El-Niño, are in agreement with the observations. Also, the shoaling of the S maximum associated with the 1994-1995 warm event and the increase in the salinity maximum starting at the beginning of 1996 are represented by *TOIS*. Figure 7.10 also shows the dates on which the two profiles of Figure 7.9 were taken. Because of the relatively high frequency variability in both model assimilations, it is clear that comparing individual profiles can give only limited information on how well interannual variability is represented. This fact, coupled with the sparsity of the observed data and thus our inability to produce plots such as Figure 7.10 from data, means that a detailed and reliable assessment of *TOI* and *TOIS* in terms of salinity variability is not possible. Clearly some broad features are captured, as shown in Figure 7.8, but salinity data does not (yet) have the space time coverage to say much more than this.

7.3.3 Sea level variability

We will now assess the impact of the salinity scheme on the sea level variability. We begin by considering the 1995–96 period. Ji et al.'s temperature data assimilation experiment showed poor representation of sea level in the case when only T was assimilated and this lead them to examine the role of salinity. Our corresponding experiment, *TOI*, does not show this disagreement when compared to T/P altimeter data. This does not mean that we recreate the subsurface salinity well but the convective readjustments present in *TOI* lead to little or no changes in sea level. In particular, in terms of sea level, both *TOI* and *TOIS* are able to reproduce this particular event rather well: differences between *TOI* and *TOIS*, as well as between each of them and altimeter data, are within 2–3 cm, for this region (after removing the 1993-1995 mean in each case).

In Figures 7.11a-d we show the comparison between the T/P sea level observations and *TOIS* (a and c) and *TOI* (b and d) in terms of rms errors (a-b) and correlations (c-d) for the period 1993-1998. These plots have been constructed by taking the T/P gridded products (Le Traon *et al.*, 1998) and the corresponding model fields.

Along the equator in the Pacific, the agreement between the two assimilation exper-

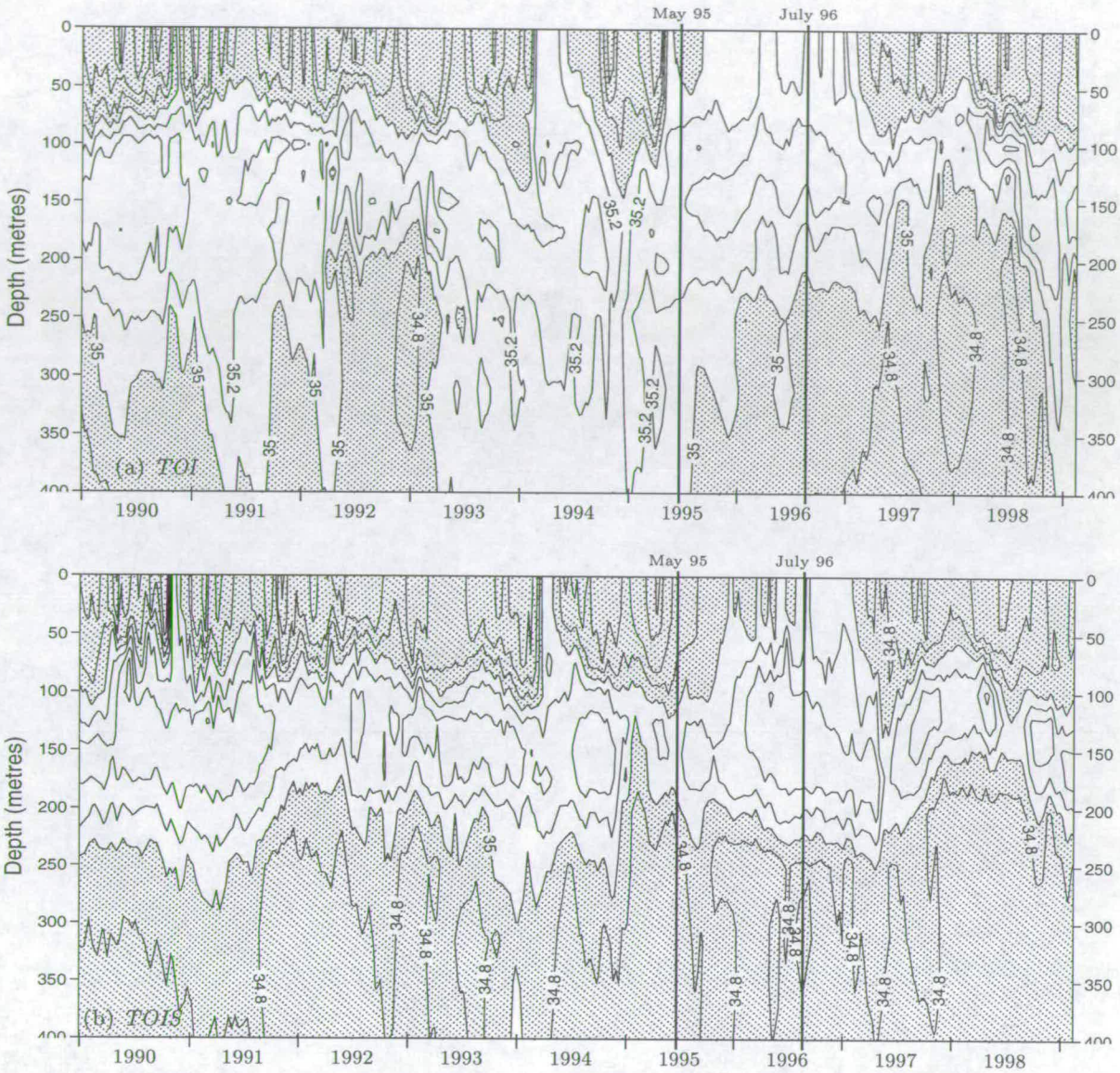


Figure 7.10: Salinity as a function of depth and time at (165°E, 2°S) for *TOI*(a) and for *TOIS* (b). Shading for values smaller than 35 psu. Contour interval is 0.2 psu.

iments and the sea level observations (i.e. T/P) is good. Rms errors with respect to T/P are about 3-4 cm for both *TOIS* and *TOI* (Figs. 7.11a-b), with *TOI* marginally better than *TOIS*. One region where the rms-error differences are larger than the 2–3 cm rms error in T/P is located in the central Pacific at (140°W, 8°S, Fig. 7.11a). What gives rise to this difference has yet to be determined but we know it is a problem in *TOIS* since the rms difference between *TOI* and T/P shows no anomalous behaviour there whereas *TOIS* shows large errors (cf. Figs. 7.11a-b). This is further confirmed by Figure 7.12 which shows the rms differences between *TOI* and *TOIS*.

Rms errors in the equatorial Atlantic are generally larger than in the equatorial

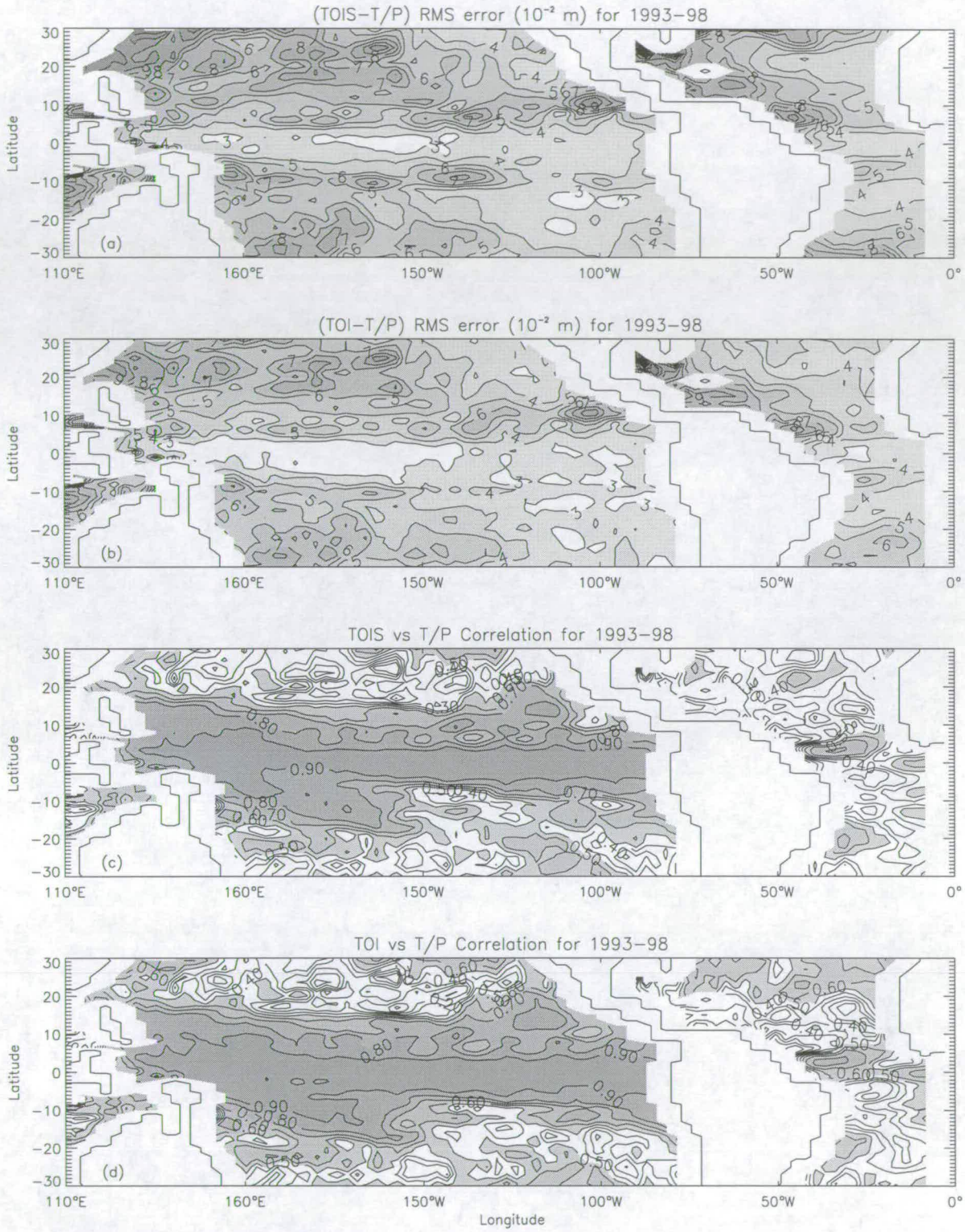


Figure 7.11: Sea surface height rms errors (a-b) and correlations (c-d) for *TOIS* and *TOI* with respect to TOPEX/Poseidon for the period 1993-98. In (a-b) contour interval is 1 cm and shading for values greater than 3 cm; in (c-d) contour interval is 0.1 (10%) and shading for values greater than 0.5 (50%). Data are masked in the vicinity of land points.

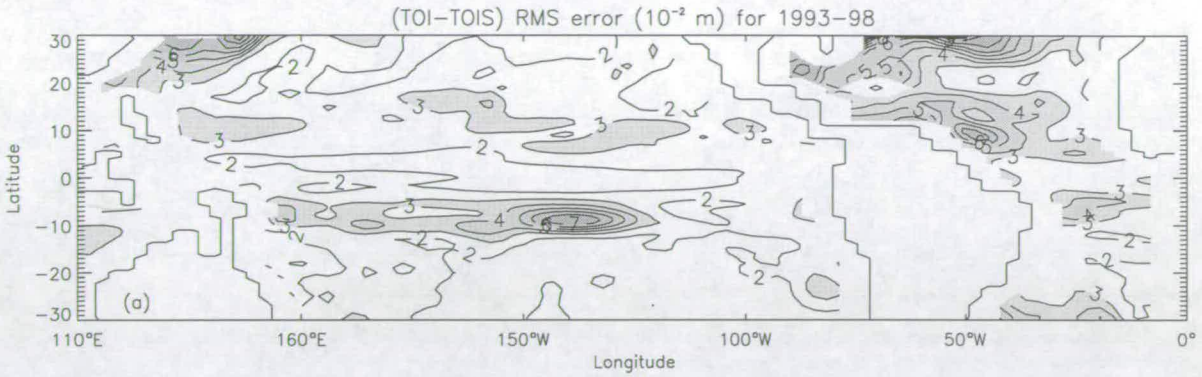


Figure 7.12: As in Figs. 7.11a-b but for *TOI* with respect to *TOI*.

Pacific. The better performance of the Pacific over the Atlantic is mainly caused, as noted in section 7.2.2, by the larger amount of temperature data available for assimilation in the Pacific. In the Atlantic, T observations are more sporadic since they derive from the XBT network rather than the TAO-type array in the Pacific which reports daily.

The correlations between T/P and model sea level (Figs. 7.11c-d) basically confirm the results supplied by the rms errors. In the equatorial Pacific, the correlation is larger than 90% for both *TOIS* and *TOI*. In the equatorial Atlantic, the correlation is less encouraging as it exceeds 70% only in a limited domain.

It should be pointed out that in the rms errors and correlations thus far presented the seasonal cycle is included. We also removed the seasonal cycle, so as to analyse the interannual variability (figures not shown), and diagnosed three different behaviours for the Pacific, Atlantic and Indian Ocean. In the Pacific the assimilation experiments (*TOI* and *TOIS*) have a better fit with T/P than experiment *CNT*. In the Atlantic, instead, the opposite is true, i.e. *CNT* is better than both *TOI* and *TOIS*. Lastly, in the Indian ocean all three experiments are roughly equivalent. These diverse behaviours can be explained by the different amount of temperature observations available for assimilation. In the case of the Pacific, the amount of data is such as to constrain well the interannual variability, whereas the sporadic availability of measurements in the Atlantic affects the variability in such a way as to worsen the interannual variability. Finally, in the Indian ocean where the T observations are even less abundant than in the Atlantic, the impact of the data assimilation is nearly negligible.

7.4 Summary and discussion

The salinity scheme has been applied to the ocean model used at ECMWF, by combining it with the pre-existing temperature Optimal Interpolation (OI) procedure. An experiment in which salinity was corrected (*TOIS*) has been run for the 1990–1998 period and was compared with one in which only temperature is updated (*TOI*). The 9-year mean analysis has shown promising results for *TOIS*, with significant salinity improvements, with respect to *TOI*, especially below 50 m depth. Indeed, persisting $S(z)$ in regions where salinity decreases with depth can lead to first-order error in the model mean state. The water column can become statically unstable and lead to spurious vertical mixing when the temperature increment tends to decrease the thermal stratification. This has a particularly dramatic effect in the tropical Atlantic where there is a strong salinity maximum and where there are not many data to constrain the temperature field. In the experiment *TOIS*, these first-order errors are virtually eliminated as the salinity scheme allows preservation of water mass properties, thus preventing spurious convection from occurring.

In spite of the fact that the salinity profile is generally better reproduced by *TOIS* than *TOI*, the sea level variability, measured by the rms errors between the T/P sea surface height and the two model experiments, is not noticeably improved with *TOIS*. In fact, rms errors and correlations are slightly better in *TOI*, when referred to an independent data set such as T/P sea level.

We have shown that the salinity scheme has its limitations. Both Vossepoel and Behringer (2000) and Maes and Behringer (2000), have extended their schemes to include altimetry. This is clearly a next step for us too. The use of altimeter data in the ECMWF system has been explored with encouraging results by Segschneider *et al.* (2000). We have not yet combined the scheme described here with altimeter data from T/P but work is in progress. One of the main reasons for us becoming interested in salinity came from comparing the model sea-level with real-time altimeter data as part of the DUACS programme of the European Community. This lead to a realisation that salinity was being handled badly in our real-time analysis system. Therefore, we believe that adding the altimeter information to the system presented in this work can only improve the performance of our simulations.

Chapter 8

Conclusions

8.1 Summary

An alternative approach to including a salinity analysis during the assimilation of vertical temperature profiles has been presented. It embraces the hypothesis of T–S relationships as its principal cornerstone. The novelty comes from using T and S fields from recent data, rather than from any climatological data set. The main motivation is that the usual approach of using a long-term average T–S relationship from climatological data is often inadequate in reconstructing the density field because of the long term averaging procedure of a climatology. We suggest therefore that a temporally closer T–S field, such as from a model prediction or any recent CTD data, will provide a better solution.

The method has been tested through a "follow-up strategy". First, temperature and salinity CTD observations, collected from a limited, but geographically significant, region of the western equatorial Pacific, have been used to assess the T–S preservation hypothesis by studying the T and S variances and covariations. The same CTD data are also used to test the assimilation method by combining one profile with another. These tests recover the salinity profiles and the 0-500-m dynamic heights very well (differences are smaller than 1 dyn cm). By contrast, analyses that used a climatological T–S relation did not provide a good salinity profile or dynamic height (errors were greater than 3 dyn cm). Instantaneous model realisations are also used to test the method. Results have been published (Troccoli and Haines, 1999).

Second, a synthetic data assimilation experiment has been run to test the impact of the method in a simplified 3-D primitive equation ocean model. The assimilation run that used the salinity scheme has yielded an improvement larger than 15% in

terms of salinity rms errors with respect to two other reference runs at the end of the 2-year experiment. We noted, however, that, related to the technique used, there is a lower bound to the improvement of the run which used the salinity scheme, A_{ST}. This lower bound is determined by the difference in the initial condition between A_{ST} and the truth run. Because the assimilation method uses the model background for its analysis, it is not possible in principle to reduce this distance, given that in A_{ST} the different wind forcing keep forming water masses in error, with respect to the truth run. We have also noted that the changes introduced by the data assimilation are poorly retained. This might be related to the relatively small decorrelation radius adopted in this study but also to the fact that the 'wrong' forcings tend to diminish the benefit of the changes inserted in the assimilation through air-sea flux exchange. In addition, water mass analyses in T–S space has shown the potential for diagnosing model defects, particularly if the changes inserted at assimilation time are stored in what we call it *inventory*.

Third, a final test has been carried out by applying the salinity scheme to the ocean model used at ECMWF, by combining it with the pre-existing temperature Optimal Interpolation (OI) procedure. Two data assimilation experiments are performed for the 9-year period 1990-1998, one in which the salinity scheme is applied and the other without. These show that the salinity scheme is effective at maintaining the halocline and thermocline structures especially in tropical regions. In addition to the improvement of the mean state, the scheme allows more temporal variability than relaxation of salinity to climatological data. Some limitations of the scheme are on occasion apparent, however. Results have been submitted in Troccoli *et al.* (2000a) and published in Troccoli *et al.* (2000b).

8.2 Discussion

Previous water mass analyses (e.g. Emery and Dewar, 1982) together with the results presented here have shown that T–S relationships are well preserved over different time scales which depend mainly on the location. Indeed, the T–S preservation assumption holds generally better at low and mid latitudes. In fact, one of the implicit requirements of the scheme is that a wide enough T range be present in the a priori water column. In the tropical regions this condition is met easily but problems may arise as one moves poleward, as inferred by Emery and Dewar (1982) but also as seen in the synthetic data

assimilation experiment discussed in this work. Emery and Dewar (1982) suggested the borderline is at around 40°N (the observations available in the austral hemisphere were only within 10°S), whereas we found that it is a bit northward of that, at about 52°N (our domain covered only the boreal hemisphere), that the T–S relation becomes unusable.

While the results obtained from applying the salinity scheme are promising, it should be noted that some limitations of the scheme are on occasion apparent. These limitations are mainly related to the fact that the T–S relationships are not well preserved when non-isentropic processes are present, such as near the air-sea interface, or when water mass intrusions, with different T–S relations, due to advection occur.

The data assimilation approach of this work has been to use the T–S relationships from the model background along with the observed vertical temperature profiles to correct salinity. A EOF-based similar type of approach has also been tested by Maes (1999) and Vossepoel *et al.* (1999), but in their schemes an extensive back history of salinity is needed both in space and time in order to derive the EOFs. This is a serious limitation in applying the scheme in a global assimilation system such as that used at ECMWF. Indeed, one of the regions of improved response of our scheme in the experiment with real observations was shown to be the tropical Atlantic where the mean state was substantially improved. The tropical Atlantic, an area with limited T and S data coverage, was not considered by either Maes (1999) or Vossepoel *et al.* (1999).

It should be observed, however, that given the simplicity of the salinity scheme, there is a limit to the amount of improvement that can be obtained with it. Therefore other pieces of information might be used in order to further improve the salinity field. This information could be represented by other available observations such as altimeter data, or even by observations which could become available in a near future, namely sea surface salinity (SSS).

Both Vossepoel and Behringer (2000) and Maes and Behringer (2000), have extended their schemes to include altimetry. This is clearly a next step for us too. We have not yet combined the scheme described here with altimeter data from T/P but, at ECMWF, work is in progress. One of the main reasons for ECMWF becoming interested in salinity came from comparing their model sea-level with real-time altimeter data as part of the DUACS programme of the European Community. This led to a

realisation that salinity was being handled badly in their real-time analysis system. Therefore, we believe that adding the altimeter information to a system such as that used at ECMWF one can only improve the performance of the model simulations.

Again, both Vossepoel and Behringer (2000) and Maes and Behringer (2000) have considered using surface salinity, too. A better representation of the SSS would greatly improve the top 50 m of the vertical salinity profile, as found by Reynolds *et al.* (1998). The SSS signal is unable to penetrate below this depth (Reynolds *et al.*, 1998), but combining surface salinity measurements with the salinity scheme should provide a better analysis throughout the water column. This is not idle speculation as there is a real prospect that SSS observations from satellite will become available in the not-too-distant future (Lagerloef *et al.*, 1995), which would thus render this solution possible. In addition, a new network of autonomous profiling floats (Argo), part of the Global Ocean Data Assimilation Experiment (GODAE) project, is being planned. This network will enhance real-time capability for measurement of temperature and salinity through the upper 2000 m and contribute to a global description of the seasonal cycle and interannual variability of the upper ocean thermohaline circulation.

All in all, our results show a method which can overcome many of the troublesome aspects of a univariate temperature scheme. It is not, however, a panacea. The concept of T–S conservation is inappropriate in the surface layer, but the salinity method does seem to work moderately well beneath this layer. Hence, SSS data would greatly help to improve the assimilation scheme. In fact, whilst we could obtain some improvement in the salinity analysis either by including altimeter data or improving the assimilation scheme, it seems unlikely that the salinity field will be well reproduced in ocean models without the inclusion of salinity observations, not only at the surface but also from the subsurface.

8.3 Suggested further work

Presently, the salinity method is being used by Alan Fox and Keith Haines at the University of Edinburgh. Also, on the wake of the promising results in the experiment shown in chapter 7, tests are underway for a possible inclusion of the salinity scheme in the operational version of the ocean model (HOPE model) of the Seasonal Forecasting group at ECMWF.

In the previous section we touched upon two ways to improve upon the salinity

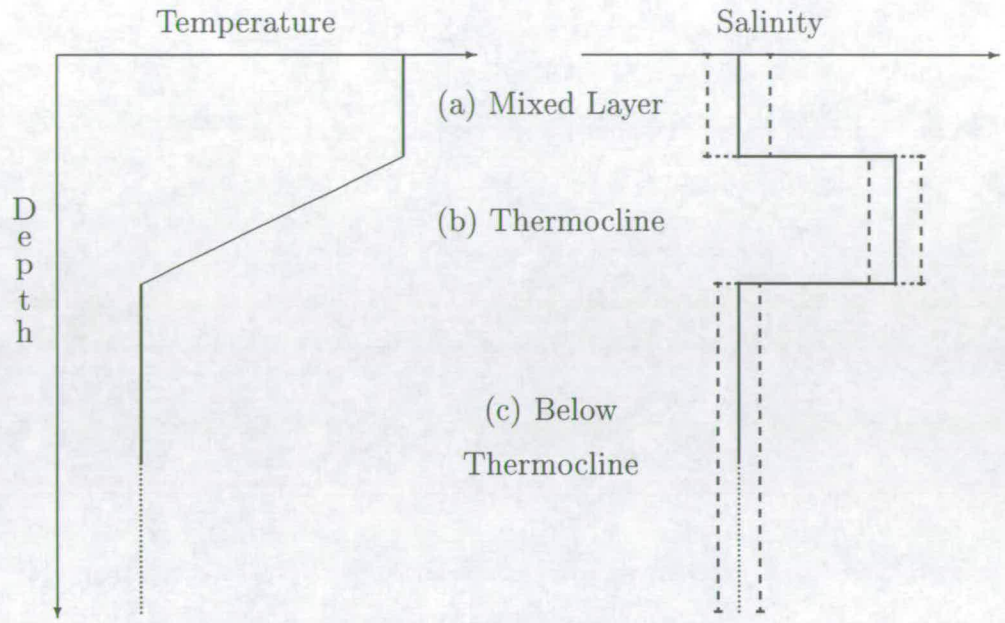


Figure 8.1: Sketch of a temperature (left) and a salinity (right) vertical profile highlighting three principal parts: a) the mixed layer, b) the thermocline and c) the below the thermocline. The dashed lines around the salinity profile represent its uncertainty.

analysis supplied by our salinity method, even though we did not suggest any actual approach to them. We will outline some possible strategies in this section. To recap, one way to improve the salinity method was to complement the salinity scheme with the use of SSH observations and the other with the use of SSS observations. Let us consider them individually.

If we only had SSH available, how could we proceed? Consider two typical low-latitude temperature and salinity profiles. Figure 8.1 shows a schematic for such profiles (solid plus dotted lines) highlighting three principal parts to them: a) the mixed layer, or upper water column, b) the thermocline and c) below the thermocline. Since we need to correct the salinity profile, dashed lines bordering the profile have been drawn (Fig. 8.1), which represent our ignorance, i.e. the uncertainty, of the true profile. Therefore, in our schematic, the true salinity profile could be anywhere within the dashed band. Note that, as we might expect, the uncertainty band decreases with depth, that is it is at a maximum in the mixed layer.

Now, we will use the SSH signal, or rather the difference between the observed and the model SSH, to improve the salinity profile by allowing this profile to move inside the dashed band. To this purpose we introduce three coefficients, that is one for each

layer: c_a, c_b, c_c, respectively, starting from the mixed layer. Further, in general, we would expect the coefficient for the mixed layer, c_a, to be the largest, given the presence of errors both in the model mixed layer and in the surface forcings, and the lowest for that below the thermocline, c_c. These coefficients will then be adopted to generate a new salinity profile which, integrated together with the temperature profile, yields the observed SSH.

In spite of the fact that some difficulties can already be anticipated, such as the value and the sign of the three coefficients (c_a, c_b and c_c), we believe that the approach suggested here could represent a valid starting point towards an improvement of the vertical salinity profiles. For example, depth or location dependent coefficients might be eventually conceived as a further step.

Note that in the preceding discussion, no reference to a particular data assimilation system was made. In fact, the two T and S profiles could indeed be any two profiles. However, the use of the three coefficients will depend upon any prior knowledge of the uncertainties of the profiles. For instance, we may use the fact that, with the salinity method, the main uncertainty lies generally in the mixed layer.

If we also had SSS observations, we would use them to correct the upper water column salinity. In the case in which SSH is also available, as would often happen, the latter would be used to correct the mid and lower part of the salinity profile. Therefore, the above three coefficients (c_a, c_b and c_c) would be reduced to two: c_b and c_c only.

Lastly, we just briefly mention two other possible research tracks which deserve some development. The first track is the spatial spreading of the salinity analyses, similarly to that applied to the T field, e.g. through the OI procedure in chapter 7; the second track is the introduction of a feedback of the salinity analysis, possibly after the salinity spreading, to the temperature field, so as to further optimise the density field by taking care that the T–S relation is preserved at the end of the assimilation procedure.

Bibliography

Alves, J. O. S., Anderson, D. L. T., Stockdale, T. N., Balmaseda, M. A. and Segschneider, J.: 1999, Sensitivity of ENSO forecasts to ocean initial conditions, *Proceedings of the International Symposium, Triangle'98, Sep 29-Oct 2, Kyoto, Japan*, pp. 21–30.

Anderson, D. L. T.: 1995, The Tropical Ocean Global Atmosphere programme, *Contemp. Phys.* **36**, 245–265.

Anderson, D. L. T., Scheinbaum, J. and Haines, K.: 1996, Data assimilation in ocean models, *Rep. Progr. Phys.* **10**, 1209–1266.

Ando, K. and McPhaden, M. J.: 1997, Variability of surface layer hydrography in the tropical Pacific ocean, *J. Geophys. Res.* **102**, 23 063–23 078.

Apel, J. R.: 1987, *Principles of Ocean Physics*, Academic Press Inc. 634 pp.

Bailey, R., Gronell, A., Phillips, H., Tanner, E. and Meyers, G.: 1994, Quality control cookbook for XBT data, *Technical Report No. 221*, CSIRO Marine Laboratories. 20 pp.

Baum, S. K.: 1997, Glossary of oceanography and the related geosciences with references, Texas Center for Climate Studies, Texas A&M University, http://stommel.tamu.edu/~baum/paleo/paleogloss/paleogloss.html.

Behringer, D. W., Ji, M. and Leetmaa, A.: 1998, An improved coupled model for ENSO prediction and implications for ocean initialization. Part I: The ocean data assimilation system, *Mon. Wea. Rev.* **126**, 1013–1021.

Bell, T. H.: 1975, Statistical features of sea-floor topography, *Deep Sea Res.* **22**, 883–892.

Bindoff, N. L. and McDougall, T. J.: 1994, Diagnosing climate change and ocean ventilation using hydrographic data, *J. Phys. Oceanogr.* **24**, 1137–1152.

Böning, C. W.: 1989, Influences of a rough bottom topography on flow kinematics in an eddy-resolving circulation model, *J. Phys. Oceanogr.* **19**, 77–97.

Böning, C. W., Doscher, R. and Isemer, H. J.: 1991, Monthly mean wind stress and Sverdrup transports in the North Atlantic - A comparison of the Hellerman-Rosenstein and Isemer-Hasse climatologies, *J. Phys. Oceanogr.* **21**, 221–235.

Bryan, K.: 1969, A numerical method for the study of the circulation of the World Ocean, *J. Comput. Phys.* **4**, 347–376.

Carton, J. A. and Hackert, E. C.: 1989, Application of multi-variate statistical objective analysis to the circulation in the tropical Atlantic Ocean, *Dynamics of Atmospheres and Oceans* **13**, 491–515.

Carton, J. A., Giese, B. S., Cao, X. and Miller, L.: 1996, Impact of altimeter, thermistor, and expendable bathythermograph data on retrospective analyses of the tropical Pacific Ocean, *J. Geophys. Res.* **101**, 14 147–14 159.

Cooper, M. and Haines, K.: 1996, Altimetric assimilation with water property conservation, *J. Geophys. Res.* **24**, 1059–1077.

Cooper, N.: 1988, The effect of salinity on tropical ocean models, *J. Phys. Oceanogr.* **18**, 697–707.

Cox, M. D.: 1984, A primitive equation, 3-dimensional model of the ocean, *Technical Report No. 1*, Geophysical Fluid Dynamics Laboratory/NOAA, Princeton University, Ocean Group.

Cox, M. D.: 1985, An eddy resolving numerical-model of the ventilated thermocline, *J. Phys. Oceanogr.* **15**, 1312–1324.

Cox, M. D.: 1987, An eddy-resolving numerical-model of the ventilated thermocline - Time-dependence, *J. Phys. Oceanogr.* **17**, 1044–1056.

Cox, M. D. and Bryan, K.: 1984, A numerical model of the ventilated thermocline, *J. Phys. Oceanogr.* **14**, 674–687.

Cushman-Roisin, B.: 1994, *Introduction to Geophysical Fluid Dynamics*, Prentice Hall, Englewood Cliffs, New Jersey. 320 pp.

Da Silva, A. M., Young, C. C. and Levitus, S.: 1994, Atlas of surface marine data 1994. volume 4: Anomalies of fresh water fluxes, *Technical Report 1*, U.S. Department of Commerce, National Oceanographic and Atmospheric Administration.

Daley, R.: 1991, *Atmospheric Data Analysis*, Cambridge University Press. 457 pp.

Delcroix, T., Eldin, G. and Hénin, C.: 1987, Upper ocean water masses and transports in the western tropical Pacific (165°E), *J. Phys. Oceanogr.* **17**, 2248–2262.

Derber, J. and Rosati, A.: 1989, A global oceanic data assimilation system, *J. Phys. Oceanogr.* **19**, 1333–1347.

Donguy, J. R.: 1994, Surface and subsurface salinity in the tropical Pacific Ocean. Relations to climate, *Prog. in Oceanography* **34**, 45–78.

Emery, W. J.: 1975, Dynamic height from temperature profiles, *J. Phys. Oceanogr.* **5**, 369–375.

Emery, W. J. and Dewar, L. J.: 1982, Mean temperature-salinity, salinity-depth and temperature-depth curves in the North Atlantic and North Pacific, *Prog. in Oceanography* **16**, 219–305.

Emery, W. J. and Meincke, J.: 1986, Global water masses: summary and review, *Oceanol. Acta* **9**, 383–391.

Emery, W. J. and O'Brien, A.: 1978, Inferring salinity from temperature or depth for dynamic height computations in the North Pacific, *Atmos.-Ocean* **16**, 348–366.

Fischer, M., Latif, M., Flugel, M. and Ji, M.: 1997, The impact of data assimilation on ENSO simulations and predictions, *Mon. Wea. Rev.* **125**, 819–829.

Fox, A. D., Haines, K., de Cuevas, B. A. and Webb, D. J.: 2000a, Altimeter assimilation in the OCCAM global model, Part I : A twin experiment, *J. Mar. Sys.* submitted.

Fox, A. D., Haines, K., de Cuevas, B. A. and Webb, D. J.: 2000b, Altimeter assimilation in the OCCAM global model, Part II: TOPEX/POSEIDON and ERS1 assimilation, *J. Mar. Sys.* submitted.

Ghil, M. and Malanotte-Rizzoli, P.: 1991, Data assimilation in meteorology and oceanography, *Adv. Geophys.* **33**, 141–266.

Gill, A. E.: 1982, *Atmosphere-Ocean Dynamics*, Academic Press Inc. 662 pp.

Grey, S. M., Haines, K. and Troccoli, A.: 2000, A study of temperature changes in the upper North Atlantic: 1950-94, *Journal of Climate* **13**, 2697–2711.

Haines, K.: 1994, *Dynamics and Data Assimilation in Oceanography*, Vol. 19 of *Data Assimilation: Tools for Modelling the Ocean in a Global Change Perspective.*, P. Brasseur and J. Nihoul Eds., NATO ASI, pp. 1–32.

Hasumi, H. and Suginohara, N.: 1999, Atlantic deep circulation controlled by heating in the Southern Ocean error estimates, *Geophys. Res. Letters* **26**, 1873–1876.

Helland-Hansen, B.: 1916, Nogen hydrografiske metoder, *Forhandlinger ved de 16 Skandinaviske Naturforskeremøte* pp. 357–359.

Hellerman, S. and Rosenstein, M.: 1983, Normal monthly wind stress over the world ocean with error estimates, *J. Phys. Oceanogr.* **13**, 1093–1104.

Hogg, N. G.: 1996, *Oceanographic data for parameter estimation*, Vol. 17 of *Modern Approaches to Data Assimilation in Ocean Modelling*, P. Malanotte-Rizzoli, Ed., Elsevier, p. 455.

Isemer, H. J. and Hasse, L.: 1987, *The Bunker climate atlas of the North Atlantic Ocean*, Vol. 2 *Air-Sea Interactions*, Springer-Verlag. 256 pp.

Ji, M., Behringer, D. W. and Leetmaa, A.: 1998, An improved coupled model for ENSO prediction and implications for ocean initialization. Part II: The coupled model, *Mon. Wea. Rev.* **126**, 1022–1034.

Ji, M., Reynolds, R. W. and Behringer, D. W.: 2000, Use of TOPEX/Poseidon sea level data for ocean analyses and ENSO prediction: Some early results, *Journal of Climate* **13**, 216–231.

Josey, S., Kent, E. and Taylor, P.: 1999, New insights into the ocean heat budget closure problem from analysis of the SOC air-sea flux climatology, *Journal of Climate* pp. 2856–2880.

Katz, E. J., Busalacchi, A., Bushnell, F., Gonzalez, F., Gourdeau, L., McPhaden, M. and Picaut, J.: 1995, A comparison of the ocean surface height by satellite altimeter, mooring, and inverted echo sounder, *J. Geophys. Res.* **100**, 25 101–25 108.

Kessler, W. S.: 1999, Interannual variability of the subsurface high salinity tongue south of the Equator at 165°E, *J. Phys. Oceanogr.* **29**, 2038–2049.

Kessler, W. S. and Taft, B. A.: 1987, Dynamic heights and zonal geostrophic transports in the central tropical Pacific during 1979–84, *J. Phys. Oceanogr.* **17**, 97–122.

Killworth, P. D., Stainforth, D., Webb, D. J. and Paterson, S. M.: 1991, The development of a free-surface Bryan-Cox-Semtner ocean model, *J. Phys. Oceanogr.* **21**, 1333–1348.

Kleeman, R., Moore, A. M. and Smith, N. R.: 1995, Assimilation of subsurface thermal data into a simple ocean model for the initialization of an intermediate tropical coupled ocean-atmosphere forecast model, *Mon. Wea. Rev.* **123**, 3103–3113.

Lagerloef, G. S. E., Swift, C. T. and Vine, D. M. L.: 1995, Sea surface salinity: the next remote sensing challenge, *Oceanography* **8**, 44–50.

Le Traon, P. Y., Nadal, F. and Ducet, N.: 1998, An improved mapping method of multisatellite altimeter data, *J. Atmos. Oceanic Technol.* **15**, 522–534.

Levitus, S. and Boyer, T. P.: 1994, World Ocean atlas 1994. Volume 4: Temperature, *Technical Report No. 4*, U.S. Department of Commerce, National Oceanographic and Atmospheric Administration. 129 pp.

Levitus, S., Burgett, R. and Boyer, T. P.: 1994, World Ocean atlas 1994. Volume 3: Salinity, *Technical Report No. 3*, U.S. Department of Commerce, National Oceanographic and Atmospheric Administration. 111 pp.

Lorenc, A. C.: 1986, Analysis methods for numerical weather prediction, *Quar. J. R. Meteor. Soc.* **112**, 1177–1194.

Lozier, M. S., McCartney, M. S. and Owens, W. B.: 1994, Anomalous anomalies in averaged hydrographic data, *J. Phys. Oceanogr.* **24**, 2624–2638.

Lozier, M. S., Owens, W. B. and Curry, R. G.: 1995, The climatology of the North Atlantic, *Prog. in Oceanography* **36**, 1–44.

Lukas, R. and Lindstrom, E.: 1991, The mixed layer of the western equatorial Pacific Ocean, *J. Geophys. Res.* **96**, 3343–3357. (Suppl.).

Maes, C.: 1998, Estimating the influence of salinity on sea level anomaly in the ocean, *Geophys. Res. Letters* **25**, 3351–3354.

Maes, C.: 1999, A note on the vertical scales of temperature and salinity and their signature in dynamic height in the western Pacific Ocean: Implications for data assimilation, *J. Geophys. Res.* **104**, 11 037–11 048.

Maes, C. and Behringer, D. W.: 2000, Using satellite-derived sea level and temperature profiles for determining the salinity variability: A new approach, *J. Geophys. Res.* **105**, 8537–8547.

Maes, C., Behringer, D. W., Reynolds, R. W. and Ji, M.: 2000, Retrospective analysis of the salinity variability in the western tropical Pacific ocean using an indirect minimization approach, *J. Atmos. Oceanic Technol.* **17**, 512–524.

Malanotte-Rizzoli, P. and Holland, W. R.: 1986, Data constraints applied to models of the ocean general circulation. Part I: The steady case, *J. Phys. Oceanogr.* **16**, 1665–1682.

Malanotte-Rizzoli, P. and Holland, W. R.: 1988, Data constraints applied to models of the ocean general circulation. Part II: The transient, eddy-resolving case, *J. Phys. Oceanogr.* **18**, 1093–1107.

Malanotte-Rizzoli, P. and Tziperman, E.: 1996, *The oceanographic data assimilation problem: overview, motivation and purposes*, Vol. 17 of *Modern Approaches to Data Assimilation in Ocean Modelling*, P. Malanotte-Rizzoli, Ed., Elsevier, p. 455.

Malanotte-Rizzoli, P., Young, R. E. and Haidvogel, D. B.: 1989, Initialization and data assimilation experiments with a primitive equation model, *Dynamics of Atmospheres and Oceans* **13**, 349–378.

Mellor, G. L.: 1996, *Introduction to Physical Oceanography*, Springer-Verlag. 260 pp.

Moore, A. M. and Anderson, D. L. T.: 1989, The assimilation of xbt data into a layer model of the tropical Pacific Ocean, *Dynamics of Atmospheres and Oceans* **13**, 441–464.

Moore, A. M., Cooper, N. S. and Anderson, D. L. T.: 1987, Initialization and data assimilation in models of the Indian Ocean, *J. Phys. Oceanogr.* **17**, 1965–1977.

Myers, P. G., Haines, K. and Josey, S.: 1998, On the importance of the choice of wind stress forcing to the modelling of the Mediterranean Sea circulation, *J. Geophys. Res.* **103**, 15 729–15 749.

Niiler, P. P.: 1992, *The ocean circulation*, Climate system modeling, edited by Trenberth K.E., Cambridge Univ. Press, p. 788.

Pacanowski, R. C. and Philander, S. G. H.: 1981, Parameterization of vertical mixing in numerical models of the tropical oceans, *J. Phys. Oceanogr.* **11**, 1443–1451.

Pedlosky, J.: 1987, *Geophysical Fluid Dynamics*, Springer-Verlag. 710 pp.

Percival, D. B. and Walden, A.: 1998, *Spectral Analysis for Physical Applications*, Cambridge University Press. 584 pp.

Philander, S. G. H.: 1990, *El Niño, La Niña and the Southern Oscillation*, Academic Press, San Diego, CA. 289 pp.

Philander, S. G. H., Hurlin, W. J. and Pacanowski, R. C.: 1987, Initial conditions for a general circulation model of tropical oceans, *J. Phys. Oceanogr.* **17**, 147–157.

Pickard, G. L. and Emery, W. J.: 1992, *Descriptive Physical Oceanography*, sixth edn, Pergamon Press, Oxford, England. 241 pp.

Pond, S. and Pickard, G. L.: 1983, *Introductory Dynamical Oceanography*, second edn, Pergamon Press. 329 pp.

Redi, M. H.: 1982, Ocean isopycnal mixing by coordinate rotation, *J. Phys. Oceanogr.* **12**, 1154–1158.

Reynolds, R. W. and Smith, T. M.: 1995, A high resolution global sea surface temperature climatology, *Journal of Climate* **8**, 1571–1583.

Reynolds, R. W., Ji, M. and Leetmaa, A.: 1998, Use of salinity to improve ocean modeling, *Phys. Chem. Earth* **23**, 543–543.

Roemmich, D., Morris, M., Young, W. R. and Donguy, J. R.: 1994, Fresh equatorial jets, *J. Phys. Oceanogr.* **24**, 540–558.

Rosati, A., Gudgel, R. and Miyakoda, K.: 1995, Decadal analysis produced from an ocean data assimilation system, *Mon. Wea. Rev.* **123**, 2206–2228.

Rosati, A., Gudgel, R. and Miyakoda, K.: 1996, *Global ocean data assimilation system*, Vol. 17 of *Modern Approaches to Data Assimilation in Ocean Modelling*, P. Malanotte-Rizzoli, Ed., Elsevier, p. 455.

Rosati, A., Miyakoda, K. and Gudgel, R.: 1997, The impact of ocean initial conditions on ENSO forecasting with a coupled model, *Mon. Wea. Rev.* **125**, 754–772.

Saunders, P. M., Coward, A. C. and deCuevas, B. A.: 1999, Circulation of the Pacific Ocean seen in a global ocean model: Ocean Circulation and Climate Advanced Modelling project (OCCAM), *J. Geophys. Res.* **104**, 18 281–18 289.

Segschneider, J., Anderson, D. and Stockdale, T.: 2000, Towards the use of altimetry for operational seasonal forecasting, *Journal of Climate*. in press.

Semtner, A. J.: 1974, A general circulation model for the World Ocean, *Technical Report No. 8*, UCLA Department of Meteorology. 99 pp.

Smith, N. R., Blomley, J. E. and Meyers, G.: 1991, A univariate statistical interpolation scheme for subsurface thermal analyses in the tropical oceans, *Prog. in Oceanography* **28**, 219–256.

Sprintall, J. and McPhaden, M. J.: 1994, Surface layer variations observed in a multiyear time series measurements from the western equatorial Pacific, *J. Geophys. Res.* **99**, 963–979.

Stewart, R. H.: 2000, Introduction to Physical Oceanography, Department of Oceanography, Texas A&M University, http://www-ocean.tamu.edu/education/-common/notes/contents.html.

Stockdale, T. N., Anderson, D. L. T., Alves, J. O. S. and Balmaseda, M. A.: 1998, Global seasonal rainfall forecasts using a coupled ocean-atmosphere model, *Nature* **392**, 370–373.

Stommel, H. S.: 1947, Note on the use of the T-S correlation for the dynamic height anomaly computaytions, *J. Mar. Res.* **2**, 85–92.

Trenberth, K., Olson, J. and Large, W.: 1989, A Global Ocean Wind Stress Climatology based on ECMWF Analyses World, *Technical Report NCAR/TN-338+STR*, National Center for Atmospheric Research, Boulder, Colorado. 93 pp.

Troccoli, A. and Haines, K.: 1999, Use of the Temperature-Salinity relation in a data assimilation context, *J. Atmos. Oceanic Technol.* **16**, 2011–2025.

Troccoli, A., Balmaseda, M., Segnschneider, J., Vialard, J., Anderson, D., Haines, K., Stockdale, T. and Vitart, F.: 2000a, Salinity adjustments in the presence of temperature data assimilation, *Mon. Wea. Rev.* to be submitted.

Troccoli, A., Balmaseda, M., Segnschneider, J., Vialard, J., Anderson, D., Haines, K., Stockdale, T. and Vitart, F.: 2000b, Salinity adjustments in the presence of temperature data assimilation, *Technical Report Technical Memorandum No. 305*, ECMWF, Reading, UK.

Tziperman, E.: 1986, On the role of interior mixing and air-sea fluxes in determining the stratification and circulation of the oceans, *J. Phys. Oceanogr.* **22**, 680–693.

Tziperman, E. and Speer, K.: 1994, A study of water mass transformation in the Mediterranean sea: Analysis of climatological data and a simple 3-box model, *Dynamics of Atmospheres and Oceans* **21**, 53–82.

UNESCO: 1981, Tenth report of the joint panel on oceanographic tables and standards, *Technical Report No. 36*, UNESCO Technical Papers in Marine Science, Paris.

Vialard, J. and Delecluse, P.: 1998a, An OGCM study for the TOGA decade. Part I: Role of salinity in the physics of the western Pacific fresh pool, *J. Phys. Oceanogr.* **28**, 1071–1088.

Vialard, J. and Delecluse, P.: 1998b, An OGCM study for the TOGA decade. Part II: Barrier layer formation and variability, *J. Phys. Oceanogr.* **28**, 1089–1106.

Vossepoel, F. C.: 1999, *Sea-level data assimilation for estimating salinity variability in the tropical Pacific*, PhD thesis, University of Delft.

Vossepoel, F. C. and Behringer, D. W.: 2000, Impact of sea level assimilation on salinity variability in the western equatorial Pacific, *J. Phys. Oceanogr.* in press.

Vossepoel, F. C., Reynolds, R. W. and Miller, L.: 1999, Use of sea level observations to estimate salinity variability in the tropical Pacific, *J. Atmos. Oceanic Technol.* **16**, 1401–1415.

Walin, G.: 1982, On the relation between sea-surface heat flow and thermal circulation in the ocean, *Tellus* **34**, 187–195.

Webb, D. J.: 1993, An ocean model code for array processor computers, *Technical Report No. 324*, Institute of Oceanographic Sciences, Wormley, U.K.

WOCE: 1997, World ocean circulation experiment data guide, WOCE International Project Office, Southampton, http://www.soc.soton.ac.uk/OTHERS/woceipo/dguide97.

Wolff, J., Maier-Reimer, E. and Legutke, S.: 1997, The Hamburg Ocean Primitive Equation model, *Technical Report No. 13*, Deutsches KlimaRechenZentrum, Hamburg.

Woodgate, R. A.: 1997, Can we assimilate temperature data alone into a full equation of state model?, *Ocean Modelling* **114**, 4–5.

Worthington, L. V.: 1981, *The water masses of the world ocean: some results of a fine-scale census*, Evolution of Physical Oceanography, MIT Press, Cambridge, Massachusetts, chapter 2, pp. 42–69.

Wyrtki, K., Magaard, L. and Hagar, J.: 1976, Eddy energy in the oceans, *J. Geophys. Res.* **81**, 2641–2646.

Yu, X. and McPhaden, M.: 1999, Seasonal variability in the equatorial Pacific, *J. Phys. Oceanogr.* **29**, 925–947.

A.1 Assimilation Algorithm

```
c=======================================================================c
c  From MOMA main program
c
      CALL ASS_spr_1 (totday,kmt,t_b)
c
c=======================================================================c
c
      SUBROUTINE ASS_spr_1 (totday,kmt,t_b)
c
c***********************************************************************
c          AUTHOR: Alberto TROCCOLI - Nov 1999                         *
c    Department of Meteorology at the Edinburgh University             *
c        Please report any imperfection to the author.                 *
c            E-mail: alberto.troccoli@pd.infn.it                       *
c               or : alberto@met.ed.ac.uk                              *
c                                                                      *
c (see Troccoli and Haines, 1999, J. Atmos. Oceanic Tech., 2011-2025) *
c                                                                      *
c ------   ONLY NON-MONOTONIC SUBROUTINE (ie khatnm)  ------           *
c***********************************************************************
c
c===================    LEGEND for ASSALB   ==========================c
c                                                                      c
c     ddzm : max vertical displacement (in m)                          c
c            (=150m: in principle, latitudinal dependent)              c
c     dtass: min T difference for assim (in C) - if smaller no assim   c
c            (=0.05C: if diff smaller no assim )                       c
c     dzlv : z increments for 'zlev' (in m)                            c
c     dzz  : mid depth levels (differ from model_depth for bottom lev)c
c     kxbt : assimilation level (deepest xbt)                          c
c     lev  : number of arbitrary depth levels                          c
c     ssm  : background (or model) salinity profile                    c
c     ssc  : analysis salinity profile                                 c
c     tsm  : background (or model) temperature profile                 c
c     tsc  : xbt-like temperature profile (e.g. down to 500m) before   c
c            assimilation and analysis T profile after assimilation    c
c     tmask: mask value (or valnull)                                   c
c     zlev : arbitrary depth levels to be used in sub khatnm           c
c=======================================================================c
c
#include "param.h"
#include "assvar.h"
#include "assmoma.h"
```

```
c
      parameter (kxbt=13)              ! kxbt =13 corresponds to 525m
c
      real t_b(km,imt,jmt,nt),t_o(km,imt,jmt,nt)
      real t_in(imt,jmt,km),t_ins(imt,jmt,km)
      real t1(imt,jmt,km),t2(imt,jmt,km),tt(imt,jmt,km)
      real s1(imt,jmt,km),s2(imt,jmt,km),st(imt,jmt,km)
      integer kmt(imt,jmt)
      real dzed(km)                              ! dzed: thickness
      real ddzt(imt,jmt)
c
      real dzlv(lev)
      character fname*80
      logical fass
      logical fasm(imt,jmt)
c
c--                DATA
      data dzz / 10.0,  30.0,  51.0,  75.0, 100.0, 125.0, 150.0,
     &          175.0, 206.0, 250.0, 313.0, 400.0, 525.0, 700.0,
     &          950.0,1375.0,1925.0,2375.0,2725.0,3075.0,3425.0,
     &         3775.0,4175.0/
      data dzed / 20.0e2, 20.0e2, 22.0e2, 26.0e2, 24.0e2, 26.0e2,
     &      24.0e2, 26.0e2, 36.0e2, 52.0e2, 74.0e2, 100.0e2, 150.0e2,
     &      200.0e2, 300.0e2, 550.0e2, 550.0e2, 350.0e2, 350.0e2,
     &      350.0e2, 350.0e2, 350.0e2, 450.0e2/
      data tmask/-2.e0/,smask/45.e0/
      data dtass/1.e-2/
      data dzlv / 1500*5.0e-1, 1000*2.5, 150*5./  ! z range increments
      data ddzm/1.5e2/
c
c=======================================================================
c
c   Choose 'zlev' levels by using 'dzlv' steps.
c
      zlev(1)=5.e-1
      do l=2,lev
        zlev(l)=zlev(l-1)+dzlv(l)
      end do
c
c=======================================================================
c    initialise fields
      do i = 1,imt
      do j = 1,jmt
       fasm(i,j)=.false.
      end do
      end do
```

```
c
c=======================================================================
c time lag in assimilation run
c
      totday=totday + 0.
c
c=======================================================================
c             Get truth field from twin run
c=======================================================================
c
      iof=16
      write (fname,'(i10.10)')nint(totday)
      fname='d'//fname(6:10)//'.rst'
      fname='/ocean/med1/alberto/momarun/run_rb_30d/'//fname
      open(iof,file=fname,form='unformatted',status='old')
c -------------------------------------------------------------
        call readhisa(iof,t_o,totday2)
c -------------------------------------------------------------
      close(iof)
c
c=======================================================================
c
      do i = 1,imt
      do j = 1,jmt
       kmij=kmt(i,j)
      do k=1,km
        t1(i,j,k)=t_b(k,i,j,1)
        tt(i,j,k)=t_o(k,i,j,1)
       if(k.le.kmij) then
        s1(i,j,k)=(t_b(k,i,j,2)+0.035)*1.e3
        st(i,j,k)=(t_o(k,i,j,2)+0.035)*1.e3
       else
        s1(i,j,k)=smask
        st(i,j,k)=smask
       end if
      end do
      end do
      end do
c
c       Calculate increments
c
      do i=1,imt
      do j=1,jmt
      do k=1,km
        t_in(i,j,k)=0.
      end do
```

```
      end do
      end do
c
      do i = 1,imt
       if(i.eq.21.or.i.eq.41.or.i.eq.61) then
        do j = 1,jmt
         kmij=kmt(i,j)
         kbt=min(kxbt,kmij)
        do k=1,kbt
          t_in(i,j,k)=tt(i,j,k)-t1(i,j,k)
        end do
        end do
       end if
      end do
c
      do j = 1,jmt
       if(j.eq.40.or.j.eq.60) then
        do i = 1,imt
         kmij=kmt(i,j)
         kbt=min(kxbt,kmij)
        do k=1,kbt
          t_in(i,j,k)=tt(i,j,k)-t1(i,j,k)
        end do
        end do
       end if
      end do
c
c       Spread increments
c
      call t_map(kxbt,t_in,t_ins)
c
c**********************************************************************
c             SINGLE WATER COLUMN ASSIMILATION                        *
c**********************************************************************
c                           \\|//                                     *
c                           (o o)                                     *
c         ~~~~~~~~~~~~~~oOOo~(_)~oOOo~~~~~~~~~~                       *
c                                                                     *
c**********************************************************************
c             SINGLE WATER COLUMN ASSIMILATION                        *
c**********************************************************************
c                                                                     *
c  The ASSIMILATION subroutine performs an XBT-like data assimilation.*
c  In other words, if your aim is to improve the salinity background  *
c  (or model) field and you only have the temperature measurement     *
c  field (on top of the background one), down to a certain depth,     *
```

```
c  then this code may help you.                                          *
c                                                                        *
c  Schematically:                                                        *
c                                                                        *
c   background (or model) |     ----->     |      analysis              *
c   ---------------------|----------------|----------------             *
c          tsm           |  measurement   |         tsc                *
c          ssm           |  assimilation  |         ssc                *
c                                                                        *
c                PLEASE DO NOT REMOVE THIS NOTICE.                       *
c************************************************************************
c                                                                        *
                    DO i = 2,imt
                    DO j = 2,jmt

      fass=.false.

      kmij=kmt(i,j)

c   Do not assimilate if too shallow
c
      if (kmij.le.2) goto 8501
c
c**    Extract single water column profiles
c
      do k=1,km
        tsm(k)=t1(i,j,k)
        ssm(k)=s1(i,j,k)
        tsc(k)=t1(i,j,k)+t_ins(i,j,k)
      end do
c
      do k=1,km
        ssc(k)=ssm(k)
      end do
c
      kbt=min(kxbt,kmij)
      kbtp1=kbt+1
c
c   OPTIONAL:
c   Calculate max difference between xbt-like and model Ts
c   for the same level. If less than 'dtass' don't assimilate.
c   Note: first point (k=1) not considered.
c
      delt=0.
      do k=2,kbt
       if(tsm(k).gt.tmask) then
```

```
          deltp=abs(tsm(k)-tsc(k))
          delt=max(delt,deltp)
         end if
        end do
        if(delt.lt.dtass) then
         do k=1,kmij
          t2(i,j,k)=t_b(k,i,j,1)
          s2(i,j,k)=(t_b(k,i,j,2)+0.035)*1.e3
         end do
         goto 8501
        end if

c  OPTIONAL:
c   Lower limit to temperature gradient (above a certain depth)
c   in order to avoid T(S) preservation where stratification is low:
c             S(z) persistence used instead
c
        trlm=1.0e-2
        totm=0.0
        totc=0.0
        do k=2,kbtp1
         zrt= dzz(k) -dzz(k-1)
         tltm= tsm(k)-tsm(k-1)
         tltm= tltm / zrt
         tltm= abs(tltm)
         totm= max(tltm,totm)
         tltc= tt(i,j,k)-tt(i,j,k-1)
         tltc= tltc / zrt
         tltc= abs(tltc)
         totc= max(tltc,totc)
        end do
        if(totm.gt.0..or.totc.gt.0.) then
        if(totm.lt.trlm.or.totc.lt.trlm) then
         do k=1,kbt
          t_b(k,i,j,1)=t_o(k,i,j,1)
          t2(i,j,k)=t_o(k,i,j,1)
          s2(i,j,k)=(t_b(k,i,j,2)+0.035)*1.e3
         end do
         do k=kbtp1,km
          t_b(k,i,j,1)=t_b(k,i,j,1)
          t2(i,j,k)=t_b(k,i,j,1)
          s2(i,j,k)=(t_b(k,i,j,2)+0.035)*1.e3
         end do
         if(totm.lt.trlm) then
          write(26,*) 'TBAG in tsm: S(z) assim'
     &          , i,j, kmij,dzz(kmij),tsm(1), tsm(kxbt), tltm
```

```
        else
          write(26,*) 'TBAG in tsc: S(z) assim'
     &          , i,j,kmij,dzz(kmij),tt(i,j,1),tt(i,j,kxbt),tltc
        end if
        goto 8501
       end if
       end if

c*********************************************************************
c                                                                     *
       CALL KHATNM (kmij,kxbt,ddzm,ddz)
c
c*********************************************************************
c                                                                     *
        fass=.true.
        fasm(i,j)=fass
        ddzt(i,j)=ddz
c                                                                     *
c**     Put the analysis single columns in the 3-D array
c
        if (fass) then
         do k=1,km
           t2(i,j,k)=tsc(k)
           s2(i,j,k)=ssc(k)
         end do
        end if
c
 8501 continue
                     END DO
                     END DO
c
c%%%
```

```
c%%%
```

```
      end do
      end do
c**
c
c1  Take the reference temperature (tref) equal to the bottom of
c   the observed (eg XBT) temperature.
c
      tref=tsc(kxbt)

c2  Calculate Tmod=f(z) and Smod=h(z) in 'zlev' levels.
c   Spline returns a km array (eg y2tm) of derivatives
c   Splint returns a lev array (eg ttsm) of interpolated values
c
      call spline(dzz,tsm,kmx,yp1,ypn,y2tm)
      call spline(dzz,ssm,kmx,yp1,ypn,y2sm)

      do L=1,lev
        if(zlev(L).le.dzz(kmx)) then
          call splint(dzz,tsm,y2tm,kmx,zlev(L),ttsm(L,1))
          call splint(dzz,ssm,y2sm,kmx,zlev(L),ttsm(L,2))
        end if
      end do

c   If bathymetry shallower than assimilation level then
c   skip water column displacement bit.
c
      if(kmx.le.kxbt) then
        goto 6251
      end if


c     ********    Displacement section    **********

c3  Determine first max (tmx) & min (tmn) model temp.
c
      tmx=-1.e5
      tmn=1.e5
      do k=1,kmx
       tmx=max(tsm(k),tmx)
       tmn=min(tsm(k),tmn)
      end do

c4  Find, if at all, at what depth 'tref' corresponds
c   in the model temperature profile.
c             First case:
c   if tref is out of the model T range, adopt the
```

```
c   following solution:
c         do not perform displacement of T profile
c         and preserve S=S(z)
c
      if(tref.gt.tmx.or.tref.lt.tmn) then
         do k=kxbt+1,kmx
          tsc(k)=tsm(k)
         end do
         do k=1,kmx
          ssc(k)=ssm(k)
         end do
         goto 9992
      end if

c5            Second (and last) case:
c   if tref is within the model T range, calculate
c   displacement of model T profile with respect to z(tref)
c       (note that search starts from bottom)
c

 5431 continue

c6a Include 'tref' tolerance.
c
      trup=tref+tl1
      trdo=tref-tl1

      do L=lev,1,-1
       if(zlev(L).le.dzz(kmx)) then
         if(ttsm(L,1).ge.trdo.and.ttsm(L,1).lt.trup) then
          ddz=zlev(L)-dzz(kxbt)
          goto 6001
         end if
       end if
      end do

c6b When temperature interval is too small try with a bigger one
c
      tl1=tl1*2

      goto 5431

 6001 continue


c6c optional:
```

```
c   Limiter to prevent large displacements
c
       if(ddz.gt.ddzm) then
         ddz=ddzm
       end if
       if(ddz.lt.-ddzm) then
         ddz=-ddzm
       end if

c    *****   end Displacement section    **********


c7  Complete XBT-like T profile using model T profile
c    (ie by shifting the model T high resolution
c        profile below kxbt)
c
      do k=kxbt+1,kmx
        znn=dzz(k)+ddz
        call splint(dzz,tsm,y2tm,kmx,znn,tn)
        tsc(k)=tn
        if(znn.ge.dzz(kmx)) then
          tsc(k)=tsm(kmx)
        end if
      end do


c8  Assign salinity below kxbt by displacing the model S profile
c    (like for temperature, point 7)
c
      do k=kxbt+1,kmx
        znn=dzz(k)+ddz
        call splint(dzz,ssm,y2sm,kmx,znn,sn)
        ssc(k)=sn
        if(znn.ge.dzz(kmx)) then
          ssc(k)=ssm(kmx)
        end if
      end do

 6251 continue


c9  Assign S to completed T xbt-like profile (sub scann).
c
      call scann (kmx,kxbt,km,lev,dzz,tsm,tsc,ssm,ssc,zlev,ttsm)
```

```
 9992 return
      end

c**********************************************************************
c
      SUBROUTINE SPLINE(X,Y,N,YP1,YPN,Y2)
      PARAMETER (NMAX=1000)
      DIMENSION X(N),Y(N),Y2(N),U(NMAX)
      IF (YP1.GT..99E30) THEN
        Y2(1)=0.
        U(1)=0.
      ELSE
        Y2(1)=-0.5
        U(1)=(3./(X(2)-X(1)))*((Y(2)-Y(1))/(X(2)-X(1))-YP1)
      ENDIF
      DO 11 I=2,N-1
        SIG=(X(I)-X(I-1))/(X(I+1)-X(I-1))
        P=SIG*Y2(I-1)+2.
        Y2(I)=(SIG-1.)/P
        U(I)=(6.*((Y(I+1)-Y(I))/(X(I+1)-X(I))-(Y(I)-Y(I-1))
     *      /(X(I)-X(I-1)))/(X(I+1)-X(I-1))-SIG*U(I-1))/P
11    CONTINUE
      IF (YPN.GT..99E30) THEN
        QN=0.
        UN=0.
      ELSE
        QN=0.5
        UN=(3./(X(N)-X(N-1)))*(YPN-(Y(N)-Y(N-1))/(X(N)-X(N-1)))
      ENDIF
      Y2(N)=(UN-QN*U(N-1))/(QN*Y2(N-1)+1.)
      DO 12 K=N-1,1,-1
        Y2(K)=Y2(K)*Y2(K+1)+U(K)
12    CONTINUE
      RETURN
      END

c**********************************************************************

      SUBROUTINE SPLINT(XA,YA,Y2A,N,X,Y)
      DIMENSION XA(N),YA(N),Y2A(N)
      KLO=1
      KHI=N
1     IF (KHI-KLO.GT.1) THEN
        K=(KHI+KLO)/2
        IF(XA(K).GT.X)THEN
          KHI=K
```

```
        ELSE
          KLO=K
        ENDIF
      GOTO 1
      ENDIF
      H=XA(KHI)-XA(KLO)
      IF (H.EQ.0.) PAUSE 'Bad XA input.'
      A=(XA(KHI)-X)/H
      B=(X-XA(KLO))/H
      Y=A*YA(KLO)+B*YA(KHI)+
     *      ((A**3-A)*Y2A(KLO)+(B**3-B)*Y2A(KHI))*(H**2)/6.
      RETURN
      END

c*****************************************************************
c
      subroutine scann (kmx,kxbt,km,lev,dzz,tsm,tsc,ssm,ssc,zlev,ttsm)
c
c ================================================================
c  This subroutine works out the new S profile preserving the T/S
c  relationship as better as we can. This is done by seeking the new
c  T in the model T/S profile. A depth limiter is also used.
c  Called in KHATNM.
c ================================================================

c==================    LEGEND for Scann ============================c
c                                                                   c
c     cf   : coefficient for T tolerance (adim)                     c
c     cfmx : max cf (adim)                                          c
c     ncto : upper limit for S variables stored in 'smul' (it depends c
c            upon 'tl' and 'zbm')                                   c
c     tl   : temperature (semi-)tolerance (in C)                    c
c     tlmx : max tl (in C)                                          c
c     zbm  : min vertical tolerance - depth dependent (in m)        c
c            (=100m: in principle, it will depend upon the time     c
c             interval chosen for the assimilation (i.e. the longer c
c             the time period between two consecutive assimilations, c
c             the bigger the max distance), and also upon the       c
c             location (it should be larger at higher latitude)     c
c     zbmx : max vertical tolerance - depth dependent (in m)        c
c     zml  : max dist from surface for t_obs=t_mod(1) (in m)        c
c            (=50m: in principle, latitudinal and regional dependent) c
c     zrf  : min vertical distance (in m)                           c
c     zrfm : max vertical distance (in m)                           c
c     zx   : slope for the zbm=zx*dzz+q fn (adim)                   c
c===================================================================c
```

```
      parameter (ncto=5000)
      real ttsm(lev,2)
      real tsc(km),tsm(km),ssc(km),ssm(km)
      real dzz(km),zlev(lev)
      real smul(2,ncto)           ! array to store multiple sal values

      tl=1.0e-1        !  (in C)
      tlmx=5.0e-1      !  (in C)
      cfmx=tlmx/tl     !  (adim)
      zbm=1.0e+2       !  (in m)  overwritten by fn (see below)
      zbmx=2.5e+2      !  (in m)  overwritten by fn (see below)
      zml=5.0e+1       !  (in m)
      zrf = 4.e1       !  (in m)
      zrfm= 2.5e2      !  (in m)
c
c  fn: z=a0+a1*z+a2*z**2
c
      a0=32.8531
      a1=0.169567
      a2=7.10711e-5

      ksa=min(kxbt,kmx)
      do k=ksa,1,-1            ! model levels form bottom to kxbt
        if(tsc(k).lt.tsm(kmx)) then    ! obs < T of deepest model level
          ssc(k)=ssm(kmx)
c    Obs > T of top layer but not deeper than zml
c    (the latter, to avoid too deep unrealistic mixed layers)
        else if(tsc(k).ge.tsm(1).and.dzz(k).lt.zml) then
          ssc(k)=ssm(1)
        else
c
c  variable zbm depending on depth
c
          if (dzz(k).le.zrf) then
           zbm =zrf
           zbmx=zbm
          else
           zbm= a0 + a1*dzz(k) + a2*dzz(k)**2
           zbmx=min(zbm,zrfm)
          end if
c
          cf=1.e0
          do nj=1,ncto
            smul(1,nj)=0.e0
            smul(2,nj)=0.e0
```

```
          end do
 1715     continue
          smul(1,1)=0.e0
          nct=1
          tpep=tsc(k)+tl*cf
          tmep=tsc(k)-tl*cf
          do L=lev,1,-1
           if(zlev(L).le.dzz(kmx)) then
            if(ttsm(L,1).ge.tmep.and.ttsm(L,1).lt.tpep) then
             smul(1,nct)=ttsm(L,2)
             smul(2,nct)=zlev(L)
             nct=nct+1
            end if
           end if
          end do
          if(smul(1,1).gt.1.e-2) then
           ssc(k)=smul(1,1)
           dist=abs(smul(2,1)-dzz(k))
           do nj=2,nct-1
             adist=abs(smul(2,nj)-dzz(k))
             if(adist.lt.dist) then     ! find smallest distance
               ssc(k)=smul(1,nj)
               dist=adist
             end if
           end do
          end if
          if(dist.gt.zbm.or.smul(1,1).lt.1.e-2) then
            cf=cf*1.1e0
            if(cf.gt.cfmx) then
              cf=cfmx
              zbm=zbm*1.1e0
            end if
            if(zbm.gt.zbmx) then
c if outside max T tolerance (tlmx) and max z tolerance (zbmx)
c do not update salinity (for that k level)
              ssc(k)=ssm(k)
              goto 2322
            end if
            goto 1715
          end if
        end if
 2322   continue
      end do

      return
      end
```

```
c
c*****************************************************************
c
      subroutine densm(ti,si,prs,rhoo)
c
c ================================================================
c  This subroutine computes density- 1.025. Called in KHATNM.
c         T = Potential temperature
c    (See: Mellor, 1991, J. Atmos. Oceanic Tech., 609-611)
c ================================================================

      real*4 si,ti,rhoo,prs
      real*8 rhor

      TR=dreal(TI)
      SR=dreal(SI)
c  Approximate pressure in units of bars
      P=dreal(PRS)
c
      rhor = 999.842594 + 6.793952E-2*TR
     $        - 9.095290E-3*TR**2 + 1.001685E-4*TR**3
     $        - 1.120083E-6*TR**4 + 6.536332E-9*TR**5
c
      rhor = rhor + (0.824493 - 4.0899E-3*TR
     $       + 7.6438E-5*TR**2 - 8.2467E-7*TR**3
     $       + 5.3875E-9*TR**4) * SR
     $       + (-5.72466E-3 + 1.0227E-4*TR
     $       - 1.6546E-6*TR**2) * SR**1.5
     $       + 4.8314E-4 * SR**2
c
      cr=1449.1+.0821*P+4.55*TR-.045*TR**2
     $                              +1.34*(SR-35.)
c
      rhor=rhor + 1.e5*P/CR**2*(1.-2.*P/CR**2)
      rhor=rhor-1.e+3
      rhoo=sngl(rhor)
c
      return
      end
c
c*****************************************************************
c ---------------------------------------------------------------
      subroutine readhisa(inf,t3,totday)
c ---------------------------------------------------------------
#include "param.h"
c
```

```
      dimension kmt(imt,jmt)
c
      dimension t3 (km,imt,jmt,nt)
      dimension h03(   imt,jmt)
      dimension u03(   imt,jmt)
      dimension v03(   imt,jmt)
c
c --- read the header for this time step
c
      read(inf) imi,jmi,kmi
      read(inf) itt, totsec, totday, years, kmt
      read(inf) h03,  u03,  v03
      read(inf) t3
c
      return
      end
c
c*****************************************************************
c ---------------------------------------------------------------
c       Spread increments
c ---------------------------------------------------------------
c
      subroutine t_map(kxbt,t_in,t_out)

#include "param.h"
#include "coord.h"
#include "levind.h"

      real t_in(imt,jmt,km),t_out(imt,jmt,km)
      real ytr(jmt), xtr(jmt)
      real t_inew(km),wtot(km)
      real wi,pi
c
      thr=1.e-3
      tint=0.
      do i=2,imtm1
      do j=2,jmtm1
       kmij=kmt(i,j)
       kbt=min(kxbt,kmij)
      do k=1,kbt
        if(abs(t_in(i,j,k)).gt.thr) then
         tint=tint+t_in(i,j,k)
        end if
      end do
      end do
      end do
```

```
c
c function:  a(z) exp(-((x/bx)2 + (y/by)2) cos(phi)-1)
c
      bx0=7.e1
      by=3.e1
      xrd=2.5
      byy=xrd*by
      wcost=1.e+1
      az=1.0e+2
      pi = 4.0 * atan(1.0)
      rad=6370.e0    ! in km
      circ=rad*2.*pi
      circu=circ/360.
c
      do j=1,jmt
        ytr(j) = yt(j) * pi / 180.
      end do
      do i=1,imt
        xtr(j) = xt(i) * pi / 180.
      end do
      xcircu=circu*dxdeg
      ycircu=circu*dydeg

      do i=2,imtm1
      do j=2,jmtm1
      do k=1,km
        t_out(i,j,k)=0.
      end do
      end do
      end do

      do i0=2,imtm1
      do j0=2,jmtm1

       do k=1,km
        t_inew(k)=0.
        wtot(k)=0.
       end do

       bx=bx0*cos(ytr(j0))
       bxx=xrd*bx

       kmij0=kmt(i0,j0)
       kbt0=min(kxbt,kmij0)

       do i=2,imtm1
```

```
      do j=2,jmtm1
       dx = float(i-i0)*xcircu
       if(abs(dx) .gt. bxx) goto 4675
       dy = float(j-j0)*ycircu*0.5*(cos(ytr(j))+cos(ytr(j0)))
       if(abs(dy) .gt. byy) goto 4675
       esp = ((dx/bx)**2+(dy/by)**2)/cos(ytr(j))
        kmij=kmt(i,j)
        kbt=min(kbt0,kmij)
       do k=1,kbt
        if(abs(t_in(i,j,k)).gt.0.) then
         wi = az*exp(-esp)
         t_inew(k)=t_inew(k)+t_in(i,j,k)*wi
         wtot(k)=wtot(k)+wi
        end if
       end do   ! k
4675   continue
       end do   ! i
       end do   ! j

       do k=1,kbt0
       if (wtot(k) .ne. 0) then
         t_out(i0,j0,k)=t_inew(k)/(wtot(k)+wcost)
       endif
       end do

     end do   ! j0
     end do   ! i0
c
     tout=0.
     do i=2,imtm1
     do j=2,jmtm1
       kmij=kmt(i,j)
       kbt=min(kxbt,kmij)
     do k=1,kbt
       if(abs(t_out(i,j,k)).gt.thr) then
        tout=tout+t_out(i,j,k)
       end if
     end do
     end do
     end do

     return
     end
c
c*********************************************************************
```

A.2 Include Files

```
c====================== include file "assmoma.h" ==================
c
      parameter (lev=2800)
      parameter (nin=186)
c
      common/blk1d/
     1      tsc(km),tsm(km),ssc(km),ssm(km),
     2      zlev(lev),dzz(km),                    ! dzz: mid_depth
     3      fdtm(kmm1),fdtc(kmm1),
     4      tch(nin)
c
c-------------------------------------------------------------------

c====================== include file "assvar.h" ==================
#ifdef hcomments
c
c     @(#) SCCS module: assvar.h
c
c     parameters for data assimilation
c
c     assd   = number of days for assimilation switch
c     assts  = true if this is an assimilation timestep
#endif
c
      LOGICAL_N assts
      common /assl/ assts
      common /assv/ ia1, ia2, ja1, ja2, assd
c

c====================== include file "coord.h" ==================
#ifdef hcomments
c
c     @(#) SCCS module: coord.h, version 1.17
c
c                    model grid point coordinates
c
c     grid definition:
c
c     the model uses a staggard arakawa "b" grid. horizontally,
c     tracer quantities are defined at the centers of "t" grid
c     boxes and velocities are defined at the centers of "u,v" grid
c     boxes.  the centers of "u,v" grid boxes are located at the
c     northeast corners of "t" grid boxes. the 1st "t" grid box is
```

```
c     located in the southwest corner of the "t" grid. this grid
c     system is replicated and stacked vertically one on top of
c     another from the surface of the ocean downward. vertically,
c     tracers & velocities are defined at the centers of their
c     corresponding boxes and are at the same depths.
c
c     primary grid information:
c
c     stlon = starting longitude of the "t" grid in degrees. It
c             defines the west face of the 1st "t" grid box.
c     stlat = starting latitude of the "t" grid in degrees. It
c             defines the south face of the 1st "t" grid box
c     dxdeg = east-wast width of grid in degrees
c     dydeg = north-south width of grid in degrees
c
c     xt(i) = longitude of the ith "t" point in degrees.   i=1..imt
c     xu(i) = longitude of the ith "u,v" point in degrees. i=1..imt
c     yt(j) = latitude of the jth "t" point in degrees.    j=1..jmt
c     yu(j) = latitude of the jth "u,v" point in degrees.  j=1..jmt
c     zt(k) = distance (cm) from surface down to center of level k
c             (depth of "t" and "u,v" grid points)
c     zw(k) = distance (cm) from surface down to bottom of level k
c
#endif
      common /coord/ stlon, stlat, dxdeg, dydeg, xt(imt), yt(jmt),
     &               xu(imt), yu(jmt), zw(km), zt(kmp1)


c======================= include file "levind.h" ==================
#ifdef hcomments
c
c     @(#) SCCS module: levind.h, version 1.17
c
c     vertical level indicators which define model geometry &
c     bottom topography:
c
c     kmt = number of vertical boxes over "t" points
c     kmu = number of vertical boxes over "u,v" points
c
#endif
      common /levind/ kmt(imt,jmt), kmu(imt,jmt)


c======================= include file "param.h" ===================
#ifdef hcomments
c
c     @(#) SCCS module: param.h, version 1.17
```

```
c
c     main parameter file which sets ocean characteristics:
c
c     imt    = number of grid points in longitudinal direction
c     jmt    = number of grid points in latitudinal direction
c     km     = number of grid points in the vertical direction
c     nt     = number of tracers
c     lseg   = maximum number of longitudinal stream function
c              segments
c
cat   parameter  (imt=61, jmt=61, km=19, nt=2, imu=imt)
#endif
#ifdef low_res
      parameter  (imt=43, jmt=61, km=19, nt=2, imu=imt)
#else
#ifdef Rough
      parameter  (imt=85, jmt=121, km=23, nt=2, imu=imt)
#else
      parameter  (imt=85, jmt=121, km=19, nt=2, imu=imt)
#endif
#endif
      parameter  (imtp1=imt+1, imtm1=imt-1, imtm2=imt-2,
     &            imum1=imu-1, imum2=imu-2, jmtp1=jmt+1,
     &            jmtm1=jmt-1, jmtm2=jmt-2,
     &            istart=2, iend=imtm1, jscan=jmtm2,
     &            kmp1=km+1, kmp2=km+2, kmm1=km-1)
#ifdef hcomments
c
c     add parameter constants
c
#endif
#include "pconst.h"

c====================== include file "pconst.h" ==================
#ifdef hcomments
c
c     @(#) SCCS module: pconst.h, version 1.17
c
c     rules for parameter constants
c
c     use prefix of "c" for whole real numbers (ie: c57 for 57.0)
c     use "m" after prefix for negative values (ie: cm7 for -7.0)
c     use prefix "p" for non repeating fractions (ie: p5 for 0.5)
c     use prefix "r" for reciprocals (ie: r3 for 1/3.0)
c     combine with "e" for scientific notation,
c       (ie: c5e4 for 5.0e4, c1em10 for 1.0e-10)
```

```
c
#endif
      parameter (c0=0.0, c1=1.0, c2=2.0, c4=4.0, c5=5.0, c8=8.0)
      parameter (c16=16.0, c360=360.0, c100=100.0)
      parameter (p25=0.25, p5=0.5, p75=0.75, p125=0.125)
      parameter (epsln=1.0e-20)
      parameter (c24=24.0, c60=60.0, c1440=1440.0)
      parameter (r24=c1/c24, r60=c1/c60, r1440=c1/c1440)
      parameter (secday=c1/(c60*c1440))
#ifdef hcomments
c
c     stdin, stdout, and stderr set the Fortran units for
c     standard input, standard output, and standard error messages
c     (used in read and write statements)
c
#endif
      integer stdin, stdout, stderr
      parameter (stdin = 5, stdout = 6, stderr = 6)
#ifdef hcomments
c
c     define length of words on different machines
c
#endif
#ifdef cray-t3d
# define LOGICAL_N logical*8
#else
# define LOGICAL_N logical*4
#endif
```